

NUREG/CR-5487
LA-11739-MS
RD

Static Load Cycle Testing of a Low-Aspect-Ratio Four-Inch Wall, TRG-Type Structure TRG-5-4 (1.0, 0.56)

Manuscript Completed: October 1990
Date Published: November 1990

Prepared by
C. R. Farrar, J. G. Bennett, W. E. Dunwoody, W. E. Baker*

Los Alamos National Laboratory
Los Alamos, NM 87545

Prepared for
Division of Engineering
Office of Nuclear Regulatory Research
U.S. Nuclear Regulatory Commission
Washington, DC 20555
NRC FIN A7221

*University of New Mexico, Albuquerque, NM 87131

PREVIOUS REPORTS IN THE SERIES

E. G. Endebrock and R. C. Dove, "Seismic Response of Nonlinear Systems," Los Alamos National Laboratory report LA-8981-MS, NUREG/CR-2310 (September 1981).

E. G. Endebrock, R. C. Dove, and C. A. Anderson, "Margins to Failure - Category I Structures Program: Background and Experimental Plan," Los Alamos National Laboratory report LA-9030-MS, NUREG/CR-2347 (December 1981).

E. G. Endebrock, R. C. Dove, and W. E. Dunwoody, "Analysis and Tests on Small-Scale Shear Walls--FY 82 Final Report," Los Alamos National Laboratory report LA-10443-MS, NUREG/CR-4274 (September 1985).

R. C. Dove and J. G. Bennett, "Scale Modeling of Reinforced Concrete Category I Structures Subjected to Seismic Loading," Los Alamos National Laboratory report LA-10624-MS, NUREG/CR-4474 (January 1986).

R. C. Dove, J. G. Bennett, C. Farrar, and C. A. Anderson, "Seismic Category I Structures Program Final Report, FY 1981-84," Los Alamos National Laboratory report LA-11013-MS, NUREG/CR-4924 (September 1987).

J. G. Bennett, R. C. Dove, W. E. Dunwoody, E. G. Endebrock, C. R. Farrar, and P. Goldman, "Simulated Seismic Tests on 1/42- and 1/14-Scale Category I, Auxiliary Buildings," Los Alamos National Laboratory report LA-11093-MS, NUREG/CR-4987 (October 1987).

J. G. Bennett, R. C. Dove, W. E. Dunwoody, C. R. Farrar, and P. Goldman, "The Seismic Category I Structures Program: Results for FY 1985," Los Alamos National Laboratory report LA-11117-MS, NUREG/CR-4998 (December 1987).

C. R. Farrar and J. G. Bennett, "Experimental Assessment of Damping in Low Aspect Ratio, Reinforced Concrete Shear Wall Structures," Los Alamos National Laboratory report LA-11325-MS, NUREG/CR-5154 (August 1988).

J. G. Bennett, R. C. Dove, W. E. Dunwoody, C. R. Farrar, and P. Goldman, "The Seismic Category I Structures Program: Results for FY 1986," Los Alamos National Laboratory report LA-11377-MS, NUREG/CR-5182 (September 1988).

C. R. Farrar and C. M. Alvord, "Use of Linear Reduced-Stiffness Analytical Models to Predict Seismic Response of Damaged Concrete Structures," Los Alamos National Laboratory report LA-11444-MS, NUREG/CR-5237 (May 1989).

C. R. Farrar, J. G. Bennett, W. E. Dunwoody, and W. E. Baker, "Static Load Cycle Testing of a Low-Aspect-Ratio Six-Inch Wall, TRG-type Structure TRG-4-6 (1.0, 0.25)," Los Alamos National Laboratory report LA-11422-MS, NUREG/CR-5222 (June 1989).

CONTENTS

I.	INTRODUCTION	1
II.	BACKGROUND	3
III.	REVIEW OF PREVIOUS STATIC TEST RESULTS OBTAINED IN THE SEISMIC CATEGORY I STRUCTURES PROGRAM.	7
	A. Isolated Shear Walls.	7
	B. 1/30-Scale, Single-Story, Diesel Generator Buildings.	9
	C. TRG-Type Structures	10
IV.	TRG-5 MODEL CONSTRUCTION AND MATERIAL PROPERTIES	11
V.	MODAL TESTING AND RESULTS.	14
VI.	STATIC TEST SETUP AND LOAD SEQUENCE.	16
VII.	RESULTS FROM INTERNAL GAGE MEASUREMENTS.	19
VIII.	RESULTS FROM THE EXTERNAL GAGE MEASUREMENTS.	25
IX.	COMPARISON OF DEFORMATIONS FORM RELATIVE ABSOLUTE DISPLACEMENTS.	25
X.	ADDITIONAL RESULTS FROM STRAIN GAGE DATA	28
XI.	HYSTERETIC ENERGY LOSSES IN THE TRG-5 STRUCTURE.	30
XII.	OTHER INVESTIGATORS' RESULTS	33
XIII.	CONCLUSIONS.	33
	REFERENCES.	35

APPENDICES

A.	ALBUQUERQUE TEST LABORATORY REPORT	109
B.	LUKE SNELL TEST REPORT	129

FIGURES

Fig. 1.	Prototype TRG structure	38
Fig. 2.	West end wall layer of reinforcement and strain gage locations (All dimensions are in inches).	38
Fig. 3.	North side layer of reinforcement in the shear wall and strain gage locations. (All dimensions are in inches).	39

Fig. 4.	East end wall layer of reinforcement and strain gage locations. (All dimensions are in inches).	39
Fig. 5.	The modal test measurement points. (Some points can not be seen because of hidden line removal).	40
Fig. 6.	Frequency response function obtained from Point 46, in the Y direction, $A(46Y)/F(2Y)$	40
Fig. 7.	Frequency response function obtained from Point 76, Z direction, $A(76Z)/F(2Y)$	41
Fig. 8.	Mode I obtained from the experimental modal analysis of TRG-5	41
Fig. 9.	Undeformed mesh and the first three modes from the finite element analysis using free-free boundary conditions with asymmetric boundary conditions on the plane of symmetry.	42
Fig. 10.	A comparison of the experimentally obtained modal shape and frequency with the analytical computation using ABAQUS.	42
Fig. 11.	Schematic showing the instrumentation location and their purpose	43
Fig. 12.	TRG-5 load vs load step history in terms of average base shear stress.	43
Fig. 13.	TRG-5 load vs load step history in terms of applied force	44
Fig. 14.	Entire load cycle history TRG-5-4(1.0,0.56)	44
Fig. 15.	TRG-5-4 (1.0,0.56) 50-psi ABSS load Cycle 1	45
Fig. 16.	TRG-5-4 (1.0,0.56) 50-psi ABSS load Cycle 2	45
Fig. 17.	TRG-5-4 (1.0,0.56) 50-psi ABSS load Cycle 3	46
Fig. 18.	TRG-5-4 (1.0,0.56) 100-psi ABSS load Cycle I.	46
Fig. 19.	TRG-5-4 (1.0,0.56) 100-psi ABSS load Cycle 2.	47
Fig. 20.	TRG-5-4 (1.0,0.56) 100-psi ABSS load Cycle 3	47
Fig. 21.	TRG-5-4 (1.0,0.56) 150-psi ABSS load half Cycle I	48
Fig. 22.	TRG-5-4 (1.0,0.56) 200-psi ABSS load Cycle 1.	48
Fig. 23.	TRG-5-4 (1.0,0.56) 200-psi ABSS load Cycle 2.	49
Fig. 24.	TRG-5-4 (1.0,0.56) 200-psi ABSS load Cycle 3.	49
Fig. 25.	TRG-5-4 (1.0,0.56) 300-psi ABSS load Cycle 1.	50
Fig. 26.	TRG-5-4 (1.0,0.56) 300-psi ABSS load Cycle 2.	50

Fig. 27.	TRG-5-4 (1.0,0.56) 300-psi ABSS load Cycle 3.	51
Fig. 28.	TRG-5-4 (1.0,0.56) failure load cycle in first direction.	51
Fig. 29.	TRG-5-4 (1.0,0.56) failureload cycle in second direction.	52
Fig. 30.	TRG-5-4 (1.0,0.56) postfailure 50-psi load Cycle 1.	52
Fig. 31.	TRG-5-4 (1.0,0.56) postfailure 50-psi load Cycle 2.	53
Fig. 32.	The method and equations used for reducing the internal gage data	53
Fig. 33.	Free-body diagram of the shear wall	54
Fig. 34.	TRG-5-4 (1.0,0.56) 50-psi ABSS Cycle I (external gages)	54
Fig. 35.	TRG-5-4 (1.0,0.56) 50-psi ABSS load Cycle 2 (external gages). . .	55
Fig. 36.	TRG-5-4 (1.0,0.56) 50-psi ABSS load Cycle 3 (external gages). . .	55
Fig. 37.	TRG-5-4 (1.0,0.56) 100-psi ABSS load Cycle 1 (external gages). . .	56
Fig. 38.	TRG-5-4 (1.0,0.56) 100-psi ABSS load Cycle 2 (external gages) . .	56
Fig. 39.	TRG-5-4 (1.0,0.56) 100-psi ABSS load Cycle 3 (external gages) . .	57
Fig. 40.	TRG-5-4 (1.0,0.56) 150-psi ABSS load half Cycle 1 - Anomaly (external gages).	57
Fig. 41.	TRG-5-4 (1.0,0.56) 200-psi ABSS load Cycle I (external gages) . .	58
Fig. 42.	TRG-5-4 (1.0,0.56) 200-psi ABSS load Cycle 2(external gages). . .	58
Fig. 43.	TRG-5-4 (1.0,0.56) 200-psi ABSS load Cycle 3(external gages). . .	59
Fig. 44.	TRG-5-4 (1.0,0.56) 300-psi ABSS load Cycle I(external gages). . .	59
Fig. 45.	TRG-5-4 (1.0,0.56) 300-psi ABSS load Cycle 2(external gages). . .	60
Fig. 46.	TRG-5-4 (1.0,0.56) 300-psi ABSS load Cycle 3(external gages). . .	60
Fig. 47.	TRG-5-4 (1.0,0.56) failure load cycle in first direction (external gages).	61
Fig. 48.	TRG-5-4 (1.0,0.56) failure load cycle in second direction (external gages).	61
Fig. 49.	TRG-5-4 (1.0,0.56) postfailure 50-psi load Cycle 1 (external gages).	62
Fig. 50.	TRG-5-4 (1.0,0.56) postfailure 50-psi load Cycle 2 (external gages).	62

Fig. 51.	Final crack pattern on west side of the shear wall.	63
Fig. 52.	Final crack pattern on east side of the shear wall.	63
Fig. 53.	Final crack pattern in north end wall	64
Fig. 54.	Strain gage readings in the west end wall compared with SOM theory for the three 50-psi load cycles	64
Fig. 55.	Strain gage reading in the west end wall compared with SOM theory for the three 100-psi load cycles.	65
Fig. 56.	Strain gage readings in the shear wall for the 50-psi cycles. Gages 10-13 may be compared with SOM theory	65
Fig. 57.	Strain gage readings in the shear wall for the 100-psi cycles. Gages 10-13 may be compared with SOM theory	66
Fig. 58.	Strain gage readings in the east end wall compared with SOM theory for the three 50-psi load cycles	66
Fig. 59.	Strain gage readings in the east end wall compared with SOM theory for the three 100-psi load cycles.	67
Fig. 60.	Horizontal component of deformation from internal gages, 50-psi load cycle	67
Fig. 61.	Horizontal component of deformation from external gages, 50-psi load cycle	68
Fig. 62.	Horizontal component of deformation from internal gages, 100-psi load cycle.	68
Fig. 63.	Horizontal component of deformation from external gages, 100-psi load cycle.	69
Fig. 64.	Horizontal component of deformation from internal gages, 150- and 200-psi load cycle	69
Fig. 65.	Horizontal component of deformation from external gages, 150- and 200-psi load cycles.	70
Fig. 66.	Horizontal component of deformation from internal gages, 300-psi load cycle.	70
Fig. 67.	Horizontal component of deformation from external gages, 300-psi load cycle.	71
Fig. 68.	Horizontal component of deformation from internal gages, failure cycle and last 50-psi load cycle.	71
Fig. 69.	Horizontal component of deformation from external gages, failure cycle and last 50-psi load cycle.	72

Fig. 70.	Horizontal component of deformation from internal gages, first load cycle at each stress level	72
Fig. 71.	Horizontal component of deformation from external gages, first load cycle at each stress level	73
Fig. 72.	Horizontal component of deformation from uncorrected external gages, first load cycle at each stress level.	73
Fig. 73.	Horizontal component of shear deformation from internal gages, 50-psi load cycle	74
Fig. 74.	Horizontal component of shear deformation from external gages, 50-psi load cycle	74
Fig. 75.	Horizontal component of shear deformation from internal gages, 100-psi load cycle.	75
Fig. 76.	Horizontal component of shear deformation from external gages, 100-psi load cycle.	75
Fig. 77.	Horizontal component of shear deformation from internal gages, 150- and 200-load cycles.	76
Fig. 78.	Horizontal component of shear deformation from external gages, 150- and 200-psi load cycles.	76
Fig. 79.	Horizontal component of shear deformation from internal gages, 300-psi load cycles	77
Fig. 80.	Horizontal component of shear deformation from external gages, 300-psi load cycles	77
Fig. 81.	Horizontal component of shear deformation from internal gages, failure cycle and last 50-psi load cycle.	78
Fig. 82.	Horizontal component of shear deformation from external gages, failure cycle and last 50-psi load cycle.	78
Fig. 83.	Horizontal component of shear deformation from internal gages, first load cycle at each stress level	79
Fig. 84.	Horizontal component of bending deformation from internal gages, 50-psi load cycle	79
Fig. 85.	Horizontal component of bending deformation from external gages, 50-psi load cycle	80
Fig. 86.	Horizontal component of bending deformation from internal gages, 100-psi load cycle.	80
Fig. 87.	Horizontal component of bending deformation from external gages, 100-psi load cycle.	81

Fig. 88.	Horizontal component of bending deformation from internal gages, 150- and 200-psi load cycles	81
Fig. 89.	Horizontal component of bending deformation from external gages, 150- and 200-psi load cycles	82
Fig. 90.	Horizontal component of bending deformation from internal gages, 300-psi load cycle	82
Fig. 91.	Horizontal component of bending deformation from external gages, 300-psi load cycle	83
Fig. 92.	Horizontal component of bending deformation from internal gages, failure cycle and last 50-psi load cycle	83
Fig. 93.	Horizontal component of bending deformation from external gages, failure cycle and last 50-psi load cycle	84
Fig. 94.	Horizontal component of bending deformation from internal gages, first load cycle at each stress level.	84
Fig. 95.	Horizontal component of bending deformation from external gages, first load cycle at each stress level.	85
Fig. 96.	Ratio of shear to total deformation for the 50-psi cycles.	85
Fig. 97.	Ratio of shear to total deformation for the 100-psi cycles	86
Fig. 98.	Ratio of shear to total deformation for the 150- and 200-psi cycles	86
Fig. 99.	Ratio of shear to total deformation for the 300-psi cycles	87
Fig. 100.	Ratio of shear to total deformation for the failure load cycle and last 50-psi cycle	87
Fig. 101.	Ratio of shear to total deformation for the first load cycle at each stress level	88
Fig. 102.	Ratio of shear to total deformation for the first load cycle at each stress level from the external gages	88
Fig. 103.	Torsional deformation for the 50-psi load cycles	89
Fig. 104.	Torsional deformation for the 100-psi load cycles.	89
Fig. 105.	Torsional deformation for the 150- and 200-psi load cycles	90
Fig. 106.	Torsional deformation for the 300-psi load cycles.	90
Fig. 107.	Torsional deformation for the failure load cycle and last 50-psi load cycle.	91

Fig. 108.	Torsional deformation for the first load cycle at each stress level	91
Fig. 109.	Difference in readings of gages above and below floor for the 50-psi load cycles	92
Fig. 110.	Difference in readings of gages above and below floor for the 100-psi load cycles.	92
Fig. 111.	Difference in readings of gages above and below floor for the 150- and 200-psi load cycles	93
Fig. 112.	Difference in readings gages above and below floor for the 300-psi load cycles.	93
Fig. 113.	Difference in readings of gages above and below floor for the failure load cycle and last 50-psi run	94
Fig. 114.	Difference in readings of gages above and below floor for first load cycle at each stress level.	94
Fig. 115.	Difference in readings of gages above and below ceiling for the 50-psi load cycles	95
Fig. 116.	Difference in readings of gages above and below ceiling for the 100-psi runs	95
Fig. 117.	Difference in readings of gages above and below ceiling for the 150- and 200-psi runs.	96
Fig. 118.	Difference in readings of gages above and below ceiling for the 300-psi runs	96
Fig. 119.	Difference in readings of gages above and below ceiling for the failure load cycles and last 50-psi run.	97
Fig. 120.	Difference in readings of gages above and below ceiling for the first load cycle at each stress level.	97
Fig. 121.	Strain gage data, horizontal rebar in shear wall (Channel 7), 50-psi Cycle 1	98
Fig. 122.	Strain gage data, horizontal rebar in shear wall (Channel 7), 50-psi Cycle 2	98
Fig. 123.	Strain gage data, horizontal rebar in shear wall (Channel 7), 100-psi Cycle I.	99
Fig. 124.	Strain gage data, horizontal rebar in shear wall (Channel 7), 100-psi Cycle 2.	99
Fig. 125.	Strain gage data, horizontal rebar in shear wall (Channel 7), 100-psi Cycle 3.	100

Fig. 126.	Strain gage data, horizontal rebar in shear wall (Channel 7), 150-psi cycle.	100
Fig. 127.	Strain gage data, horizontal rebar in shear wall (Channel 7), 200-psi Cycle I.	101
Fig. 128.	Strain gage data, horizontal rebar in shear wall (Channel 7), 200-psi Cycle 2.	101
Fig. 129.	Strain gage data, horizontal rebar in shear wall (Channel 7), 200-psi Cycle 3.	102
Fig. 130.	Strain gage data, horizontal rebar in shear wall (Channel 7), 300-psi Cycle I.	102
Fig. 131.	Strain gage data, horizontal rebar in shear wall (Channel 7), 300-psi Cycle 2.	103
Fig. 132.	Strain gage data, horizontal rebar in shear wall (Channel 7), 300-psi Cycle 3.	103
Fig. 133.	Strain gage data, horizontal rebar in shear wall (Channel 7), failure cycle.	104
Fig. 134.	Strain gage data, horizontal rebar in shear wall (Channel 7), 400-psi cycle.	104
Fig. 135.	Strain gage data, horizontal rebar in shear wall (Channel 7), 50-psi Cycle 1.	105
Fig. 136.	Strain gage data, horizontal rebar in shear wall (Channel 7), 50-psi Cycle 2	105
Fig. 137.	Strain gage data, horizontal rebar in shear wall (Channel 12), 400-psi cycle.	106
Fig. 138.	Strain gage data, horizontal rebar in shear wall (Channel 12), failure cycle.	106
Fig. 139.	Other investigators' results plus this investigation: a correlation of theoretical and measured stiffness.	107
Fig. 140.	Other investigators' results plus this investigation: A correlation of ACI design load and the measured ultimate load.	107

TABLES

I.	PREVIOUS STATIC TEST RESULTS.	8
II.	MEASURED MATERIAL PROPERTIES.	14
III.	ULTRASONIC TESTING OF TRG-5	14

IV.	COMPARISON OF EXPERIMENTAL AND ANALYTICAL MODAL ANALYSIS RESULTS. .	17
V.	THE RATIO OF MEASURED STIFFNESS TO STIFFNESS CALCULATED BY FINITE ELEMENT ANALYSIS FOR VARIOUS VALUES OF E_c	17
VI.	THEORETICAL STIFFNESS VALUES.	21
VII.	PEAK-TO-PEAK HORIZONTAL DEFORMATIONS.	26
VIII.	PEAK-TO-PEAK SHEAR DEFORMATIONS	27
IX.	PEAK-TO-PEAK BENDING DEFORMATIONS	27
X.	RATIO OF SHEAR DEFORMATION TO TOTAL DEFORMATION AT PEAK LOADS . . .	28
XI.	CRACK OCCURRENCE OR GROWTH FROM STRAIN GAGES ON REBAR IN THE SHEAR WALL	31
XII.	CRACK OCCURRENCE OR GROWTH FROM STRAIN GAGES ON REBAR IN THE END WALLS	31
XIII.	HYSTERETIC ENERGY LOSSES MEASURED ON TRG-5.	32

STATIC LOAD CYCLE TESTING OF A LOW-ASPECT-RATIO
FOUR-INCH WALL, TRG-TYPE STRUCTURE
TRG-5-4 (1.0, 0.56)

by

Charles R. Farrar, Joel G. Bennett,
Wade E. Dunwoody, and William E. Baker

I. INTRODUCTION

This report is the second in a series of test reports that details the quasi-static cyclic testing of low height-to-length aspect ratio reinforced concrete structures. The test structures were designed according to the recommendations of a technical review group for the U.S. Nuclear Regulatory Commission sponsored Seismic Category I Structures Program. The structure tested and reported here had four-inch-thick shear and end walls, and the elastic deformation was dominated by shear. The background of the program and previous results are given for completeness. Details of the geometry, material property tests, construction history, ultrasonic testing, and modal testing to find the undamaged dynamic characteristics of the structures are given. Next the static test procedure and results in terms of stiffness and load deformation behavior are given. Finally results are shown relative to other known results, and conclusions are presented.

Previous work that has been carried out at Los Alamos National Laboratory (LANL) as part of the Seismic Category I Structures Program for the U.S. Nuclear Regulatory Commission (NRC) Office of Nuclear Regulatory Research has consistently measured stiffnesses less than strength-of-materials (SOM) theory would predict in scale models of low-aspect-ratio shear wall structures subjected to working loads. In this context, working loads refer to load levels equivalent to those experienced by a structure during an operating basis

earthquake, which would produce stresses on the order of 50-psi average base shear stress. The models tested thus far have been made of both microconcrete and conventional concrete and have been tested statically and dynamically.

Upon review of these results at the Technical Review Group (TRG) meeting of April 4, 1986, it was decided to extend the experimental investigation of this reduced stiffness issue by performing a series of quasi-static load cycle tests on structures with similar cross-sectional geometries as the structures previously recommended by this group (Ref. 1). The test structures were to be constructed with different aspect ratios and reinforcement percentages so that variations in these parameters that exist in actual Category I structures could be taken into account in the experiments and the sensitivity to these variables could be identified.

One of the purposes of these tests was to investigate the possibility that, at equivalent stress levels, a similar reduction in stiffness occurs during static testing as has been observed during dynamic testing.* In addition, the structures were to be instrumented so that the contribution to bending stiffness of the flexural boundary elements (shear walls in orthogonal planes) could be assessed. The structures were also instrumented so that the shear and bending contributions to the total stiffness could be measured separately. The separation of the shear and bending components of stiffness was intended to provide additional information concerning the mechanism for the reduction in stiffness.

A statistically planned test matrix covering height-to-length aspect ratios from 0.25 to 1.0 and percentage reinforcement ranging from 0.25% to 1.0% in each direction was developed (see Appendix A of Ref. 11). The first structure in the sequence was constructed with an aspect ratio of 1 and a percentage reinforcement of 0.25% in each direction. To remind the reader of the test geometries' basic characteristics, we will adopt the following notation:

* Previous comparisons between static and dynamic tests of isolated shear walls, of a 1/30-scale, single-story, diesel generator building and the TRG-1 and TRG-3 structures have shown that the reduction in stiffness reduction was much more pronounced in dynamic tests than in static tests at similar average base shear stress levels. These structures with the exception of TRG-3 were all small-scale microconcrete models.

TRG-No.-Wt (AR,%R)--sometimes abbreviated as TRG-No.-- where,

TRG = the designation for the series of structures designed and tested using guidance from the program's Technical Review Group, a group of nationally recognized experts on nuclear structures,

No. = the sequence number in the series,

Wt = the shear wall thickness,

AR = the height-to-length aspect ratio of the shear wall, and

%R = total percentage by area of steel reinforcing in both directions.

Thus, this report concerns the second structure in the quasi-static test series, TRG-5-4(1.0,0.56).

The TRG-5 geometry (wall thickness of 4 in.) was not a part of the statistically planned matrix, but rather it was a quasi-static repeat of the TRG-3-4 (1.0, 0.56), which was tested dynamically. Details of the TRG-3 test appear in Ref. 2.

II. BACKGROUND

The Seismic Category I Structures Program is being carried out at LANL under the sponsorship of the NRC's Office of Nuclear Regulatory Research and has the objective of investigating the structural dynamic response of Seismic Category I reinforced concrete structures (exclusive of containment) that are subjected to seismic loads beyond their design basis.

A number of meetings and interactions with the NRC staff have led to a set of specific program objectives, which are as follows:

1. to address the seismic response of reinforced concrete Category I structures, other than containment;
2. to develop experimental data for determining the sensitivity of structural behavior in the elastic and inelastic response range of Category I structures to variations in configuration, design practices, and earthquake loading;
3. to develop experimental data to enable validation of computer programs used to predict the behavior of Category I structures during earthquake motions that cause elastic and inelastic response;
4. to identify floor response spectra changes that occur during earthquake motions that cause elastic and inelastic structural response;
5. to develop a method for representing damping in the inelastic range and to demonstrate how this damping changes when structural response goes from the elastic to the inelastic ranges.

A principal characteristic of the typical structure under investigation is that shear rather than flexure is dominant; that is, the ratio of displacement values calculated from terms identified with shear deformation to the values contributed from bending deformation is one or greater; thus, these buildings are called "shear wall" structures.

The Seismic Category I Structures Program began in FY 1980 with an investigation that identified the typical shear wall structure of a nuclear facility and its characteristics (stiffnesses, frequencies, etc.) as areas where designers of facilities (Bechtel Corporation, Sargent & Lundy, and Tennessee Valley Authority) felt additional experimental data were needed. A combined experimental/analytical plan for investigation of the dynamic behavior of these structures was laid out as described in Ref. 3. During the first phase, the program concentrated on investigating isolated shear wall behavior using small models (1/30-scale, 1-in.-thick walls) that could be economically constructed and tested both statically and dynamically. Also, during this phase of the program, a TRG, consisting of nationally recognized seismic and concrete experts on nuclear civil structures, was established both to review the progress and to make recommendations regarding the technical directions of the program. The recommendations of this group have been evaluated in light of the needs of the NRC and, where possible, have been carefully integrated into the program.

Following the isolated shear wall phase, the program began testing and evaluating three-dimensional box-like model structures. It was recognized from the outset that scale model testing of concrete structures is a controversial issue in the U.S. civil engineering community. Thus, along with the testing of small-scale structures, a task of demonstrating scalability of the results to prototype structures was initiated. The details and results of these investigations are reported in Refs. 4-7.

To give a brief synopsis of the situation at the end of FY 1984, the program had tested (in addition to the isolated shear walls), either statically or seismically, 23 different models representing two types of structure--a diesel generator building and an auxiliary building. Two different scales [(1/30, 1/10) and (1/42, 1/14)] of these buildings were used (1-in. and 3-in. walls). In addition, stories varied from one to three. Although a number of results on items, such as aging (cure time) and effect of increasing seismic magnitude, have been reported, two important and consistent conclusions came out of the

data from these tests. First, the scalability of the results was illustrated both in the elastic and inelastic range. Second, the so-called "working load" secant stiffness of the models was lower than the computed uncracked cross-sectional values by a factor of about 4.

During their review, the TRG pointed out the following:

1. Design of prototype nuclear plant structures is normally based upon an uncracked cross-section SOM approach that may or may not use a "stiffness reduction factor" for the concrete. But, if such a factor is used, it is never as large as 4.
2. Although the structures themselves appear to have adequate reserve margin (even if the stiffness is only 25% of the theoretical), any piping and attached equipment will have been qualified using inappropriate floor response spectra.
3. Given that a nuclear structure designed to have a natural response of about 15 Hz really has a natural frequency of 7.5 Hz (corresponding to a reduction in stiffness of 4) and allowing further that the natural frequency will decrease because of degrading stiffness, the natural response of the structure will shift well down into the frequency range for which an earthquake's energy content is the largest. This will result in increased amplification in the floor response spectra at lower frequencies, and this fact potentially has significant impact on the equipment and on the piping design response spectra and their margins of safety.

Note that all three points are related to the difference between the measured and calculated stiffnesses of these structures.

Having made these observations, several questions arose. Did our previous experimental data taken on microconcrete models represent behavior that would be observed in prototype structures? What is the appropriate value of the stiffness that should be used in design and for component response spectra computations in these structures? Should this value be a function of load level? Have the equipment and piping in existing buildings been qualified to inappropriate response spectra?

Thus, the primary program emphasis at that time was to ensure the credibility of previous experimental work by beginning to resolve the "stiffness difference" issue. The TRG for this program believed that this important issue had to be addressed before the program objectives could be accomplished.

To address these stiffness-related concerns, it was agreed that a series of credibility experiments should be carried out using both large- and small-scale structures. For the large-scale structure, the TRG set limitations on the

design parameters. The recommended "ideal" structure characteristics, in order of decreasing priority, were as follows:

1. maximum predicted bending and shear mode natural frequency ≤ 30 Hz,
2. minimum wall thickness = 4 in.,
3. height-to-depth ratio of shear wall ≤ 1 ,
4. use of actual No. 3 rebar for reinforcing,
5. use of realistic material for aggregate,
6. use of 0.1-1% steel (0.3% each face, each direction, i.e., 0.6% total each direction), and
7. use of water-blasted construction joints to ensure good aggregate interlock.

A prototype "TRG" structure designed to comply with these specifications (Fig. 1) was constructed using actual batch plant concrete and No. 3 rebar. In addition, a 1/4-scale model of the TRG structure was constructed with microconcrete and wire-mesh rebar and was tested prior to the prototype. Both structures were tested statically and then seismically to failure, or in the case of the prototype, to machine limits. The 1/4-scale model was TRG-1-1 (1.0, 0.6), and the prototype was TRG-3-4 (1.0, 0.56). A second 1/4-scale model, TRG-2-1 (1.0, 0.6), was constructed and partially tested. That model had obvious visual flaws (cracked sections) upon form removal and was never fully tested or reported.

These tests were intended to show that the previously observed reductions in stiffness were not related to the use of microconcrete and that the static and dynamic test results of the microconcrete models could be scaled to conventional concrete structures.

During the static tests, the 1/4-scale model, TRG-1-1 (1.0, 0.6), showed results similar to those of the prototype, TRG-3-1 (1.0, 0.56), for stiffness and suggested that, for low-level static response, the microconcrete model did an adequate job of predicting the response of the conventional concrete prototype. A low-force-level experimental modal analysis performed before seismic excitation showed results concerning stiffness and scalability similar to those of the static test.

When the structures were tested dynamically on a shake table, both models showed reductions in stiffness consistent with previous test data, implying that the reduced stiffness could not be attributed to microconcrete. The prototype TRG structure with its added mass was too large to make reproduction of the

input signal possible. This input signal was a scaled version of the one used on the 1/4-scale model, and, because it could not be accurately reproduced (frequency content of the signal was distorted), conclusions concerning the scalability of seismic response between the conventional concrete prototype and the microconcrete model could not be made. The results of these tests appear in detail in Refs. 2 and 8.

At the TRG meeting on December 19, 1986, the group suggested that a reduced statistical plan be carried out. The TRG was not concerned with the technical merit of the plan but rather with the time and cost required to successfully complete the test matrix as well as the deviation from original program objectives. The TRG suggested that one other model with an aspect ratio of 0.25 be statically tested, as well as a structure identical to TRG-3-4 (1.0, 0.56), and this plan was adopted. This report is devoted to that structure, TRG-5-4 (1.0, 0.86).

III. REVIEW OF PREVIOUS STATIC TEST RESULTS OBTAINED IN THE SEISMIC CATEGORY I STRUCTURES PROGRAM

Previously in this program, measured stiffness values from static and dynamic tests have been compared with theoretical values that were determined using a modulus of elasticity calculated from the empirical formula in American Concrete Institute (ACI) 349-85.⁹ The same formula is used for conventional structures as covered in ACI 318-83.¹⁰ This empirical formula generally gave a higher value for the concrete's modulus than was measured from test specimens. In the following summary of previous test results, theoretical stiffness values were determined using measured moduli. This investigation is concerned with determining the proper values of stiffness to be used in the analysis of Seismic Category I structures; hence, it is felt that the best estimate of actual material properties should be used when experimental results are compared with theory. The previously reported comparisons between measured and theoretical stiffness do, however, provide information concerning errors that could occur during the design process when material properties have yet to be measured. Table I summarizes the previous results using both the measured and design values for the concrete's modulus.

TABLE I
PREVIOUS STATIC TEST RESULTS

	Measured Stiffness before Cracking (lb/in.) 1	Ultimate ^a Compressive Strength f'_c (psi)	Theoretical ^b Stiffness Using Measured Modulus (lb/in.) 2	Theoretical ^b Using ACI Empirical Modulus (lb/in.) 3	Ratio of Columns		
					$\frac{2}{1}$	$\frac{3}{1}$	$\frac{2}{3}$
Isolated Shear Walls							
1	0.78 x 10 ⁶	4.34	1.60 x 10 ⁶	2.33 x 10 ⁶	2.05	2.99	0.69
2	0.79 x 10 ⁶	5.89	-	2.71 x 10 ⁶	-	3.43	-
3	1.0 x 10 ⁶	7.35	1.90 x 10 ⁶	3.03 x 10 ⁶	1.90	3.03	0.63
4	1.06 x 10 ⁶	6.86	-	2.92 x 10 ⁶	-	2.75	-
5	0.87 x 10 ⁶	6.31	1.75 x 10 ⁶	2.80 x 10 ⁶	2.02	3.22	0.63
1/30-scale 1-Story Diesel Generator Buildings							
3D-2	0.76 x 10 ⁶	2.70	2.25 x 10 ⁶	2.90 x 10 ⁶	2.96	3.82	0.78
3D-4	1.74 x 10 ⁶	3.32	4.82 x 10 ⁶	6.08 x 10 ⁶	2.77	3.49	0.79
3D-7	0.92 x 10 ⁶	2.35	2.45 x 10 ⁶	2.71 x 10 ⁶	2.66	2.95	0.90
3D-8	0.80 x 10 ⁶	2.30	2.36 x 10 ⁶	2.68 x 10 ⁶	2.95	3.35	0.88
3D-9	1.67 x 10 ⁶	2.69	4.62 x 10 ⁶	5.47 x 10 ⁶	2.77	3.27	0.84
3D-10	1.14 x 10 ⁶	3.27	-	3.19 x 10 ⁶	-	2.80	-
3D-11	0.92 x 10 ⁶	3.09	-	3.11 x 10 ⁶	-	3.38	-
3D-12	1.23 x 10 ⁶	2.05	-	2.53 x 10 ⁶	-	2.06	-
3D-13	0.88 x 10 ⁶	2.04	-	2.52 x 10 ⁶	-	2.86	-
3D-19	0.80 x 10 ⁶	4.70	-	3.83 x 10 ⁶	-	4.79	-
3D-20	1.08 x 10 ⁶	4.30	3.22 x 10 ⁶	3.65 x 10 ⁶	2.98	3.38	0.88
TRG-Type Structures							
TRG-1	0.75 x 10 ⁶	3.77	1.2 x 10 ⁶	1.3 x 10 ⁶	1.60	1.73	0.92
TRG-3	4.4 x 10 ⁶	3.81	3.0 x 10 ⁶	5.0 x 10 ⁶	0.68	1.13	0.60
TRG-4	8.5 x 10 ⁶	4.15	8.4 x 10 ⁶	9.6 x 10 ⁶	0.99		1.13

^aThe empirical modulus, E_{cACI} is $57,000 \sqrt{f'_c}$, and the measured modulus,

E_{cm} , can be computed by the following formula:

$$E_{cm} = 57,000 \sqrt{f'_c} \frac{\text{Stiffness Col. 2}}{\text{Stiffness Col. 3}}$$

^bBased on the gross section.

A. Isolated Shear Walls

The first static tests were performed on single-story isolated shear walls and were reported in Ref. 4. Five walls were tested, two monotonically and three cyclically. These specimens were made with microconcrete and wire-mesh reinforcement. The amount of reinforcement at the interface of the shear wall base and shear wall top plate was varied along with the amount of moment reinforcement in the form of threaded steel rods located at the ends of the shear wall.

All specimens remained essentially linear up to a load producing an average base shear stress (ABSS) of 200 psi and a principal tensile stress (PTS) of 600 psi or more. The load at first cracking, as predicted from an SOM approach, agreed very well with the measured cracking strength of the walls and the average split cylinder tensile strength of 666 psi. Also, when the walls were subjected to repeated load cycles below the first cracking load, there was no evidence of stiffness degradation or of increase in the area of the hysteresis loop for a given load level. Above the first cracking load, stiffness degraded and the area of the hysteresis loop increased with increased load and increased cycles at a constant load. The ultimate strength of the walls exceeds the provisions for shear capacity as determined by ACI 349-85 11.10.⁹ The measured stiffnesses in the linear region were down by a factor of 1.90 to 2.05 from the calculated uncracked cross-section stiffness using a measured modulus.

When normalized to a common modulus of elasticity, these static stiffness values can be compared with those measured dynamically during sine sweep and simulated seismic tests of similar models. At force levels that were 10% of the load required to produce first cracking in the static test, stiffnesses measured during both the sine sweep and simulated seismic tests were reduced considerably from the static tests and even further reduced from the calculated uncracked cross-section values. The sine sweep and seismic resonant frequency values were reduced on the average by a factor of 2.60 and 2.0 from the calculated uncracked value, respectively. This reduction in frequency suggests that stiffness values were down on the average by a factor of 6.95 and 3.95 from the calculated uncracked value, respectively, and down by an average factor of 2.93 and 1.86 from the average measured static value.

B. 1/30-Scale, Single-Story, Diesel Generator Buildings

Eleven 1/30-scale, single-story, diesel generator buildings were statically tested to failure and are reported in Ref. 6. Nine models were tested

monotonically, eight in the transverse direction, and one in the longitudinal direction. Two models were tested cyclically, one each in the transverse and longitudinal directions. These specimens were all made with microconcrete and wire-mesh reinforcement. Other than the direction of applied load, the only parameters that were varied in these tests were the amount of cure time each model experienced before testing and the distance the reinforcement was embedded in the base of the structure.

As with the isolated shear walls, all specimens remained linear up to the load that produced cracking. This load produced an ABSS on the order of 200 psi and a PTS on the order of 340 psi. At a given load level below the first cracking load, the area under the hysteresis loop remained constant when the load was cycled, and the stiffness remained constant. Above the cracking load, stiffness again was observed to degrade, and the area of the hysteresis loop increased either with increases in load level or increases in the number of load cycles. The load at first cracking was in good agreement with the value predicted from SOM and with the measured tensile stress of the concrete. Provisions for the shear capacity of the walls from ACI 349-85 were exceeded. Stiffnesses based on a secant from the origin to one half the ultimate load were lower by factors ranging from 2.7 to 3.0 when compared with the calculated stiffness, based upon an uncracked cross section and a measured modulus.

When similar models were tested dynamically with a 0.5-g peak acceleration random input, producing an ABSS of 6.3 psi and a PTS of 10.6 psi, the models were again found to behave with a stiffness lower by a factor of 2.9 to 3.8 than the SOM prediction using a measured modulus.

It should be noted that the moment of inertia used in the calculated stiffness value considered the entire end wall to contribute to the flexural stiffness of the shear wall, and the modulus of elasticity was based upon the measured values. No effect from cure time or embedment length was observed.

C. TRG-Type Structures

TRG-3 and its two 1/4-scale models, TRG-1 and -2, were tested statically and monotonically at low-load levels that produced an ABSS of 28 psi and a PTS of 40 psi on TRG-3 and an ABSS of 53 psi and a PTS of 80 psi on TRG-1 and -2. These tests were repeated several times and were intended to identify the initial stiffness condition of each model while introducing a minimum amount of damage into the test structure. TRG-3 was constructed with conventional concrete

and No. 3 rebar, and TRG-1 and -2 were made with microconcrete and wire-mesh reinforcement.

TRG-3 showed a measured stiffness that was up by a factor of 1.47 from theory and TRG-1 showed a reduction of 1.60 from theory. In both cases, the theoretical stiffness was computed with a measured value of E_c . However, the measured modulus for TRG-3 was considerably less than the ACI empirical modulus (2.1×10^6 psi compared to 3.5×10^6 psi). TRG-2 was found to have significant shrinkage cracks, and results from this model were not considered meaningful. When properly scaled, the static stiffness values for the two models were in good agreement, showing that stiffness can be scaled from microconcrete to conventional concrete in this low-load-level region. Following static testing, both TRG-1 and TRG-3 were also tested seismically and dynamically. When TRG-1 was subjected to a 0.5-g peak acceleration random input, it responded with a stiffness that was low by a factor of 2.6 from theory even though this excitation produced only 16.3-psi ABSS and 16.6-psi PTS. Similar stiffness values were obtained during a 0.5-g seismic test. TRG-3 responded to a 0.73-g seismic test with a stiffness that was reduced by a factor of 4.0 from theory at an ABSS of 91 psi and a PTS of 92 psi.

TRG-4-6 (1.0, 0.25) was tested statically in a cyclic manner to failure.¹¹ This structure exhibited repeatable linear response with a stiffness that was almost identical to theory until it first cracked at an ABSS of 131 psi and at PTS of 171 psi. The components of stiffness due to shear and bending were separated and these components also agreed with their respective theoretical values. After cracking, the structure again behaved in a linear manner when loaded to levels that did not exceed the peak load during the first cracking cycle. During these cycles, the stiffness was reduced by a factor of two with the loss occurring equally in each component of the stiffness.

IV. TRG-5 MODEL CONSTRUCTION AND MATERIAL PROPERTIES

A primary concern in construction of this model was that it required a minimum amount of handling once it was built. This requirement would eliminate damage caused by handling as a possible source of any measured reduction in stiffness. Following the same procedure as in TRG-4, the model was constructed in place on the base of the load frame that was to be used in the cyclic testing. The load frame was designed to minimize base deflections. The frame

was located in an indoor test facility so that construction, concrete placement, curing, and testing of the model could be performed in a controlled environment.

The reinforcement in both the shear walls and the end walls consisted of No. 3 (3/8-in. diameter) rebar with a specified minimum yield strength of 60 000 psi. The bars were spaced at 4.5 in. on center at the middle of the walls. As shown in Fig. 1, a minimum 1.5 in. of cover was provided for all reinforcement. This exceeds the cover requirements of ACI 349-85, 7.7 for interior walls and meets the required 1.5-in. cover for exterior walls. The top and bottom slabs were heavily reinforced with two layers of No. 4 rebar spaced at 6 in. on center.

Before placing the concrete, 22 Eaton weldable strain gages were attached to the reinforcement at locations shown in Figs. 2-4. The gages were wrapped with fiber glass tape to prevent damage during compaction and damage caused by moisture.

Next, form work was put into place on top-of the load frame base. The bottom 18 in. of the interior wall forms were made of Plexiglas so that the concrete placement and compaction could be visually monitored in this structurally critical region. The concrete was placed on June 11, 1987. The first truck arrived at 10:50 a.m. containing 3 yards of concrete. Slump from this truck was measured per American Society for Testing and Materials (ASTM) standard C143-78¹² and was found to be 3.75 in. This batch of concrete was used to pour the base and bottom one-third of the wall. Mechanical vibrators were continually used to compact the concrete. Fourteen standard 6-in.-diam by 12-in.-high concrete cylinders were taken during the middle of this placement per ASTM standards C172-82¹³ and C31-84¹⁴. The second truck arrived at 1:50 p.m., approximately 50 minutes after the placement of concrete from the first truck was complete. This truck contained 4 yards of concrete. Slump from the second truck was measured at 3.25 in. The concrete from this second truck was used to complete the model. Again, 14 test specimens were taken during the middle of the placement.

The concrete was specified as minimum 3000-psi ultimate compressive strength. Five and one-half sacks of cement were used per cubic yard of concrete, and the cement was Ideal Type 1-2 low alkali. The coarse aggregate was 0.75-in.-maximum, crusher run, Rio Grande river rock, and the fine aggregate was No. 4 sand with gradation conforming to ASTM standard C33-85.¹⁵

The test cylinders were removed from their forms and were placed in a curing chamber approximately 80 h after they had been poured and remained in the chamber for the next 46 d. Forms were left on the model until June 30, 19 days after the model was poured. Exposed surfaces of both the top and bottom slab were kept moist and covered with tarps during this 19-d period. Upon removal of the forms, several voids were found in the end wall of the structure. The voids were repaired using generally acceptable casting techniques, and it was assumed that the structural integrity of the model would be maintained.

The test cylinders were taken to Albuquerque Testing Laboratories (ATL), where they were tested on September 12, 1987. To avoid damage to the specimens while in transit to Albuquerque, a form-lined transportation box was constructed and foam was placed between each of the individual cylinders. Tests included ultimate compressive strength (ASTM C39-84), 16 modulus of elasticity (ASTM C469-83), 17 split cylinder tensile strength (ASTM C4.96-85), 18 and density. Eight specimens from each truck were tested for ultimate compressive strength and modulus of elasticity, and four specimens from each truck were tested for tensile strength. The specimens were weighed to the nearest 0.01 lb. The results of the tests are summarized in Table II, and the report from the testing lab is included as Appendix A.

On August 24-25, 1987, Luke Snell, a faculty member at Southern Illinois University and an experienced independent consultant in the field of ultrasonic testing of reinforced concrete structures, performed an ultrasonic test on the model. He began by visually inspecting the model for surface cracks and found none. Next, he calibrated his testing equipment with a standard steel specimen and proceeded to test the 6-in.-diam by 12-in.-long test specimens. The test consisted of applying an audio pulse to the end of the specimen and measuring the time required for that pulse to travel over the distance of the specimen. From this information, the speed of sound in the concrete can be estimated and defects in the concrete can be identified when the speed is altered as the sound wave cannot travel across a void but, rather, must go around it. The cylinders from the two different trucks showed no significant difference in pulse speed, and tests at different locations on the model that were known to contain concrete from the different trucks showed no significant difference in pulse velocity. Pulse velocities were determined at 128 locations on the model and the results are summarized in Table III. From these results, Mr. Snell,

TABLE II
MEASURED MATERIAL PROPERTIES

	Density (lb/ft ³)	Ultimate ^a Compressive Strength (psi)	Tensile ^b Strength (psi)	Modulus of Elasticity ^c (psi)	57,000 $\sqrt{f_c^T}$ ^d (psi)	33w ^{3/2} $\sqrt{f_c^T}$ ^d (psi)
Average Truck 1	143	4870	355.	3.80x10 ⁶	3.98x10 ⁶	3.94x10 ⁶
Minimum	142	4420	305.	3.33x10 ⁶	3.79x10 ⁶	3.74x10 ⁶
Maximum	144	5130	395.	4.17x10 ⁶	4.08x10 ⁶	4.09x10 ⁶
Average Truck 2	144	5190	345.	3.94x10 ⁶	4.11x10 ⁶	4.11x10 ⁶
Minimum	143	4790	290.	3.55x10 ⁶	3.94x10 ⁶	3.93x10 ⁶
Maximum	145	5410	370.	4.60x10 ⁶	4.19x10 ⁶	4.22x10 ⁶
Ave. Both Trucks	144	5030	350.	3.87x10 ⁶	4.04x10 ⁶	4.02x10 ⁶

^a Measured on 6-in.-diam x 12-in. specimens per ASTM C39-84.

^b Measured on 6-in.-diam x 12-in. specimens per ASTM C496-85.

^c Measured on 6-in.-diam x 12-in. specimens per ASTM C469-83.

^d Modulus of elasticity determined per ACI 349-85, 8.5.1.

TABLE III
ULTRASONIC TESTING OF TRG-5

	Cylinders	Shear Wall	West End Wall	East End Wall	Top	Base
Average Pulse Velocity (ft/s)	14 500	13 500	13 500	13 450	13 000	13 300

concluded that the model indeed showed signs of defects and that material properties determined from the cylinder test specimens might not be indicative of the properties of the TRG-5 structure. The defects were presumed to be the voids that were repaired by standard methods (see the conclusions in Mr. Snell's test report, which is included as Appendix B).

Other investigations¹⁹ have correlated the speed of sound in concrete to the static modulus of elasticity. However, these investigations do not specify the type of static modulus (that is, initial tangent), secant to 40% of ultimate, etc. A similar correlation, made by interpolating between the data points in Ref. 19 with the results of Mr. Snell's test, yields an average modulus of 4.06×10^6 psi for the TRG-5 structure.

V. MODAL TESTING AND RESULTS

The first test performed on the TRG-5 structure was a low-load-level experimental modal analysis. This test was used to characterize the initial stiffness of the model without introducing damage and to demonstrate that the

dynamic properties of the structure could be accurately measured at very low-load levels (less than 1-psi ABSS). The test configuration consisted of supporting the model with five air bearings under its base. This configuration was used because it was very easy to adjust the height of the model by changing the pressure in the air bearings and the motion caused by people walking on the model dampened out much faster. Free-boundary conditions were chosen because they can be most accurately compared with analytical results from either finite element analysis (FEA) or SOM analysis's.

A 300-lb-peak force shaker was attached to the northwest end wall 4 in. from the bottom. A transducer, located between the shaker's stinger and the model, measured force as the input quantity. A random excitation signal with a uniform power spectral density between 0 and 200 Hz was used to drive the shaker. Acceleration response was measured in three orthogonal directions at 89 points on the structure. The measurement points are shown in Fig. 5 along with the excitation point.

The force input and acceleration responses were recorded, transformed into the frequency domain, and analyzed with a commercially available experimental modal analysis software package. Coherence functions showed that the 300-lb shaker had only enough energy to excite the structure at its resonant frequencies. The frequency domain representation of the input and response were used to calculate a set of frequency response functions. Typical examples of the frequency response functions are shown in Figs. 6 and 7 and correspond to responses measured at points 46 and 76 in the Y and Z directions, respectively. Using these plots, resonant frequencies can be identified from zero crossings in the real portion that correspond to peaks at the same frequency in the imaginary portion. Mode shapes were experimentally identified between 0 and 200 Hz. The mode corresponding to the fundamental frequency is shown in Fig. 8.

An FEA modal analysis was also used for comparison with the experimental modal analysis. Half the structure was modeled with free boundary conditions at the base and appropriate boundary conditions applied along the plane of symmetry so that all modes below 200 Hz could be identified. The undeformed mesh and the first three modes are shown in Fig. 9, and a direct comparison between an experimental and FEA mode is shown in Fig. 10. Measured material properties were used in these calculations (modulus of elasticity of concrete = 3.87×10^6 psi). A comparison of the corresponding analytical and experimental modal frequencies is presented in Table IV. The modes that showed up in the FEA but did not show up

in the experimental modal analysis were not sufficiently excited by the amplitude and direction of the applied excitation. A larger shaker and/or change in the direction and location of excitation would have identified these modes. However, it was felt the objectives of the modal testing were accomplished with the one excitation location.

$$\left(\frac{f_{\text{measured}}}{f_{\text{calculated}}}\right)^2 = \frac{k_{\text{measured}}}{k_{\text{calculated}}} \quad (1)$$

Based on the fundamental frequency and noting that where f is frequency in Hz and k is stiffness, a comparison can be made between the low-load-level dynamic stiffness and the calculated stiffness from FEA. The measured stiffness as a percentage of theoretical is summarized for various moduli values in Table V.

Finally, by adjusting the modulus in the finite element analysis so that the fundamental frequencies match the measured fundamental frequency, one can indirectly estimate the actual modulus of the concrete in the TRG-5 model. The value of E_c that made the FEA agree with the measured fundamental frequency was 3.87×10^6 psi, the same value that was determined from the material testing.

The results of the experimental modal analysis show good agreement with the analytical modal analyses and seem to indicate that the initial state of the TRG-5 model was good and the initial stiffness was very close to theoretical. When examining the results, it should be remembered that if nonlinearities due to cracking or voids had existed, they would have produced an excitation amplitude dependent response in the structure and at the load levels used in this test, and the effects of these nonlinearities might not be evident.

The lifting of the TRG-5 structure during the modal analysis was the only handling of the structure during the entire testing sequence and amounted to lifting the structure a few feet vertically and replacing it on the base.

VI. STATIC TEST SETUP AND LOAD SEQUENCE

After the modal testing had been completed, the structure was bolted to the load frame base as depicted in Fig. 1. Two 2-in.-thick steel plates were placed on top of the base, grouted level, and thirty-six, 1.25-in.-diam, steel bolts were placed through the plates in an attempt to obtain a fixed boundary

TABLE IV
COMPARISON OF EXPERIMENTAL AND
ANALYTICAL MODAL ANALYSIS RESULTS

Mode	<u>Experimental</u>	<u>FEA with Measured Modulus</u>
1	31.9	31.9
2	67.0	72.3
3	73.9	79.7
4	77.8	88.4
5	84.4	95.2
6	a	112
7	117	113
8	126	129
9	a	133
10	a	135
11	159	152
12	170	196
13	198	230

a Not identified.

TABLE V
THE RATIO OF MEASURED STIFFNESS TO STIFFNESS
CALCULATED BY FINITE ELEMENT ANALYSIS
FOR VARIOUS VALUES OF E_c

K_m / K_t	Measured E_c	$E_c = 57,000 \sqrt{f'_c}$	$E_c = 33w^{3/2} \sqrt{f'_c}$
	1.01	0.95	0.96

condition. The bolts were torqued to 400 ft-lbs. Next, the two 6-in.-thick steel plates in Fig. 1 were placed on top of the model, grouted level, and held in place by thirty-six 1.25-in.-diam. steel bolts torqued to 400 ft-lbs. Because the load was to be applied by a force acting on the bottom 6-in.-thick steel plate, the connection of these steel plates to the concrete slab was designed to provide a friction connection and hopefully produce a distributed load over the top of the structure. This type of loading would be more indicative of that introduced by a seismic event.

The load frame was then assembled around the model, and an instrumentation frame was also assembled around the model independent from the load frame. Twenty-four Ono-Sokki EG-233 displacement transducers were placed on the model and on the instrumentation frame as shown Fig. 11. Ten gages were mounted on the model itself, providing relative displacement readings that were independent of a rigid body rotation and translation. Of these ten, eight were located on the shear wall and were used to obtain the readings necessary to separate shear and bending components of displacement. Overall structural deformations, including rigid body motion, were monitored with the remaining 14 gages attached to the instrumentation frame. These external gages were also used to measure torsional motion and sliding shear at the base of the structure and the relative displacement between the steel plates on top of the structure and the top concrete slab.

An ENERPAC hydraulic actuator was used to load the structure, and force input was monitored with a load cell located between the actuator and the steel plate. At specified load increments, the strain gages, displacement transducers, and load cell were scanned with an HP 3497A data scanner and recorded onto floppy disks with an HP 87 computer. After some initial low-level tests to check out the instrumentation, the load history shown in Figs. 12 and 13 in terms of ABSS and applied force, respectively, was followed until the structure failed. Each integer on the horizontal axis in Figs. 12 and 13 represents a point at which the data was scanned. The complete load reversals shown in this load history were intended to represent the forces induced in a Seismic Category I structure during seismic excitation. The breaks in the load history at the end of a cycle were the result of zeroing the hydraulic actuator before the start of the next cycle. This discontinuity was accounted for in the final data reduction.

The load cycling began with three 50-psi ABSS cycles followed by three 100-psi cycles. Before the start of the first 150-psi ABSS cycle, the voltmeter that was being used to monitor the load cell had been adjusted to an alternate voltage scale. The voltmeter was not readjusted to the proper scale at the start of this cycle; hence the structure was loaded well past 150-psi ABSS (in the negative direction) and into the cracking region. Following this unplanned excursion in the load sequence, the structure was loaded to 150-psi ABSS in the positive direction, i.e., opposite to that of the excursion loading (Cycle 7), and during the unloading part of this half cycle, portions of the

data were not recorded. Load Cycle 8 was then made to be a 200-psi ABSS cycle but with the directions reversed (loading in the positive direction first). Cycle 8 was followed by two more 200-psi ABSS cycle loads in the same sequence of load directions as the first six cycles. These cycles were followed by three 300-psi ABSS cycles, a 400-psi cycle during which the structure failed in one direction, and a 500-psi ABSS cycle during which the structure failed in the other direction. The load cycling was completed with two final 50-psi ABSS cycles.

VII. RESULTS FROM INTERNAL GAGE MEASUREMENTS

The overall horizontal deformation vs load, as determined from the interior relative displacement gages is shown in Figs. 14-31 for the entire load history and for each individual load cycle. This displacement is the top of the structure relative to the bottom. Because the displacement field over this region is nonuniform, the displacements computed in this manner represent an average value for the wall. The method for computing the horizontal displacement was identical to the method used for the TRG-4 data and is illustrated in Fig. 32. With the instrumentation used in this test, four values of horizontal displacement could be determined and averaged. Also, it is assumed that these displacement values do not significantly change when extrapolated to the exterior of the structure. This assumption was verified with a two-dimensional finite element analysis of the shear wall. The data from the interior relative displacement gages are independent from rigid-body rotation and translation and from the assumptions necessary to remove those quantities.

Stiffness based on these relative displacement readings was determined using Castigliano's theorem. By examining the free-body diagram in Fig. 33, the expression for internal strain energy stored in the structure between Sections A-A and B-B can be written as

$$U = \int_0^L \frac{(M + Px + wx)^2}{2EI} dx + \int_0^L \frac{(P + w)^2}{2 A_e G} dx \quad , \quad (2)$$

where

- U = internal strain energy,
- M = moment at Section A-A,
- P = shear force at Section A-A,
- w = imaginary unit load,
- E = concrete modulus of elasticity,
- I = cross-sectional moment of inertia, which includes entire end wall but neglects steel effects,
- G = shear modulus,
- A_e = effective shear area, and
- L = length of the wall between Planes A-A and B-B.

Using standard procedures described by Popov, 20 the horizontal displacement of the structure at Plane A-A relative to Plane B-B can be determined, and the stiffness of this portion of the structure can be expressed as

$$K_T = \frac{1}{\frac{hL^2}{2EI} + \frac{L^3}{3EI} + \frac{L}{A_e G}} \quad (3)$$

This total stiffness may be decomposed into a bending component and a shear component yielding

$$K_B = \frac{6EI}{2L^3 + 3hL^2} \quad (4)$$

and

$$K_S = \frac{A_e G}{L} \quad (5)$$

Table VI summarizes the various stiffness values that could be calculated for this test structure, depending upon how effective the end walls are assumed to be and also depending upon which value for modulus of elasticity is used.

The structure showed linear response through all of the 50-psi and 100-psi ABSS load cycles, and the measured stiffnesses during these precracking load cycles, based on the average displacements determined from the interior gage readings, are nearly identical to those predicted from an uncracked cross-section SOM approach.

TABLE VI
THEORETICAL STIFFNESS VALUES

Effect of End Wall on the Moment of Inertia / Modulus of Elasticity	Average from Test* Cylinder 3.87 x 10 ⁶ psi	$33w^{1.5} \sqrt{f'_c}$ $57,000 \sqrt{f'_c}$ Ultrasonic 4.04 x 10 ⁶ psi	} Ave.**
Full Section I = 1.96x10 ⁶ in. ⁴	K _T = 6.79x10 ⁶ K _B = 43.0x10 ⁶ K _S = 8.06x10 ⁶	K _T = 7.09x10 ⁶ K _B = 44.9x10 ⁶ K _S = 8.41x10 ⁶	
ACI T-Beam I = 4.21x10 ⁵ in. ⁴	K _T = 4.31x10 ⁶ K _B = 9.24x10 ⁶ K _S = 8.06x10 ⁶	K _T = 4.50x10 ⁶ K _B = 9.65x10 ⁶ K _S = 8.41x10 ⁶	
Neglect End Walls I = 2.43x10 ⁵ in. ⁴	K _T = 3.21x10 ⁶ K _B = 5.33x10 ⁶ K _S = 8.06x10 ⁶	K _T = 3.35x10 ⁶ K _B = 5.56x10 ⁶ K _S = 8.41x10 ⁶	

*The modulus of elasticity that was determined indirectly from the modal analysis was identical to the average modulus measured on the test cylinders.

**The modulus of elasticity determined from the two empirical formulas and ultrasonic testing were almost identical, hence, stiffness values were calculated with the average of these three values.

The measured stiffness values were

$$K_T = 6.88 \times 10^6 \text{ lb/in.},$$

$$K_B = 51.8 \times 10^6 \text{ lb/in.}, \text{ and}$$

$$K_S = 7.93 \times 10^6 \text{ lb/in.}$$

When the readings from the exterior gages were corrected for rigid body motion, similar agreement was obtained between stiffnesses determined from a 3-D FEA. Figures 34 thru 50 show the reduced data for each load cycle from the external gage measurements. The method for separating the horizontal displacement into shear and bending components is summarized in Appendix D of the TRG-4 report.¹¹

As stated previously, after the final 100-psi ABSS cycle ($K_T = 6.88 \times 10^6$ lb/in.), there was an unplanned excursion in the loading during which the structure was loaded to an ABSS of about 300 psi in the negative direction.

After the excursion, a visual inspection of the structure revealed diagonal cracks on both sides of the shear wall. Because of operational procedure error, no data were obtained during this excursion (half cycle). The excursion was followed by a half cycle (Cycle 7) in the positive direction to 150-psi ABSS during which the stiffness was found to be 2.9×10^6 lb/in.

Next, the structure was subjected to three 200-psi ABSS cycles. During the first 200-psi ABSS cycle (Cycle 8), the structure was loaded in the positive direction and then the negative direction. In the positive direction, the stiffness was 4.28×10^6 lb/in., a 48% increase from the previous cycle. The increase in stiffness is attributed to the fact that the structure did not experience a reverse or negative load cycle during the previous cycle. The load reversal would tend to open cracks and reduce the stiffness during subsequent positive load cycles. Without this reversal, the cracks that were closed during Cycle 7 remained somewhat closed and allowed the structure to exhibit the hardening or increased stiffness notices in this first part of Cycle 8. After a load of 60 000 lb was reached in the positive direction, new cracking was introduced, as is evident from the change in slope of the load-deformation curve (Fig. 22). In the negative direction, the decreased stiffness value observed in Fig. 22 would be expected because the load excursion introduced considerably more damage in this direction. The hardening effect can again be seen in the second 200-psi ABSS cycle, during which the structure was first loaded in the negative direction. Stiffness in this direction had increased to 2.55×10^6 and remained at this value during the final cycle. The stiffness measured during the positive portions of these two cycles had dropped to 3.16×10^6 lb/in. This drop in stiffness would be expected from the additional cracking that was observed during the positive portion of the first 200-psi ABSS cycle. A visual inspection of TRG-5 after Cycle 10 revealed additional diagonal cracks on the shear wall.

The load-deformation curves that were measured after the cracking showed typical behavior that has been observed by other investigators, that is, the structure exhibited an increase in stiffness as load was applied in either direction, and this increase in stiffness corresponds to the closing of cracks. The increasing stiffness was followed by a linear response region near the peak load, which in turn, was followed at times by a drop in stiffness associated with additional damage. The hardening effect observed during the repeated

cycles in the same direction and the almost linear response in the subsequent cycle have not been previously reported because other investigators have not employed this type of loading.

Three 300-psi ABSS cycle (Cycles 11, 12, 13) were next performed. Again, there was no evidence of additional damage in the negative direction, and the stiffness was measured as 2.29×10^6 lb/in. In the positive direction, additional cracking can be observed at 80 000 lbs in the load-deflection curve. Before this additional damage, the stiffness during the positive loading was comparable with that measured during the positive loading portion of Cycles 9 and 10. After the additional damage, the stiffness during the positive portions of Cycles 12 and 13 was almost identical to the stiffness during the negative portions of these cycles.

Cycle 14 was a single, 400-psi ABSS cycle, during which the structure showed similar responses in both the positive and negative load directions. The structure experienced additional damage, as was evident in the load-deflection curve at 120 000 lb. After this cycle was complete, additional cracking could be seen in the shear walls and end walls.

The structure failed in the negative direction during Cycle 15 at 180 000 lb. Extensive cracking was observed in the end walls and on the shear wall, with many of the flexural cracks in the end wall propagating into diagonal cracks in the shear wall. The final crack patterns are shown in Figs. 51-53.

Two final 50-psi ABSS cycles were run after the structure had failed (Cycles 16,17). Again, typical responses were observed, with the stiffness values varying from 3.2×10^5 to 8.0×10^5 lb/in.

During all of the testing, the relative displacement gages that monitored the slip between the bottom steel plate and the top concrete slab showed negligible displacements (less than 0.001 in.), implying that a good friction connection was obtained and the load was distributed in a uniform fashion over the top of the structure.

The peak strain gage readings on the rebar for the 50- and 100-psi ABSS load cycles are plotted in Figs. 54-59. Also shown on these plots are similar strains calculated from SOM theory. In the linear region, consistent results were obtained for both the end wall and the shear wall. These results show the proper trends, when compared with SOM theory, but the gage resolution is not good enough to expect exact numerical correspondence.

Based on the results of the modal analysis and the initial precracking load cycles up to 100-psi ABSS, the initial stiffness of this structure is within 99% of the theoretical stiffness as determined from either a FEA or a SOM approach. Also, these results show that before cracking, the entire end wall contributes to the flexural stiffness of the shear wall. The effective width exceeds the portion of the walls that would be considered effective based on ACI 349-85 T-beam criteria. However, it is believed that the thick concrete slab along with the steel plates at the top of the structure force the entire end wall to be effective. Therefore, the effectiveness may be due to the test geometry. Because of the load excursion, no exact comparisons can be made with stresses at the first cracking load and either the concrete's tensile strength or the ACI's tensile strength. However, all evidence indicates a first cracking load of 180- to 190-psi ABSS.

The first-cracking load would correspond to the load induced by 1.3-g maximum horizontal acceleration earthquake with no amplification. TRG-3, the previous large-scale shear wall structure with identical geometry as the structure reported herein, which was dynamically tested and reported in Ref. 2 showed a reduction in stiffness of 4-during a 0.73-g peak horizontal acceleration earthquake. This seismic excitation corresponded to an equivalent static load of 32 900 lb, an ABSS of 91 psi, and a PTS of 92 psi, well below stress levels predicted to produce cracking. There still remains a difference between the static and dynamic response of the similar structures tested at similar load levels.

The ultimate load of this structure exceeds the design load specified by ACI 349-85 (173 000 lb). However, it should be pointed out that the reference on which the ACI design criteria is based, Cardenas et al.,²¹ does not consider the effects of the boundary elements. The ABSS at failure 500 psi was higher than had been observed in other static tests carried out in this program on microconcrete and conventional concrete isolated shear walls and shear wall structures (i.e., TRG 4-6(1.0,0.25) 290-psi ABSS.) This higher failure value is, in part, attributable to the relatively large amount of reinforcement in TRG-5 as compared to the previous structures.

VIII. RESULTS FROM THE EXTERNAL GAGE MEASUREMENTS

The results of the data from the test of the TRG-5 model that are presented thus far in this report are based primarily upon the eight displacement gages that measure relative motion of an interior segment of the shear wall. A total of 24 displacements were measured during the test, as shown in Fig. 11 and the 16 absolute displacement measurements permit additional results to be determined. These results and the results from the 22 channels of reinforcing bar strains have been studied further to obtain a better understanding of the characteristics of the displacement measuring systems and the deformation and fracture process. The results of this additional data reduction and study are presented in the following sections.

IX. COMPARISON OF DEFORMATIONS FROM RELATIVE ABSOLUTE DISPLACEMENTS

The data reduction scheme for both the relative motion gages and the gages measuring absolute displacements has been described in the TRG-4 report and will not be repeated here.¹¹ For the results that are presented, "internal gages" and "external gages" refer to results from the relative motion and absolute motion gages, respectively.

Figures 60 through 69 are graphs that show the shear stress total deformation graphs for all of the load cycles. Results from both the internal and external gages are shown from comparison. Figures 70 and 71 show the first load cycle at each new load increment to illustrate the development of the deformation. In either of these graphs, it is noted that the first identifiable fracture for a positive load occurs at about 180 psi. The first fracture for the negative load is not identifiable from these graphs because of the unplanned load excursion.

Figure 72 is included to show the calculated total deformation when the correction for rigid-body base rotation is not made. It may be noted that the correction technique reduces the peak values by about 50% to 100%.

Table VII has been prepared to compare the peak-to-peak values of the total deformation as determined from external and internal gages. The larger values for the external gages indicate cracking outside the internal gaged area. Larger values from the internal gages probably indicate a deviation of the model behavior from the assumptions made in the derivation of the rigid-body correction equations.

TABLE VII
PEAK-TO-PEAK HORIZONTAL DEFORMATIONS

<u>Shear Stress Level, psi</u>	<u>Internal Gages</u>	Total Deformation, in.		<u>Internal Gage (Adj.)*</u>
		<u>External Gages</u>		
50 psi	0.0046	0.0108		0.0063
100 psi	0.0106	0.020		0.0144
200 psi	0.054	0.054		0.0735
300 psi	0.104	0.126		0.142
Failure	0.310	0.305		0.436

*Linearly adjusted for the difference in shear wall height covered by gaging.

Similar graphs were obtained for the shear deformation, and these are shown in Figs. 73 through 83. Figures 73 and 74 show the shear deformation response before the appearance of the first cracks. Figures 77 and 78 show that the first crack for positive loads appeared at about 180 psi. These two figures show the behavior in the negative load direction that is characteristic of postcrack response. This was expected because of the unexpected large load cycle in that direction, which caused cracking (and for which no data were obtained). Figure 83 shows the first load cycle at each load increment up through 300 psi, thus it illustrates the development of the shear deformation.

Table VIII compares the peak-to-peak shear deformation from the internal and external gages. It is noted that the differences in these values, in percent, are relatively large at low-load levels.

The corresponding graphs for the bending deformation are Figs. 84 through 95. The bending deformations also show that the initial plus-load crack was at 180 psi. Table IX shows the corresponding peak-to-peak deformations from the internal and external gages. The agreement here is not as good as has been obtained in past experiments, but this difference is understandable in view of the magnitudes of the deformations.

The deformation data were reduced to determine the ratio of shear deformation to the x component of total deformation. This ratio, as determined from the internal gages, is shown in Figs. 96 through 100. It is noted that the ratio plots do not show significant slope discontinuities at the fracture loads as were seen in the deformation plots. Figure 101, which shows the ratios for the first load cycle at each load increment, illustrates this. Figure 102 also

TABLE VIII
PEAK-TO-PEAK SHEAR DEFORMATIONS

Shear Stress Level, psi	Shear Deformations, in.		
	Internal Gages	External Gages	Internal Gage (Adj.)*
50 psi	0.0043	0.0091	0.0058
100 psi	0.0091	0.017	0.0123
200 psi	0.045	0.061	0.061
300 psi	0.095	0.120	0.129
Failure	0.26	**	0.34

*Linearly adjusted for the difference in shear wall.

**Gage malfunction.

TABLE IX
PEAK-TO-PEAK BENDING DEFORMATIONS

Shear Stress Level, psi	Bending Deformations		
	Internal Gages	External Gages	Internal Gage (Adj.)*
50	0.00071	0.0123	0.00096
100	0.0014	0.003	0.0019
200	0.0077	0.0075	0.010
300	0.015	0.138	0.020
Failure	0.062	0.09	0.084

*Linearly adjusted for the shear wall height covered by the gaging.

shows the ratios for the first load cycle at each load increment determined from the external gages. Table X summarizes the results from the graphs, and it shows the near independence of the ratio on stress level or degree of fracture of the model.

The torsional deformation at each load level is shown in Fig. 103 through 108. It is of interest to note that in Fig. 105, the deformation was of the order of 10^{-5} rad to about 100 psi and then it changed abruptly to about 3×10^{-4} . The load cycle of the change was the first positive load after the unplanned negative load excursion, and the step change represents distortion from the initial fracture. Once that torsional deformation occurred, the peak-to-peak changes remained on the order of 10^{-4} rad until additional fracturing (see Fig. 107).

TABLE X
RATIO OF SHEAR DEFORMATION TO TOTAL DEFORMATION AT PEAK LOADS

Shear Stress Level	Internal Gages	External Gages
50 psi	0.82 - 0.84	0.83 - 0.85
100 psi	0.83 - 0.84	0.82 - 0.85
200 psi	0.82 - 0.83	0.84 - 0.85
300 psi	0.82 - 0.83	0.84 - 0.85
Failure, + load	0.81	0.84
Failure, - load	0.79	0.68

Two of the external gages were mounted 4 in. above and below the floor level at the shear wall, and two were mounted 4 in. above and below the ceiling level. The purpose of these gages was to look at the deformations of the floor shear wall and shear wall-ceiling interface. Plots of the difference in the readings of these two sets of gages, corrected for rigid-body rotation, are shown in Figs. 109 through 114 and Figs. 115 through 120, respectively. A study of these figures shows that the difference in these readings is small, on the order of the resolution of the measuring system. Also, Figs. 111 and 117 show that the unplanned load excursion caused some fracture at the floor interface and not the ceiling interface. Further, Fig. 112 shows a slope discontinuity at about 240 psi indicating an additional fracture at this stress not identified with the internal gages. The plots for the ceiling interface do not show a fracture there until a stress of about 320 psi is reached.

X. ADDITIONAL RESULTS FROM STRAIN GAGE DATA

The locations of the strain gages that were placed on the rebar are shown in Figs. 2 through 4. A study of the data reveals additional information on the deformation and fracture process of the model during the test. This section of the report contains additional data and results from the strain gages.

Initially, all the data from one gage are shown. Figures 124 through 136 show these data for gage 7. Gage 7 is on a horizontal rebar. Figures 121 through 125 show the linear behavior before fracture (stress levels ≤ 100 -psi), and the resolution of the measuring system of $1 \mu\epsilon$. The 150-psi cycle, after the unexpected load excursion, shows a significant increase in strain magnitudes over the data of the previous load cycle, i.e., the maximum strain

increased from $8 \mu\epsilon$ for the 100-psi test to $> 90 \mu\epsilon$ for the 150-psi test. This is the result of changes in the strain field in the model brought about by the fracture(s). On the next load cycle (Fig. 127), a crack initiated earlier apparently grew at a stress of about 180 psi. The behavior in the negative load direction did not indicate further cracking, showing the unexpected load excursion could have been at a stress level greater than 200-psi. The subsequent 200-psi tests did not cause additional fracture. On the first test at the next load level (Fig. 130), the + load caused additional cracking at 200+ psi, and the fracture pattern changed enough to cause a reversal of the sign of strain in the rebar for the same load direction. This behavior continues on subsequent tests. Figure 134 is for the failure load cycle in the negative load direction, and it shows that additional fractures occurred at a shear stress slightly above 400-psi.

Data from other strain gages also show the occurrence and growth of cracks. It is assumed that the cracks are in the vicinity of the strain gage showing the sudden change. The indications can be quite convincing. For example, Fig. 137 shows the signal from Strain Gage 12 during the 400-psi cycle. The negative stress was applied first, and the crack growth at 350-psi is obvious. Then, for the positive load, another crack occurred at the +350-psi stress level and again dramatically changed the strain field at this rebar location. On the subsequent negative load, further cracking occurred in the vicinity of Gage 12 at about 475 psi (Fig. 138).

Table XI has been included to show the occurrence and growth of cracks in the shear wall based upon a study of the strain measurements of the reinforcing bars. Normally, the first entry would represent the first occurrence of a crack in the vicinity of the strain gage; but for this test, the unexpected load excursion, during which data were not taken, clouds the results somewhat. However, the unexpected load was in the negative direction only, and it is fairly clear that the first cracking due to a positive load occurred in the vicinity of 170 psi. Consequently, it is believed the initial fracture strength of the model may be identified as 170 psi. Further study of this table permits the following additional conclusions:

1. The first cracking for negative loads was observed at around 300 psi, indicating that the unexpected load had a peak value of less than 300 psi.

2. There was also additional cracking for positive loads in the vicinity of 300 psi, indicating symmetrical behavior. This supports the conclusion drawn about the initial cracking load for the model.

Table XII shows similar results based upon the strain measurements on the reinforcing rods in the end walls. It is noted that the results are similar to the results from Table XI. One difference is that there was identifiable crack growth at a negative 300-psi stress during the first cycle at this level. This growth was not identified until the first 400-psi stress cycle in Table XI, though it was still observed near the 300-psi level.

Even though the difference in the results from the measurements on the shear wall and end wall do exist, the agreement between the two on the stress levels of occurrence and growth of cracks must be considered excellent. Also, it is noted that the corresponding values determined from displacement measurements, where possible, are good.

XI. HYSTERETIC ENERGY LOSSES IN THE TRG-5 STRUCTURE

The hysteretic energy losses that occurred during each load cycle were deduced based on the displacement determined from the interior relative displacement gages. Data from the exterior gages were also examined, but the results were not as consistent, even with the corrections for rigid-body motion. For all the load cycles, the hysteretic energy losses have been related to equivalent viscous damping coefficients.

Table XIII summarizes the hysteretic energy losses measured during each load cycle. The hysteretic energy loss is defined as the area between the load deformation curve and was calculated numerically using a trapezoid integration rule. Several load cycles did not form a closed load-deformation loop. When this occurred, the integration scheme connected the terminal point with a straight line to the initial point. Errors induced by this scheme were considered negligible.

To obtain an equivalent viscous damping coefficient, the energy dissipated by viscous damping, UVDI in a linear single degree of freedom system during a steady-state response to one cycle of harmonic-forced excitation is equated to the hysteretic energy loss, U_H , during one cycle of static loading.²² A detailed development of this relationship can be found in Ref. 11.

These equivalent viscous damping computations yielded values slightly less than those measured on the microconcrete isolated shear walls.⁴ The values

TABLE XI

CRACK OCCURRENCES OR GROWTH FROM STRAIN GAGES ON REBAR IN THE SHEAR WALL

Load Cycle Shear Stress, psi	Strain Gage Identification*									
	7	8	9	10	11	12	13	14	15	16
50 thru 150 psi	[No clear indication of crack formation for these tests]									
200-1	+180	+170			+170	+170	+170	+180		
-2										
-3										
300-1	+220			+300	+220			+220	+290	+280
-2										
-3										
400	+350	-400		-300	-370	-290	-340		-340	
					+320	+350	+340		+340	
Failure	-420		-420	-420	-420	-420	-390	-460		-400

*Table values are stress levels of slope discontinuities in the load-vs-strain plots.

TABLE XII

CRACK OCCURRENCE OR GROWTH FROM STRAIN GAGES ON REBAR IN THE END WALLS

Load Cycle Shear Stress psi	Strain Gage Identification*											
	West End Wall						East End Wall					
	1	2	3	4	5	6	17	18	19	20	21	22
50 thru 150 psi	[NO clear indication of crack formation for these tests]											
200-1					+180		+180	+170	+170	+170	+170	+180
-2												
-3												
300-1	-300		+220		-210	-280		+220	+220	+220	+220	+220
-2												
-3												
400		-300	-300	-300	-300	-330		+340	+340	+340	+300	+340
						-410						
Failure	-410	-410	-410	-410	-410	-410	-410	-410	-330	-410	-410	-410
	-450	-450	-450	-450	-450	-450	-450	-450	-410	-450	-450	-450
	-470	-470	-470	-470	-470	-470	-470	-470	-450	-470	-470	-470
								-470				
	1	2	3	4	5	6	17	18	19	20	22	22

*Table values are stress levels of shape discontinuities in the load-vs-strain plots.

TABLE XIII
HYSTERETIC ENERGY LOSSES MEASURED ON TRG-5

Load Cycle	Peak Average Base Shear Stress (psi)	Peak Force (lbs)	Hysteretic Energy Loss (in.-lb)	Equivalent Viscous Damping (% of Critical)
1	50	18 000	10	3.5
2	50	18 000	10	3.4
3	50	18 000	11	4.0
4	100	36 000	39	3.3
5	100	36 000	33	2.7
6	100	36 000	32	2.8
7	150	54 000	156	*
8	200	72 000	786	*
9	200	72 000	475	3.8
10	200	72 000	449	3.5
11	300	108 000	2 630	*
12	300	108 000	1 690	4.6
13	300	108 000	1 300	3.4
14	400	144 000	12 000	*
15	500	180 000	11 300	*
16	50	18 000	434	*
17	50	18 000	293	8.0

*Cycles that exhibited nonlinear responses. Stiffness was not well defined during these cycles.

measured on TRG-5 are also slightly less than those reported by Housner,²³ et al. (5% of critical), and those allowed by the NRC Regulatory Guide 1.61²⁴ for an operating basis earthquake of one-half safe shutdown earthquake (4% of critical). The damping at low stress values suggested by Newmark and Hall²⁵ are much lower than those determined in this investigation. As an example, Newmark and Hall suggest values of 0.5-1.0% of critical before cracking, and values of 2.7-4.0% of critical were measured before cracking on TRG-5. The damping values measured on TRG-5 also are slightly less than the average measured data from the nuclear power plant shear wall buildings reported in Ref. 26. The buildings were tested at stress levels below 25% of yield, and an average damping value of 5.2% of critical was determined from these data.

During the unplanned load excursion and the first 200-psi ABSS Cycle, the structure cracked and the hysteresis area was considerably larger than that found during the previous load cycles. However, the subsequent load cycles at 200-psi ABSS had a hysteretic energy loss that was only on the average of 59% of the loss during the first 200-psi Cycle. This finding implies that the

damping that occurs during the first nonlinear load cycle is significantly greater than that which occurs during subsequent cycles at a similar or lower load level. Also, this result implies that the damping in the nonlinear range is a function of the structure's prior load history. The largest energy loss occurred during the failure cycle (500-psi ABSS, Cycle 15), as expected.

Finally, it is of interest to compare the hysteretic energy loss before and after the structure failed. During the first three 50-psi ABSS Cycles, the energy loss averaged 10 in.-lb while an energy loss of 293 in.-lb was measured during the final 50-psi ABSS Cycle. The equivalent viscous damping was initially measured at an average value of 3.6% of critical and was found to be 8.0 of critical during the final cycle.

XII. OTHER INVESTIGATORS RESULTS

Figures 139 and 140 provide a summary of the available static test data for low-aspect-ratio reinforced concrete shear walls. These figures give a comparison of other investigators' results and the results obtained in the Seismic Category I Structures Program.

Before first cracking, the measured secant stiffness vs theoretical (SOM) stiffness is plotted in Fig. 139. The majority of test data on actual concrete test specimens, including the structure tested in this investigation, indicate that, prior to cracking, an SOM analysis gives an accurate prediction of the shear wall stiffness prior to the first-cracking load. There are several investigations of actual concrete structures that show similar reductions in stiffness prior to cracking, as was observed in the Los Alamos microconcrete models.

Finally, Fig. 140 compares the ultimate strength of the shear walls with the ACI 349-85 design strength. In almost all cases, the ACI value appears to be conservative. Data for Figs. 139 and 140 were obtained from Refs. 2, 4, 6, 7, and 27-33.

XIII. CONCLUSIONS

One of the primary purposes of this test was to determine if, during a carefully monitored static-load-cycle test, a stiffness reduction of four would occur at similar load levels as have been observed in dynamic tests. During

the precracking load cycles and the low-level modal analysis, no stiffness reduction was observed, and the response of the structure was accurately predicted with currently used linear analysis techniques based on SOM. These same linear analysis techniques have not adequately predicted the dynamic response of structures previously tested in the program even though stress levels during the dynamic tests were well below those predicted to crack the structure. Hence, several questions remain about previous tests conducted in this program and the dynamic behavior of actual Seismic Category I structures. In particular, the following possibilities must still be considered: (1) Does microconcrete adequately simulate actual concrete in both static and dynamic response? (2) Were previous models damaged before testing either by handling or, in the case of smaller structures, shrinkage cracks? (3) Are there dynamic effects that cause the discrepancy between the reductions in stiffness observed statically and dynamically? and (4) In all testing and analysis, have the boundary conditions been properly accounted for? These questions are currently being examined in light of the latest test results.

This test was also to provide information on the effectiveness of the end walls, and up until first cracking, they appear to be fully effective. However, the concrete and steel slabs at the top of the structure force the cross section to remain plane, thus reducing the shear lag effect. After cracking, the extent of their contribution is not clear and data are still being evaluated at this time.

The ability to separate shear and bending components of deformation was clearly demonstrated. Loss of stiffness was shown to occur equally in each component of deformation.

REFERENCES

1. "Seismic Safety Research Program Plan," U.S. Nuclear Regulatory Commission, Office of Nuclear Regulatory Research, NUREG-1147, Rev. 1, Appendix C (May 1987).
2. J. G. Bennett, R. C. Dove, W. E. Dunwoody, C. R. Farrar, and P. Goldman, "The Seismic Category I Structures Program: Results for FY 1986," Los Alamos National Laboratory report LA-11377-MS, NUREG/CR-5182 (September 1988).
3. E. G. Endebrock, R. C. Dove, and C. A. Anderson, "Margins to Failure--Category I Structures Program: Background and Experimental Program Plan," Los Alamos National Laboratory report LA-9030-MS, NUREG/CR-2347 (December 1981).
4. E. G. Endebrock, R. C. Dove, and W. E. Dunwoody, "Analysis and Tests on Small-Scale Shear Walls--FY 82 Final Report," Los Alamos National Laboratory report LA-10443-MS, NUREG/CR-4274 (September 1985).
5. R. C. Dove and J. G. Bennett, "Scale Modeling of Reinforced Concrete Category I Structures Subjected to Seismic Loads," Los Alamos National Laboratory report LA-10624-MS, NUREG/CR-4474 (January 1986).
6. R. C. Dove, J. G. Bennett, C. R. Farrar, and C. A. Anderson, "Seismic Category I Structures Program: Final Report FY 83-84," Los Alamos National Laboratory report LA-11013-MS, NUREG/CR-4924 (September 1987).
7. J. G. Bennett, R. C. Dove, W. E. Dunwoody, E. G. Endebrock, C. R. Farrar, and P. Goldman, "Simulated Seismic Tests on 1/42- and 1/14-Scale Category I, Auxiliary Buildings," Los Alamos National Laboratory report LA-11093-MS, NUREG/CR-4987 (October 1987).
8. J. G. Bennett, R. C. Dove, W. E. Dunwoody, C. R. Farrar, and P. Goldman, "The Seismic Category I Structures Program: Results for FY 1985," Los Alamos National Laboratory report LA-11117-MS, NUREG/CR-4998 (December 1987).
9. ACI Committee 349, Code Requirements for Nuclear Safety Related Concrete Structures and Commentary, American Concrete Institute, Detroit, Michigan (1985).
10. ACI Committee 318, Building Code Requirements for Reinforced Concrete American Concrete Institute, Detroit, Michigan (1983).
11. C. R. Farrar, J. G. Bennett, W. E. Dunwoody, and W. E. Baker, "Static Load Cycle Testing of a Low Aspect Ratio Six-Inch Wall, TRG-Type Structure TRG-4-6 (1.0, 0.25)" Los Alamos National Laboratory report LA-11422, NUREG-CR-5222 (June 1989).
12. "Standard Test Method for Slump of Portland Cement Concrete," in Annual Book of ASTM Standards, Roberta A. Prieman-Storer, Ed. (American Society for Testing and Materials, Philadelphia, Pennsylvania, 1985), Vol. 4.02, C143-78, pp. 109-112.

13. "Method of Sampling Freshly Mixed Concrete," in Annual Book of ASTM Standards, Roberta A. Prieman-Storer, Ed. (American Society for Testing and Materials, Philadelphia, Pennsylvania, 1985), Vol. 4.02, C172-82, pp. 133-135.
14. "Standard Method of Making and Curing Concrete Specimen in the Field," in Annual Book of ASTM Standards, Roberta A. Prieman-Storer, Ed. (American Society for Testing and Materials, Philadelphia, Pennsylvania, 1985), Vol. 4.02, C31-84, pp. 5-10.
15. "Specification for Concrete Aggregates," in Annual Book of ASTM Standards, Roberta A. Prieman-Storer, Ed. (American Society for Testing and Materials, Philadelphia, Pennsylvania, 1985), Vol. 4.02, C33-85, pp. 11-20.
16. "Standard Test Method for Compressive Strength of Cylindrical Concrete Specimen," in Annual Book of ASTM Standards, Roberta A. Prieman-Storer, Ed. (American Society for Testing and Materials, Philadelphia, Pennsylvania, 1985), Vol. 4.02, C39-84, pp. 24-29.
17. "Standard Test Method for Static Modulus of Elasticity and Poisson's Ratio of Concrete in Compression," in Annual Book of ASTM Standards, Roberta A. Prieman-Storer, Ed. (American Society for Testing and Materials, Philadelphia, Pennsylvania, 1985), Vol. 4.02, C469-83, pp. 303-307.
18. "Standard Test Method for Splitting Tensile Strength of Cylindrical Concrete Specimens," in Annual Book of ASTM Standards, Roberta A. Prieman-Storer, Ed. (American Society for Testing and Materials, Philadelphia, Pennsylvania, 1985), Vol. 4.02, C496-85, pp. 335-339.
19. T. R. Naik, "Ultrasonic Testing of Concrete," Experimental Methods In Concrete Structures for Practitioners, G. M. Sabnis and N. Fitz Simmons, Eds. (American Concrete Institute, Detroit, Michigan, 1979).
20. E. P. Popov, Introduction to Mechanics of Solids (Prentice-Hall, Englewood Cliffs, New Jersey, 1969).
21. A. E. Cardenas, J. M. Hanson, W. G. Corley, and E. Hognested, "Design Provisions for Shear Walls," J. Am. Concr. Inst., 70, No. 3 (March 1973) pp. 221-230,.
22. S. Timoshenko, D. Young, and W. Weaver, Vibration Problems in Engineering 4th ed. (John Wiley & Sons, Inc., New York, 1974) pp. 81-84.
23. G. W. Housner, R. R. Martel, and J. L. Alford, "Spectrum Analysis of Strong-Motion Earthquakes," Bull. Seismol. Soc. AM. (U.S.A.) 43, pp. 97-119 (1953).
24. "Damping Values for Seismic Design of Nuclear Power Plants," Nuclear Regulatory Guide 1.61, U.S. Nuclear Regulatory Commission (December 1983).

25. H. Newmark and W. Hall, "Seismic Design Criteria for Nuclear Reactor Facilities," in Proc. 4th World Conference on Earthquake Engineering, B4, pp. 37-50 (Santiago, Chile, 1969).
26. J. D. Stevenson, "Structural Damping Values as a Function of Dynamic Response Stress and Deformation Levels," Nuclear Eng. and Design, 60 pp. 211-238 (September 1980).
27. G. D. Galletly, "An Experimental and Analytical Investigation of Reinforced Concrete Shear Panels," Ph.D. thesis, Department of Civil and Sanitary Engineering, Massachusetts Institute of Technology, Cambridge, Massachusetts (1952).
28. J. R. Benjamin and H. A. Williams, "The Behavior of One-Story Reinforced Concrete Shear Walls," J. Struct. Eng., American Society of Civil Engineers, 83, No. ST3, Proc. Paper 1254, pp. 1254-1 to 1254-49 (May 1957).
29. J. Antebi, "Model Analysis of the Response of Shear Walls to Dynamic Loads," Ph.D. thesis, Department of Civil and Sanitary Engineering, Massachusetts Institute of Technology, Cambridge, Massachusetts (1961).
30. F. Barda, "Shear Strength of Low-Rise Walls with Boundary Elements," Ph.D. thesis, Department of Civil Engineering, Lehigh University, Bethlehem, Pennsylvania (1972).
31. V. Cervenka and K. H. Gerstle, "Inelastic Analysis of Reinforced Concrete Panels: Experimental Verification and Application," International Association of Bridge and Structural Engineering, 32-II, pp. 25-40 (1972).
32. A. E. Cardenas, H. G. Russell, and W. G. Corley, "Strength of Low-Rise Structural Walls," in Reinforced Concrete Structures Subjected to Wind and Earthquake Forces, J. Schwaighofer and S. Otani, Eds., American Concrete Institute SP-63, pp. 221-241, Detroit, Michigan (1980).
33. S. Wiradinata, "Behavior of Squat Walls Subjected to Load Reversals," Masters thesis, University of Toronto, Toronto, Canada (1985).

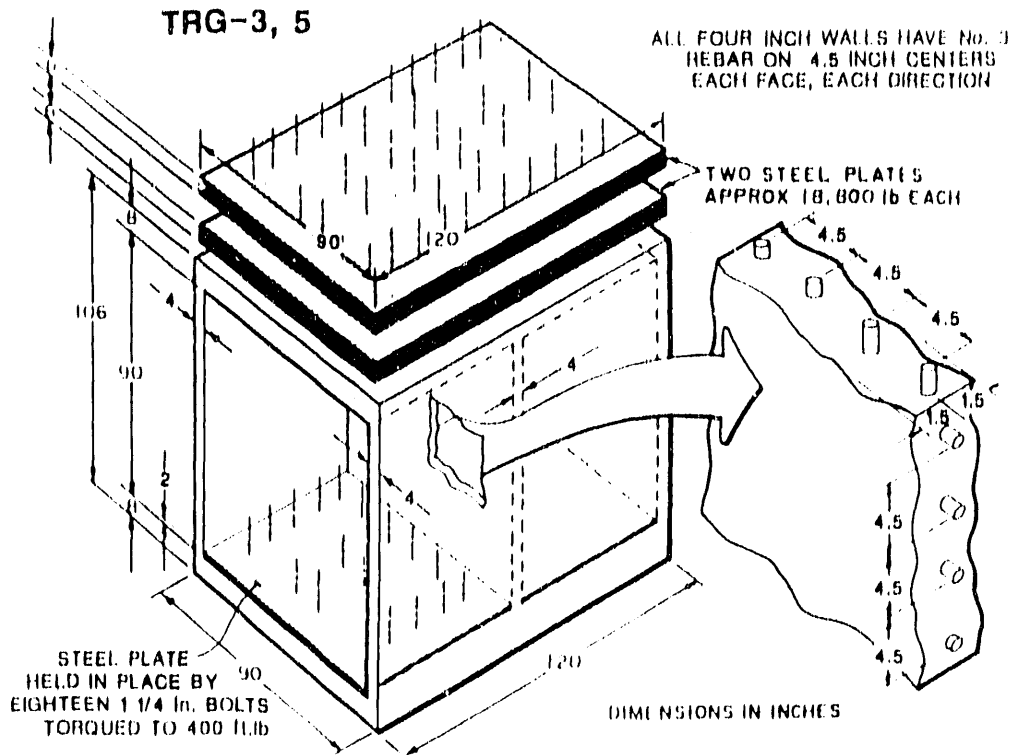


Fig. 1. Prototype TRG structure.

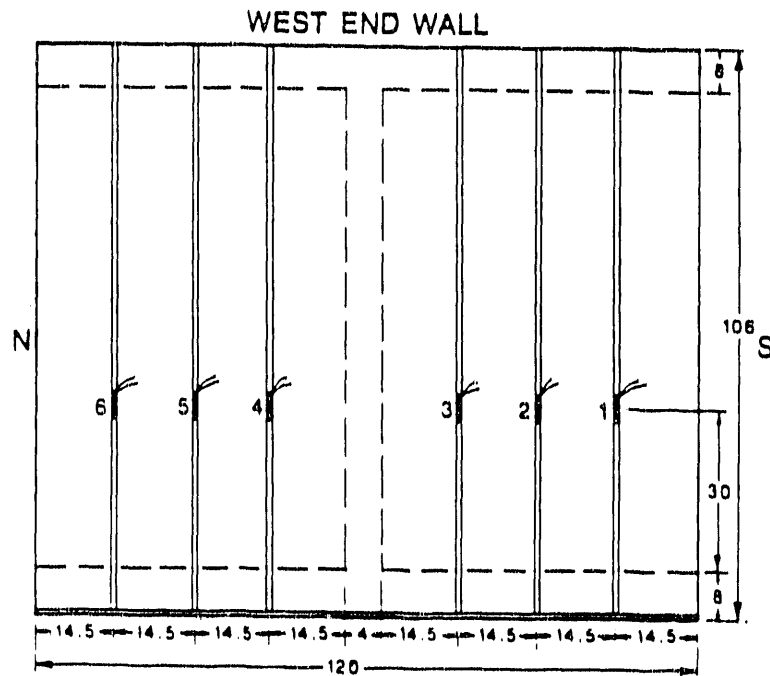


Fig. 2. West end wall layer of reinforcement and strain gage locations. (All dimensions are in inches).

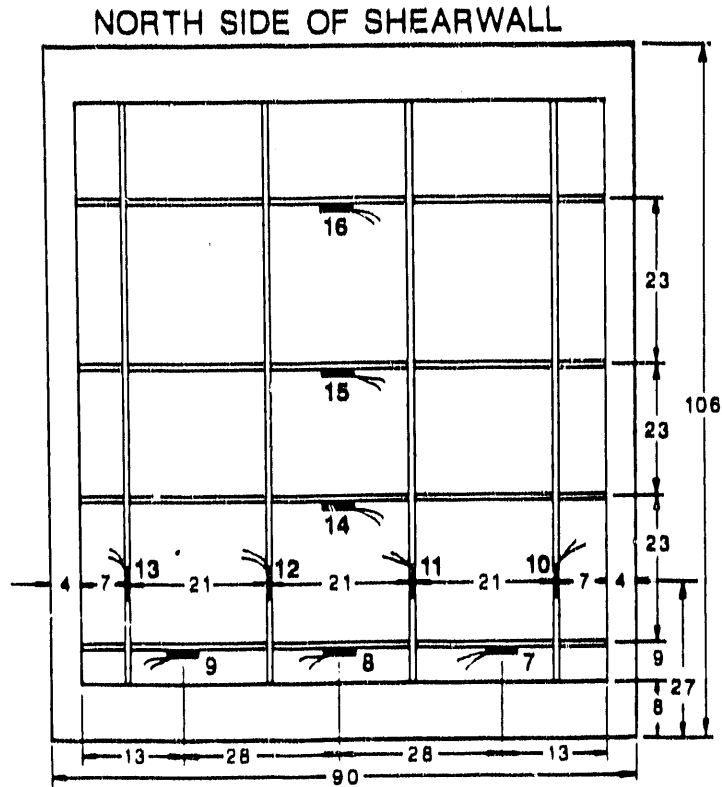


Fig. 3. North side layer of reinforcement in the shear wall and strain gage locations. (All dimensions are in inches).

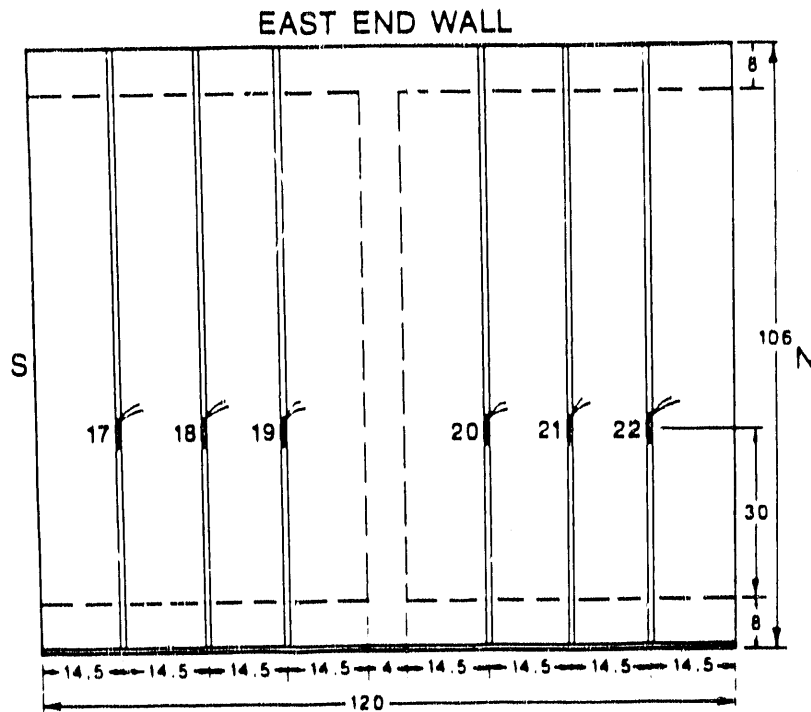


Fig. 4. East end wall layer of reinforcement and strain gage locations. (All dimensions are in inches).

UNDEFORMED STRUCTURE

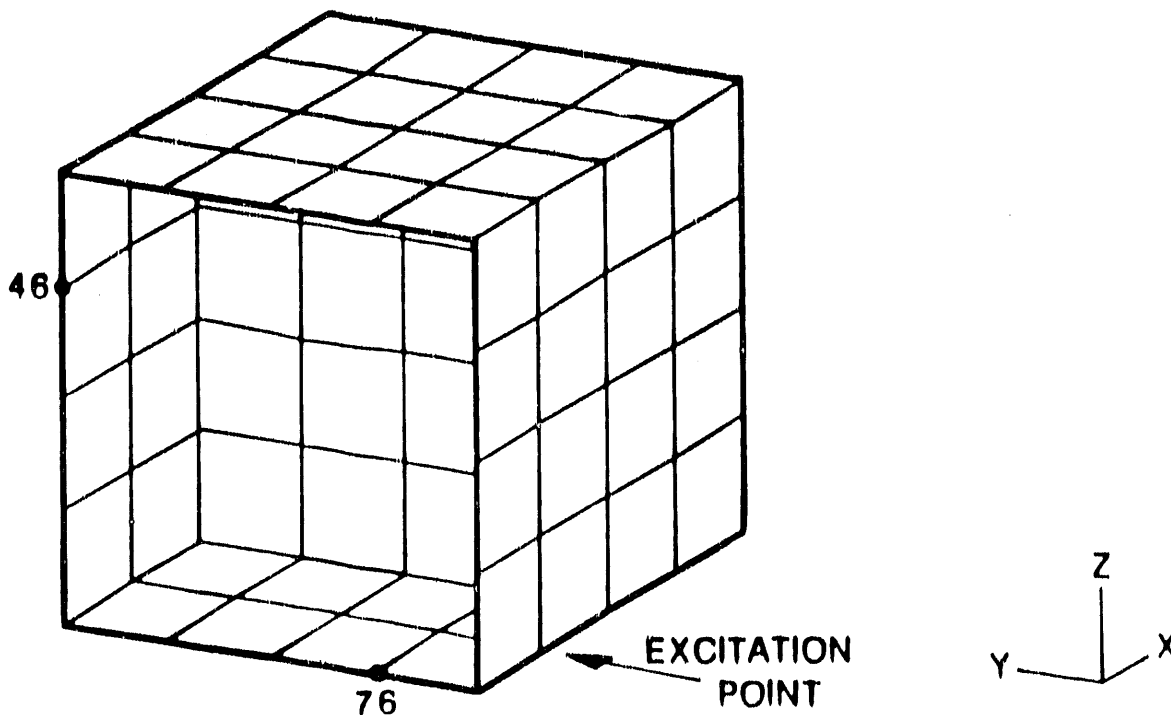


Fig. 5. The modal test measurement points. (Some points can not be seen because of hidden line removal).

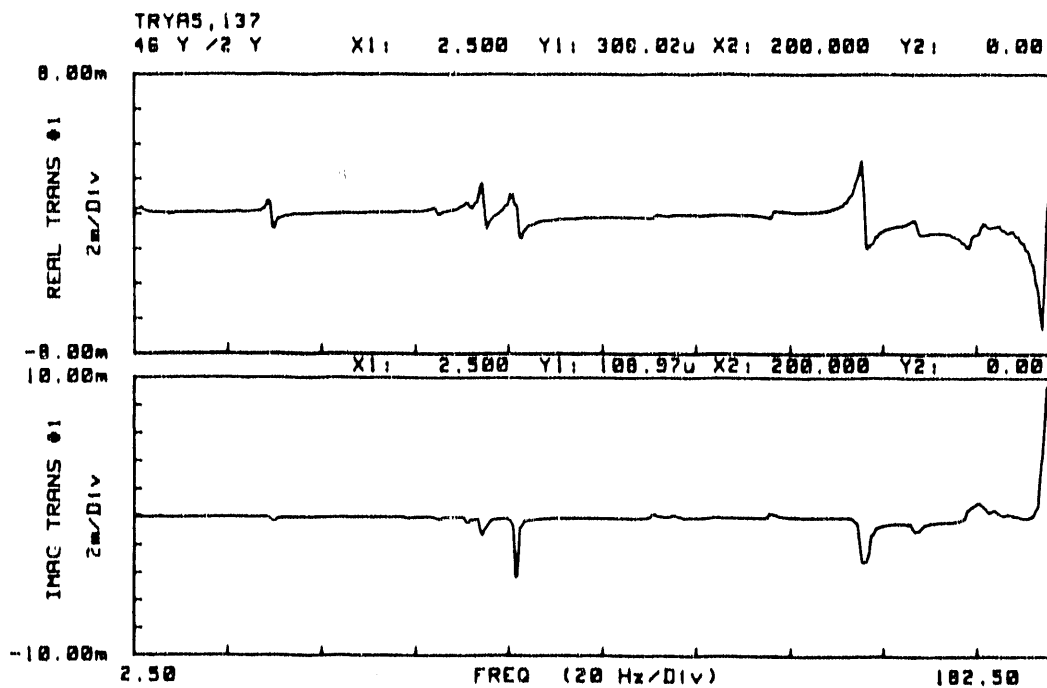


Fig. 6. Frequency response function obtained from Point 46, in the Y direction, $A(46Y)/F(2Y)$.

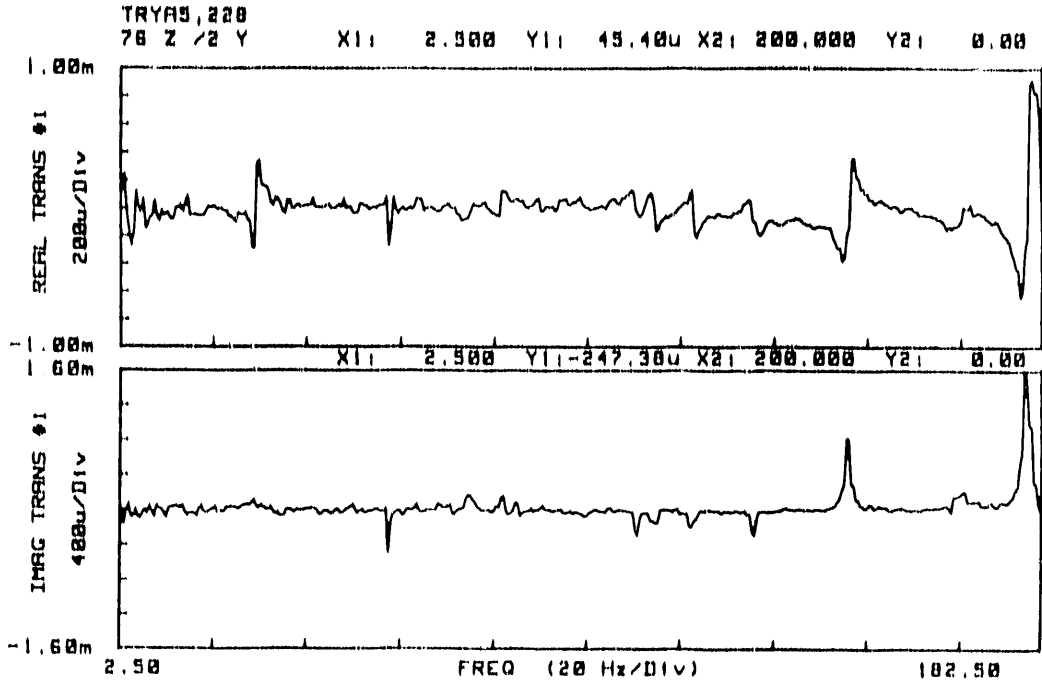


Fig. 7. Frequency response function obtained from Point 76, Z direction, $A(76Z)/F(2Y)$.

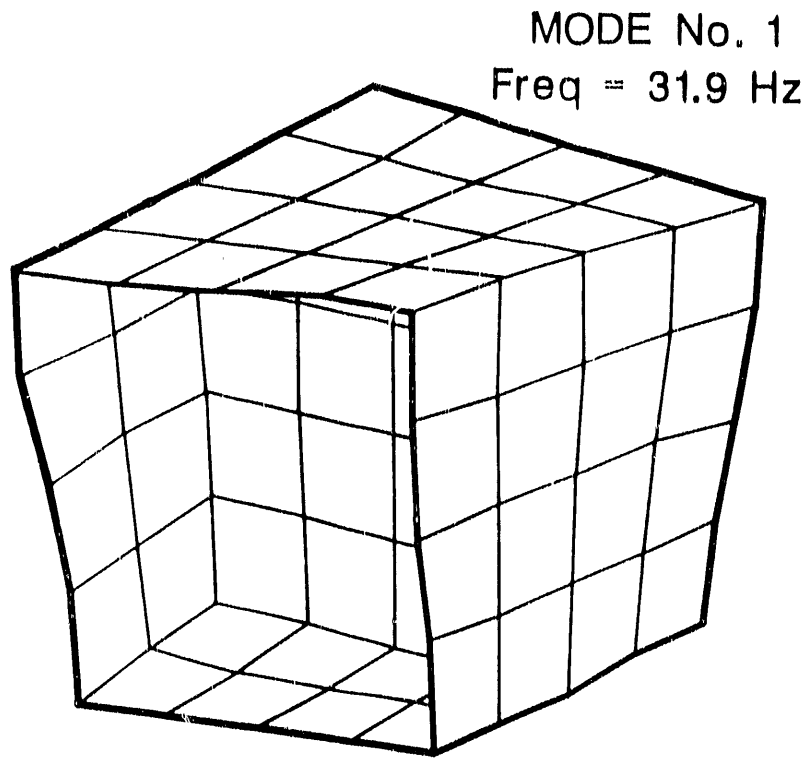


Fig. 8. Mode 1 obtained from the experimental modal analysis of TRG-5.

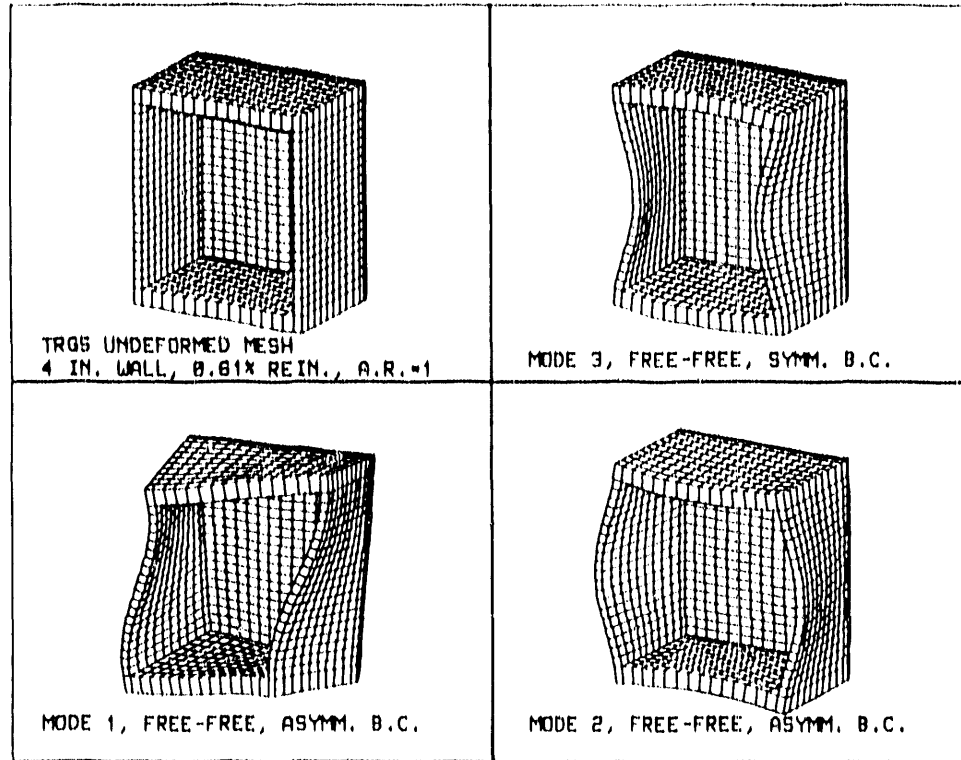
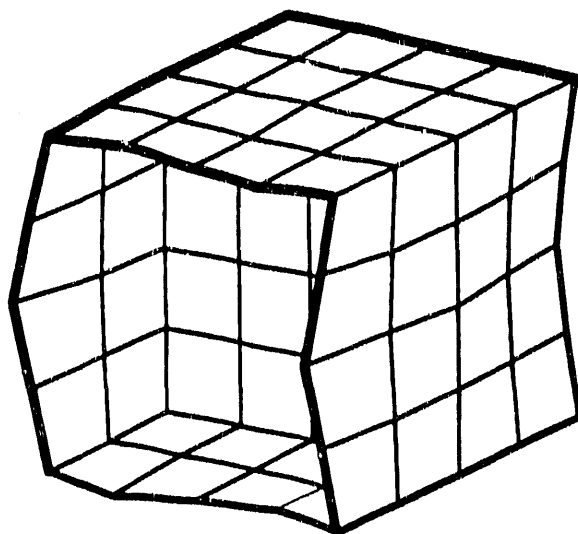
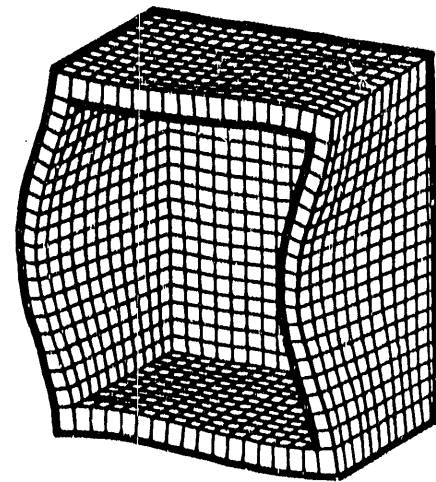


Fig. 9. Undeformed mesh and the first three modes from the finite element analysis using free-free boundary conditions with asymmetric boundary conditions on the plane of symmetry.



MODE No. 5
EXPERIMENTALLY DETERMINED
 Freq = 84.4 Hz



MODE No. 5
DETERMINED WITH ABAQUS
F. E. PROGRAM
 Freq = 95.2 Hz

Fig. 10. A comparison of the experimentally obtained modal shape and frequency with the analytical computation using ABAQUS.

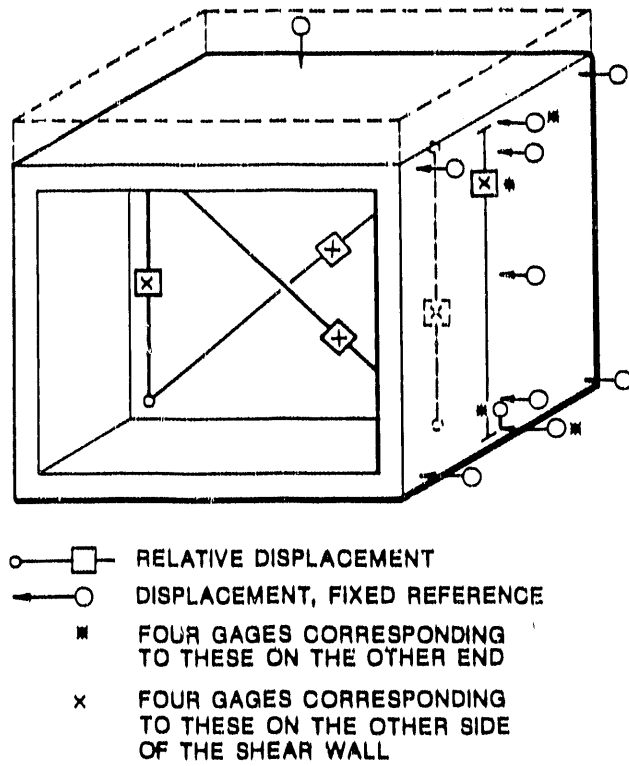


Fig. 11. Schematic showing the instrumentation location and their purpose.

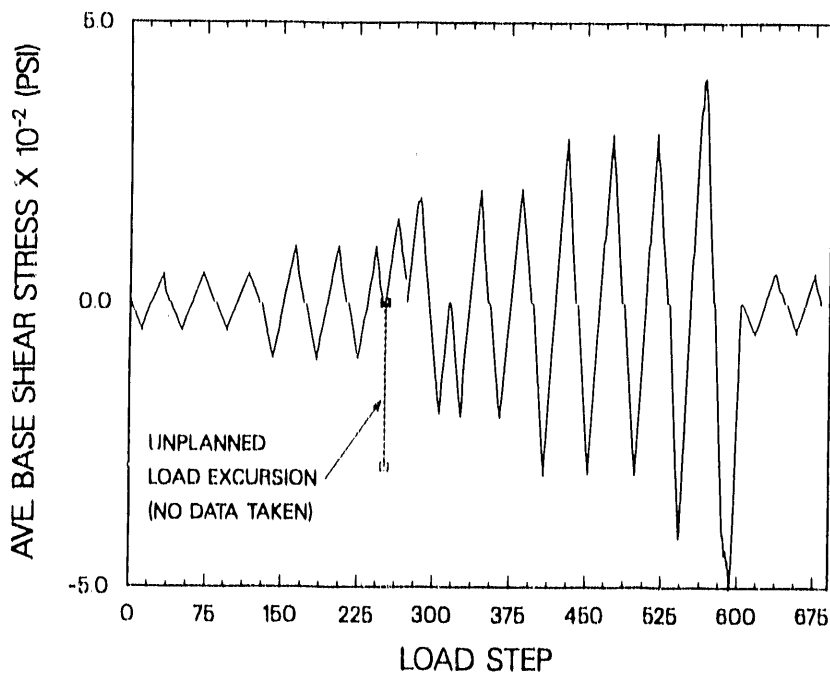


Fig. 12. TRG-5 load vs load step history in terms of average base shear stress.

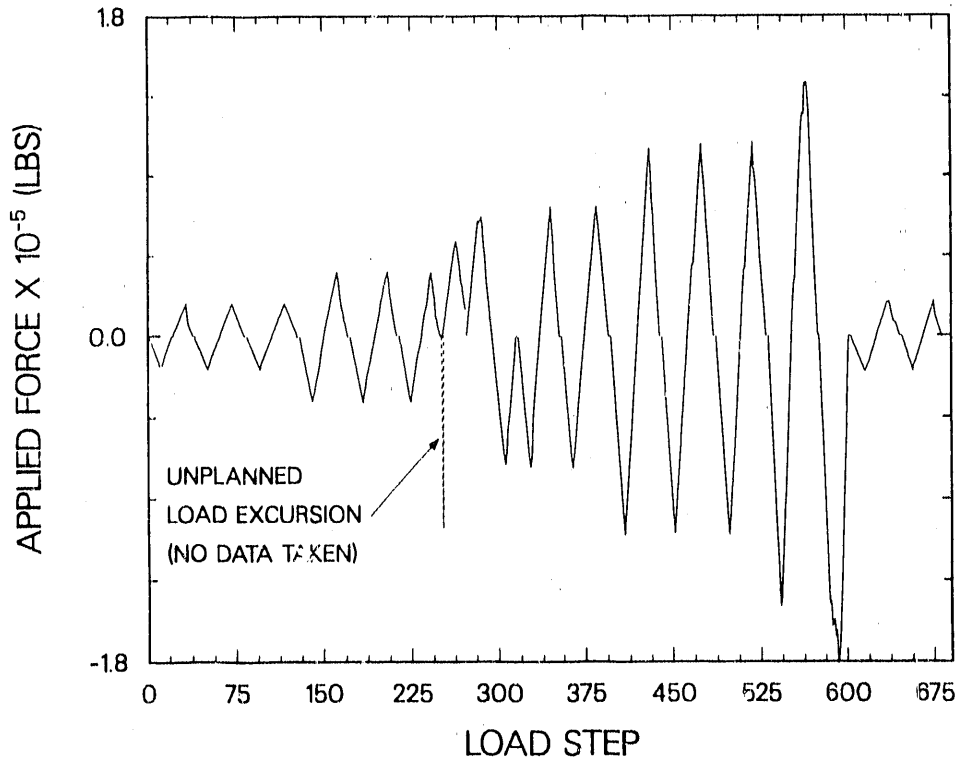


Fig. 13. TRG-5 load vs load step history in terms of applied force.

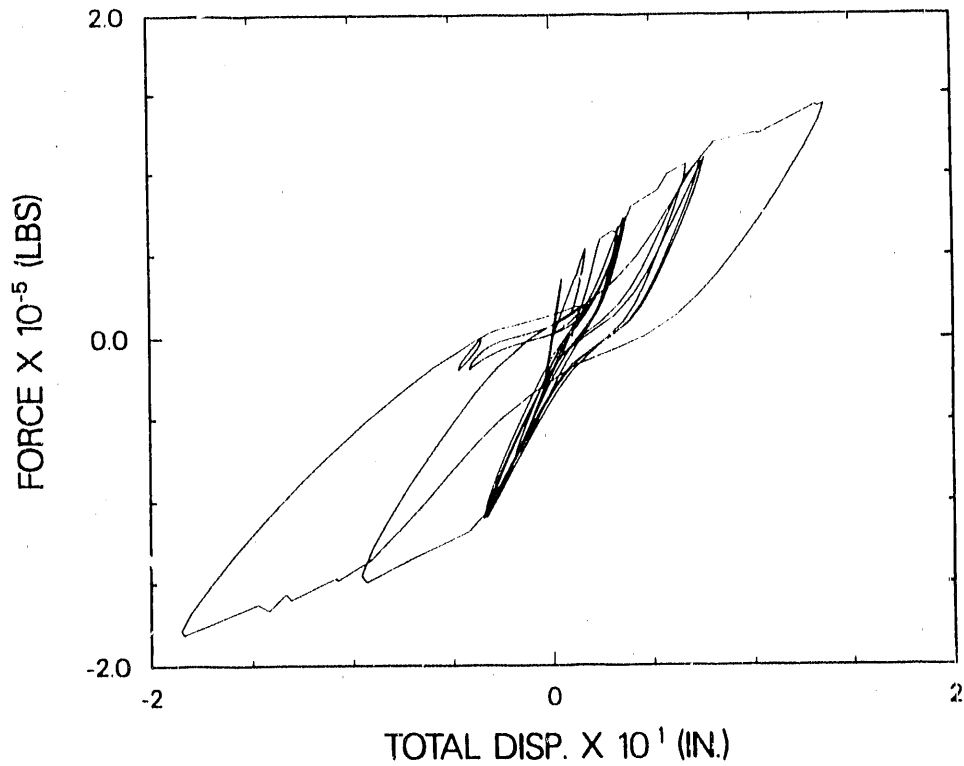


Fig. 14. Entire load cycle history TRG-5-4(1.0,0.56).

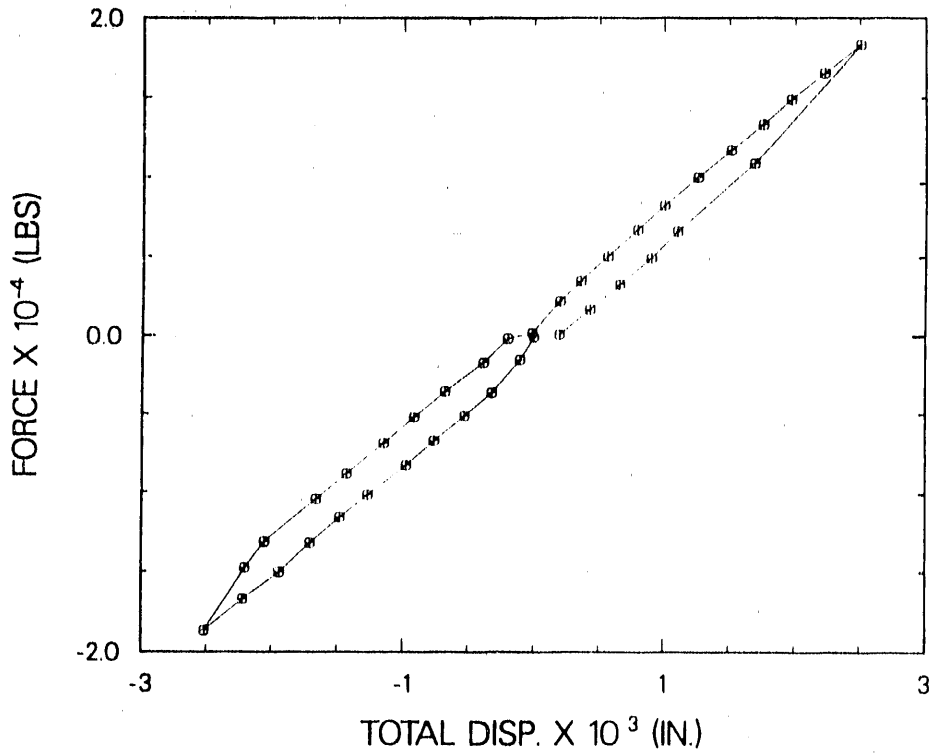


Fig. 15. TRG-5-4 (1.0,05.6) 50-psi ABSS load Cycle 1.

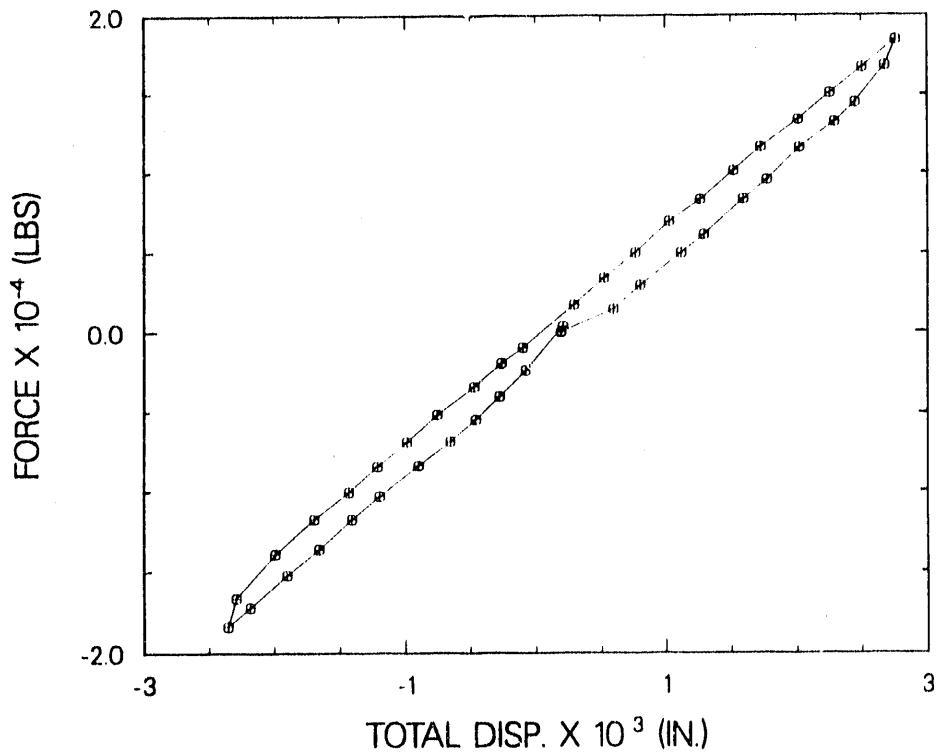


Fig. 16. TRG-5-4 (1.0,0.56) 50-psi ABSS load Cycle 2.

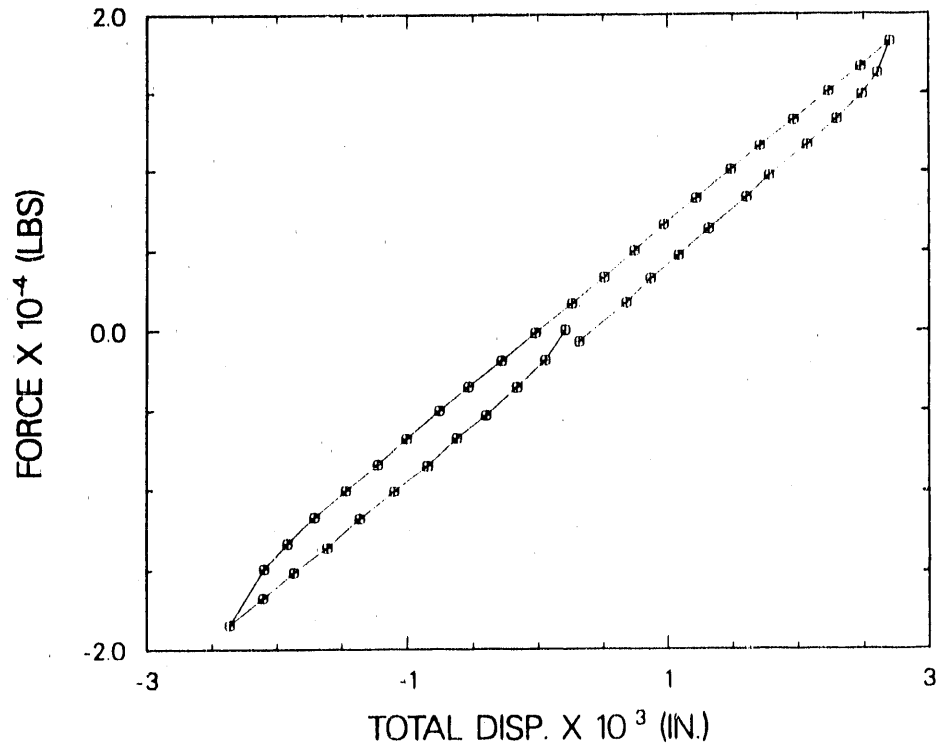


Fig. 17. TRG-5-4 (1.0,0.56) 50-psi ABSS load Cycle 3

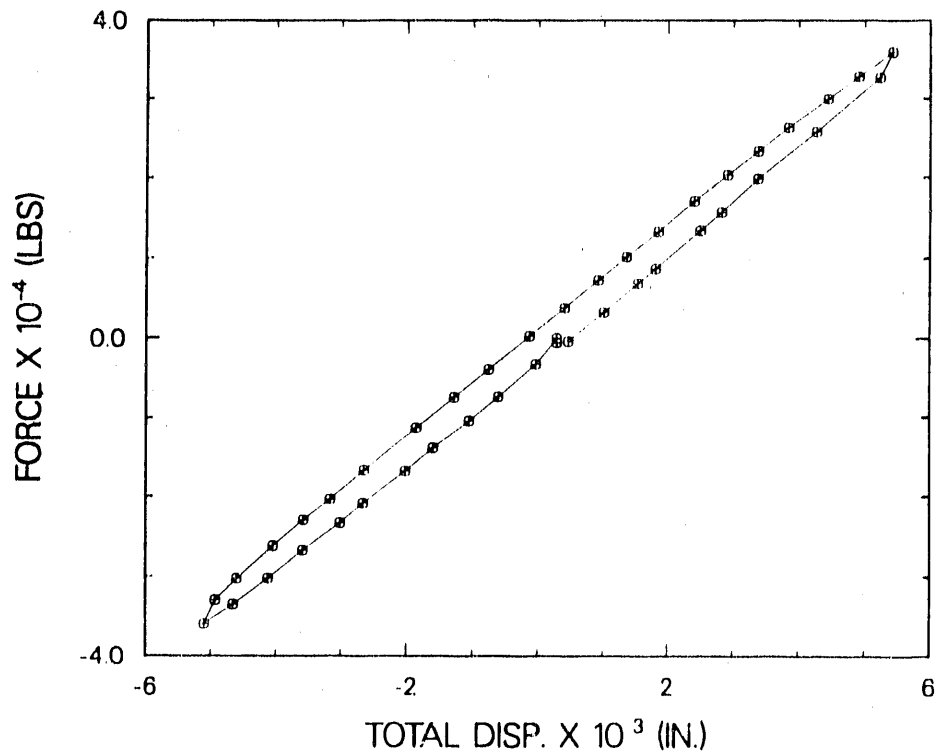


Fig. 18. TRG-5-4 (1.0,0.56) 100-psi ABSS load Cycle 1.

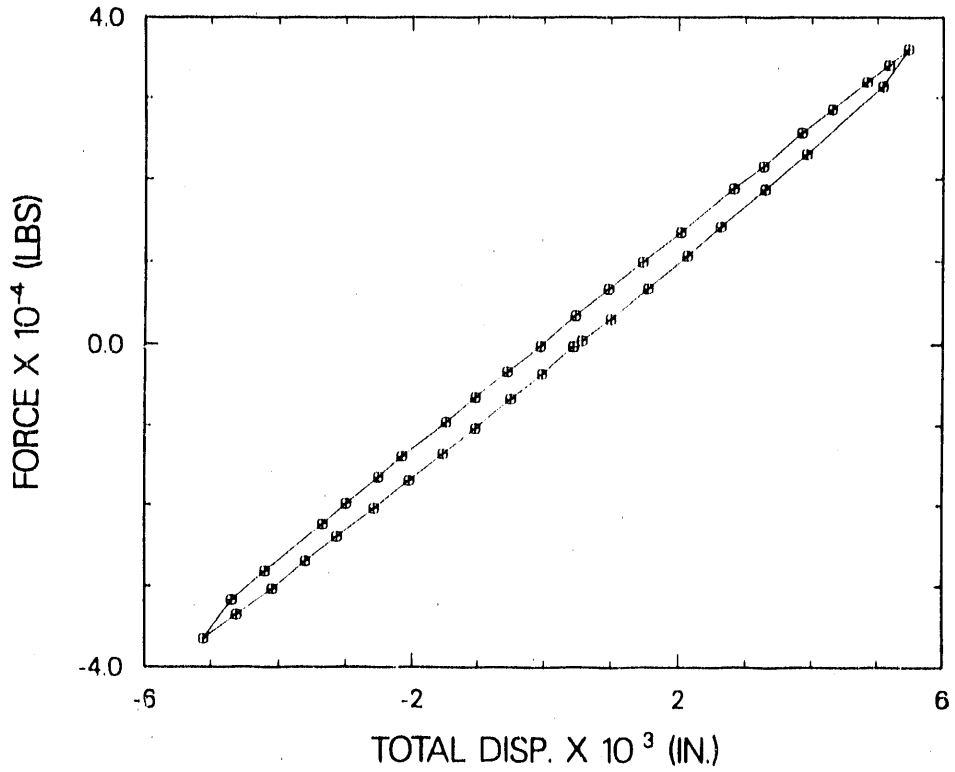


Fig. 19. TRG-5-4 (1.0,0.56) 100-psi ABSS load Cycle 2.

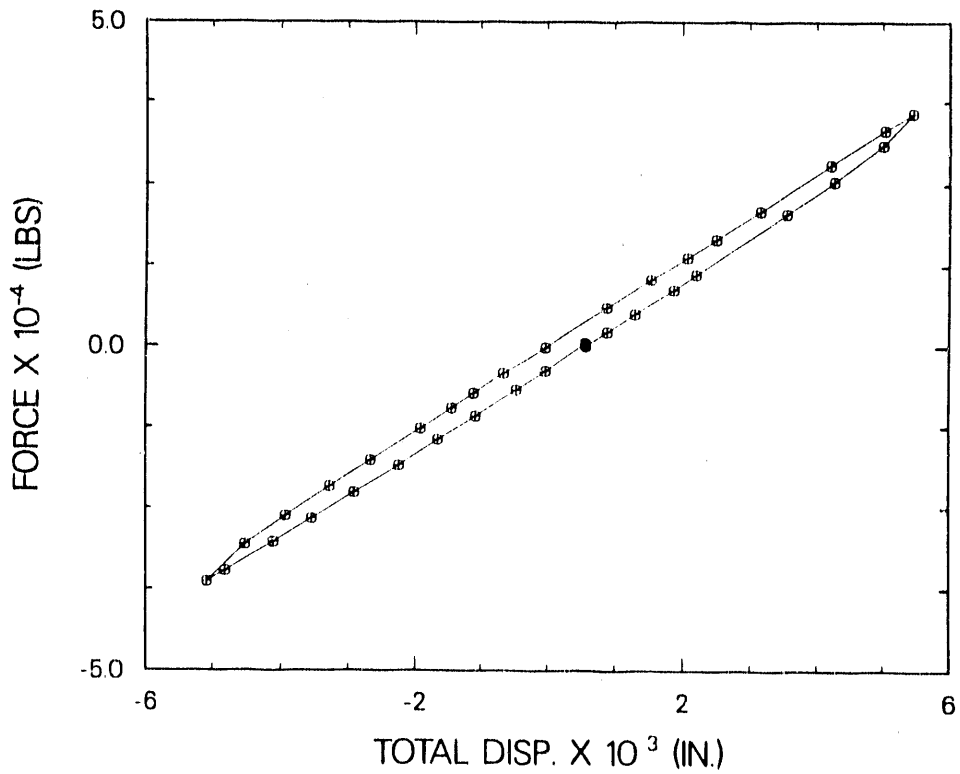


Fig. 20. TRG-5-4 (1.0,0.56) 100-psi ABSS load Cycle 3.

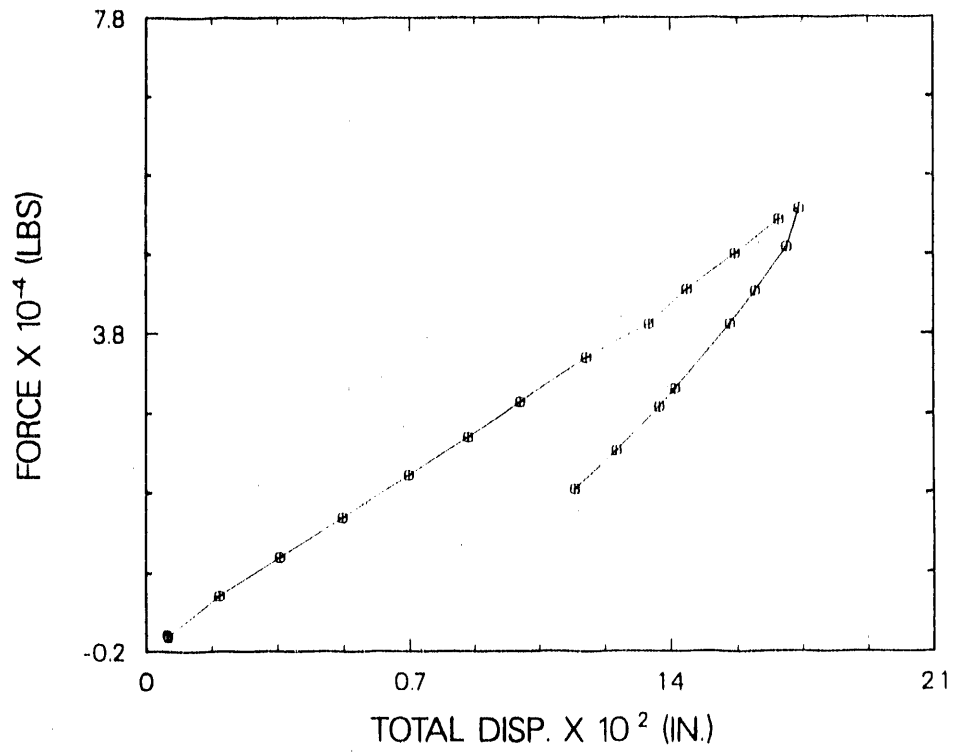


Fig. 21. TRG-5-4 (1.0,0.56) 150-psi ABSS load Halfcycle 1.

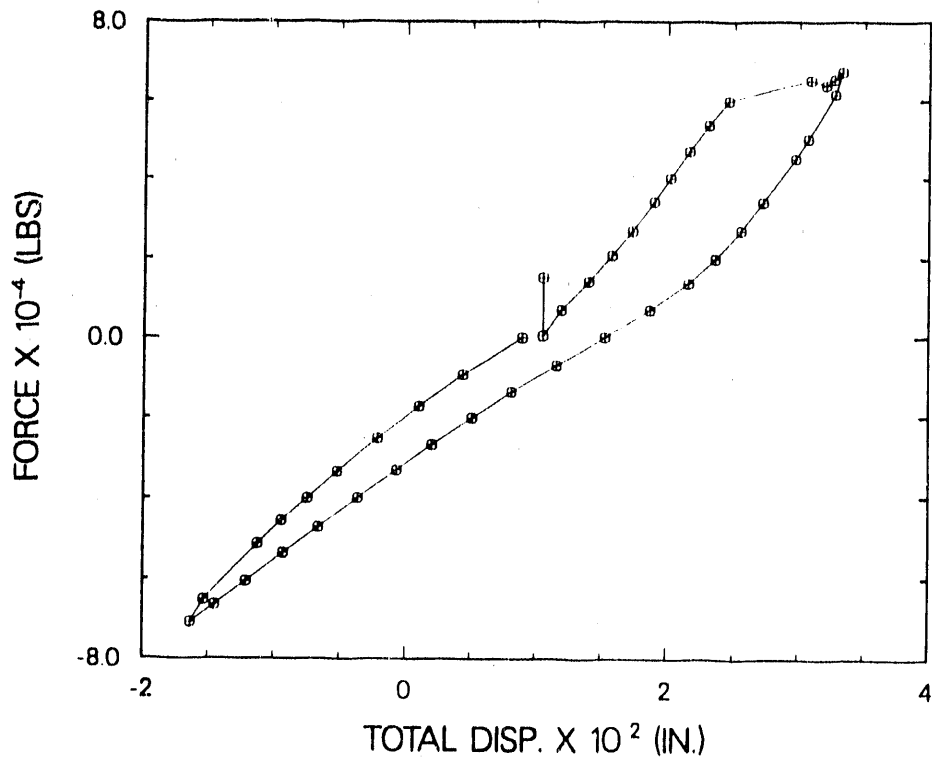


Fig. 22. TRG-5-4 (1.0,0.56) 200-psi ABSS load Cycle 1.

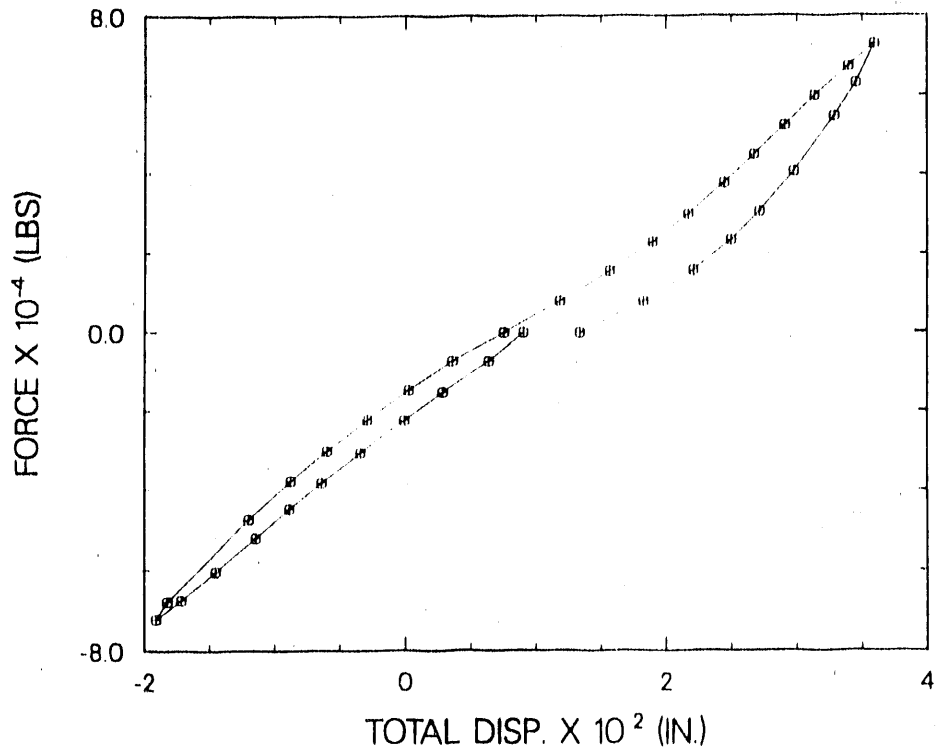


Fig. 23. TRG-5-4 (1.0,0.56) 200-psi ABSS load Cycle 2.

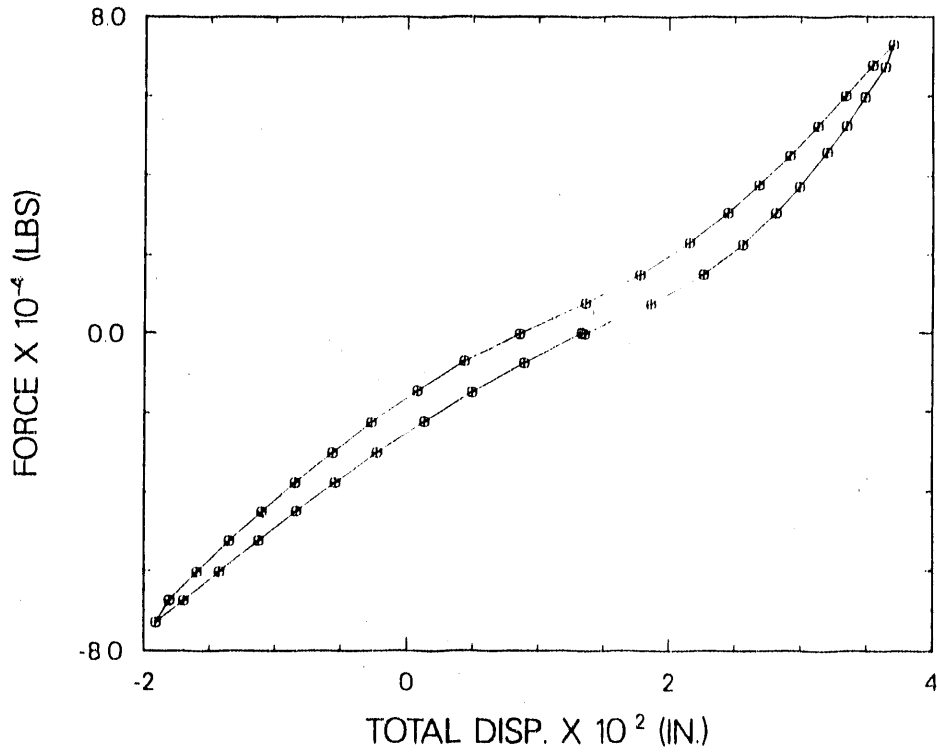


Fig. 24. TRG-5-4 (1.0,0.56) 200-psi ABSS load Cycle 3.

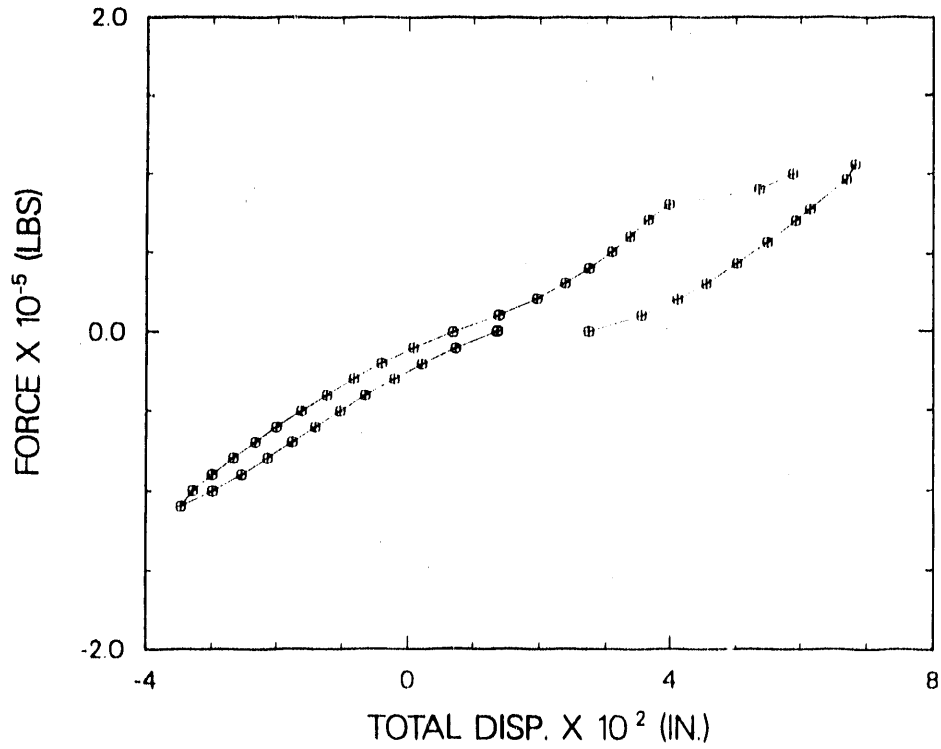


Fig. 25. TRG-5-4 (1.0,0.56) 300-psi ABSS load Cycle 1.

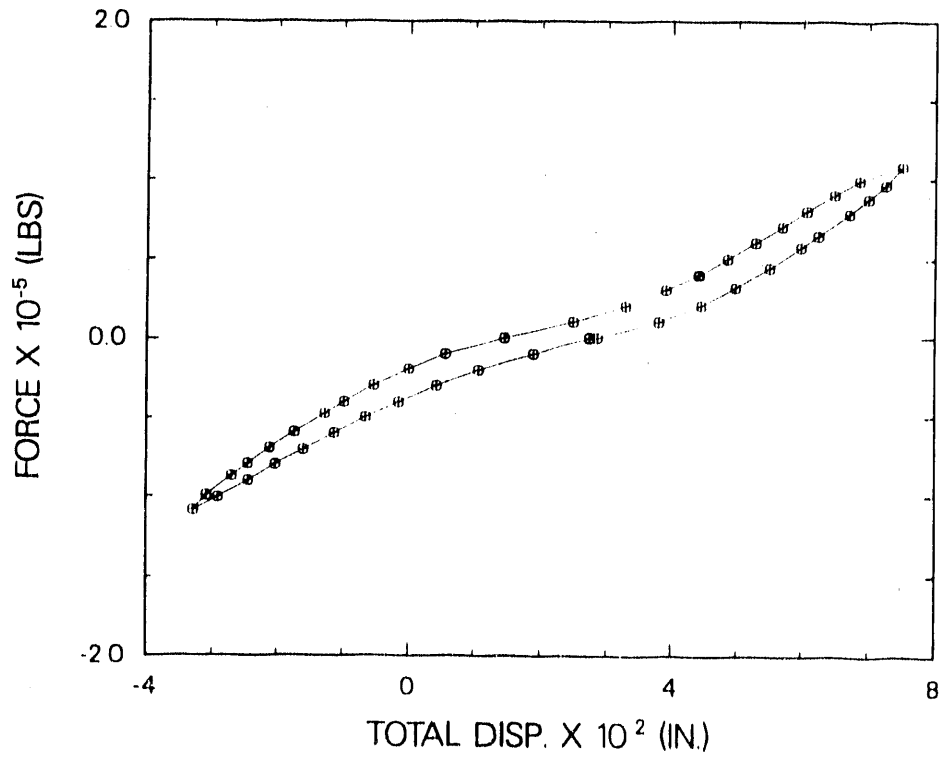


Fig. 26. TRG-5-4 (1.0,0.56) 300-psi ABSS load Cycle 2.

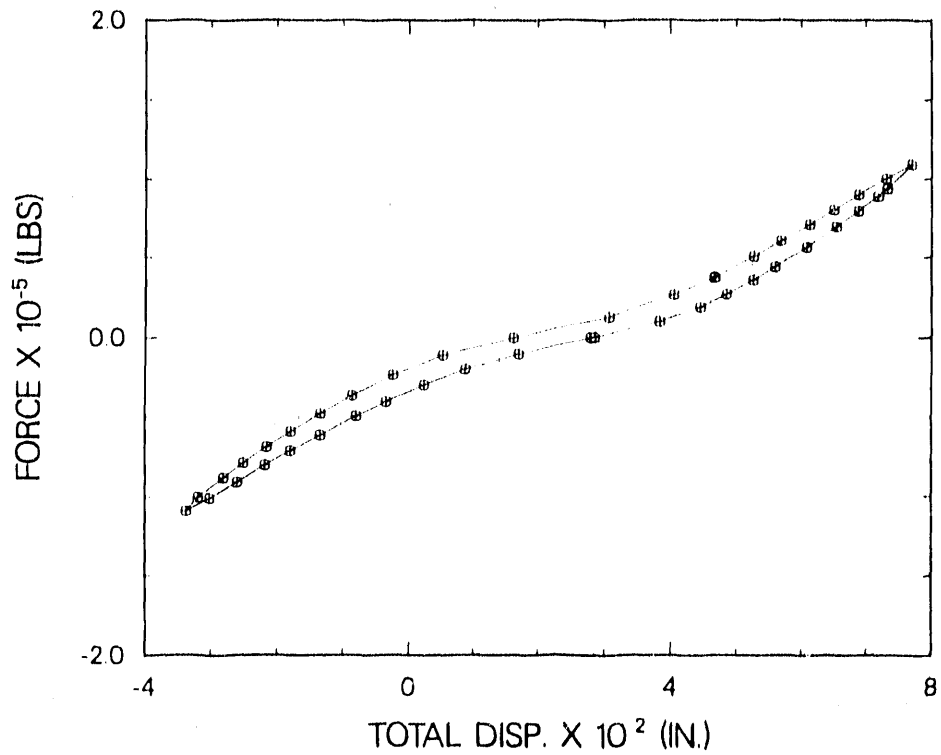


Fig. 27. TRG-5-4 (1.0,0.56) 300-psi ABSS load Cycle 3.

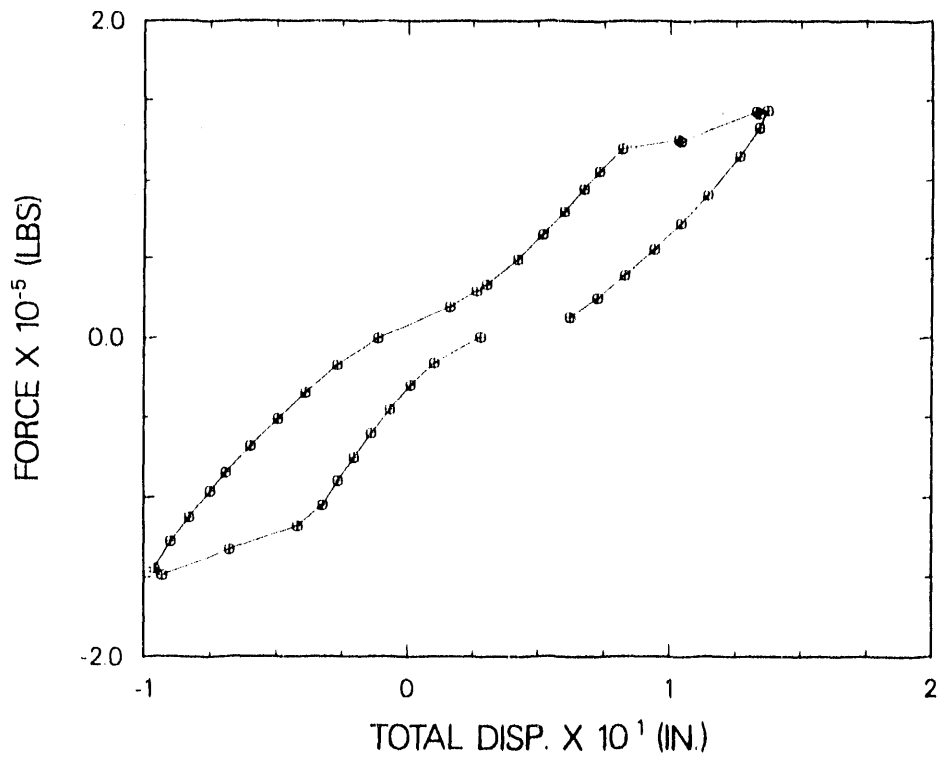


Fig. 28. TRG-5-4 (1.0,0.56) failure load cycle in first direction.

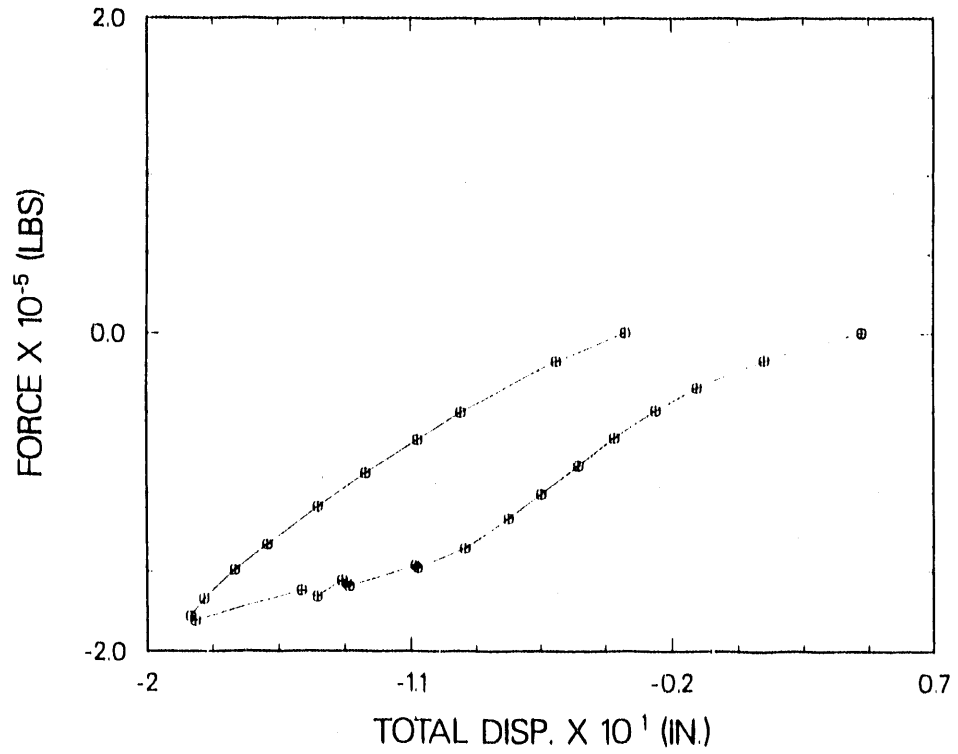


Fig. 29. TRG-5-4 (1.0,0.56) failure load cycle in second direction.

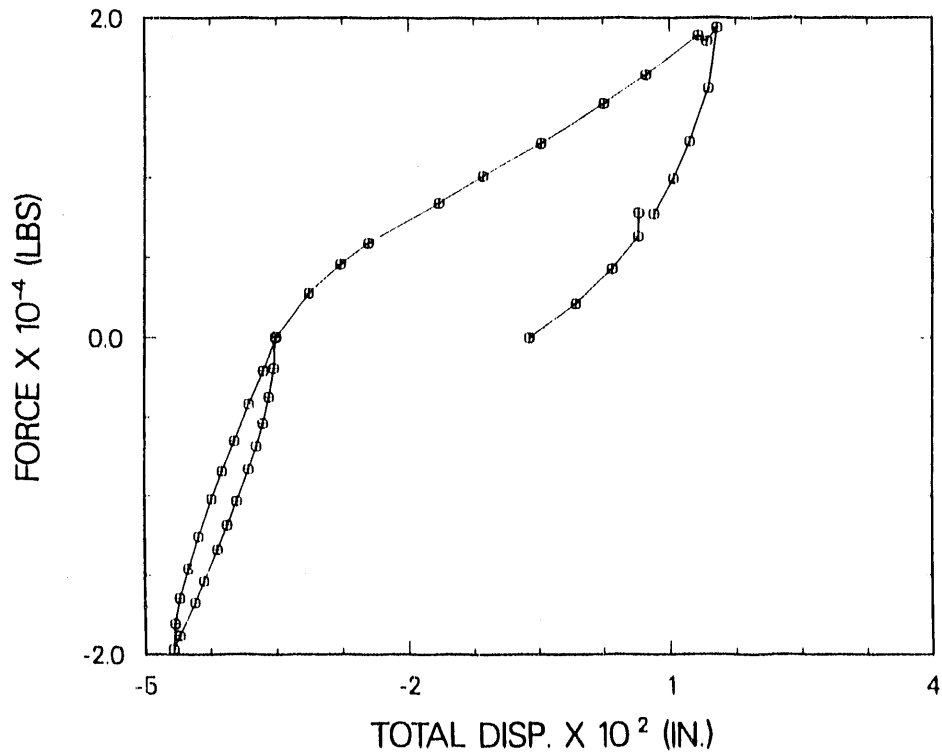


Fig. 30. TRG-5-4 (1.0,0.56) postfailure 50-psi load Cycle 1.

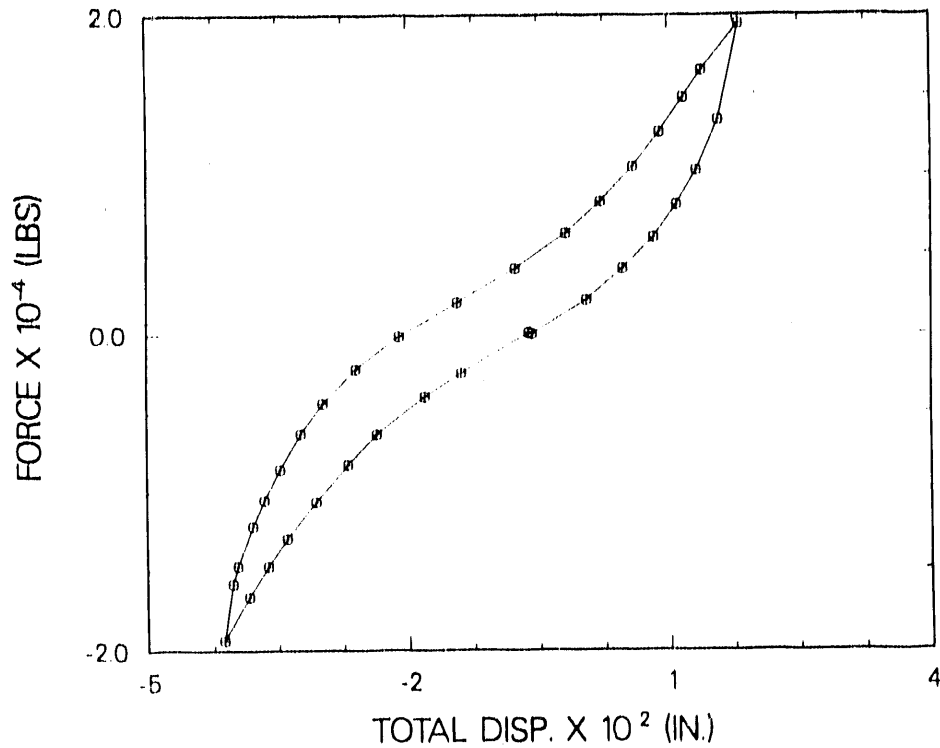
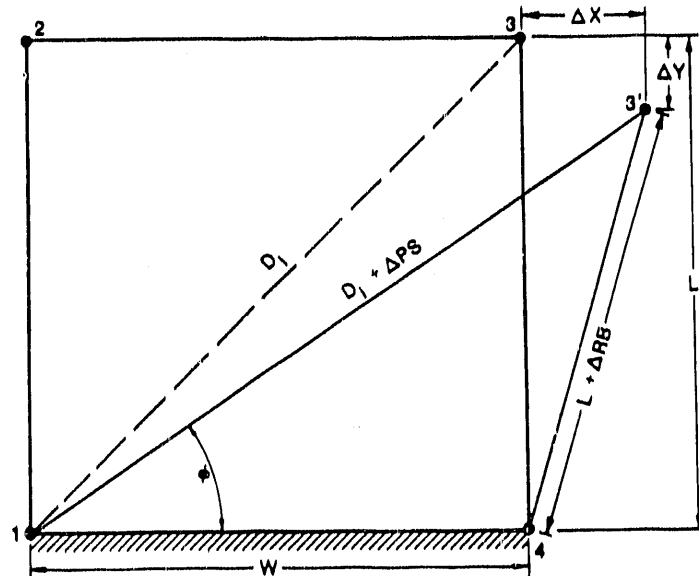


Fig. 31. TRG-5-4 (1.0,0.56) postfailure 50-psi load Cycle 2.



$$\Delta X = (D_1 + \Delta PS) \cos \phi - W$$

$$\Delta Y = (D_1 + \Delta PS) \sin \phi - L$$

$$\phi = \cos^{-1} \left[\frac{W^2 + (D_1 + \Delta PS)^2 - (L + \Delta RB)^2}{2 W (D_1 + \Delta PS)} \right]$$

ΔPS - DIAGONAL DISPLACEMENT GAGE READING
 ΔRB - VERTICAL DISPLACEMENT GAGE READING

Fig. 32. The method and equations used for reducing the internal gage data.

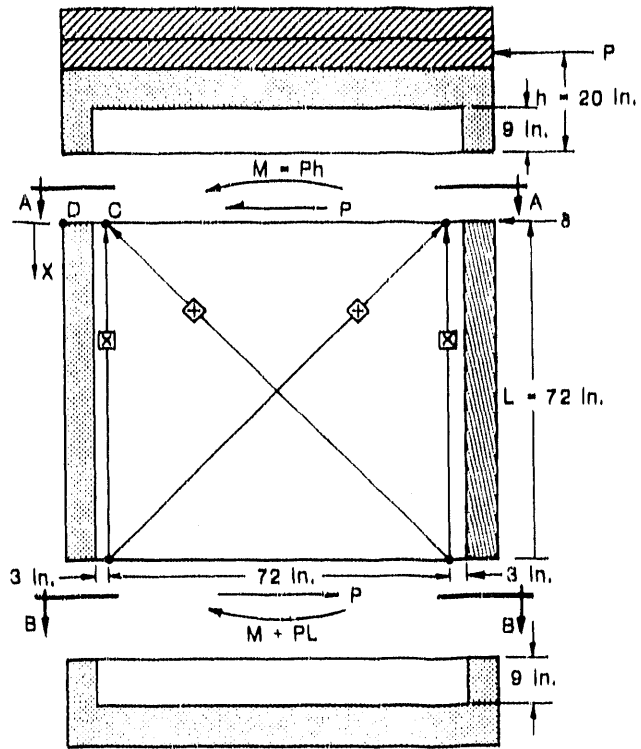


Fig. 33. Free-body diagram of the shear wall.

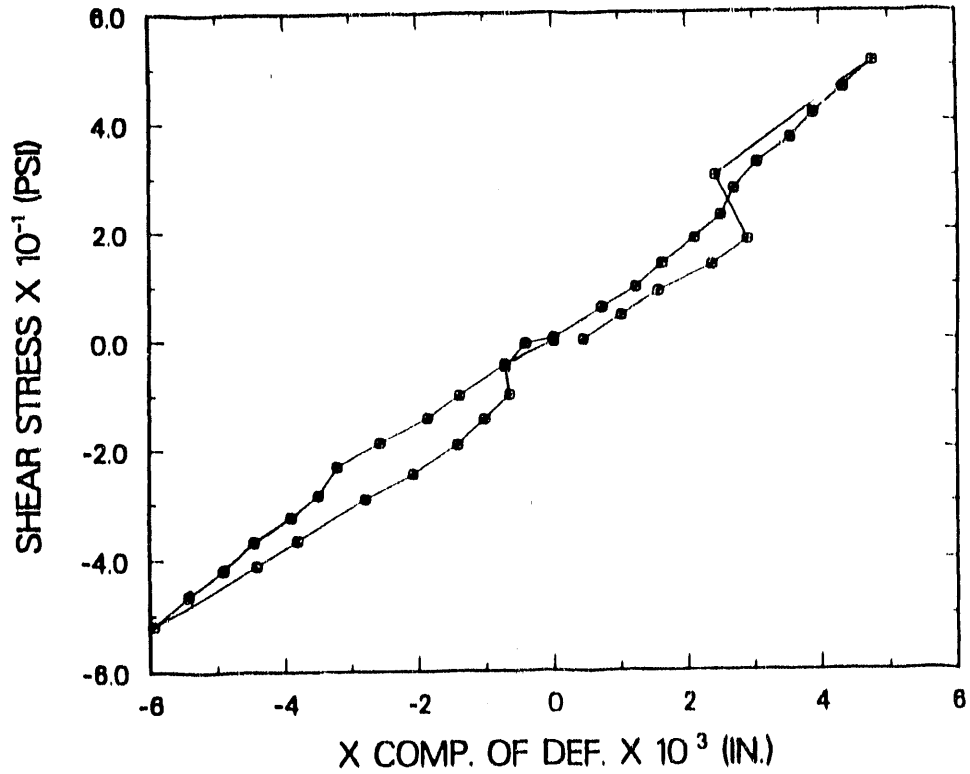


Fig. 34. TRG-5-4 (1.0,0.56) 50-psi ABSS Cycle 1 (external gages).

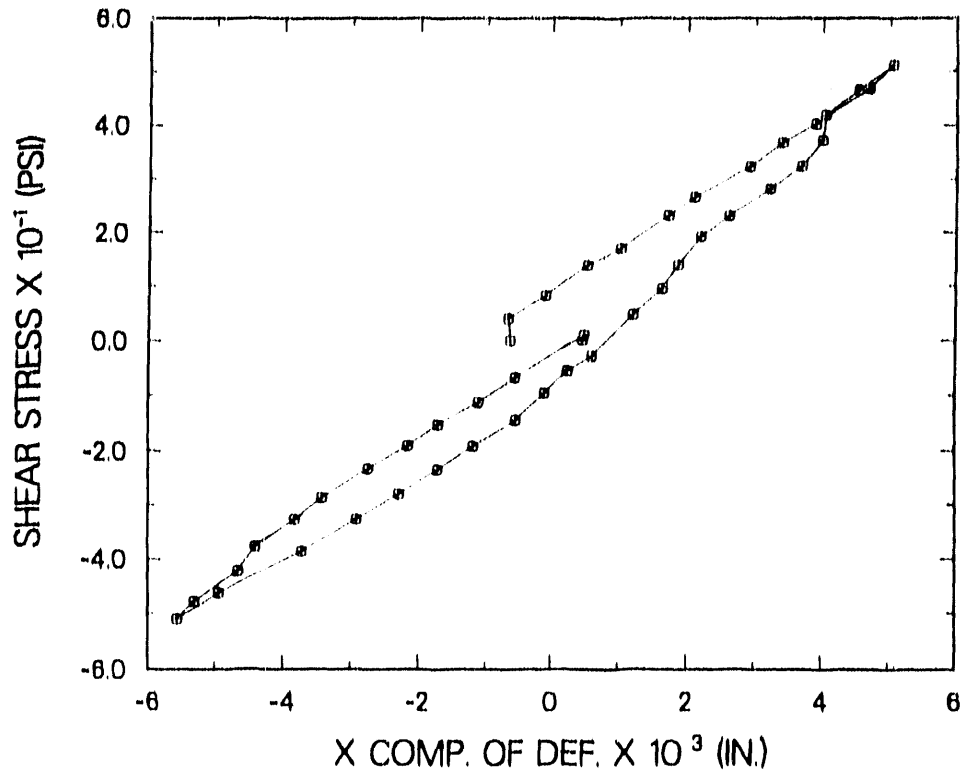


Fig. 35. TRG-5-4 (1.0,0.56) 50-psi ABSS load Cycle 2 (external gages).

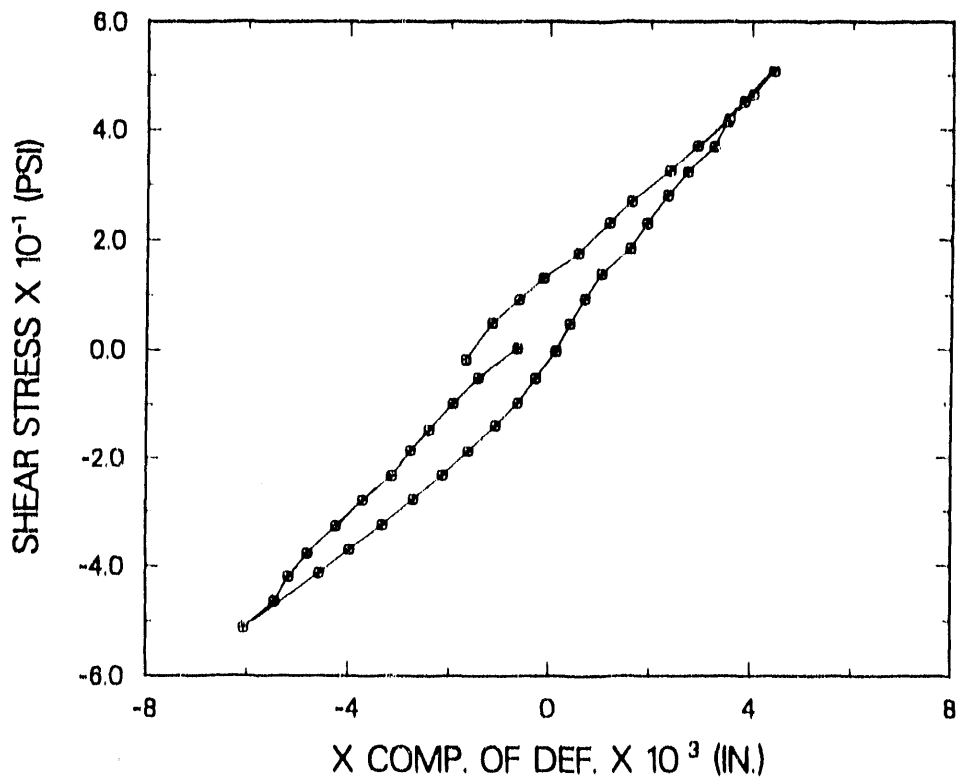


Fig. 36. TRG-5-4 (1.0,0.56) 50-psi ABSS load Cycle 3 (external gages).

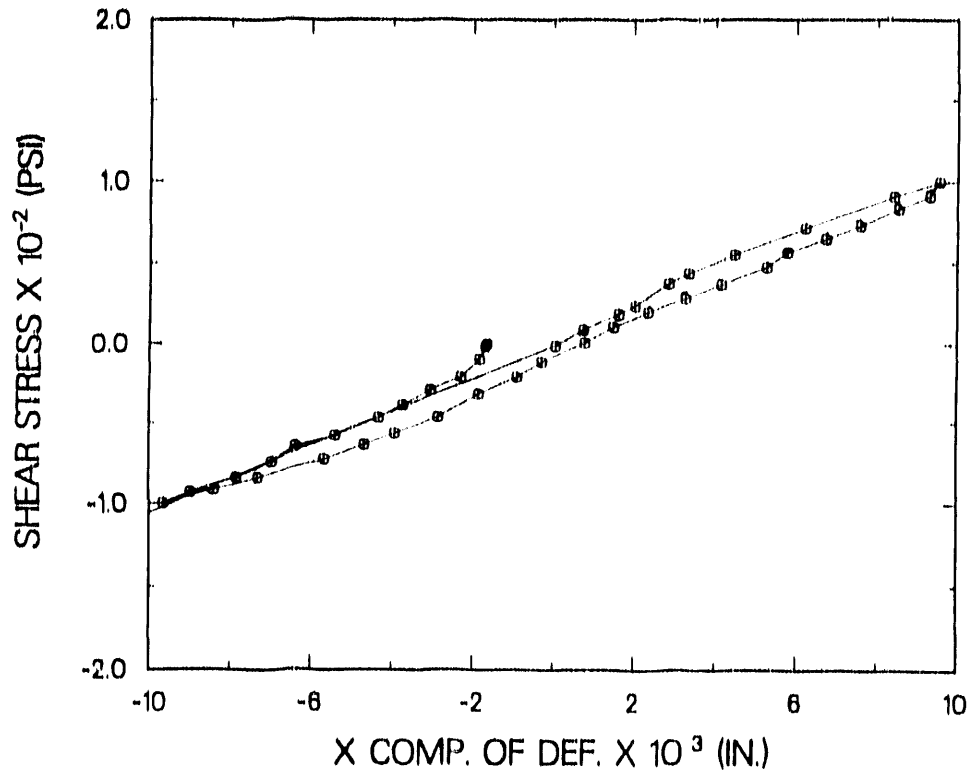


Fig. 37. TRG-5-4 (1.0,0.56) 100-psi ABSS load Cycle 1 (external gages).

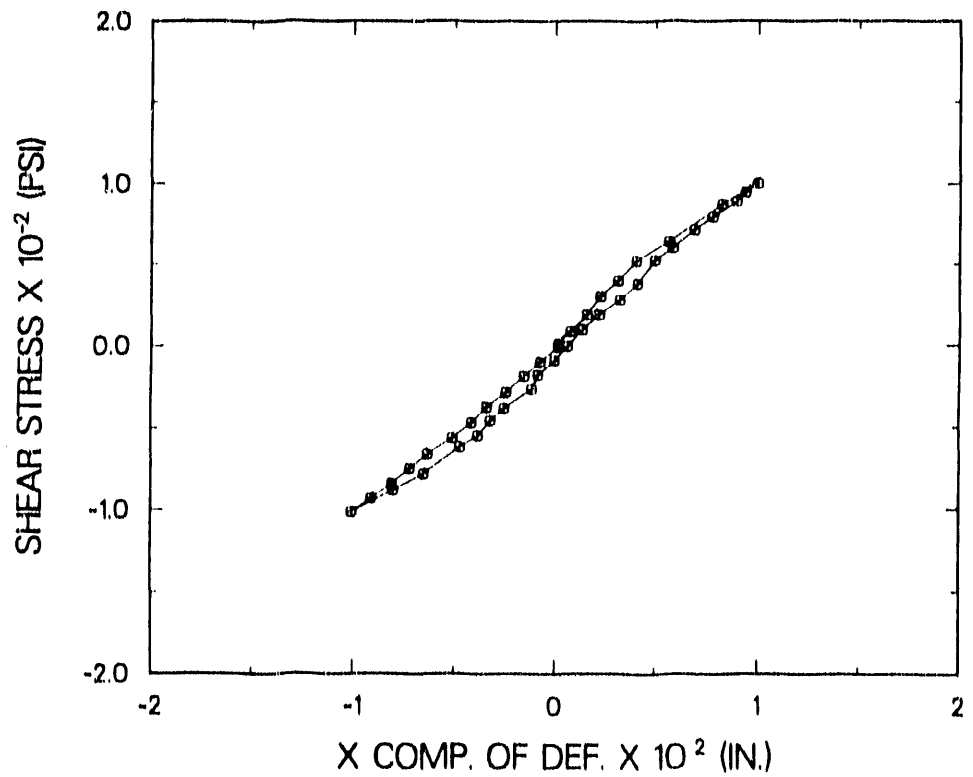


Fig. 38. TRG-5-4 (1.0,0.56) 100-psi ABSS load Cycle 2 (external gages).

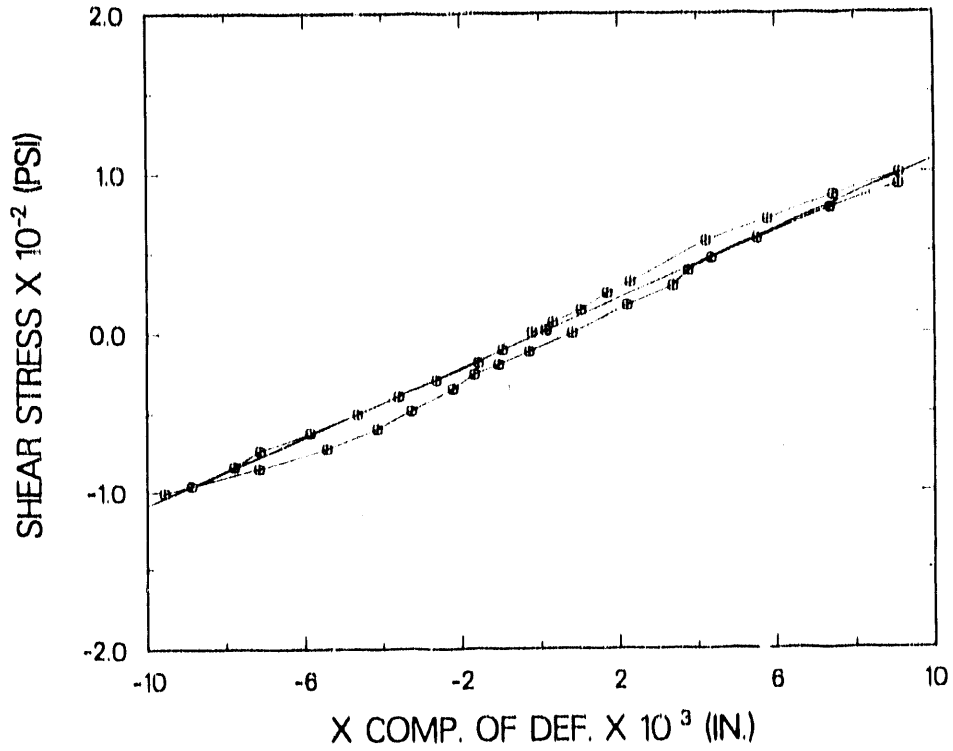


Fig. 39. TRG-5-4 (1.0,0.56) 100-psi ABSS load Cycle 3 (external gages).

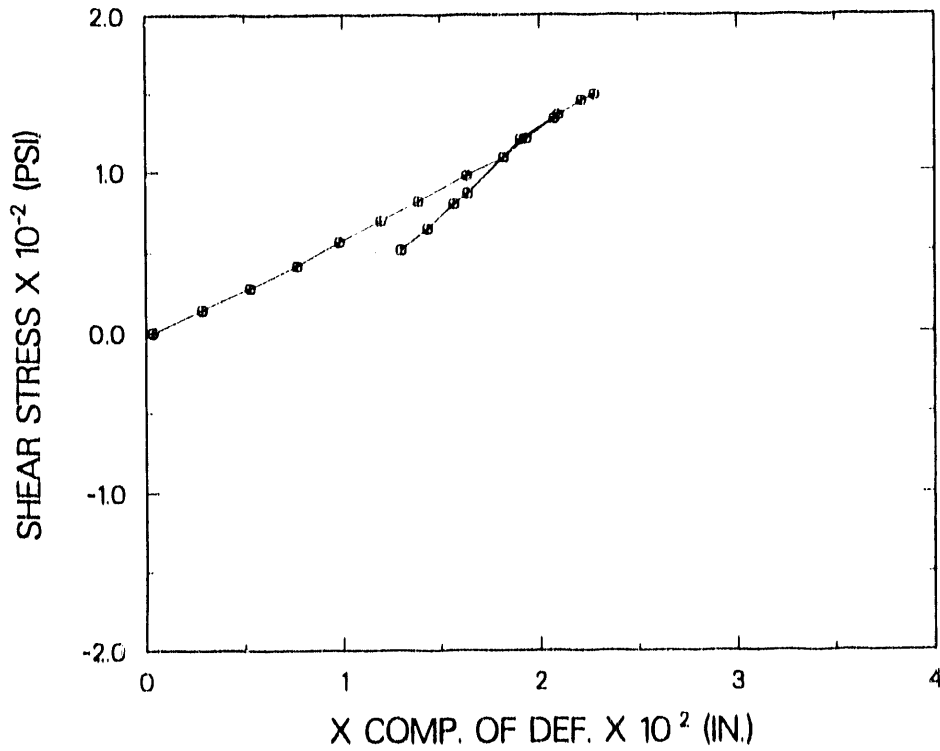


Fig. 40. TRG-5-4 (1.0,0.56) 150-psi ABSS load Halfcycle 1 (external gages).

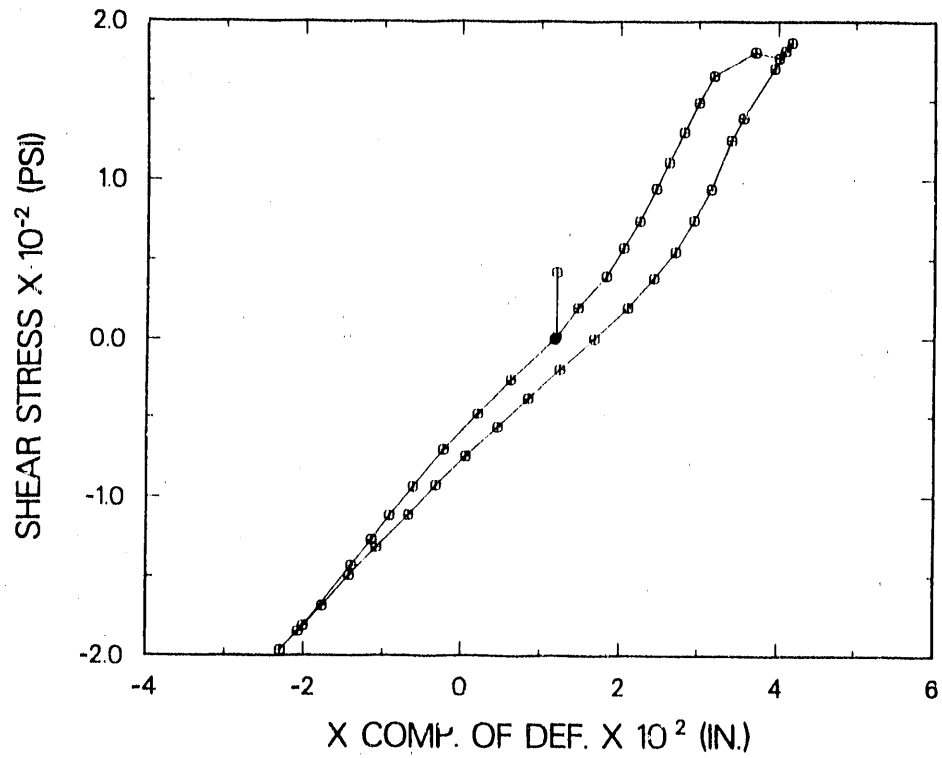


Fig. 41. TRG-5-4 (1.0,0.56) 200-psi ABSS load Cycle 1 (external gages).

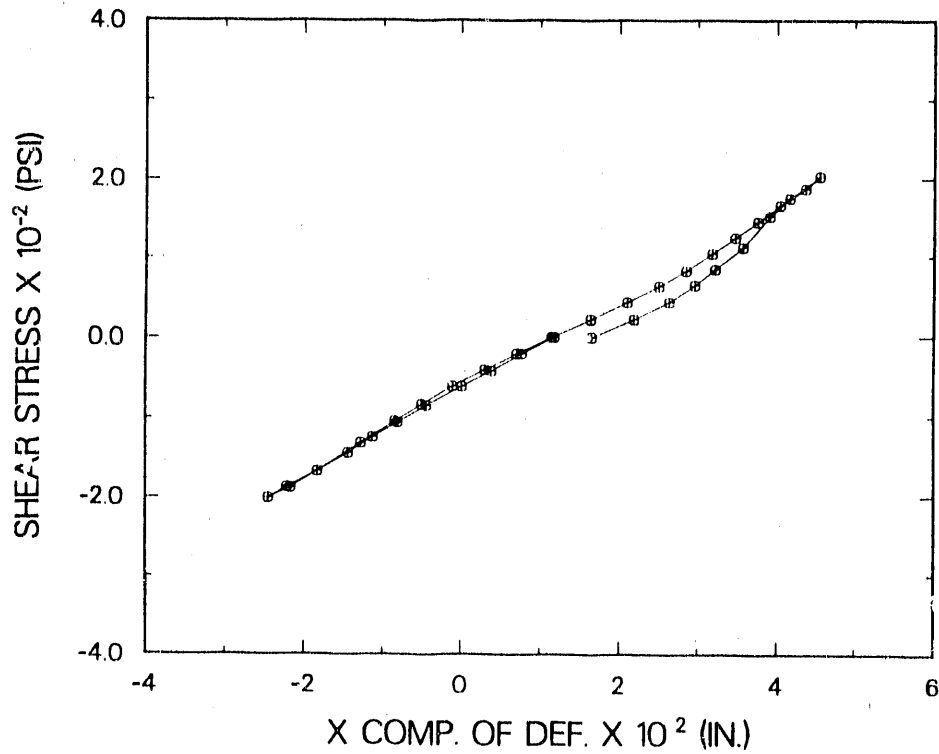


Fig. 42. TRG-5-4 (1.0,0.56) 200-psi ABSS load Cycle 2 (external gages).

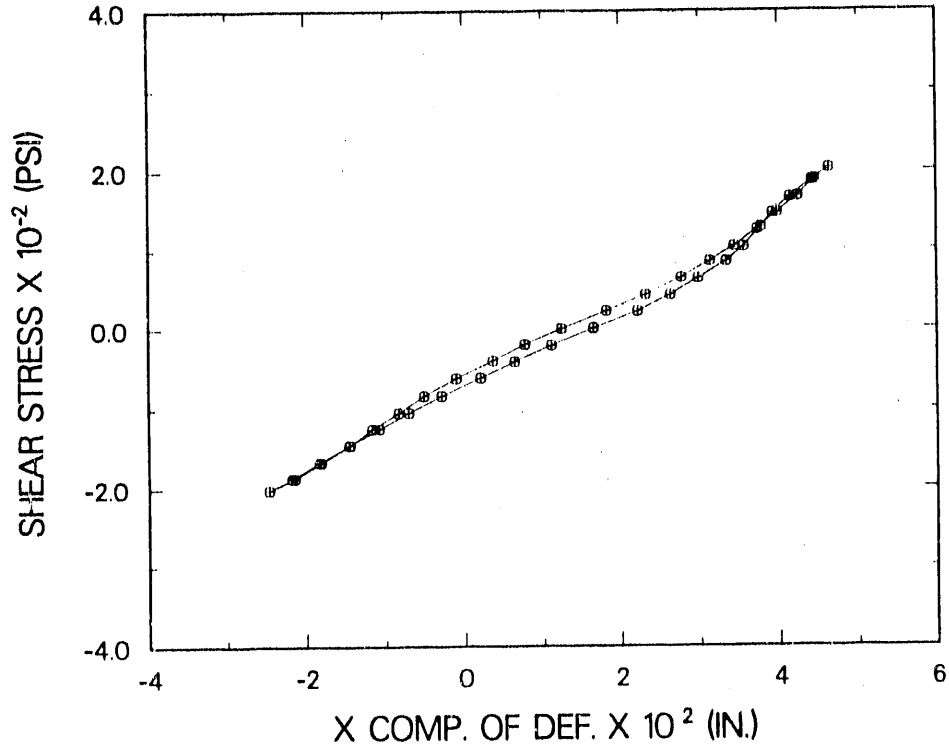


Fig. 43. TRG-5-4 (1.0,0.56) 200-psi ABSS load Cycle 3 (external gages).

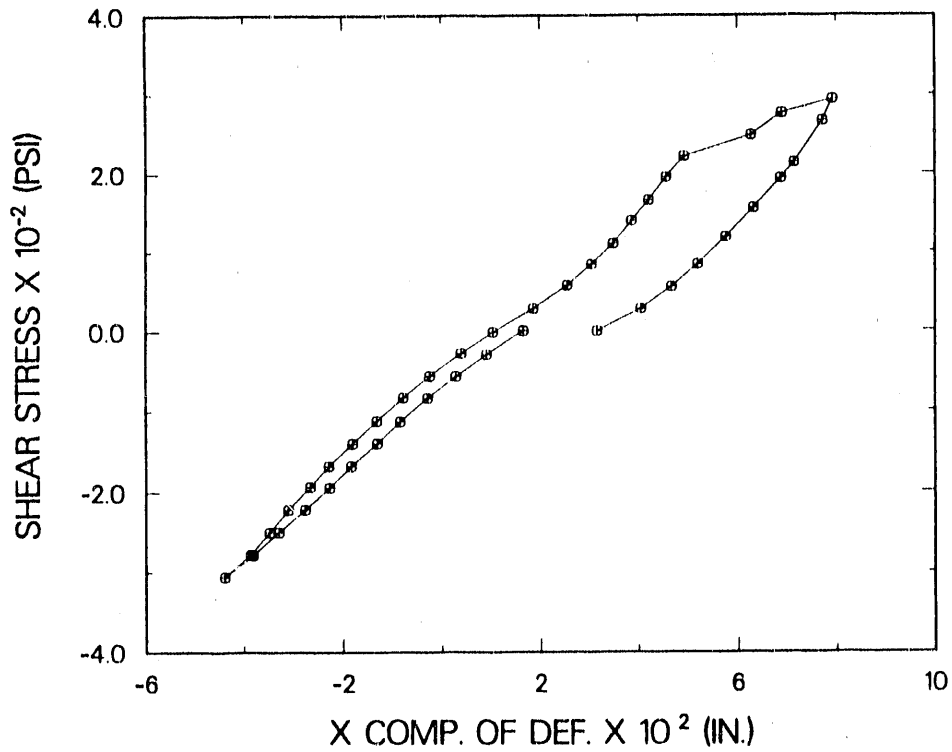


Fig. 44. TRG-5-4 (1.0,0.56) 300-psi ABSS load Cycle 1 (external gages).

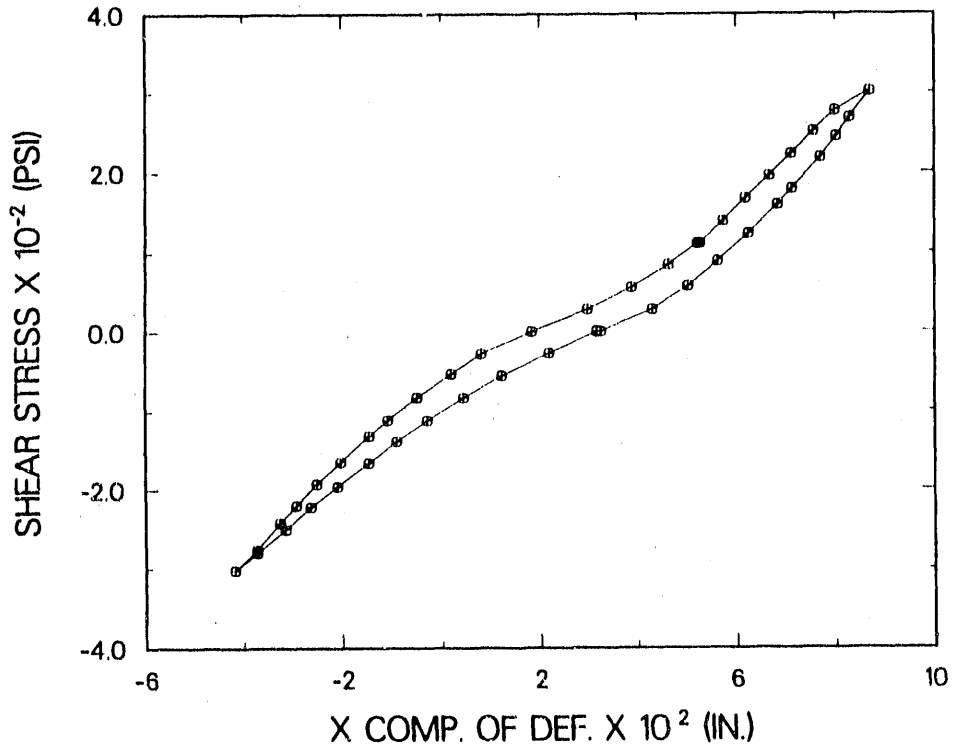


Fig. 45. TRG-5-4 (1.0,0.56) 300-psi ABSS load Cycle 2 (external gages).

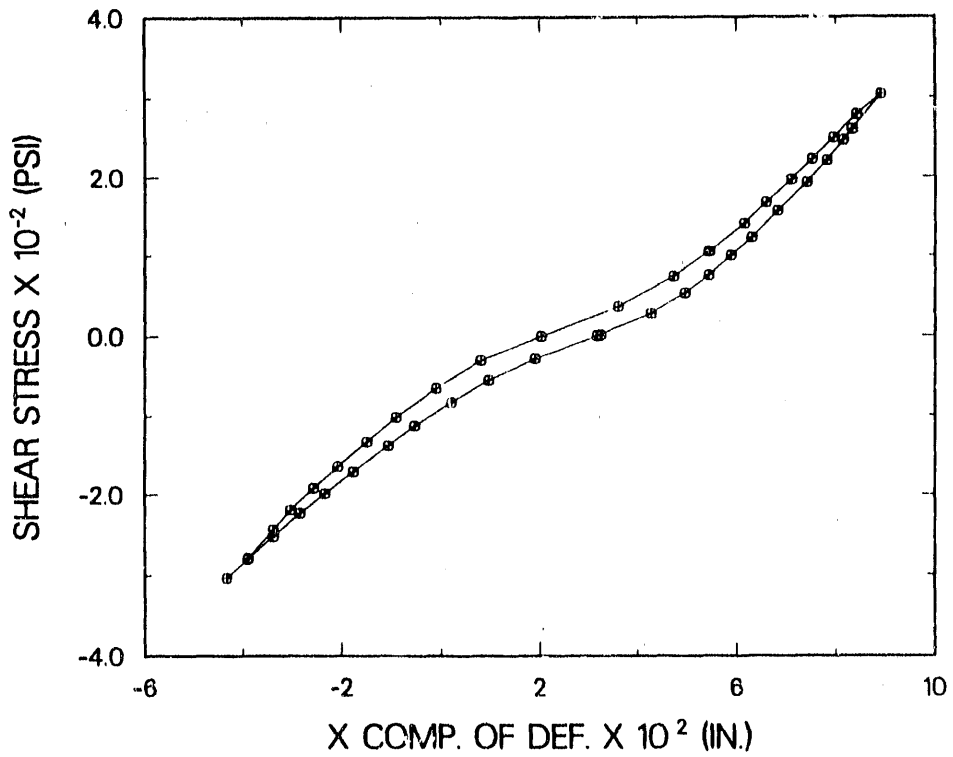


Fig. 46. TRG-5-4 (1.0,0.56) 300-psi ABSS load Cycle 3 (external gages).

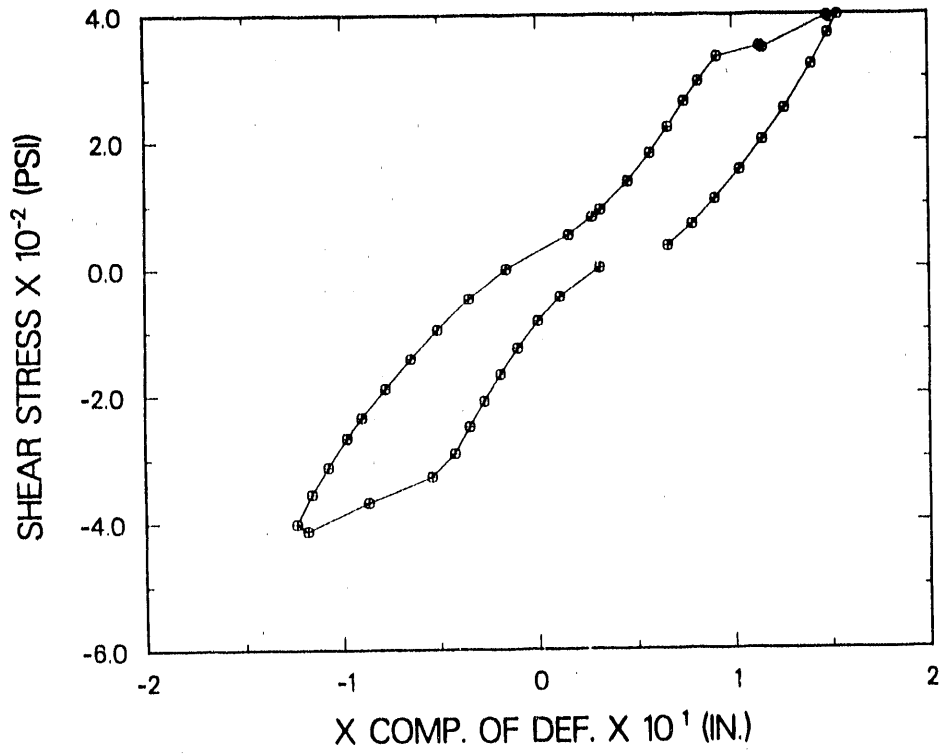


Fig. 47. TRG-5-4 (1.0,0.56) failure load cycle in first direction (external gages).

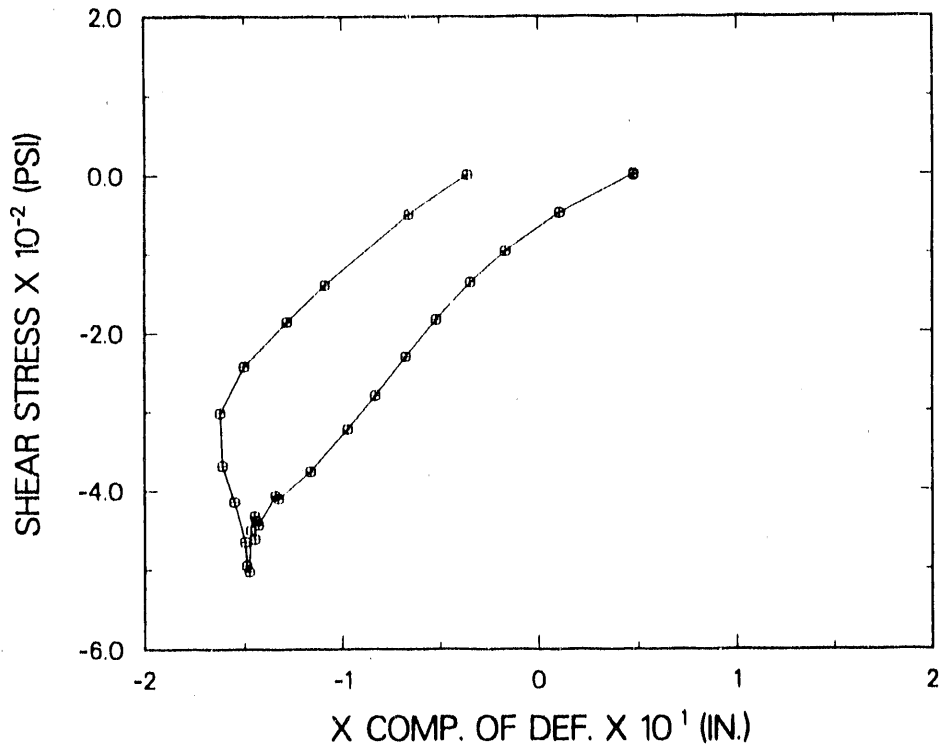


Fig. 48. TRG-5-4 (1.0,0.56) failure load cycle in second direction (external gages).

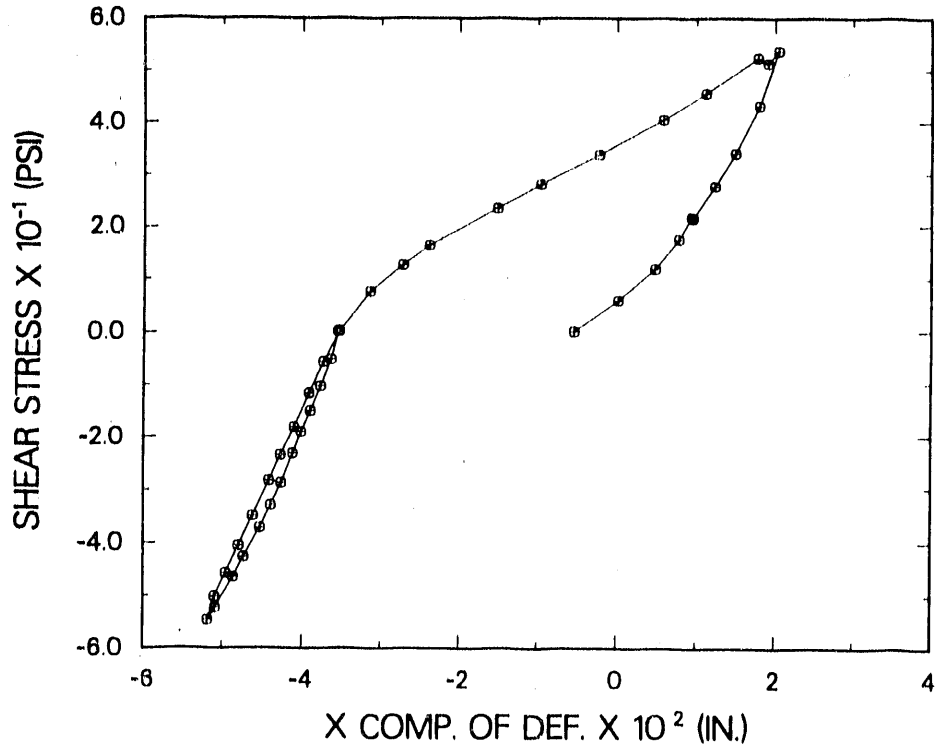


Fig. 49. TRG-5-4 (1.0,0.56) postfailure 50-psi load Cycle 1 (external gages).

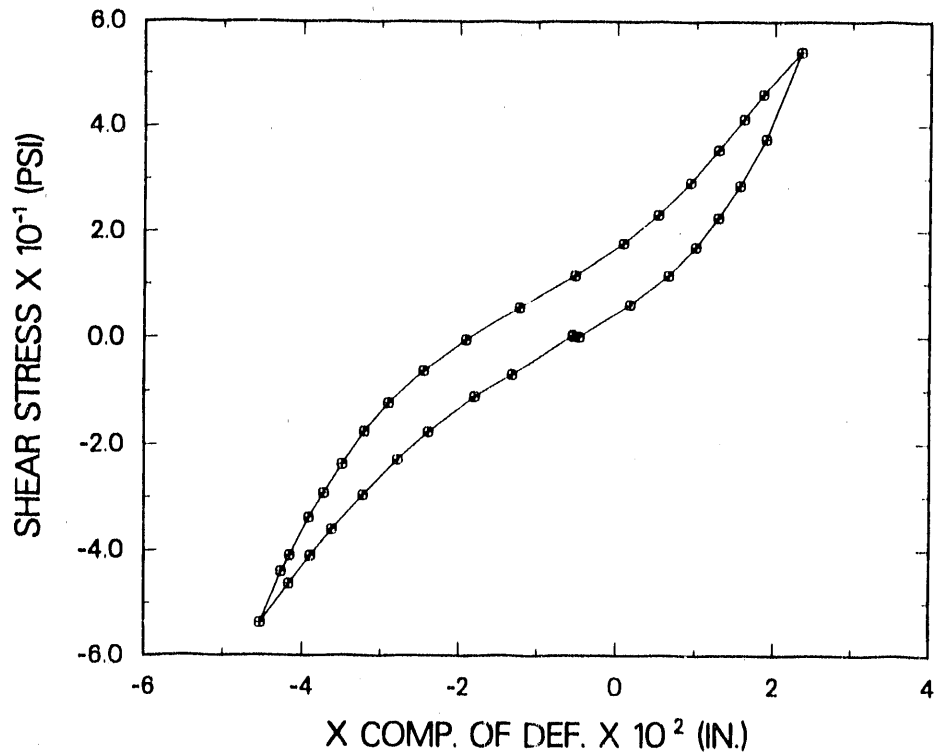


Fig. 50. TRG-5-4 (1.0,0.56) postfailure 50-psi load Cycle 2 (external gages).

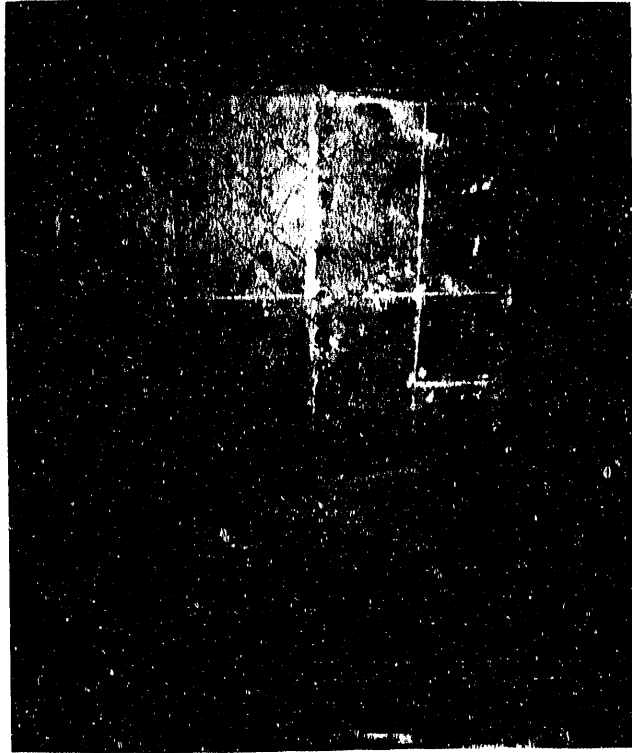


Fig. 51. Final crack pattern on west side of the shear wall.



Fig. 52. Final crack pattern on east side of the shear wall.



Fig. 53. Final crack pattern in north end wall.

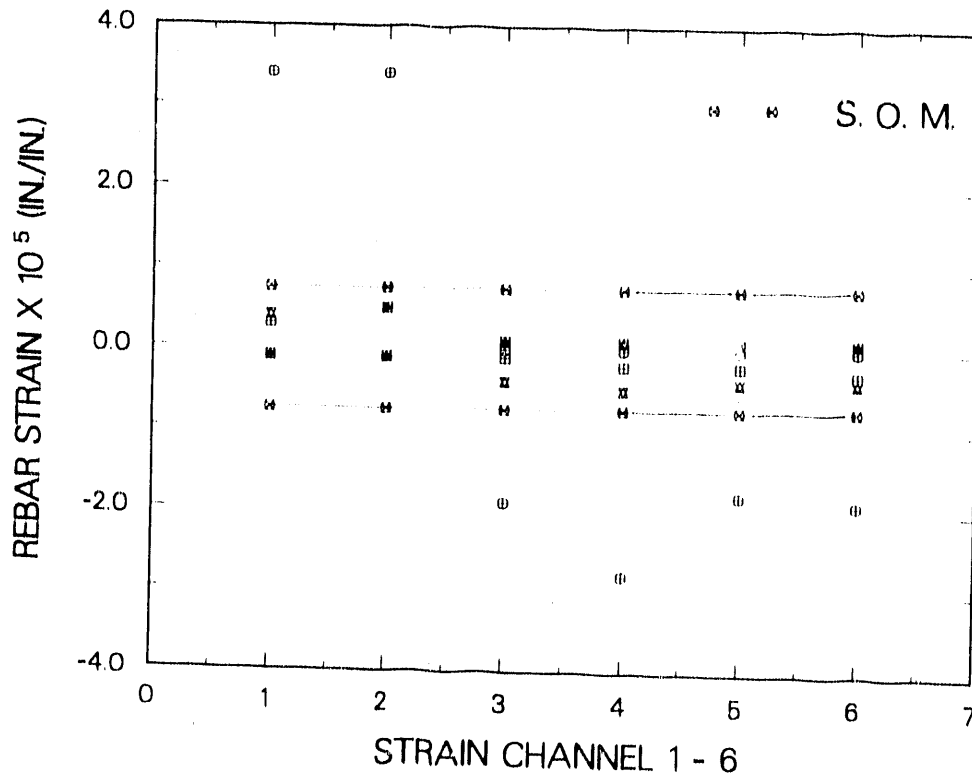


Fig. 54. Strain gage readings in the west end wall compared with SOM theory for the three 50-psi load cycles.

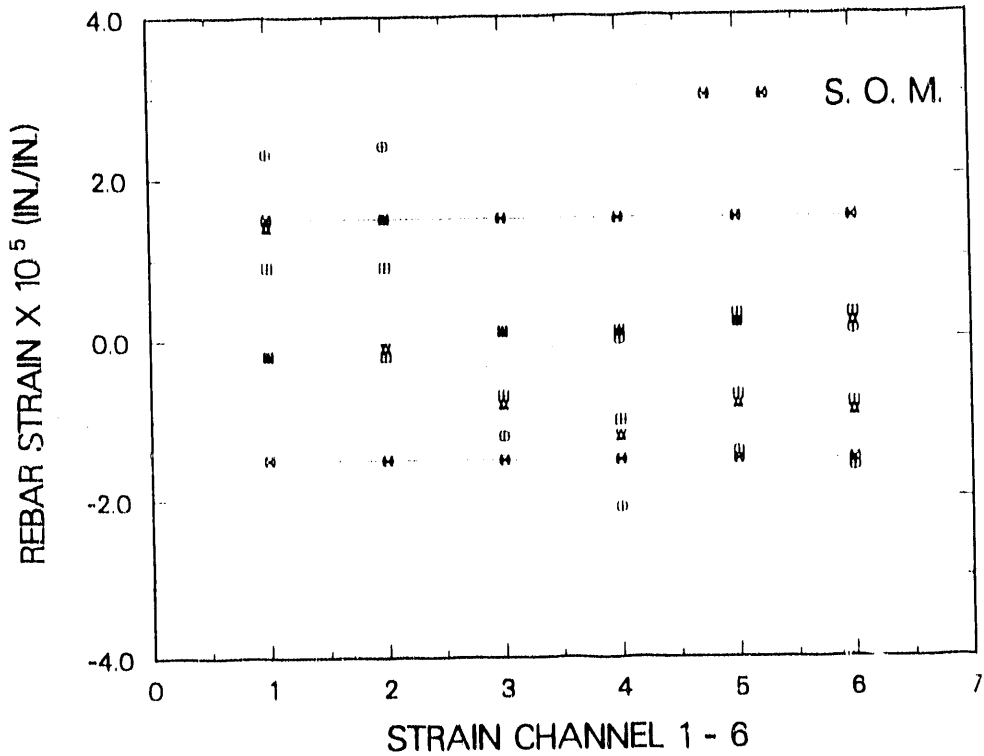


Fig. 55. Strain gage reading in the west end wall compared with SOM theory for the three 100-psi load cycles.

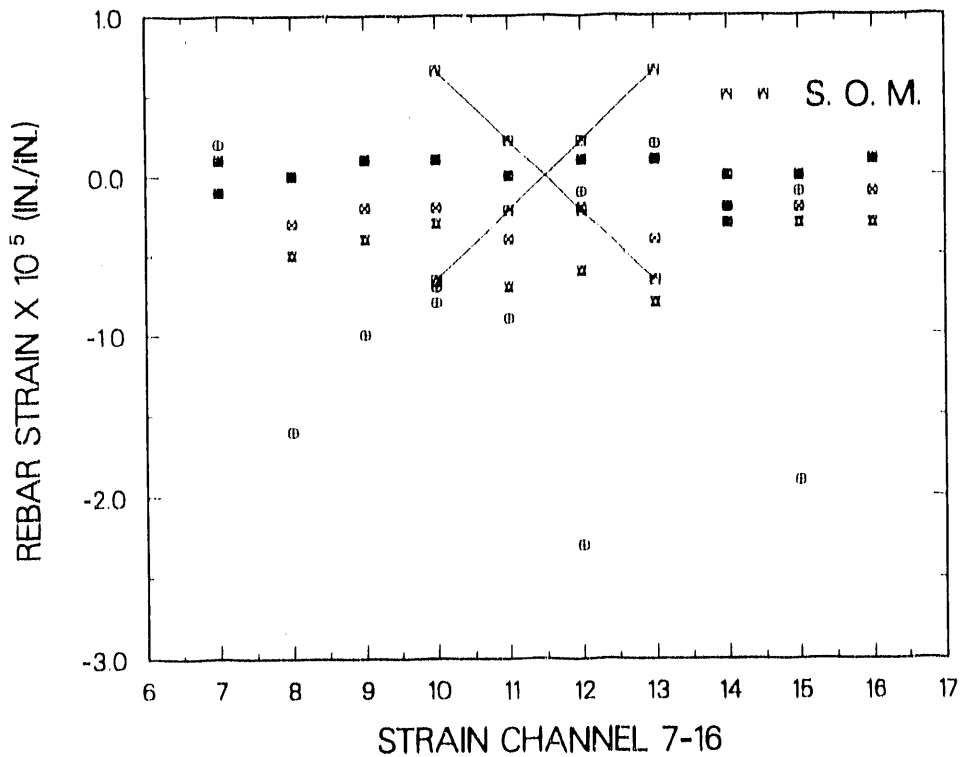


Fig. 56. Strain gage readings in the shear wall for the 50-psi cycles. Gages 10-13 may be compared with SOM theory.

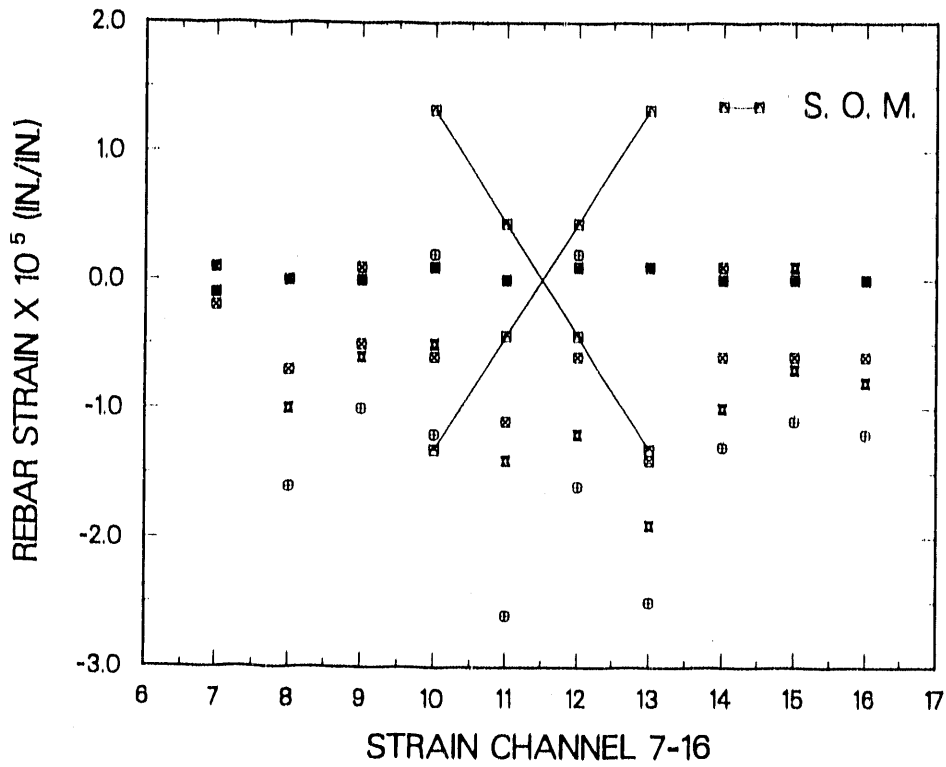


Fig. 57. Strain gage readings in the shear wall for the 100-psi cycles. Gages 10-13 may be compared with SOM theory.

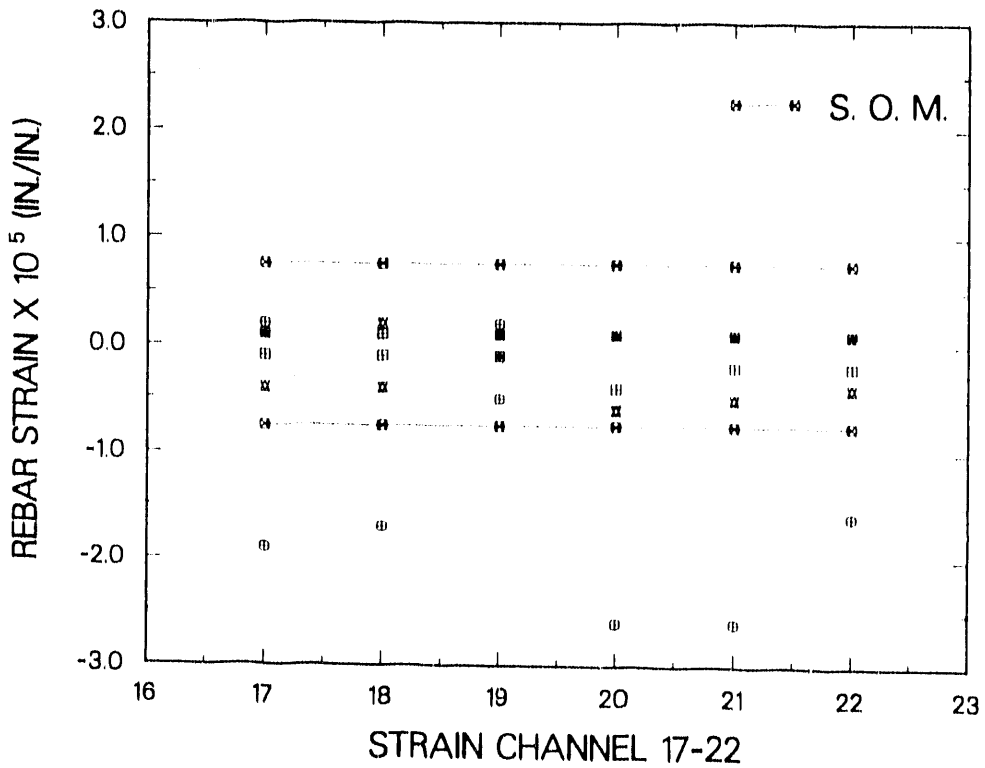


Fig. 58. Strain gage readings in the east end wall compared with SOM theory for the three 50-psi load cycles.

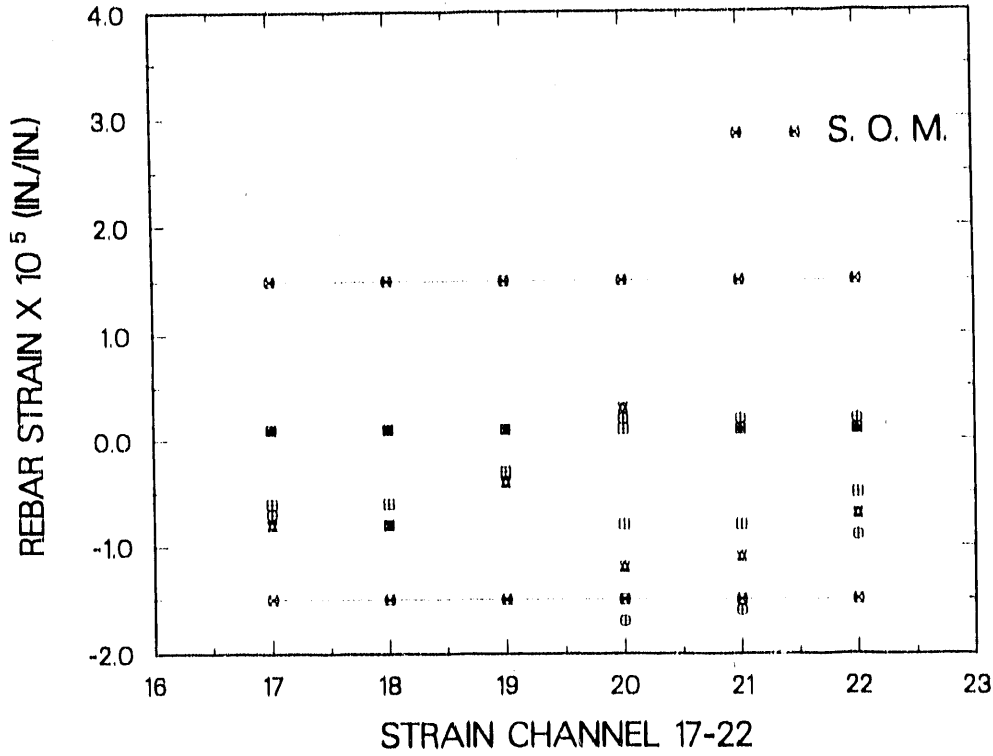


Fig. 59. Strain gage readings in the east end wall compared with SOM theory for the three 100-psi load cycles.

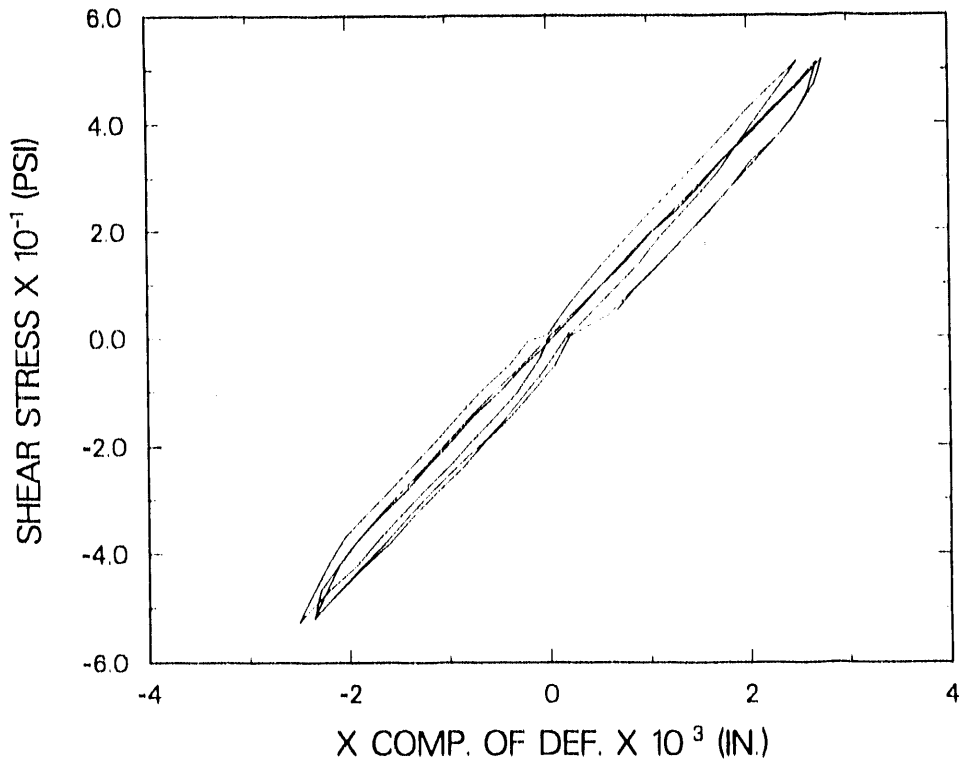


Fig. 60. Horizontal component of deformation from internal gages, 50-psi load cycle.

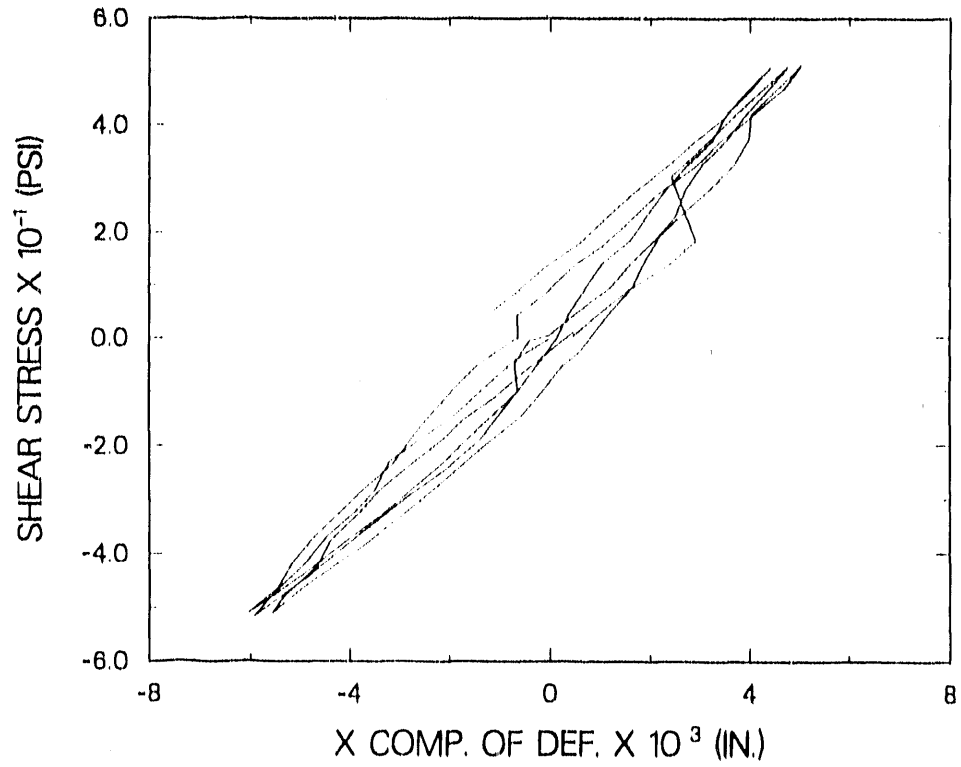


Fig. 61. Horizontal component of deformation from external gages, 50-psi load cycle.

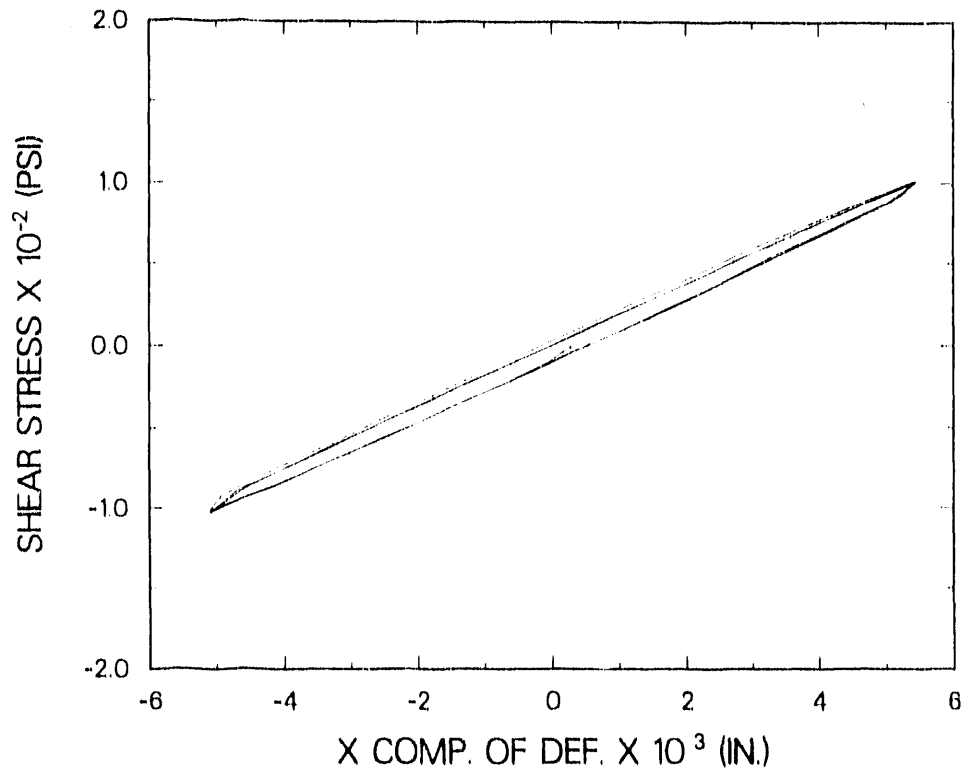


Fig. 62. Horizontal component of deformation from internal gages, 100-psi load cycle.

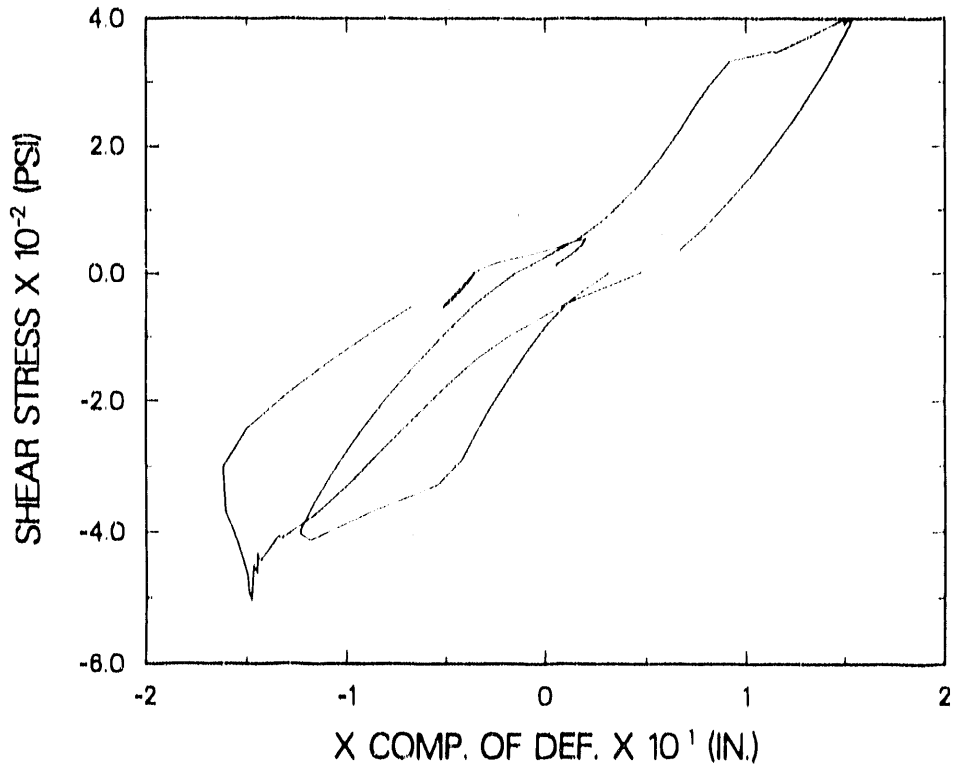


Fig. 69. Horizontal component of deformation from external gages, failure cycle and last 50-psi load cycle.

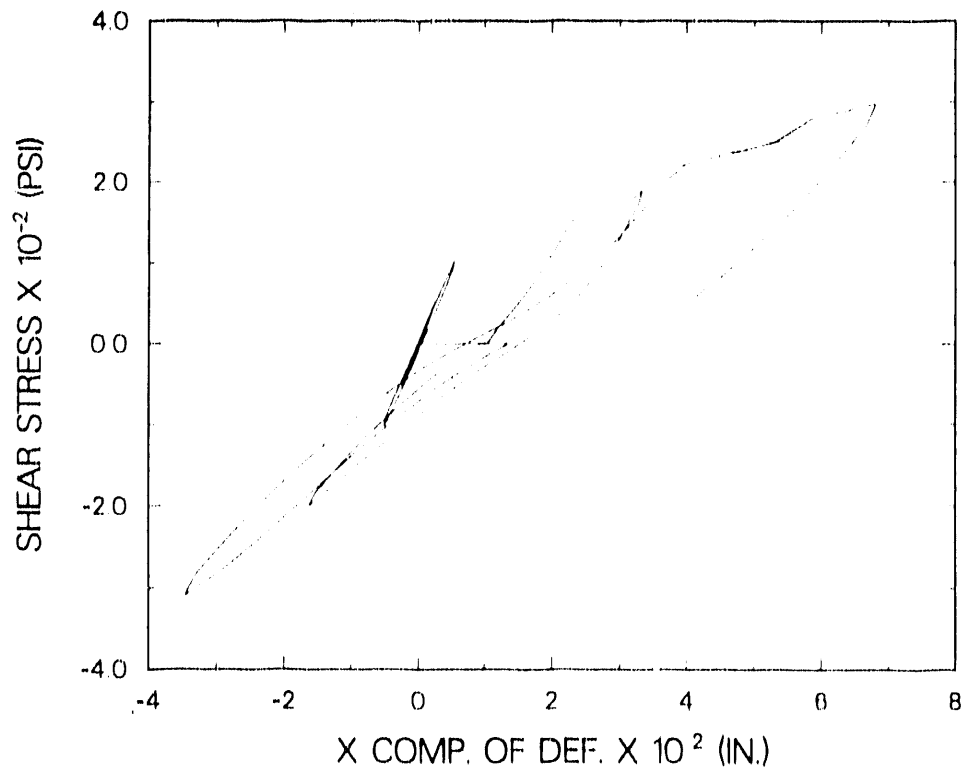


Fig. 70. Horizontal component of deformation from internal gages, first load cycle at each stress level.

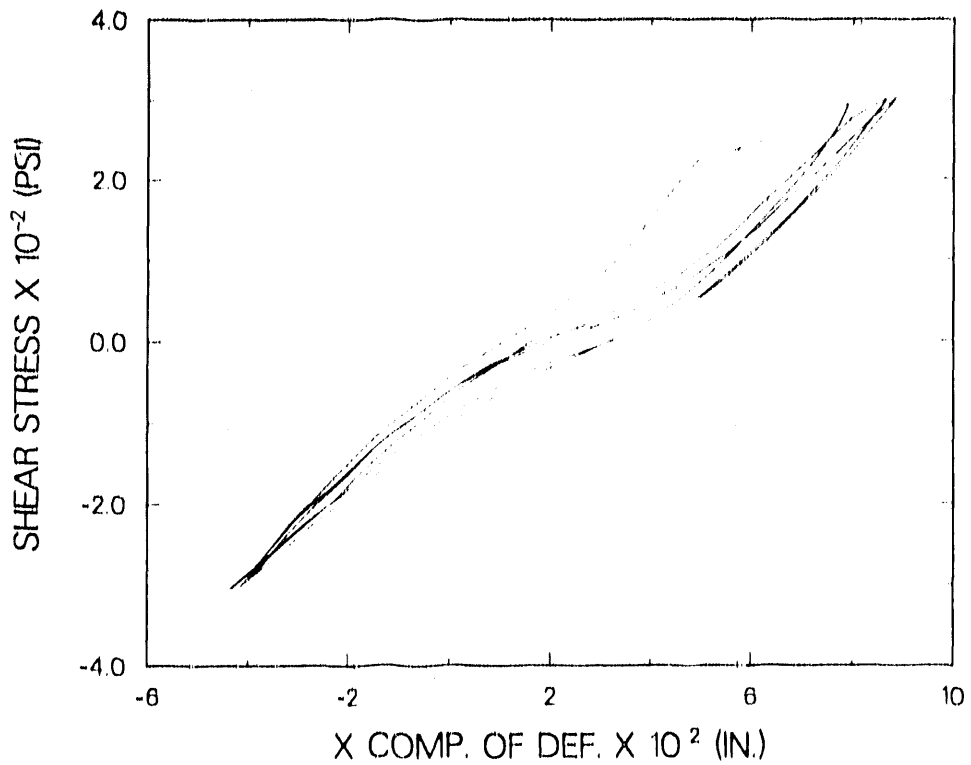


Fig. 67. Horizontal component of deformation from external gages, 300-psi load cycle.

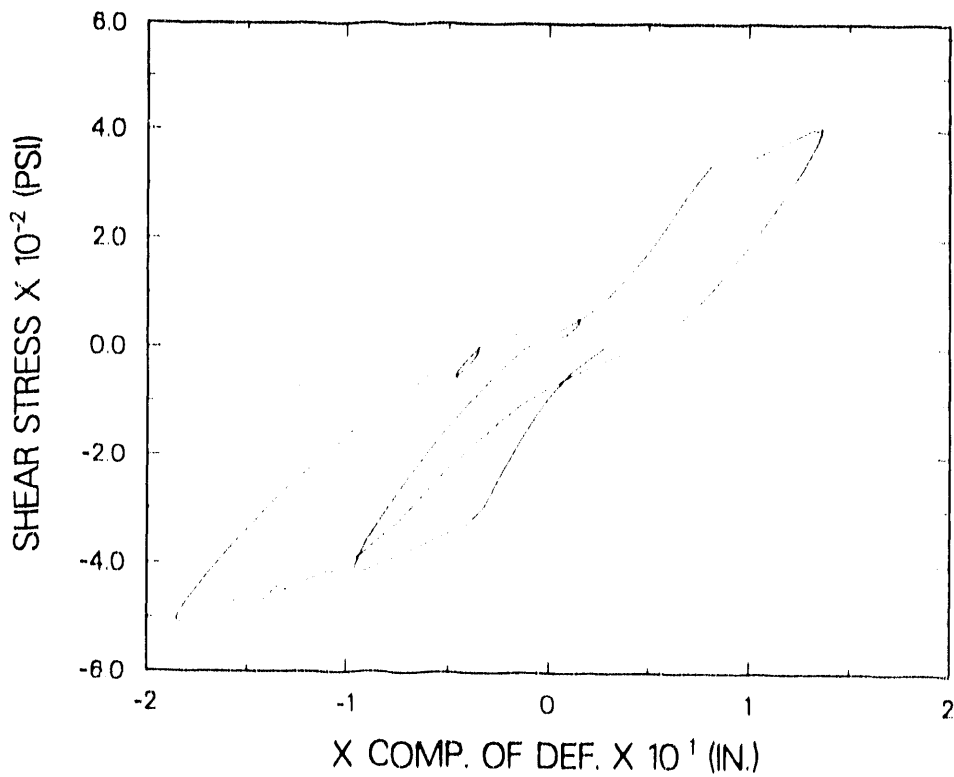


Fig. 68. Horizontal component of deformation from internal gages, failure cycle and last 50-psi load cycle.

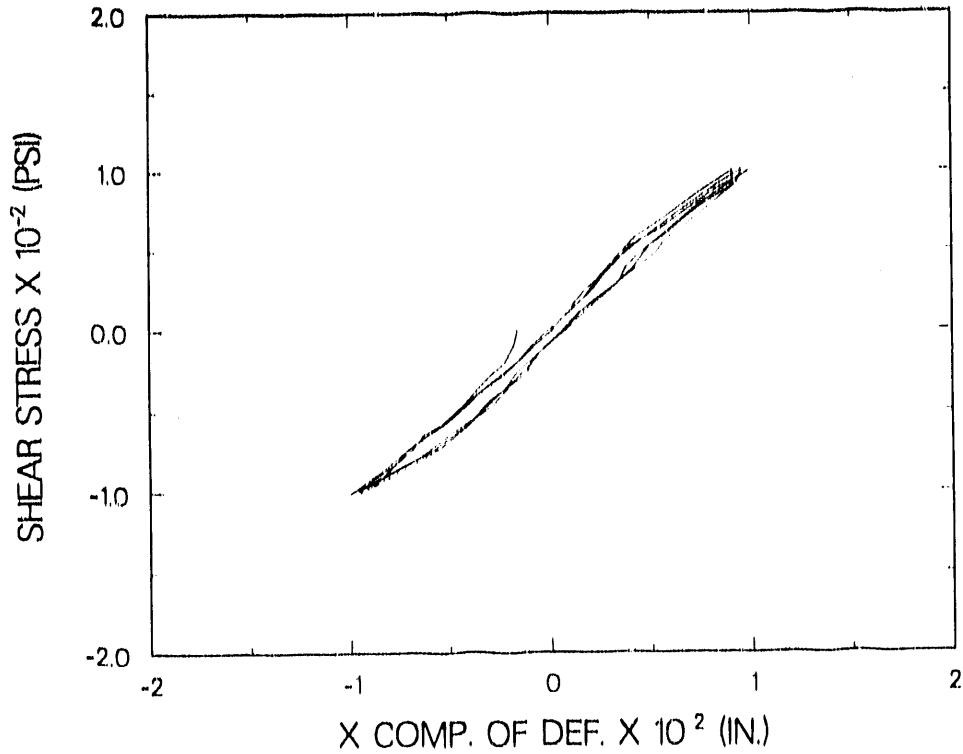


Fig. 63. Horizontal component of deformation from external gages, 100-psi load cycle.

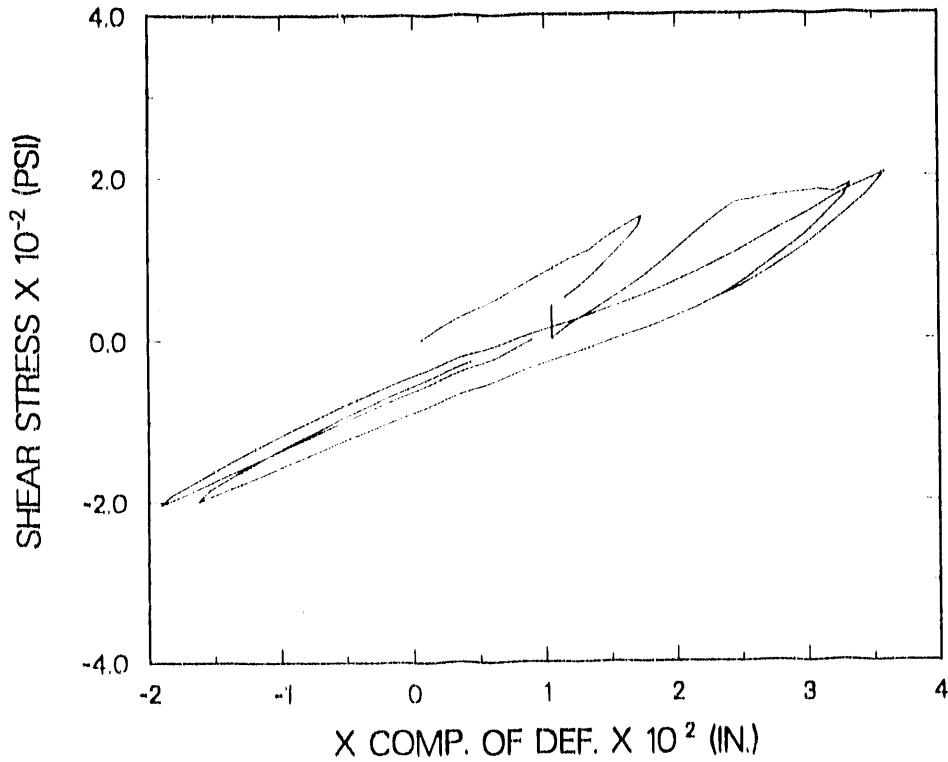


Fig. 64. Horizontal component of deformation from internal gages, 150- and 200-psi load cycle.

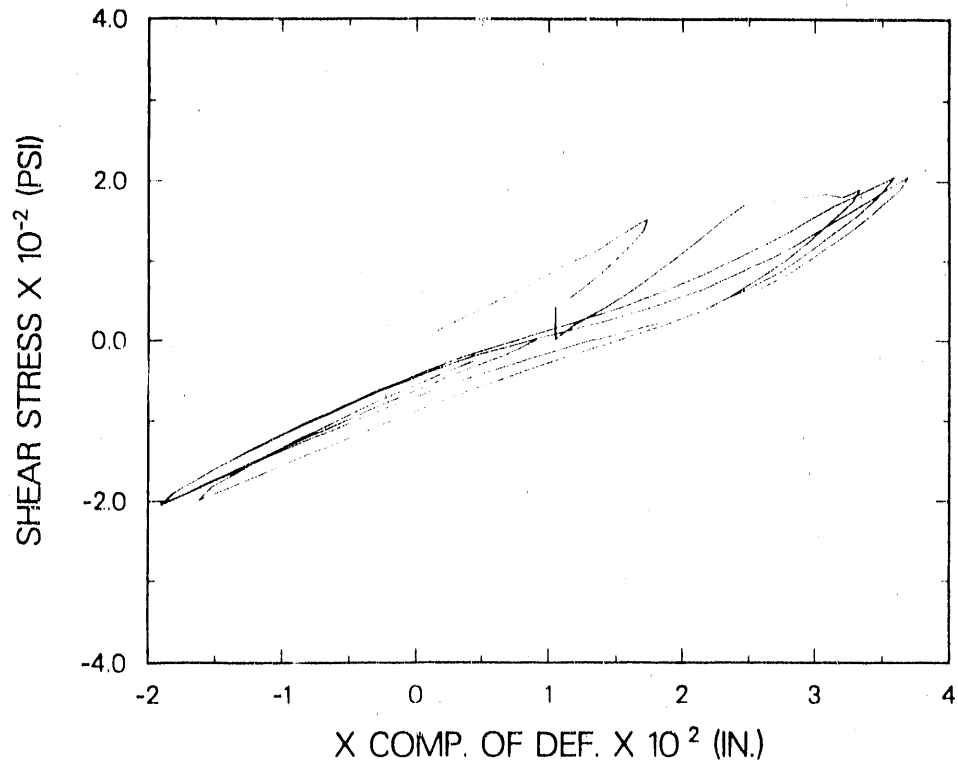


Fig. 65. Horizontal component of deformation from external gages, 150- and 200-psi load cycles.

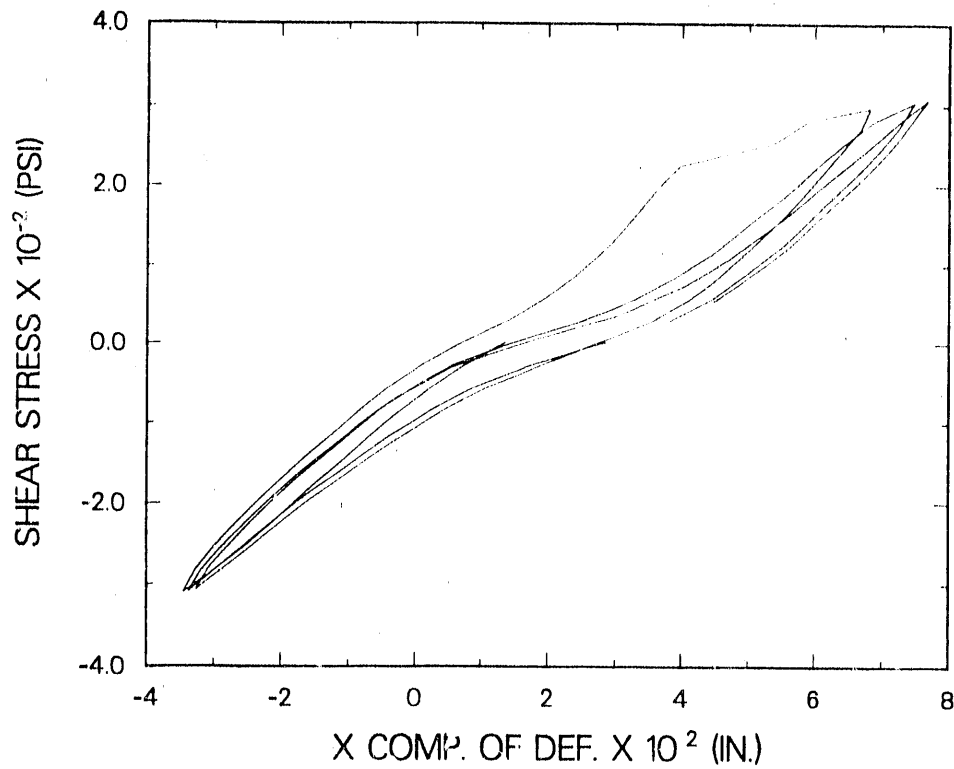


Fig. 66. Horizontal component of deformation from internal gages, 300-psi load cycle.

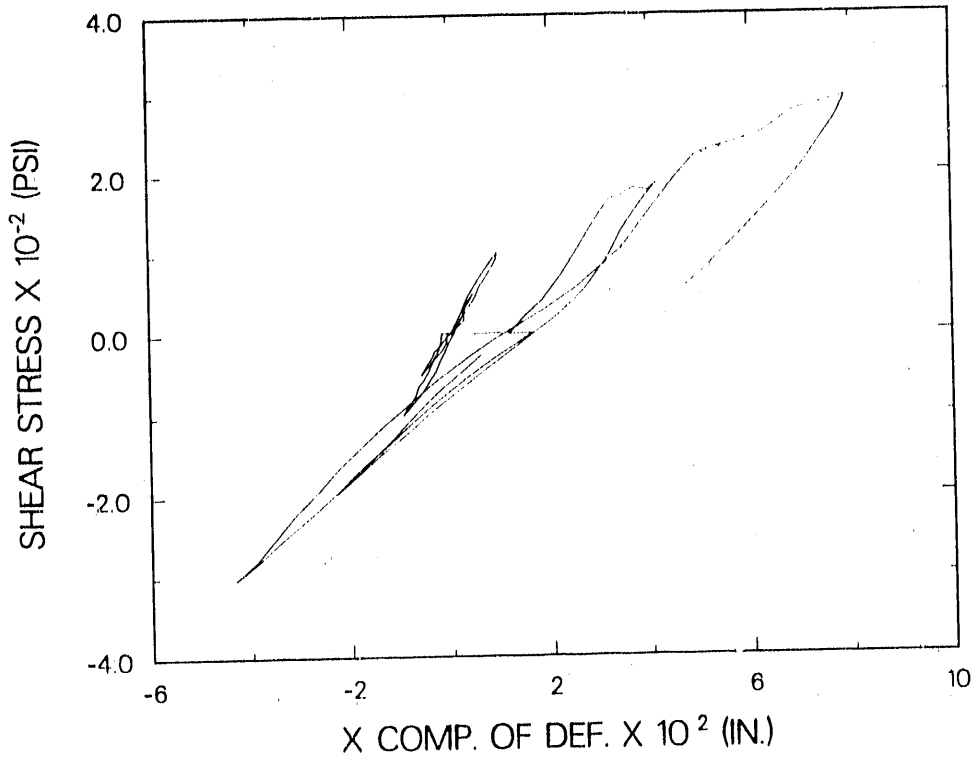


Fig. 71. Horizontal component of deformation from external gages, first load cycle at each stress level.

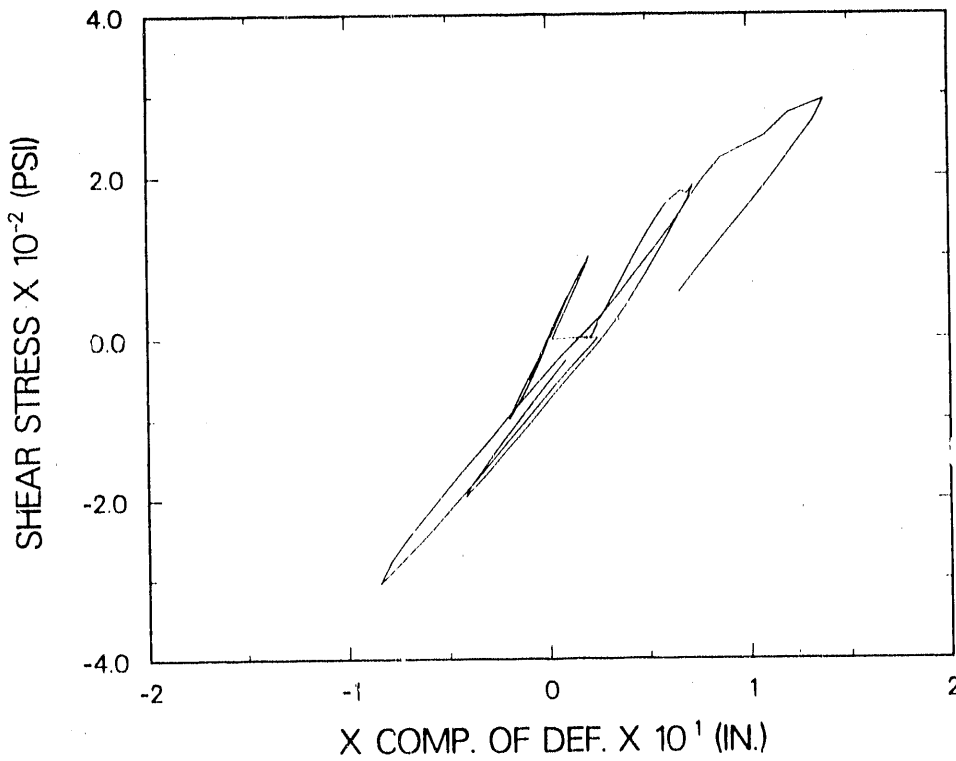


Fig. 72. Horizontal component of deformation from uncorrected external gages, first load cycle at each stress level.

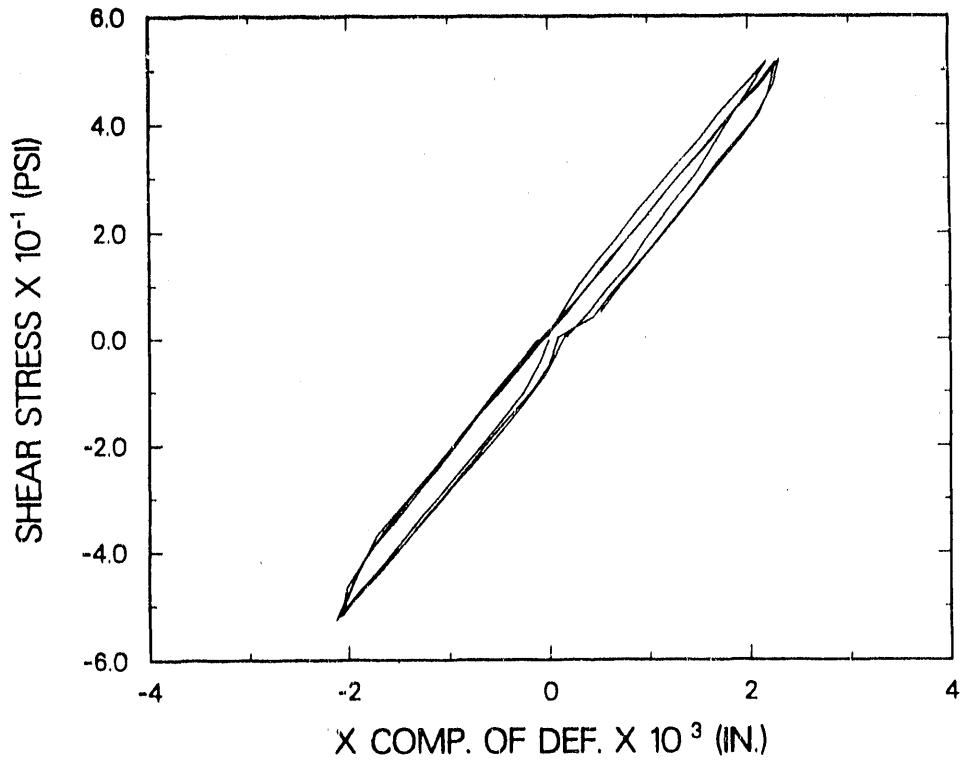


Fig. 73. Horizontal component of shear deformation from internal gages, 50-psi load cycle.

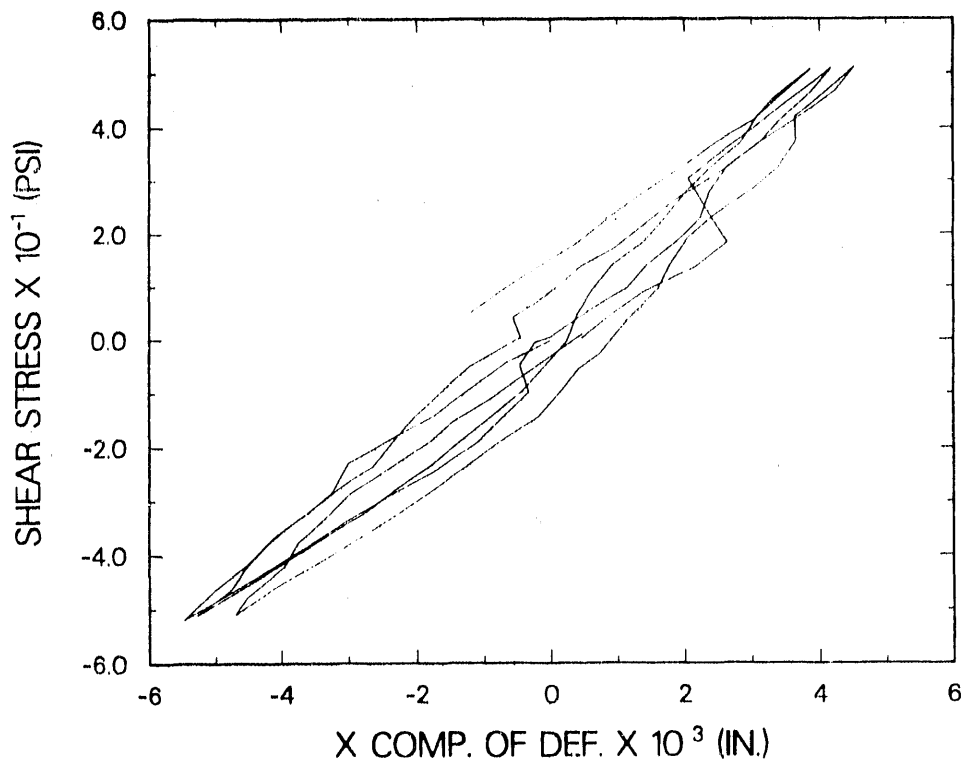


Fig. 74. Horizontal component of shear deformation from external gages, 50-psi load cycle.

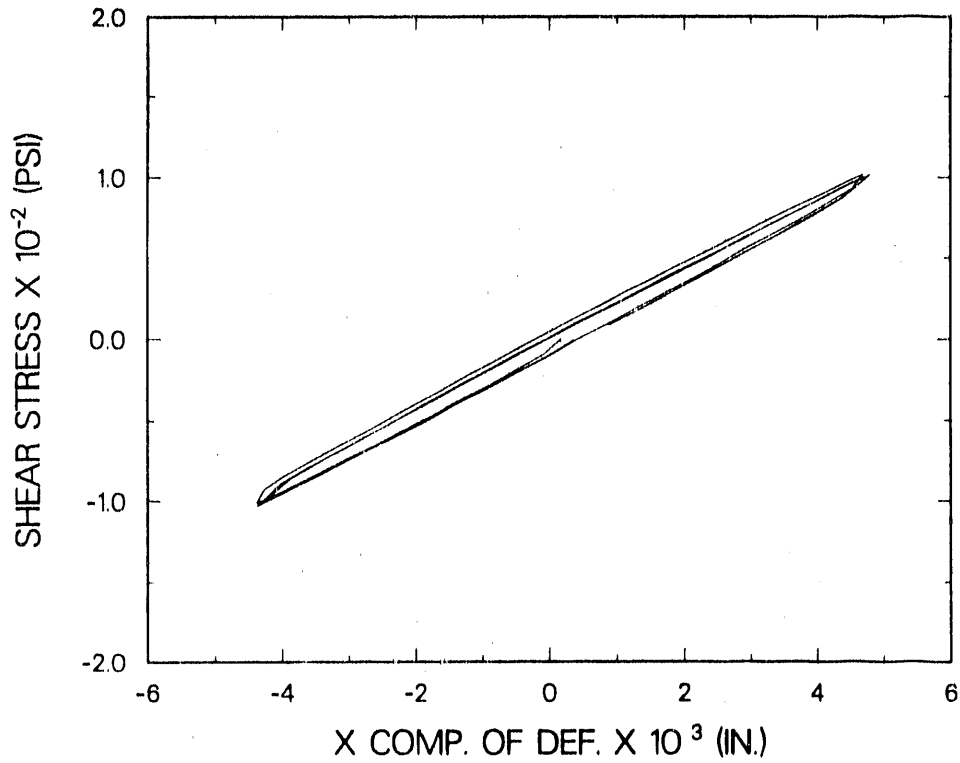


Fig. 75. Horizontal component of shear deformation from internal gages, 100-psi load cycle.

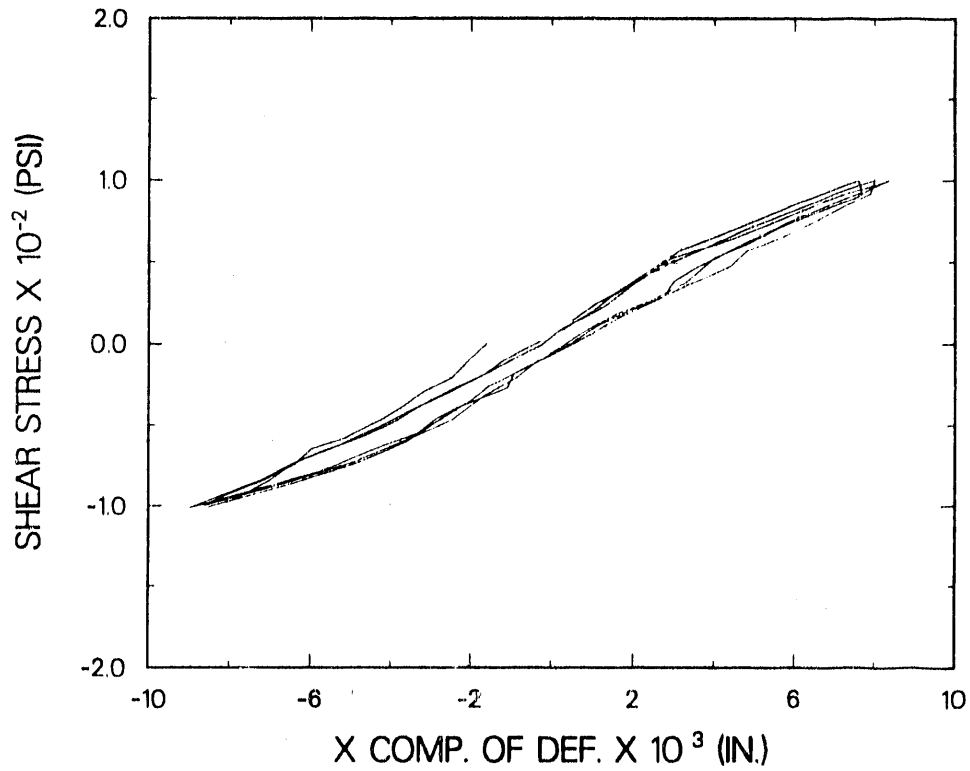


Fig. 76. Horizontal component of shear deformation from external gages, 100-psi load cycle.

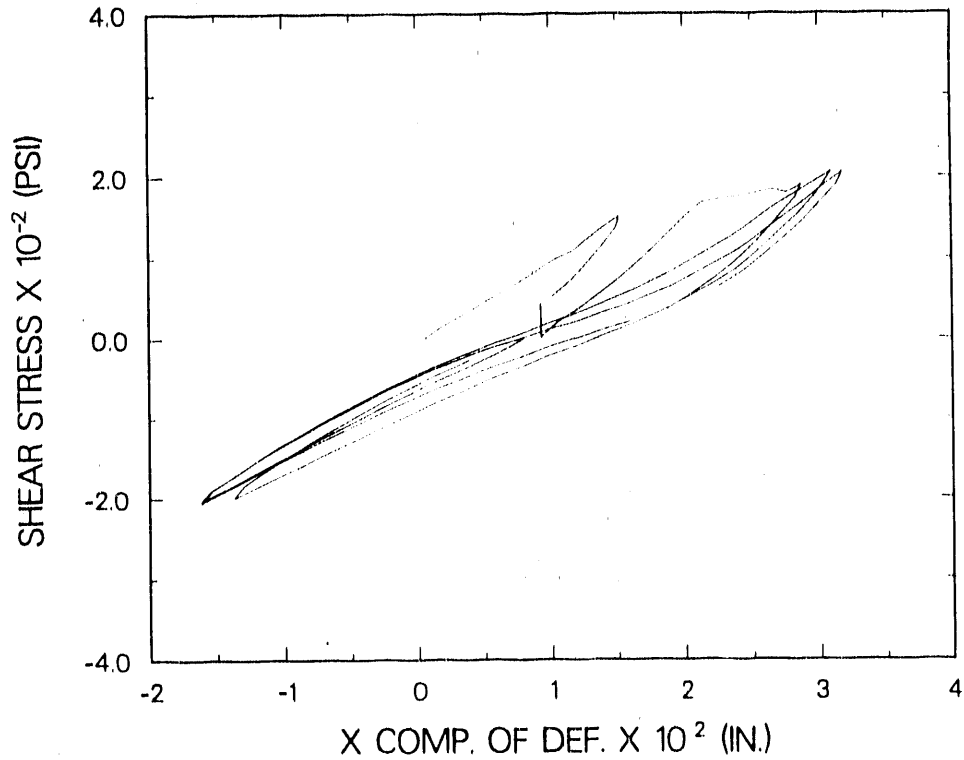


Fig. 77. Horizontal component of shear deformation from internal gages, 150- and 200-load cycles.

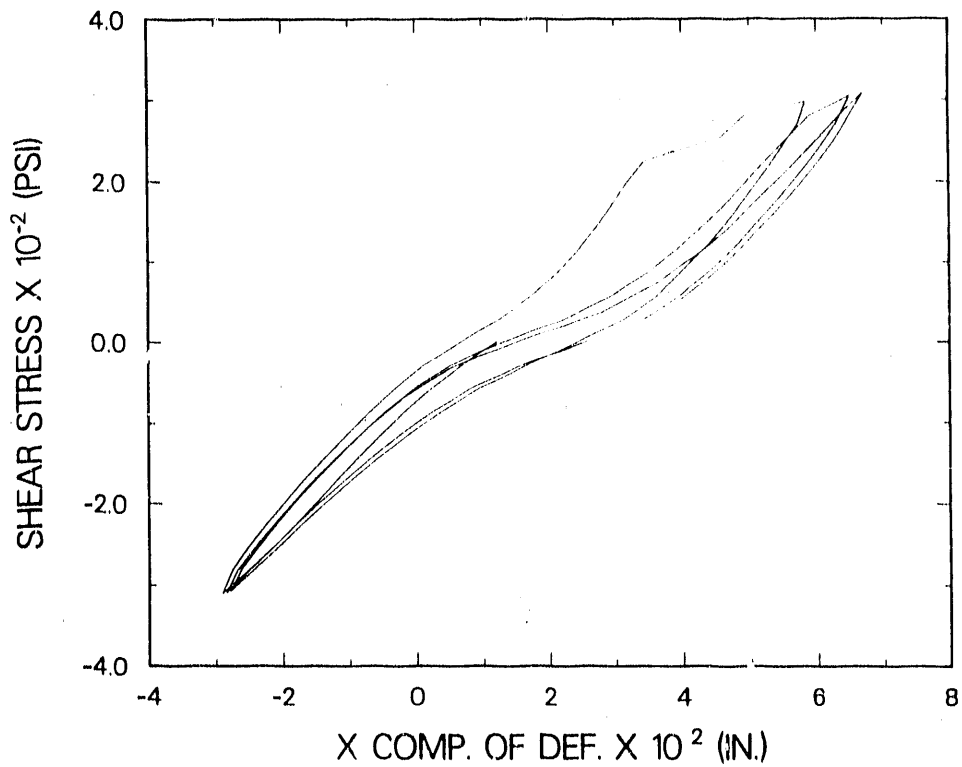


Fig. 78. Horizontal component of shear deformation from external gages, 150- and 200-psi load cycles.

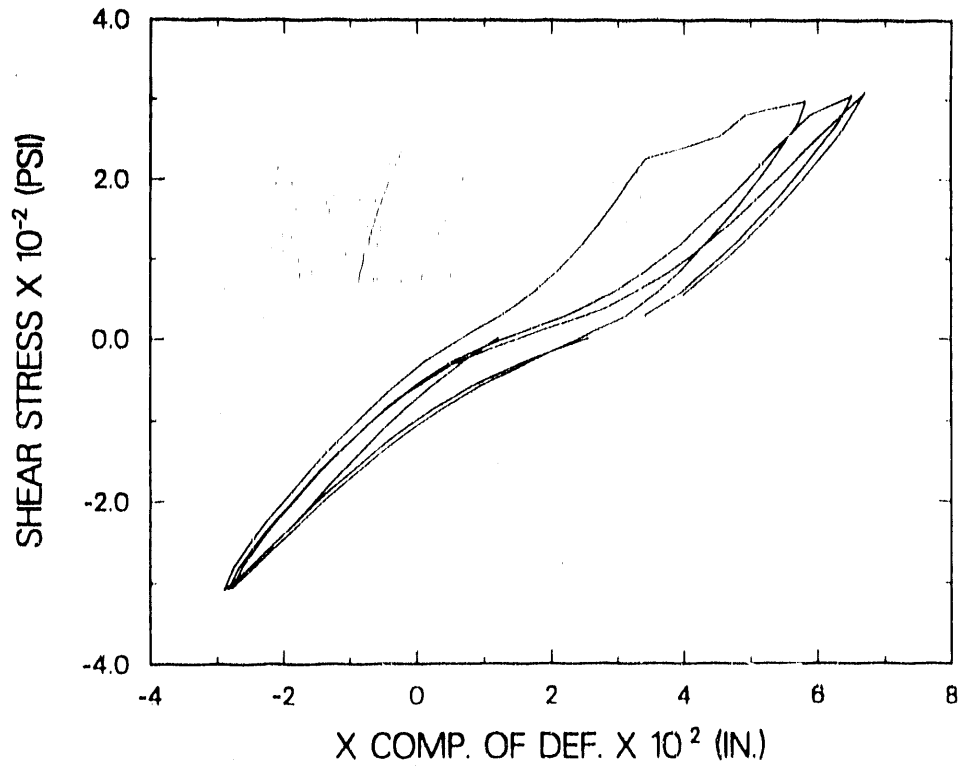


Fig. 79. Horizontal component of shear deformation from internal gages, 300-psi load cycles.

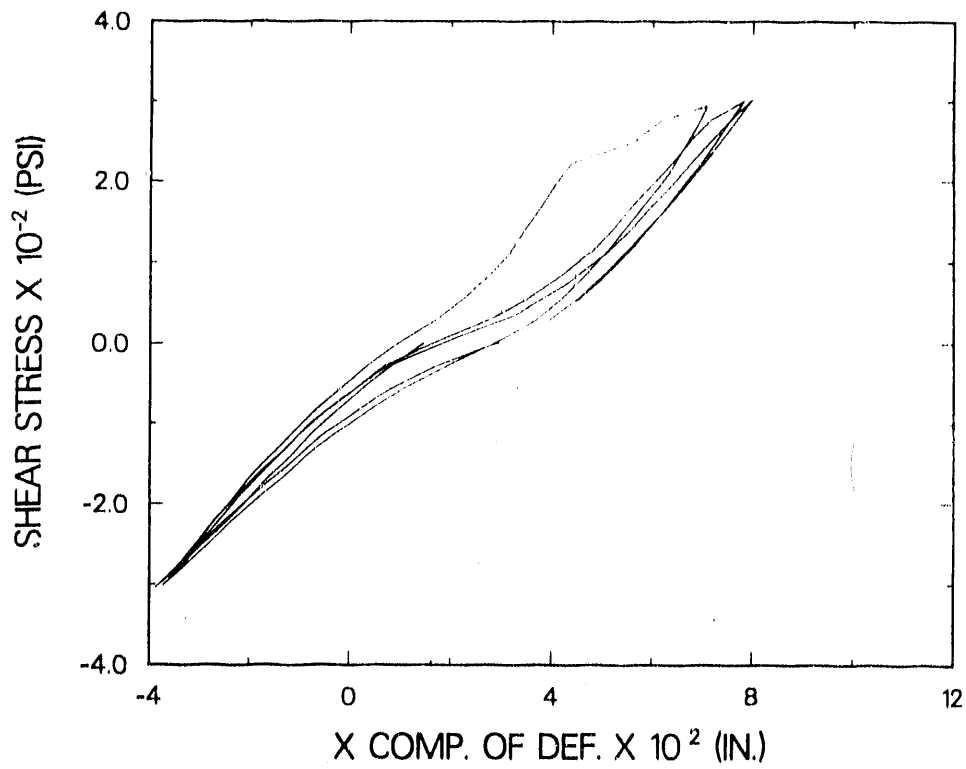


Fig. 80. Horizontal component of shear deformation from external gages, 300-psi load cycles.

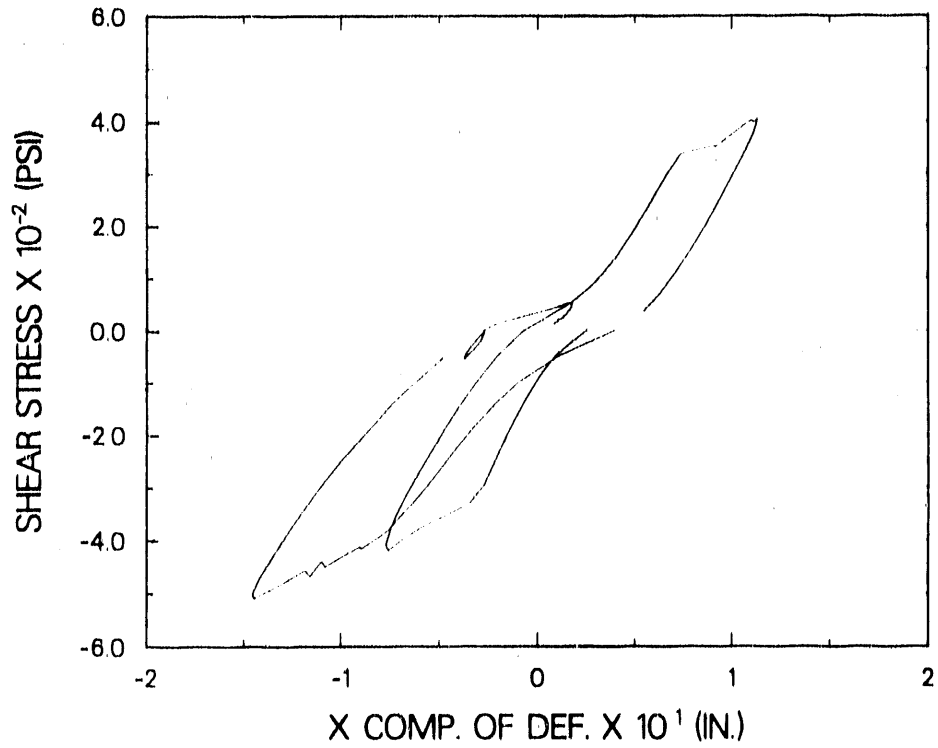


Fig. 81. Horizontal component of shear deformation from internal gages, failure cycle and last 50-psi load cycle.

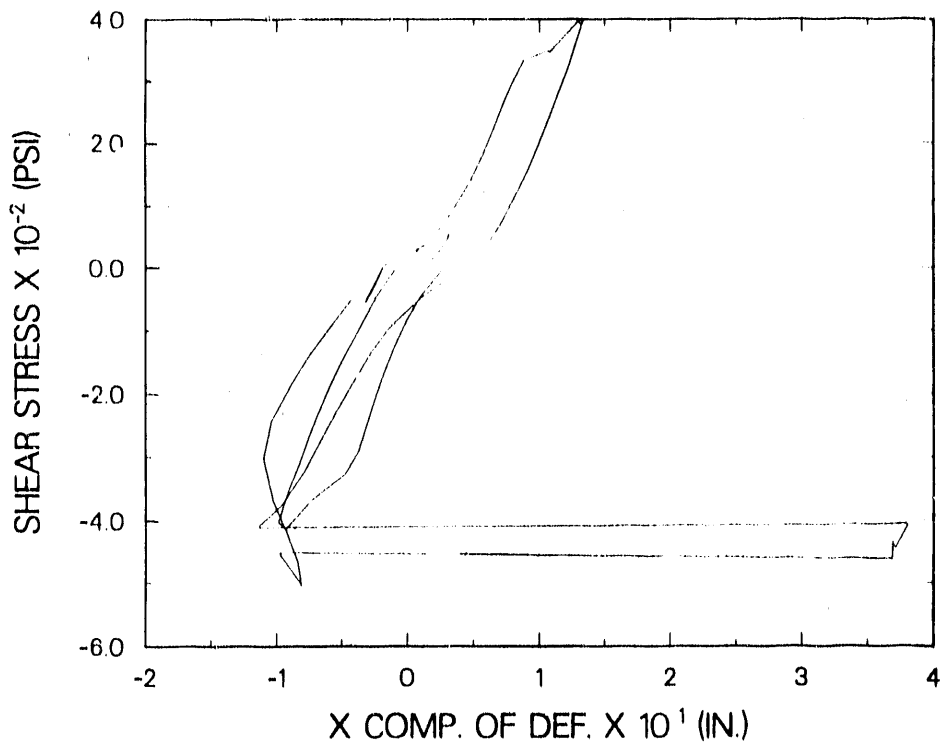


Fig. 82. Horizontal component of shear deformation from external gages, failure cycle and last 50-psi load cycle.

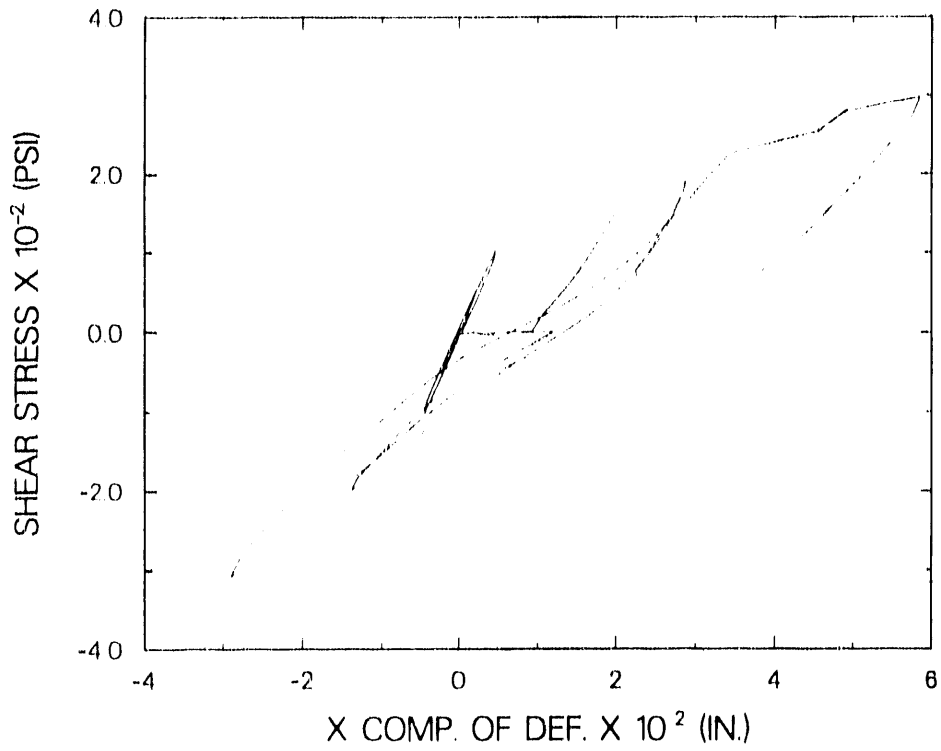


Fig. 83. Horizontal component of shear deformation from internal gages, first load cycle at each stress level.

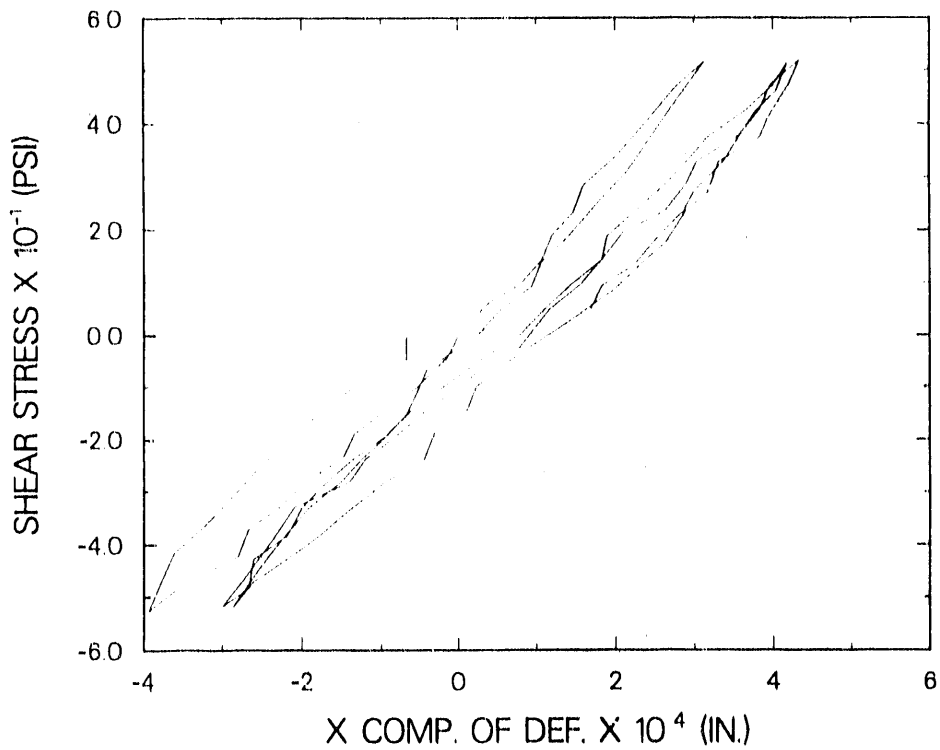


Fig. 84. Horizontal component of bending deformation from internal gages, 50-psi load cycle.

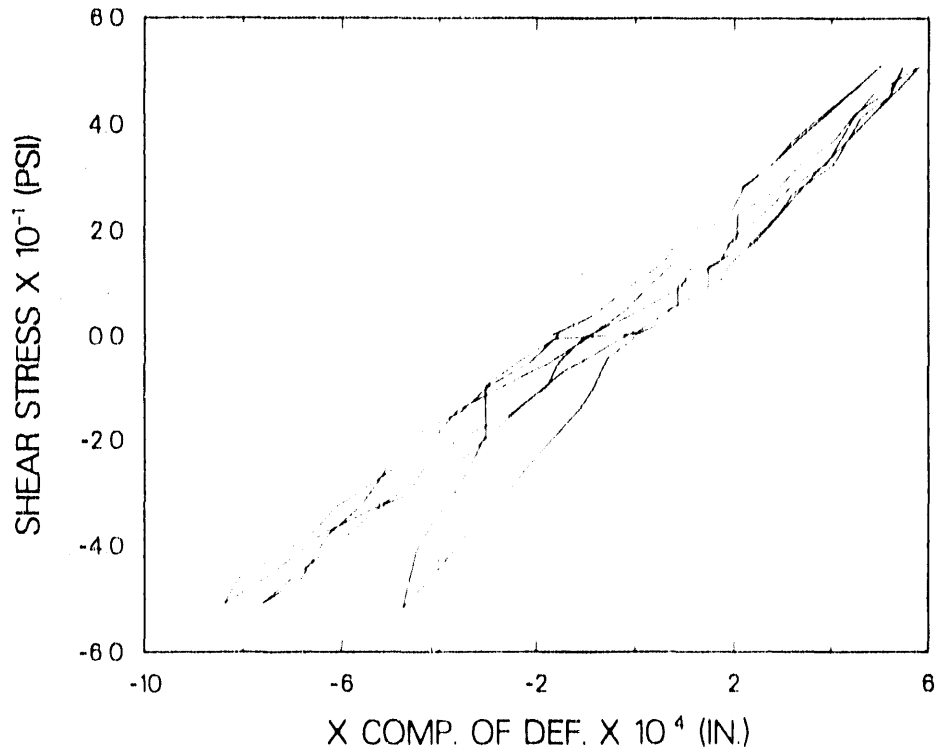


Fig. 85. Horizontal component of bending deformation from external gages, 50-psi load cycle.

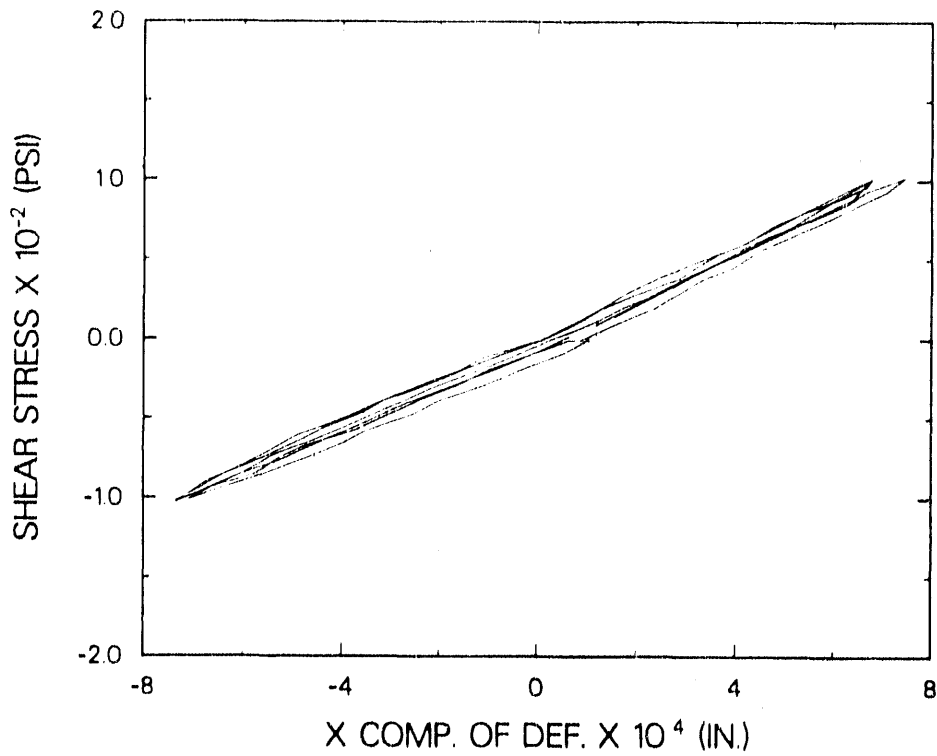


Fig. 86. Horizontal component of bending deformation from internal gages, 100-psi load cycle.

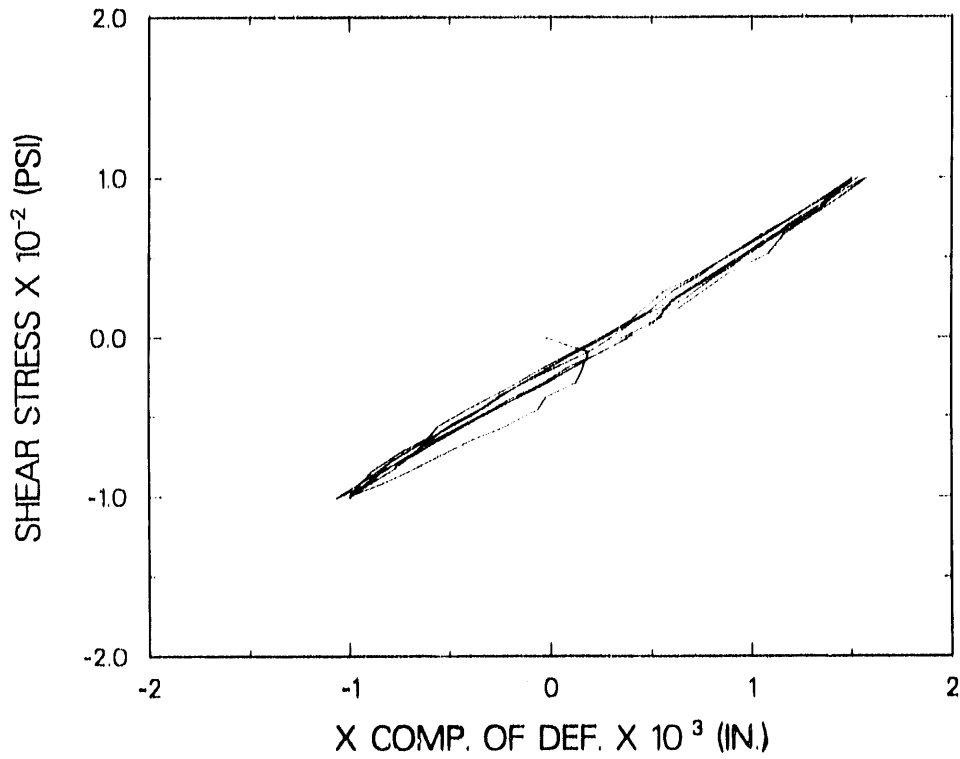


Fig. 87. Horizontal component of bending deformation from external gages, 100-psi load cycle.

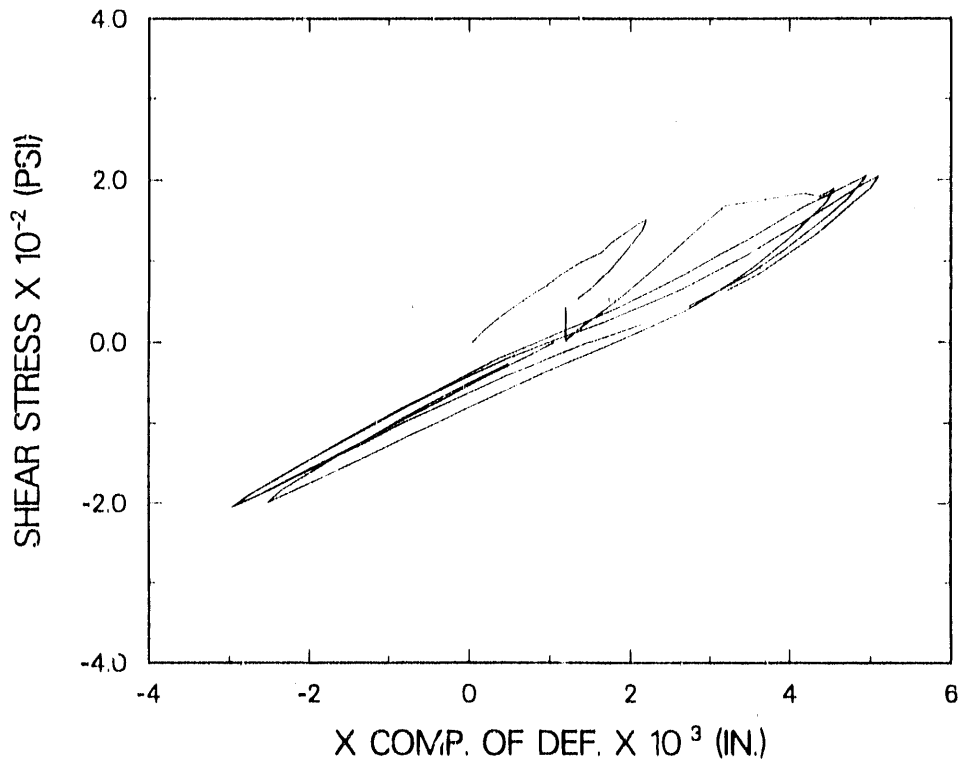


Fig. 88. Horizontal component of bending deformation from internal gages, 150- and 200-psi load cycles.

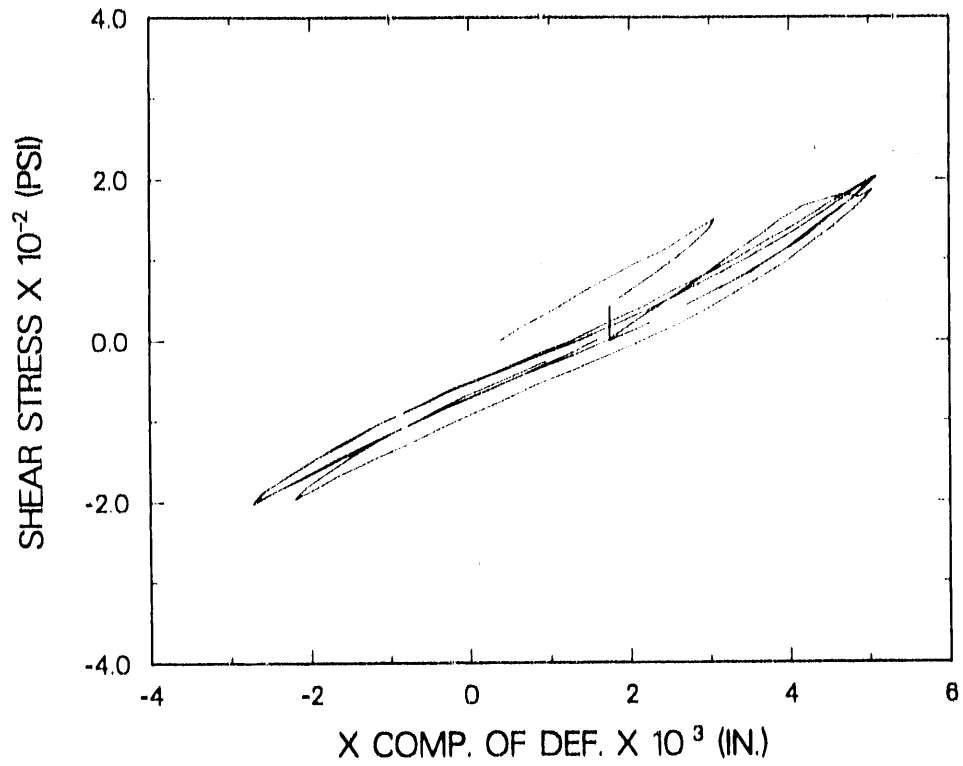


Fig. 89. Horizontal component of bending deformation from external gages, 150- and 200-psi load cycles.

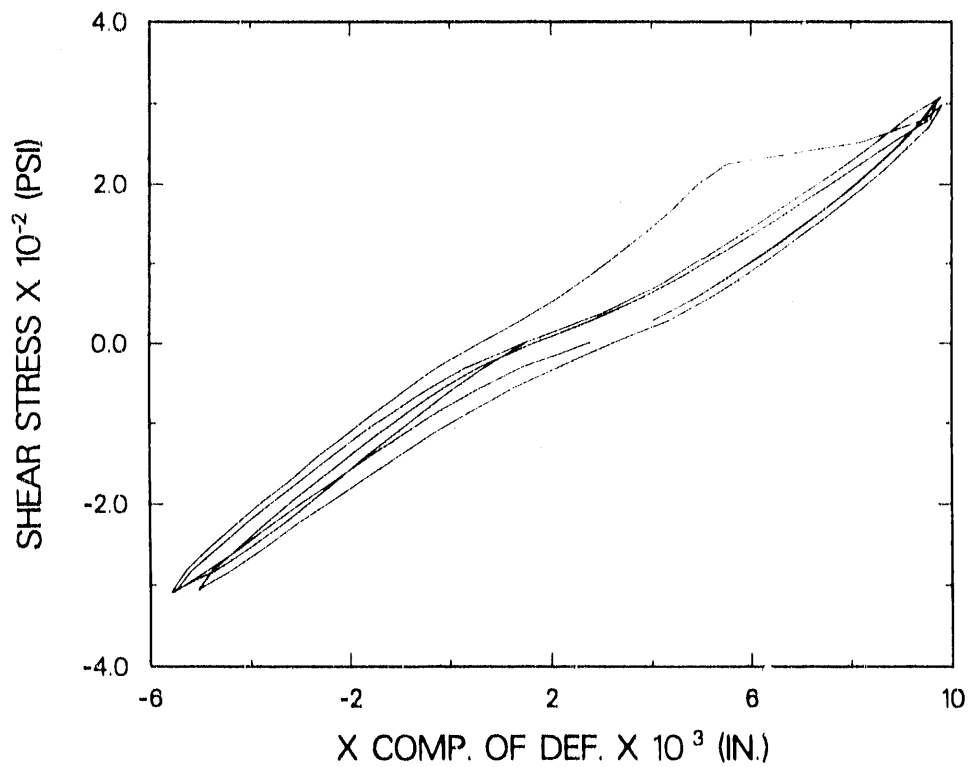


Fig. 90. Horizontal component of bending deformation from internal gages, 300-psi load cycle.

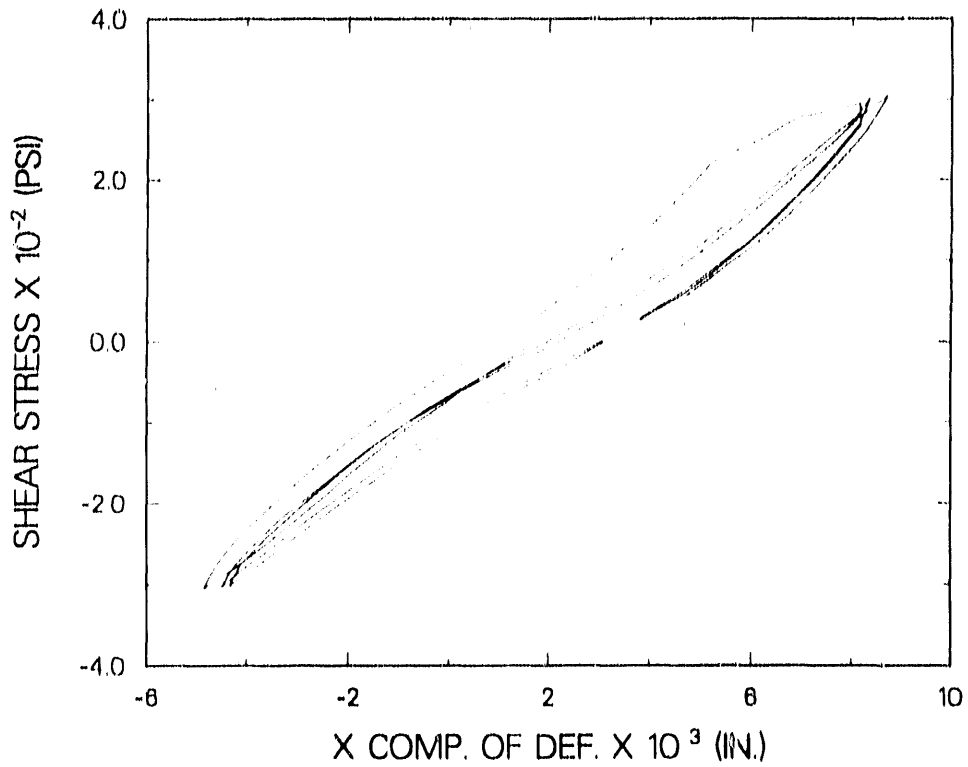


Fig. 91. Horizontal component of bending deformation from external gages, 300-psi load cycle.

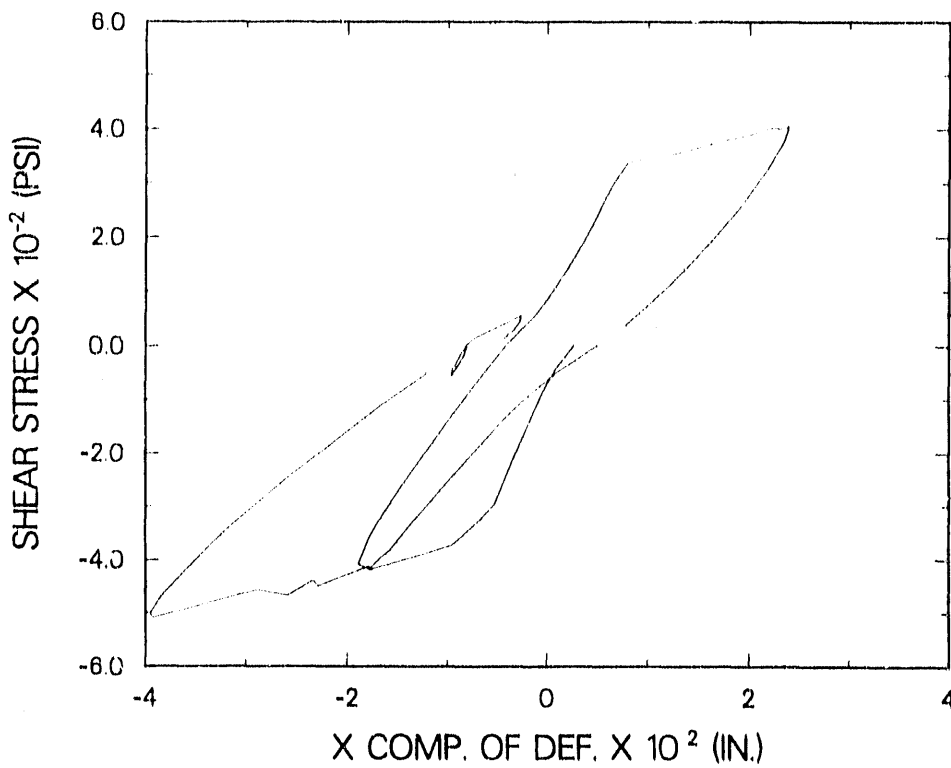


Fig. 92. Horizontal component of bending deformation from internal gages, failure cycle and last 50-psi load cycle.

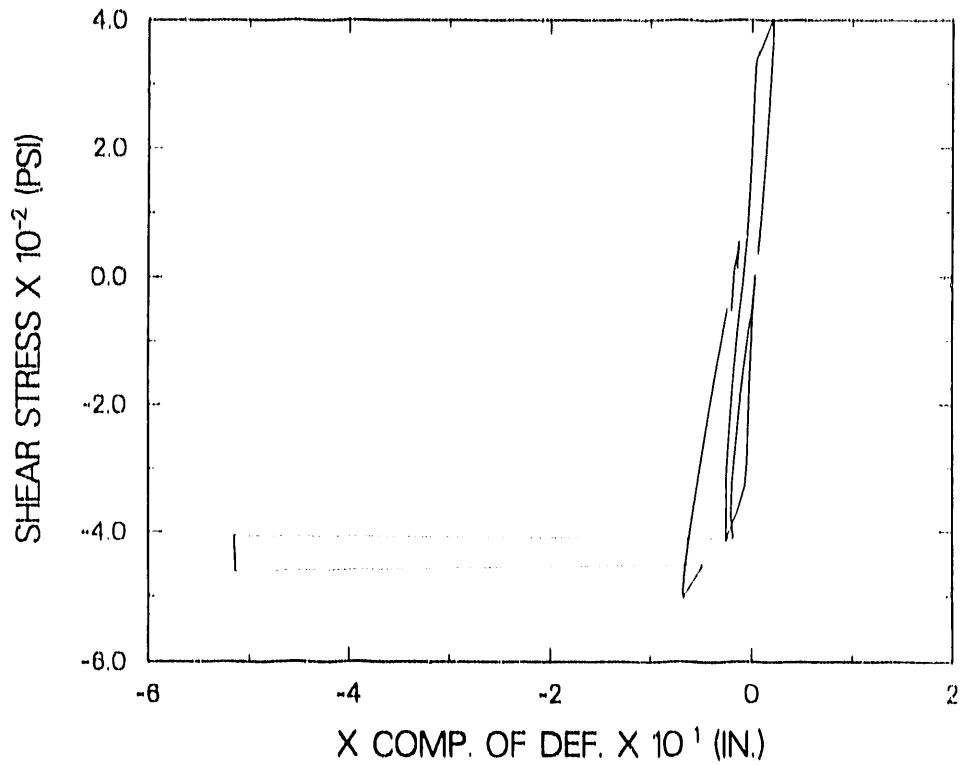


Fig. 93. Horizontal component of bending deformation from external gages, failure cycle and last 50-psi load cycle.

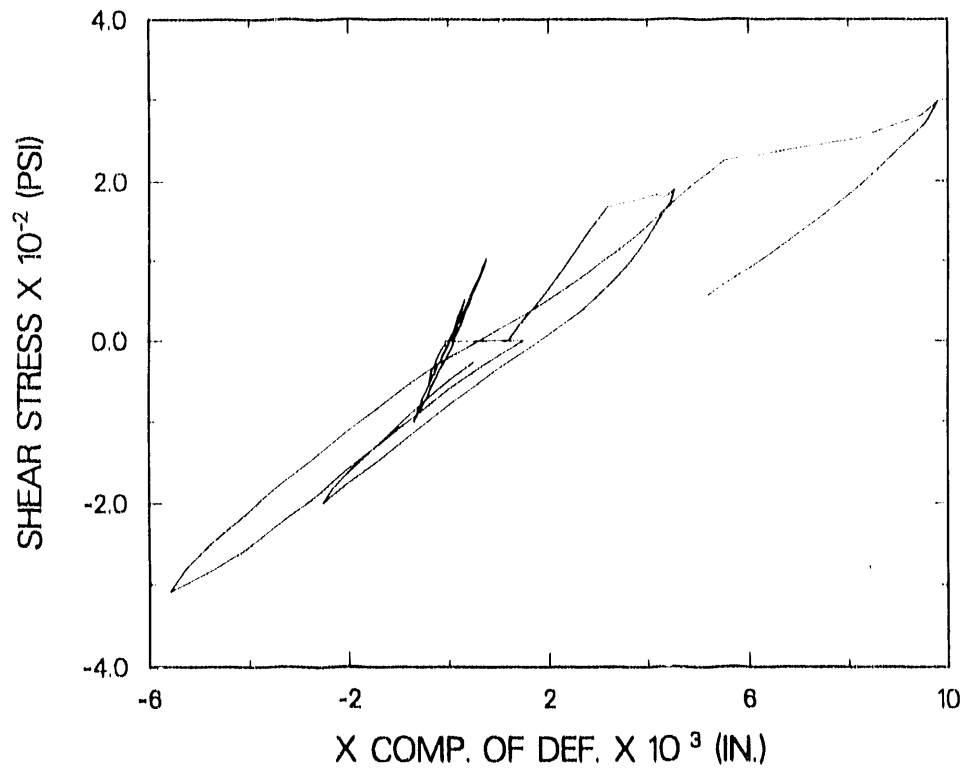


Fig. 94. Horizontal component of bending deformation from internal gages, first load cycle at each stress level.

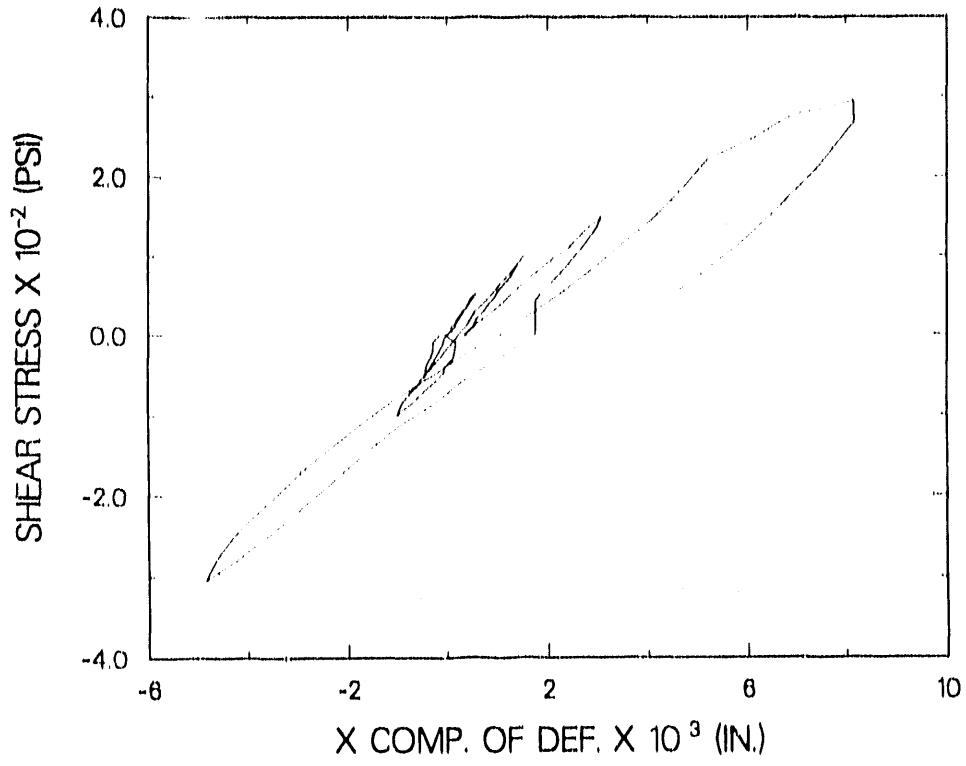


Fig. 95. Horizontal component of bending deformation from external gages, first load cycle at each stress level.

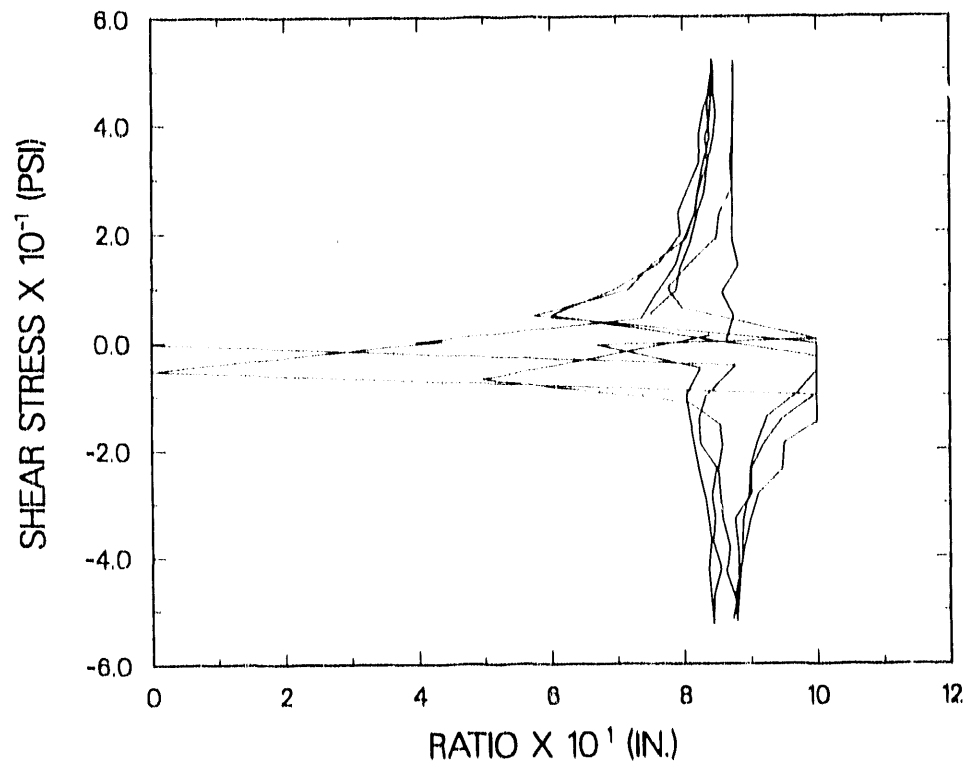


Fig. 96. Ratio of shear to total deformation for the 50-psi cycles.

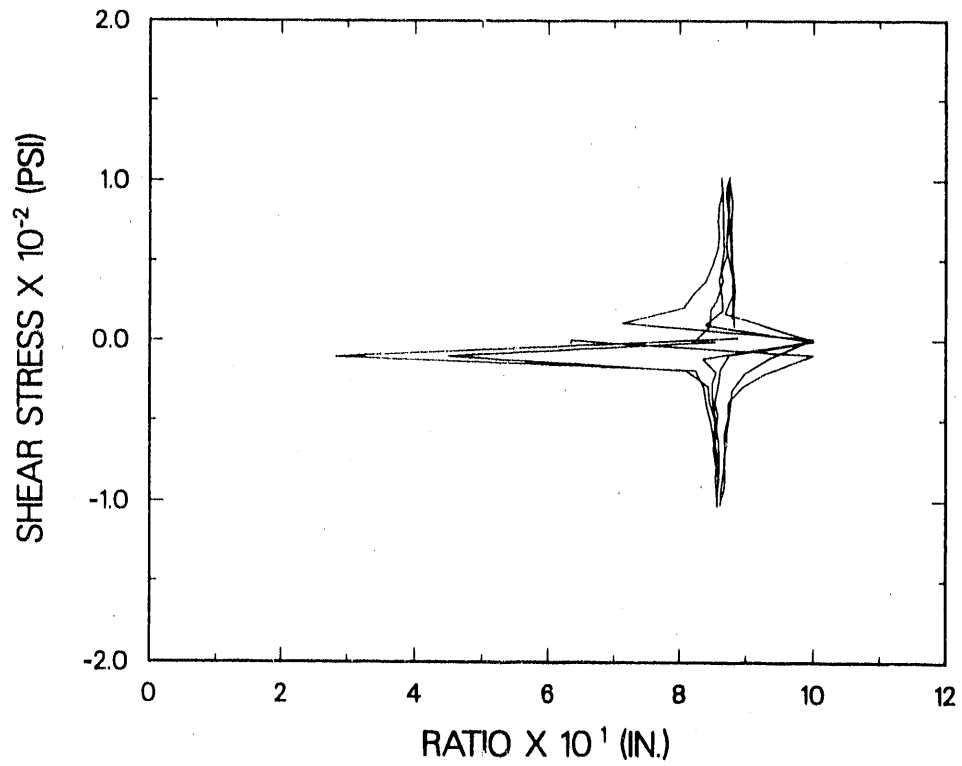


Fig. 97. Ratio of shear to total deformation for the 100-psi cycles.

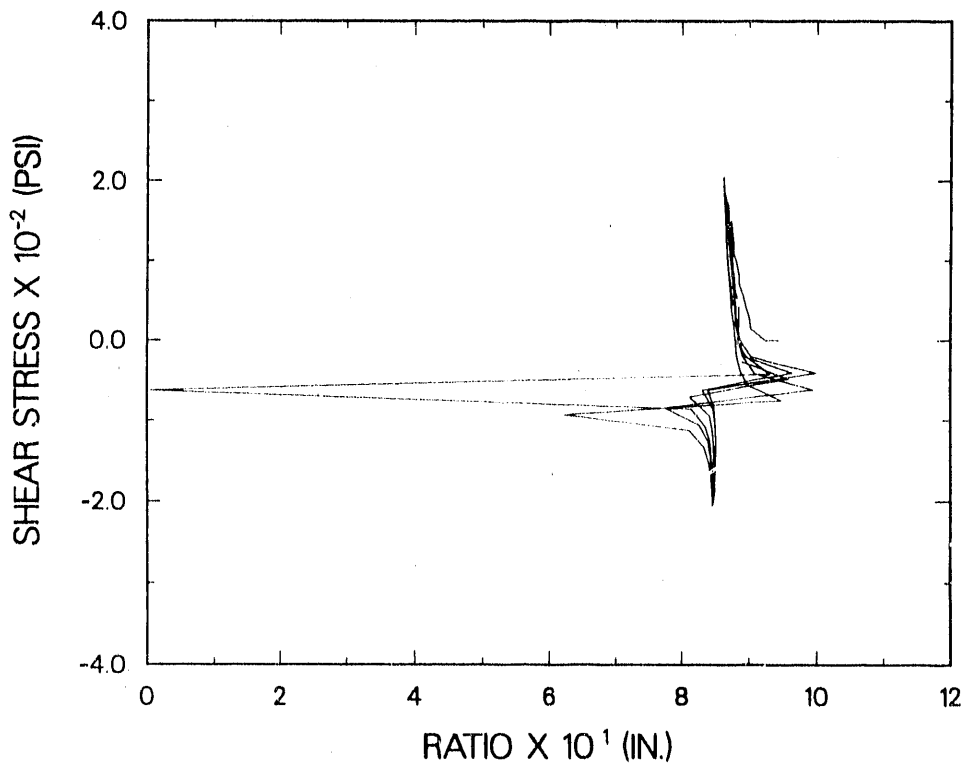


Fig. 98. Ratio of shear to total deformation for the 150- and 200-psi cycles.

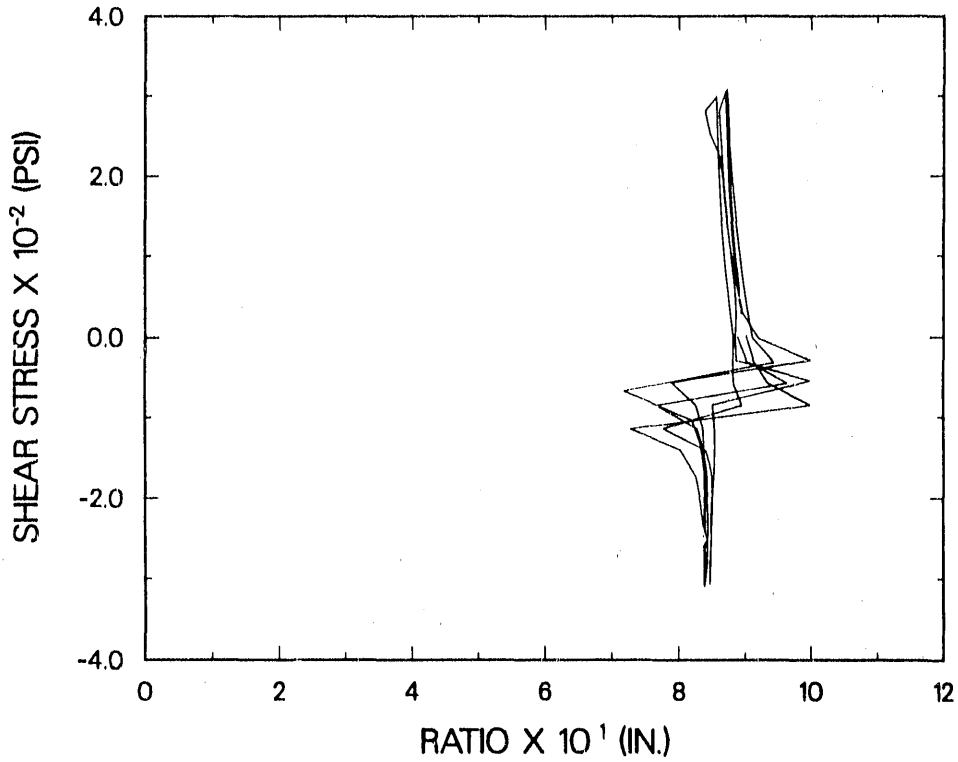


Fig. 99. Ratio of shear to total deformation for the 300-psi cycles.

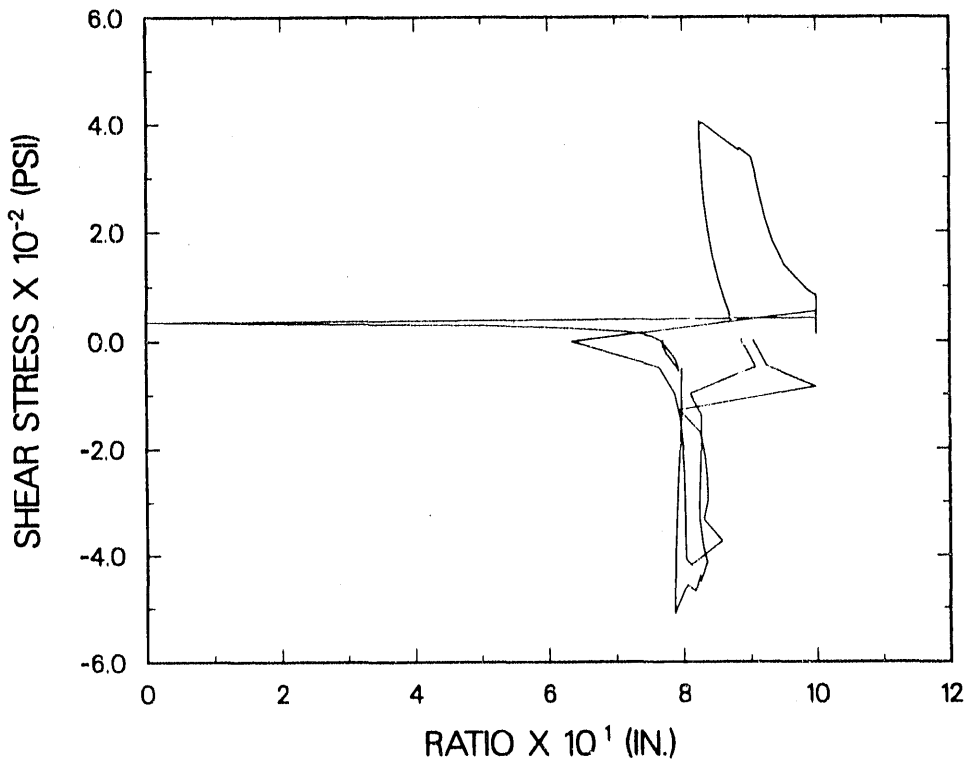


Fig. 100. Ratio of shear to total deformation for the failure load cycle and last 50-psi run.

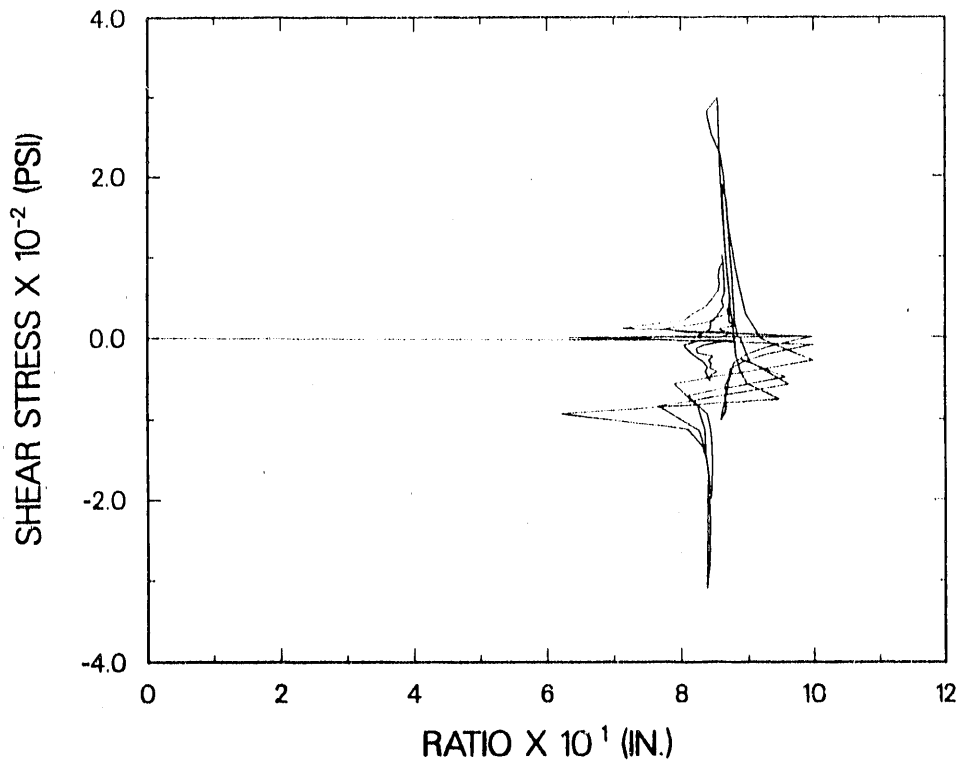


Fig. 101. Ratio of shear to total deformation for the first load cycle at each stress level.

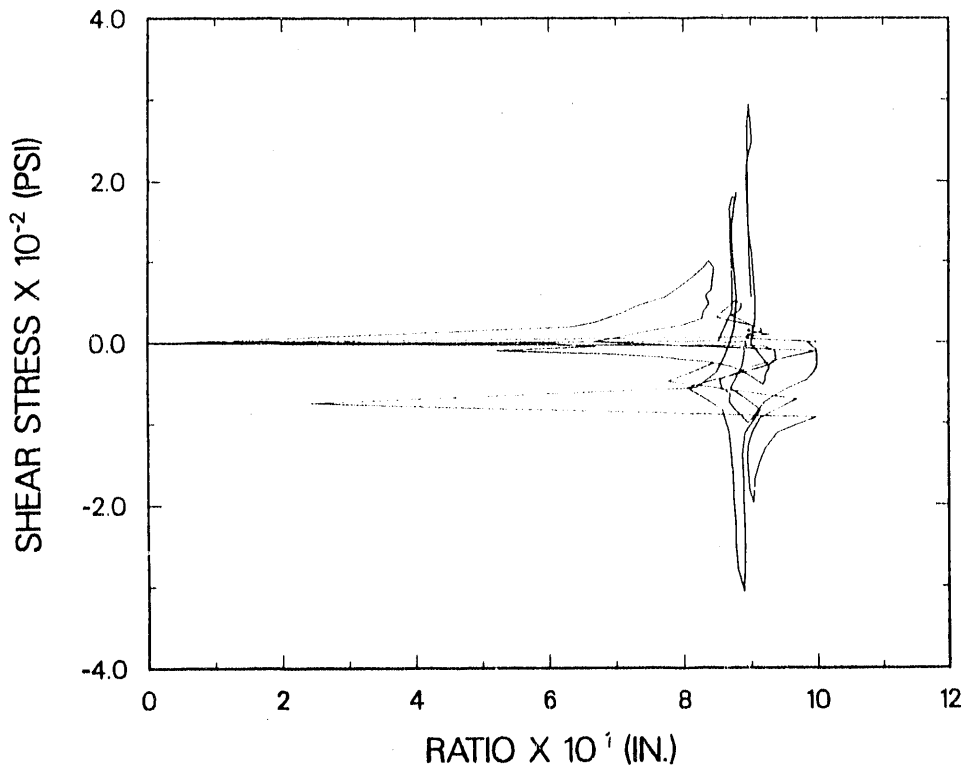


Fig. 102. Ratio of shear to total deformation for the first load cycle at each stress level from the external gages.

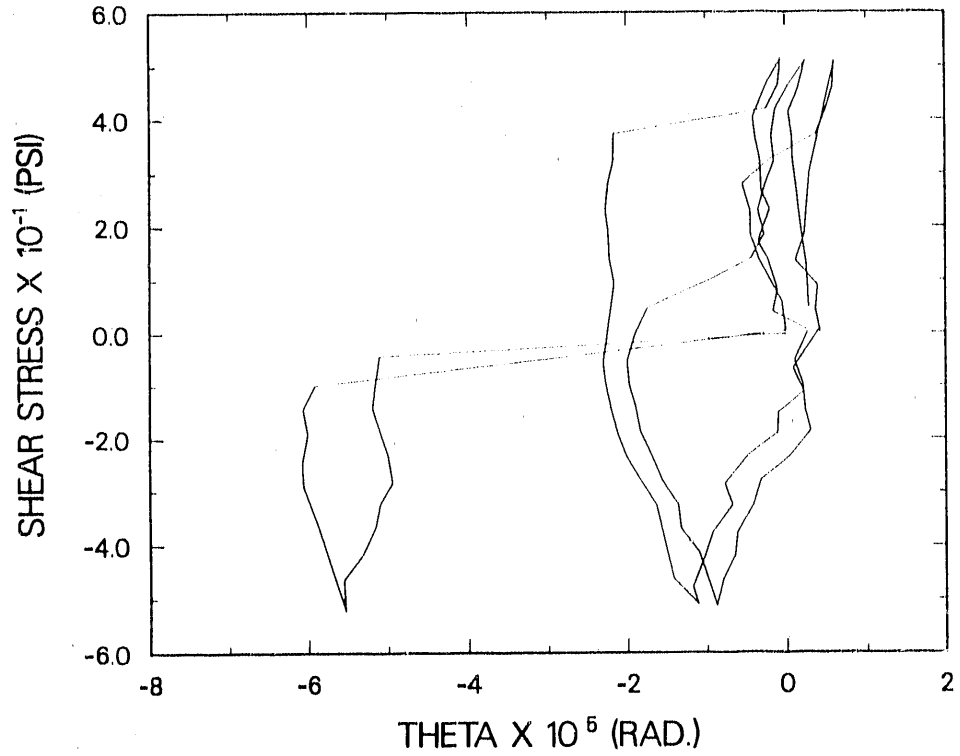


Fig. 103. Torsional deformation for the 50-psi load cycles.

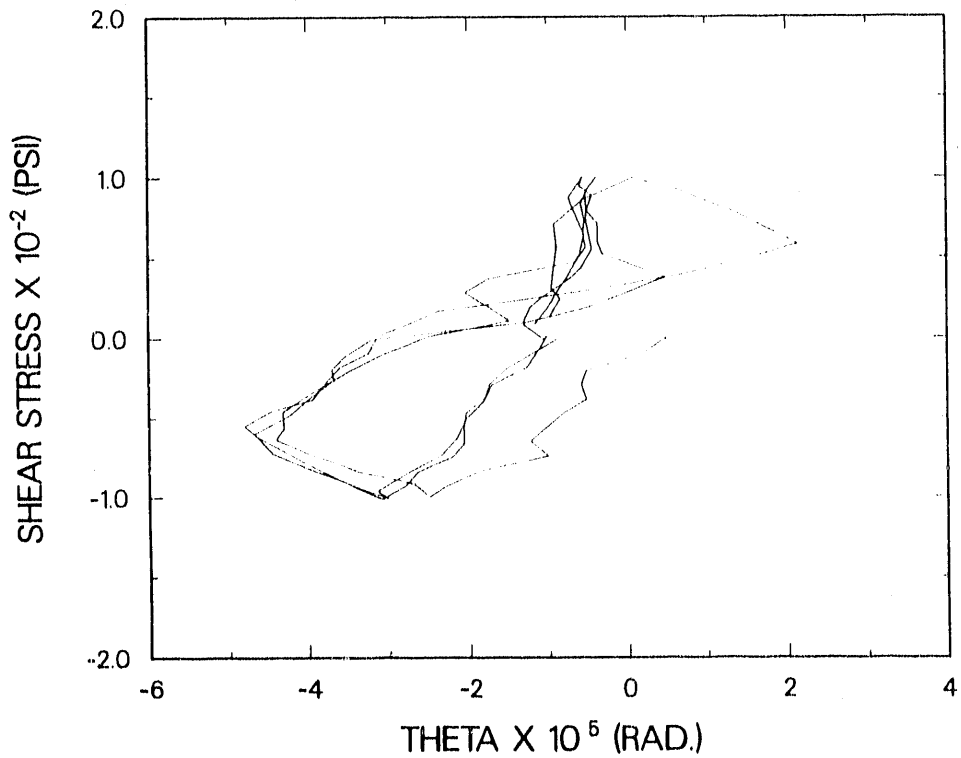


Fig. 104. Torsional deformation for the 100-psi load cycles.

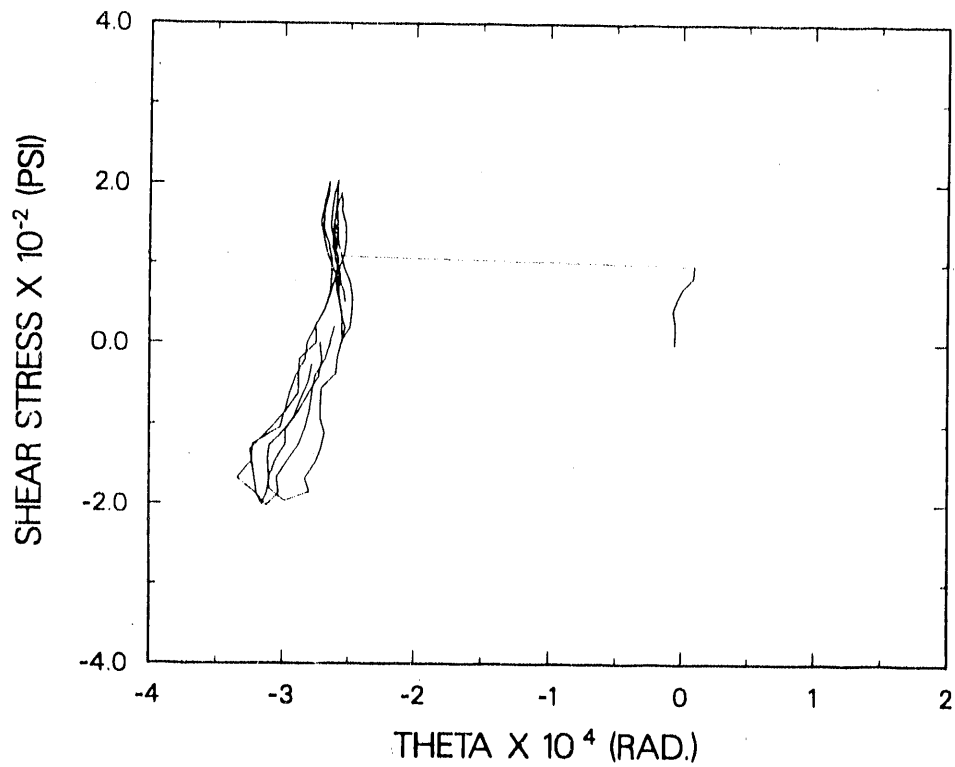


Fig. 105. Torsional deformation for the 150- and 200-psi load cycles.

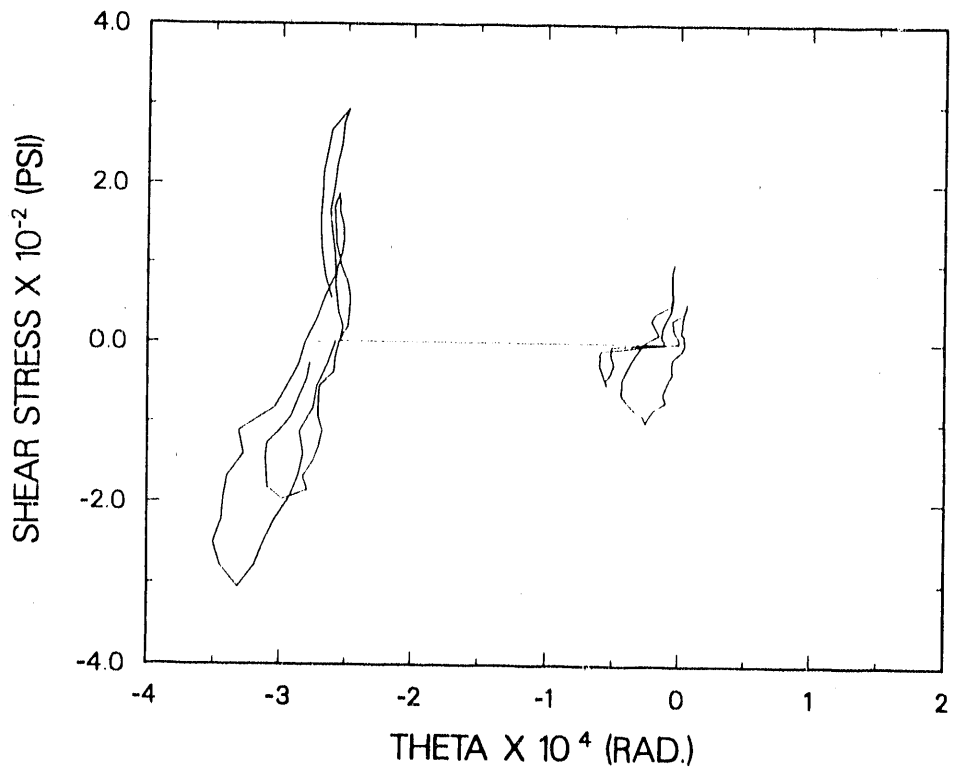


Fig. 106. Torsional deformation for the 300-psi load cycles.

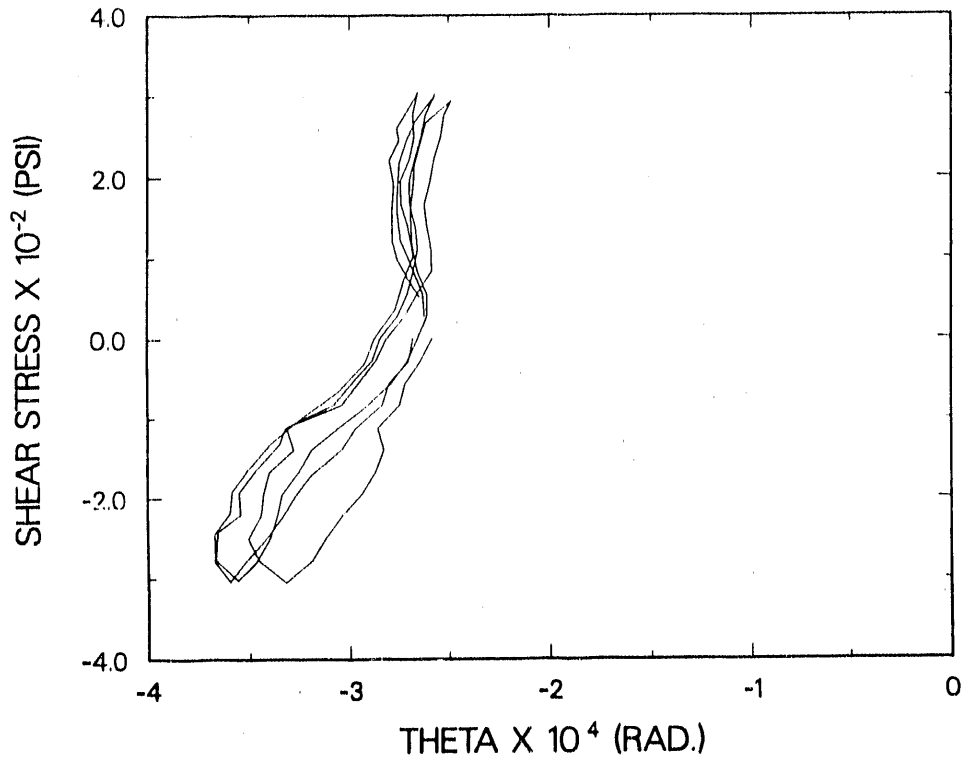


Fig. 107. Torsional deformation for the failure load cycle and last 50-psi load cycle.

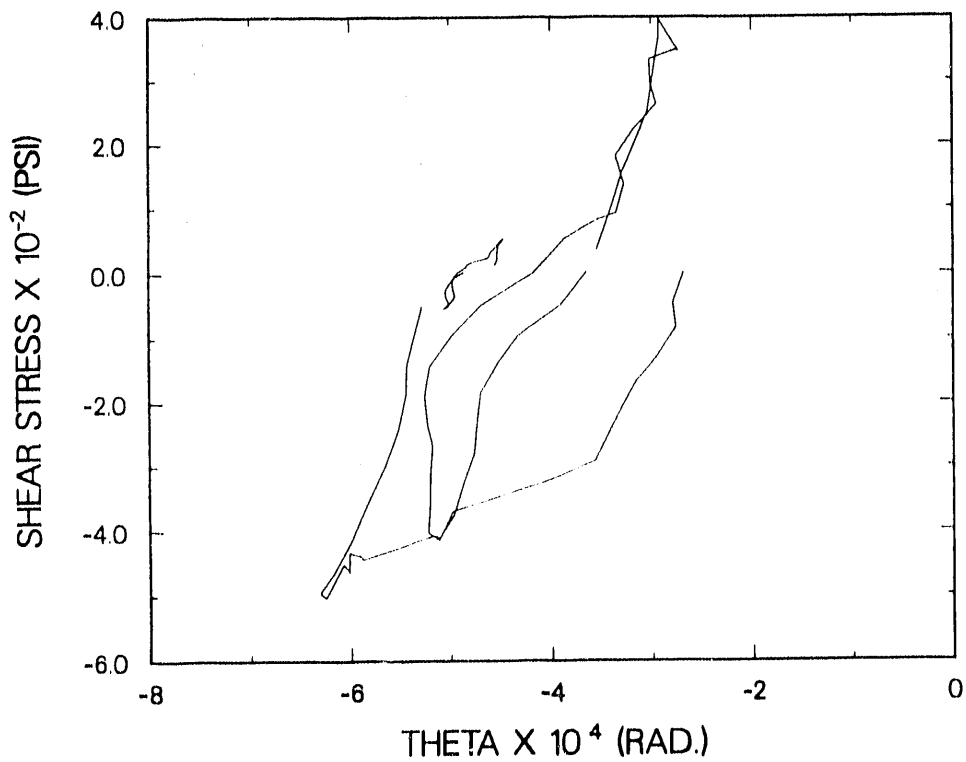


Fig. 108. Torsional deformation for the first load cycle at each stress level.

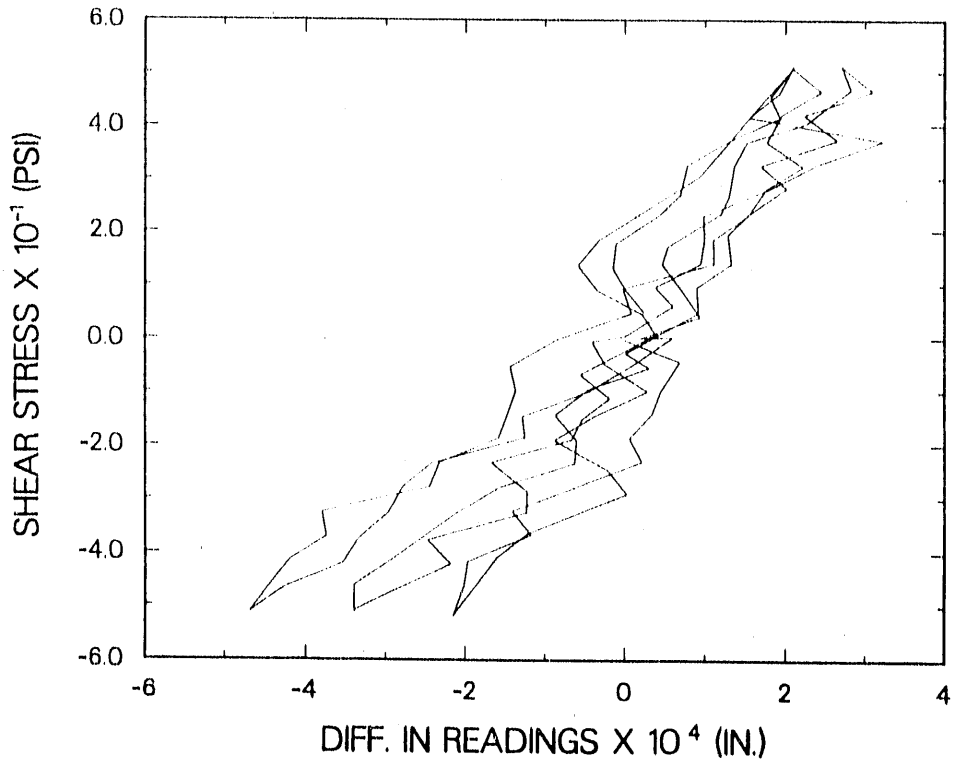


Fig. 109. Difference in readings of gages above and below floor for the 50-psi load cycles.

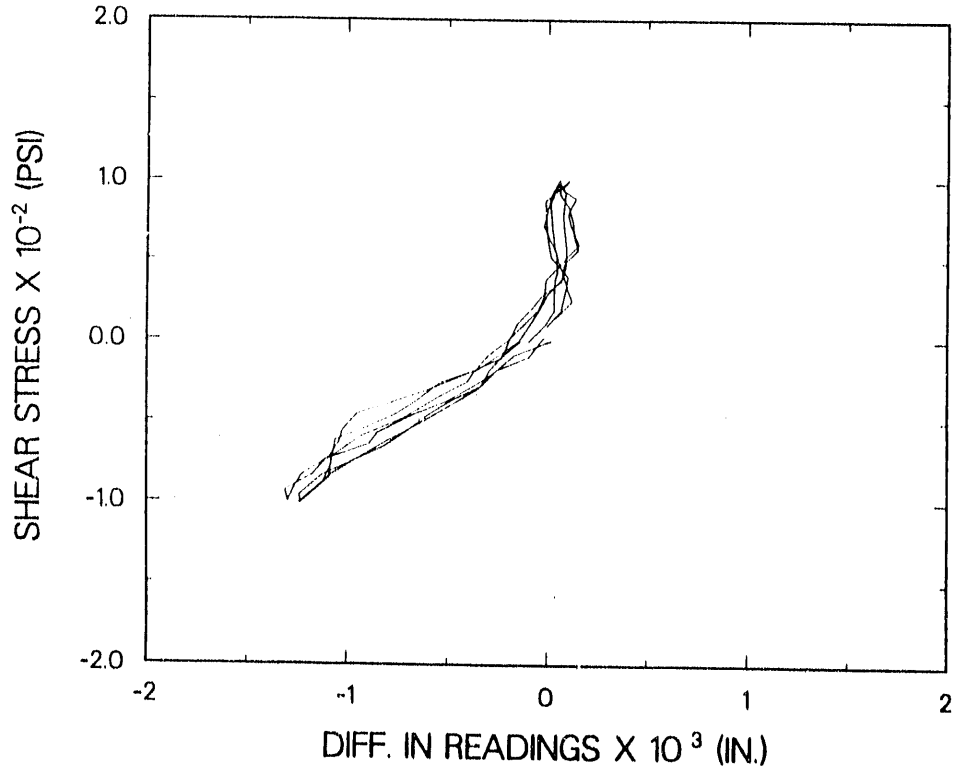


Fig. 110. Difference in readings of gages above and below floor for the 100-psi load cycles.

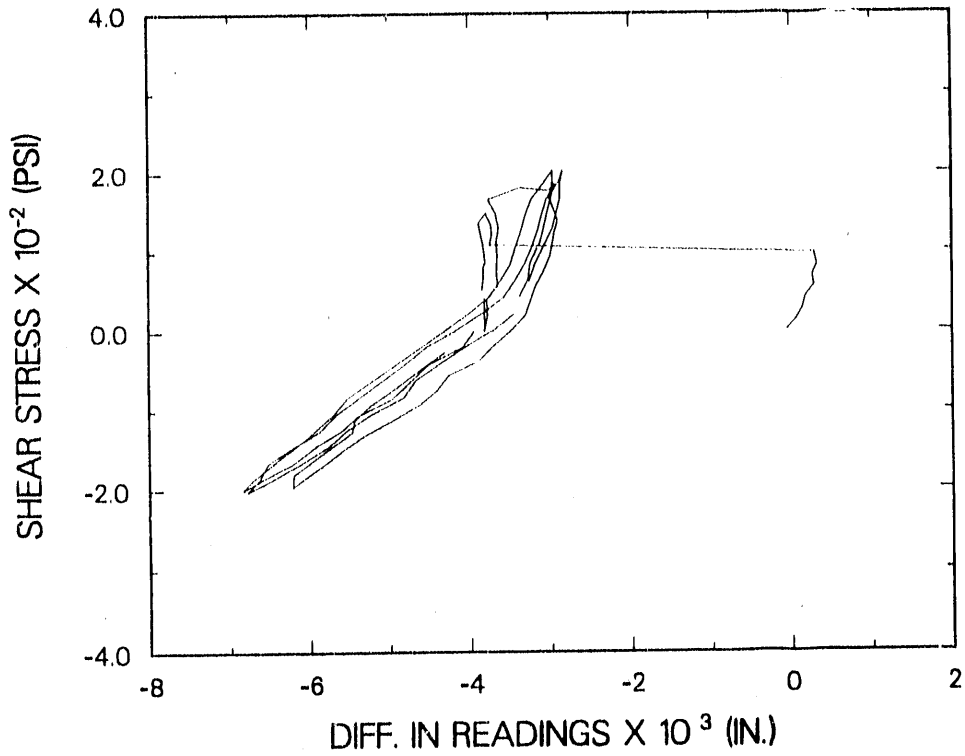


Fig. 111. Difference in readings of gages above and below floor for the 150- and 200-psi load cycles.

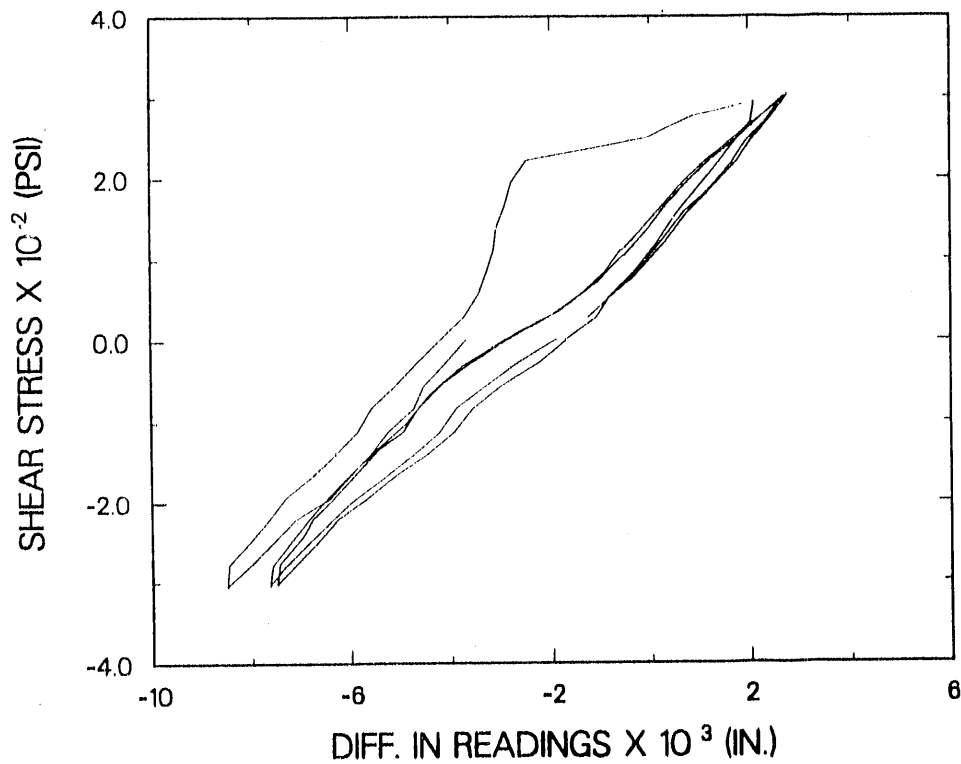


Fig. 112. Difference in readings of gages above and below floor for the 300-psi load cycles.

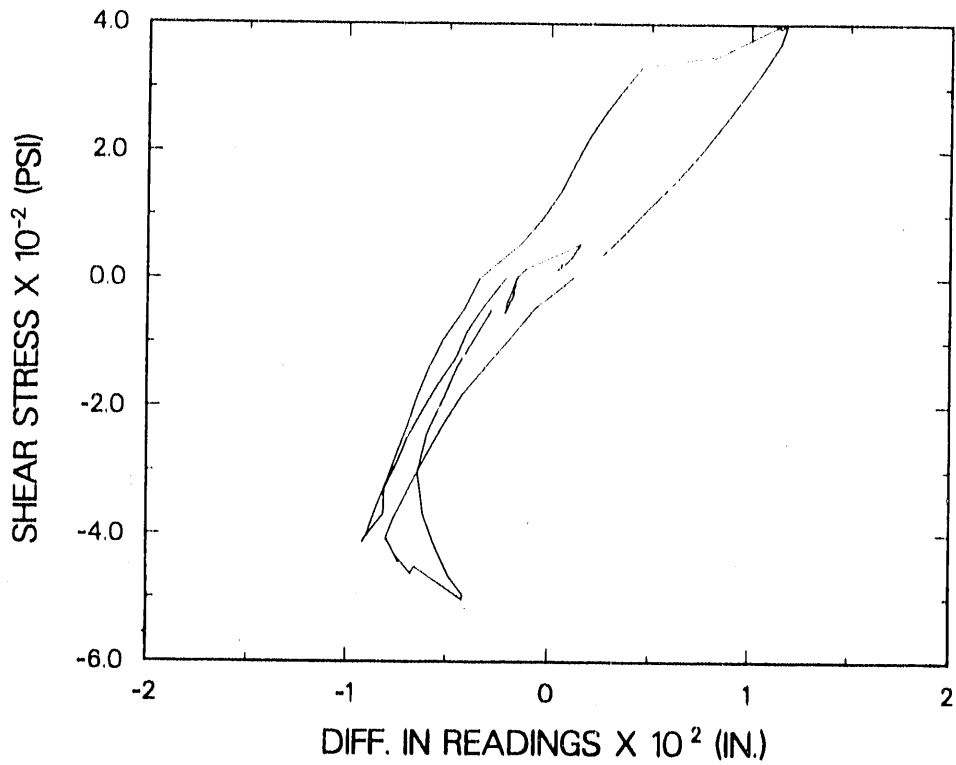


Fig. 113. Difference in readings of gages above and below floor for the failure load cycle and last 50-psi run.

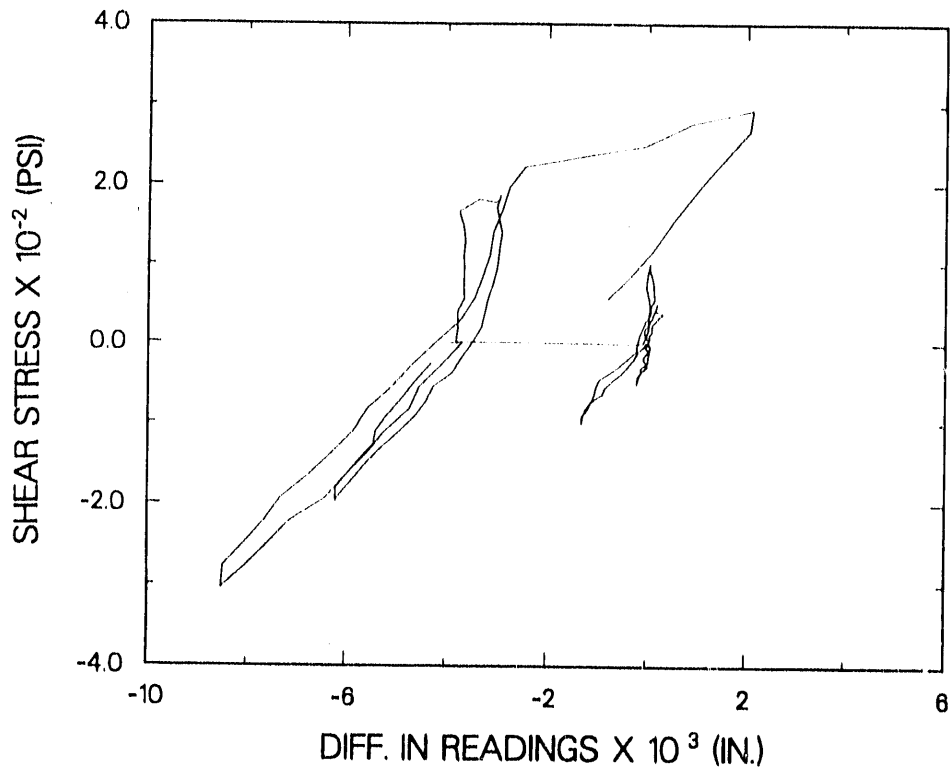


Fig. 114. Difference in readings of gages above and below floor for first load cycle at each stress level.

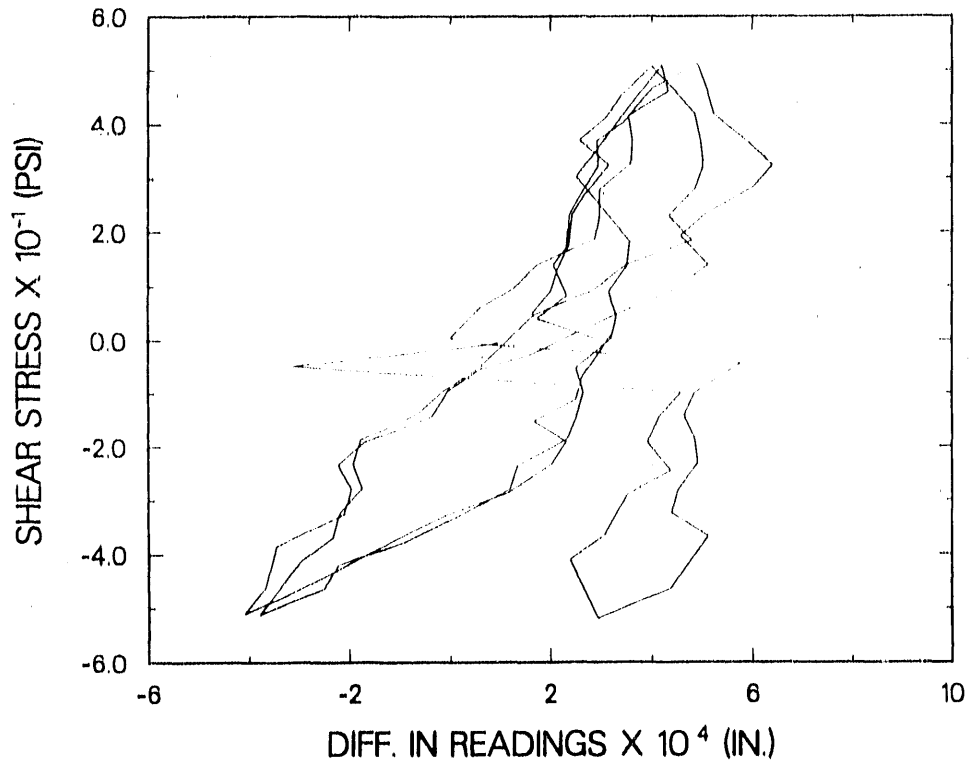


Fig. 115. Difference in readings of gages above and below ceiling for the 50-psi load cycles.

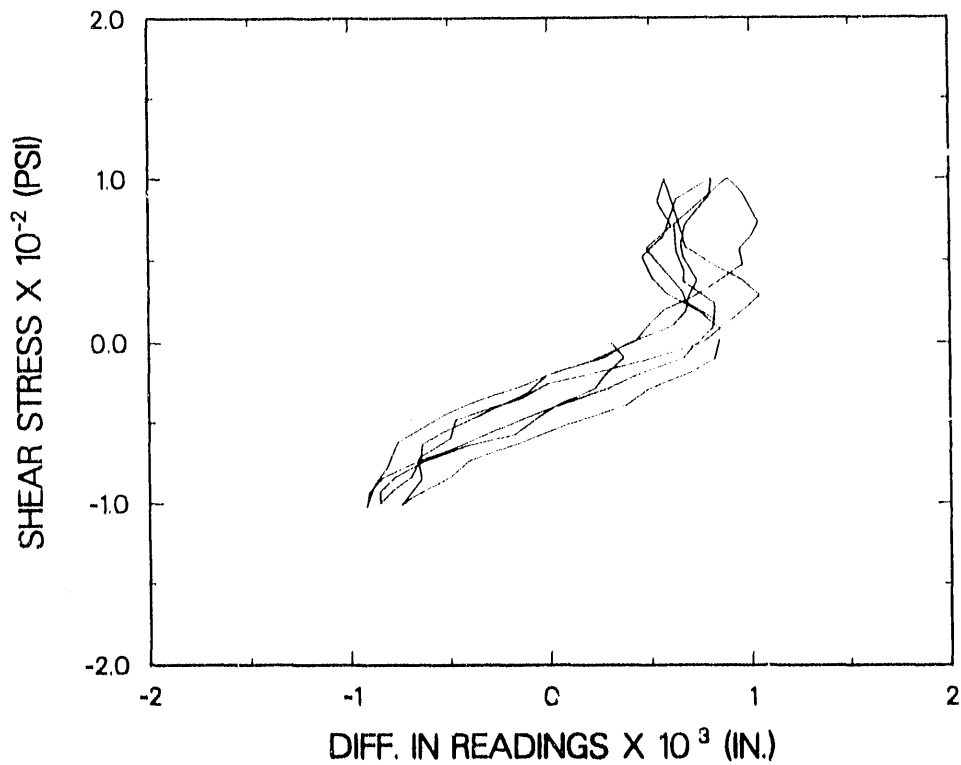


Fig. 116. Difference in readings of gages above and below ceiling for the 100-psi runs.

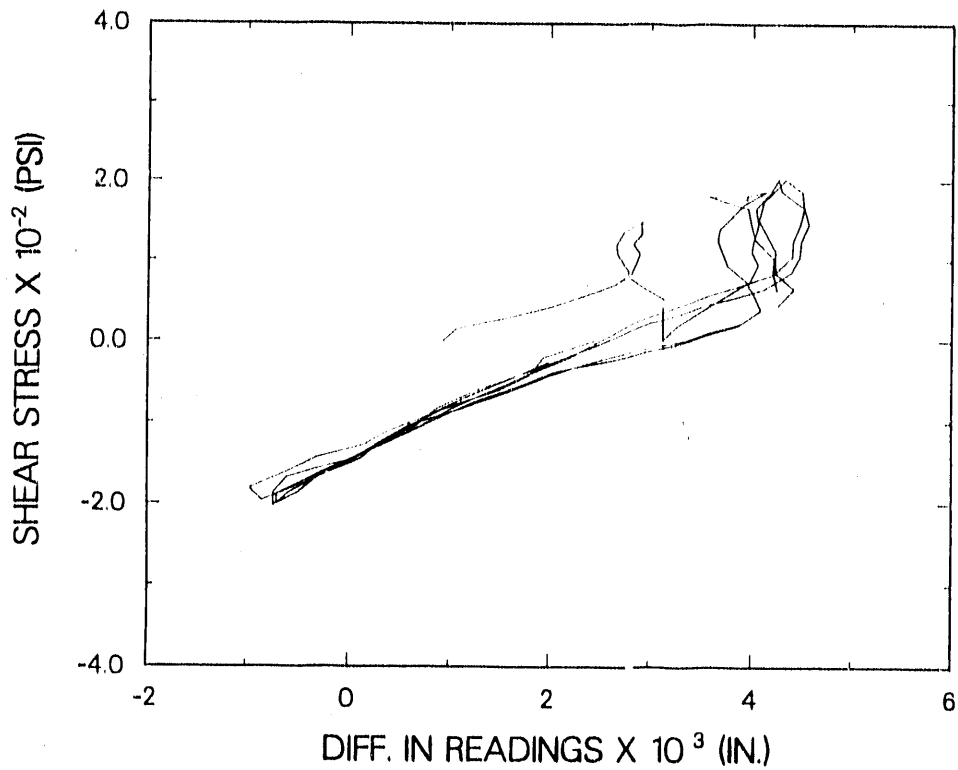


Fig. 117. Difference in readings of gages above and below ceiling for the 150- and 200-psi runs.

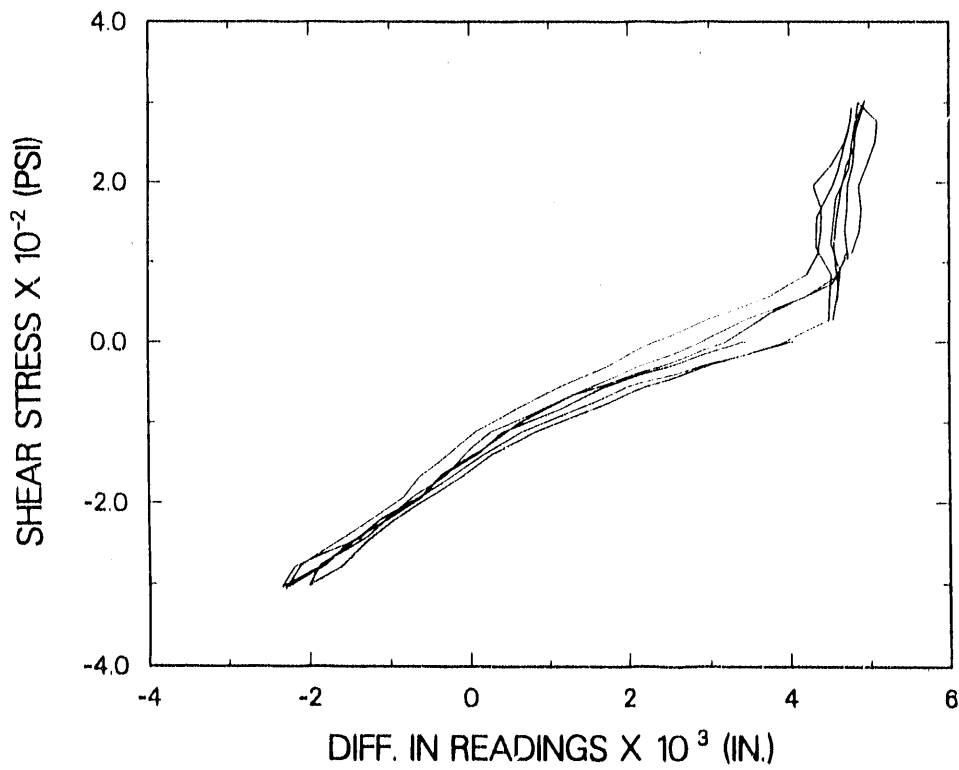


Fig. 118. Difference in readings of gages above and below ceiling for the 300-psi runs.

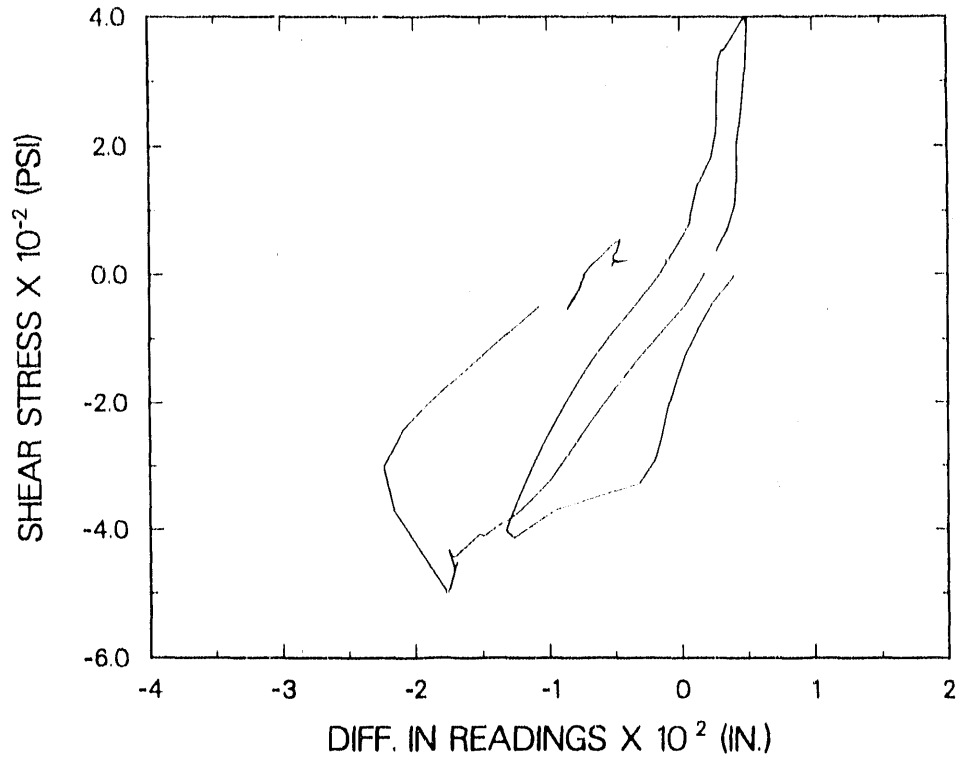


Fig. 119. Difference in readings of gages above and below ceiling for the failure load cycles and last 50-psi run.

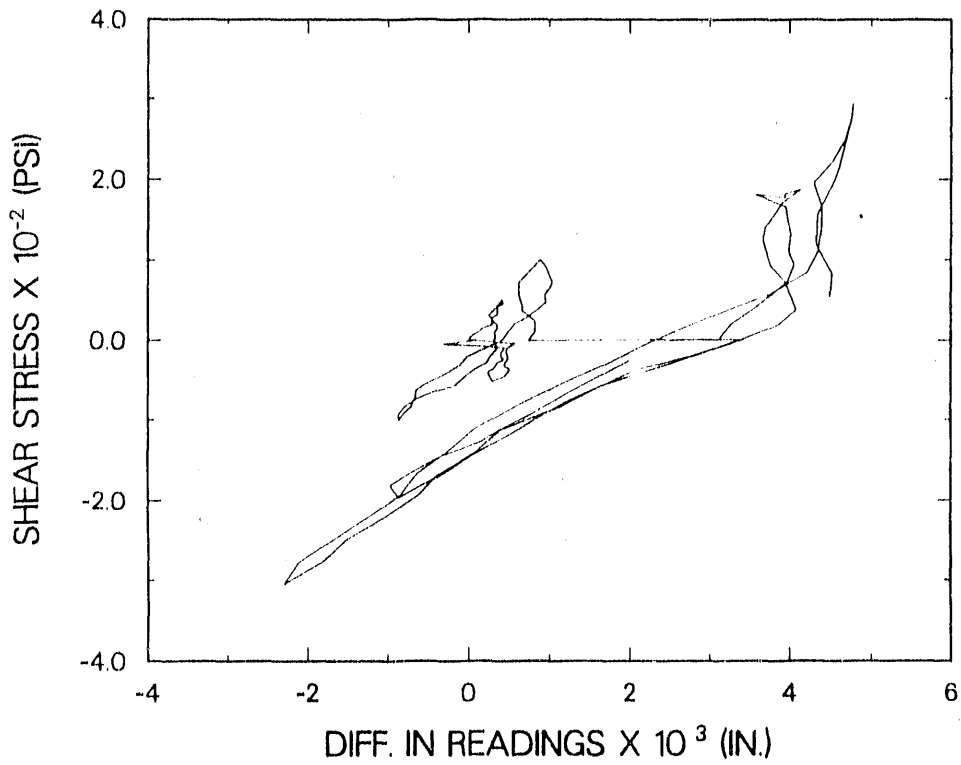


Fig. 120. Difference in readings of gages above and below ceiling for the first load cycle at each stress level.

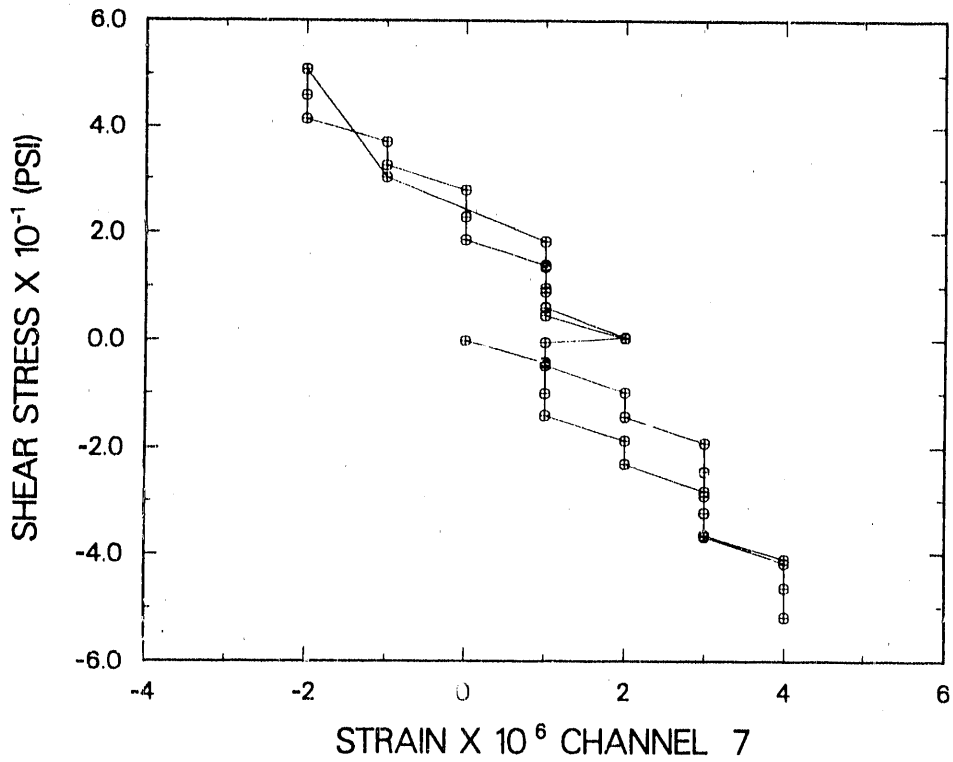


Fig. 121. Strain gage data, horizontal rebar in shear wall (channel 7), 50-psi, Cycle 1.

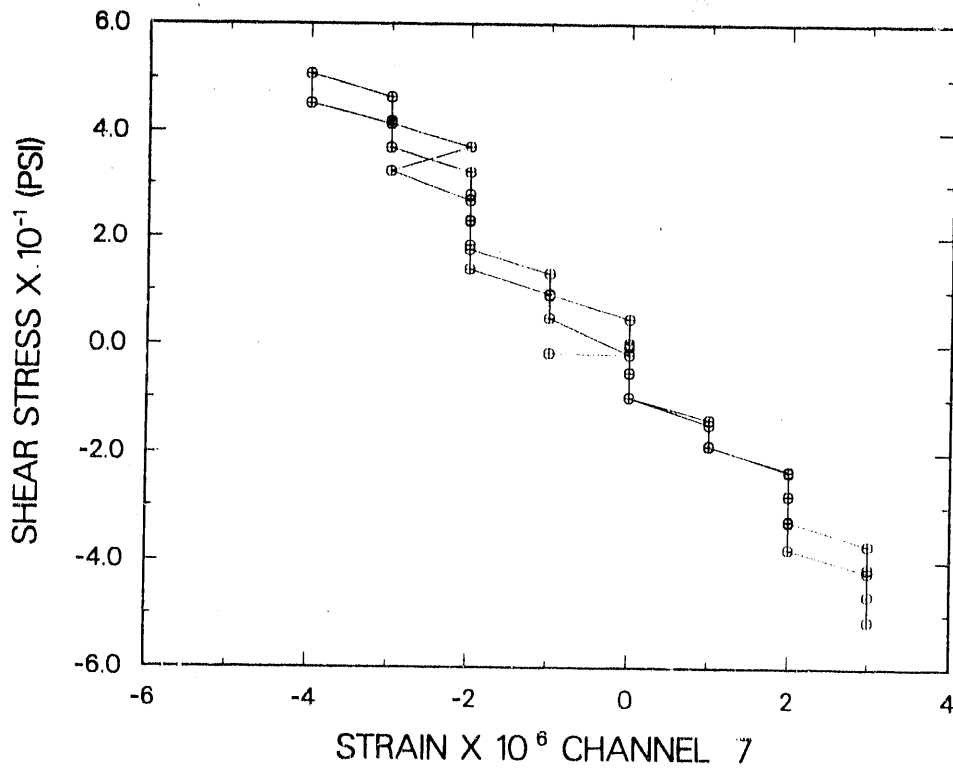


Fig. 122. Strain gage data, horizontal rebar in shear wall (channel 7), 50-psi, Cycle 2.

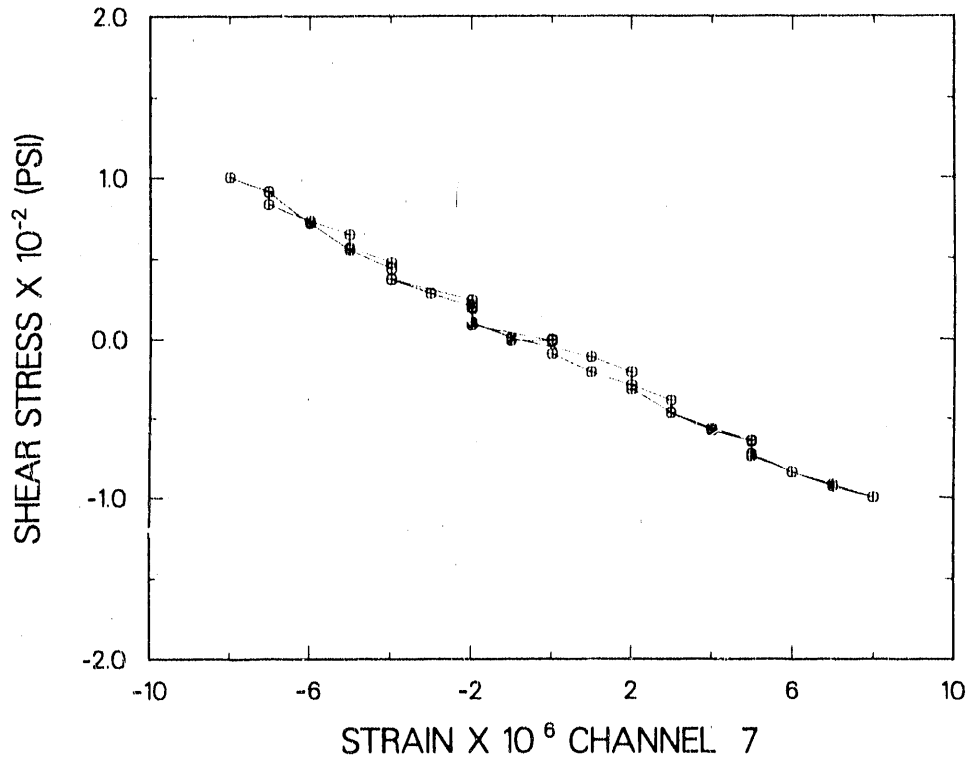


Fig. 123. Strain gage data, horizontal rebar in shear wall (channel 7), 100-psi Cycle 1.

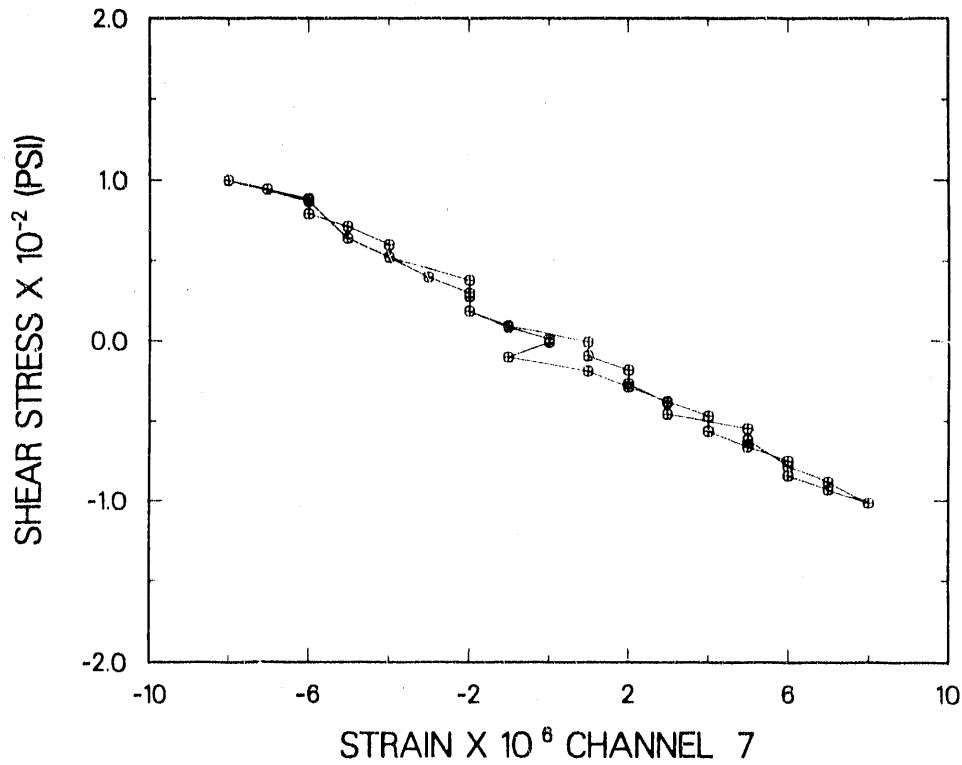


Fig. 124. Strain gage data, horizontal rebar in shear wall (channel 7), 100-psi Cycle 2.

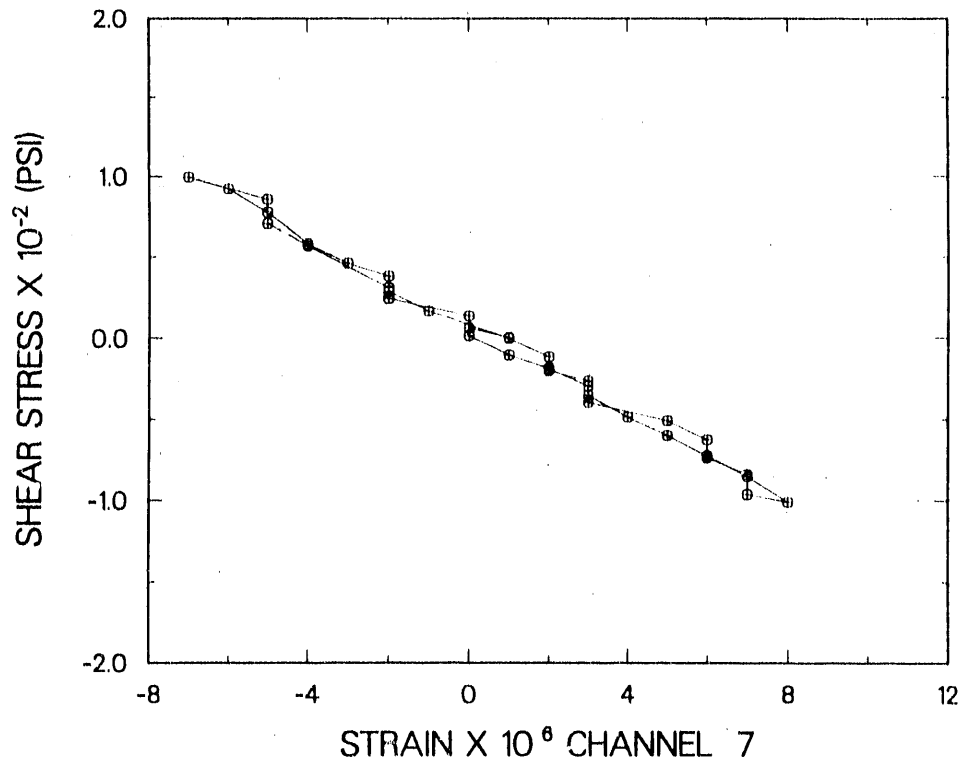


Fig. 125. Strain gage data, horizontal rebar in shear wall (channel 7), 100-psi Cycle 3.

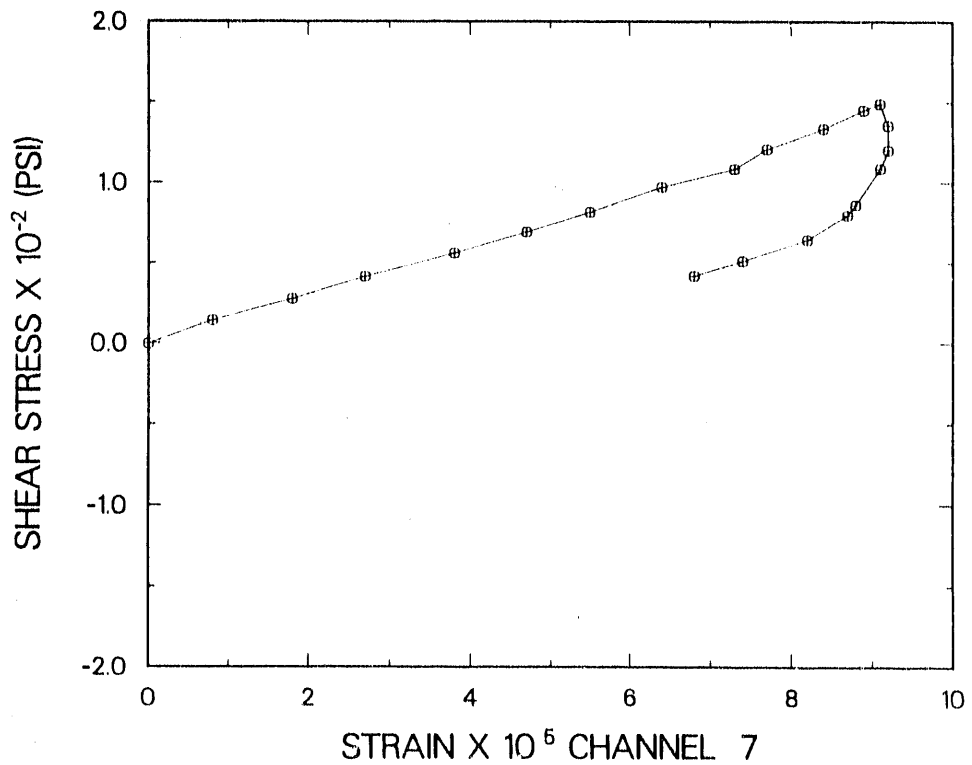


Fig. 126. Strain gage data, horizontal rebar in shear wall (channel 7), 150-psi cycle.

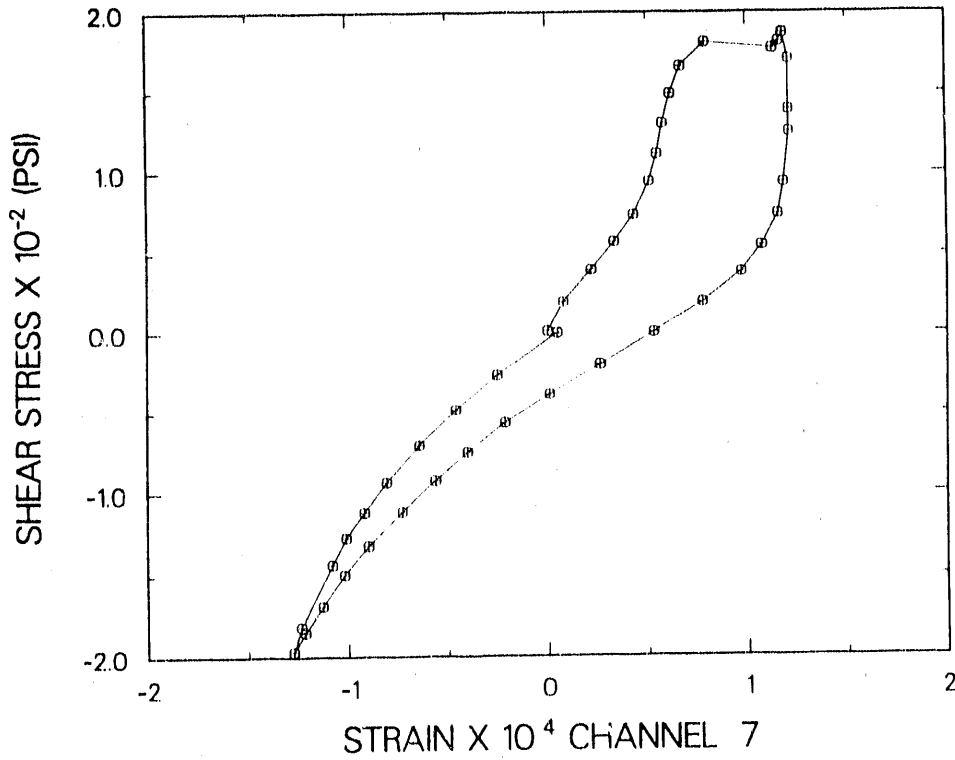


Fig. 127. Strain gage data, horizontal rebar in shear wall (channel 7), 200-psi Cycle 1.

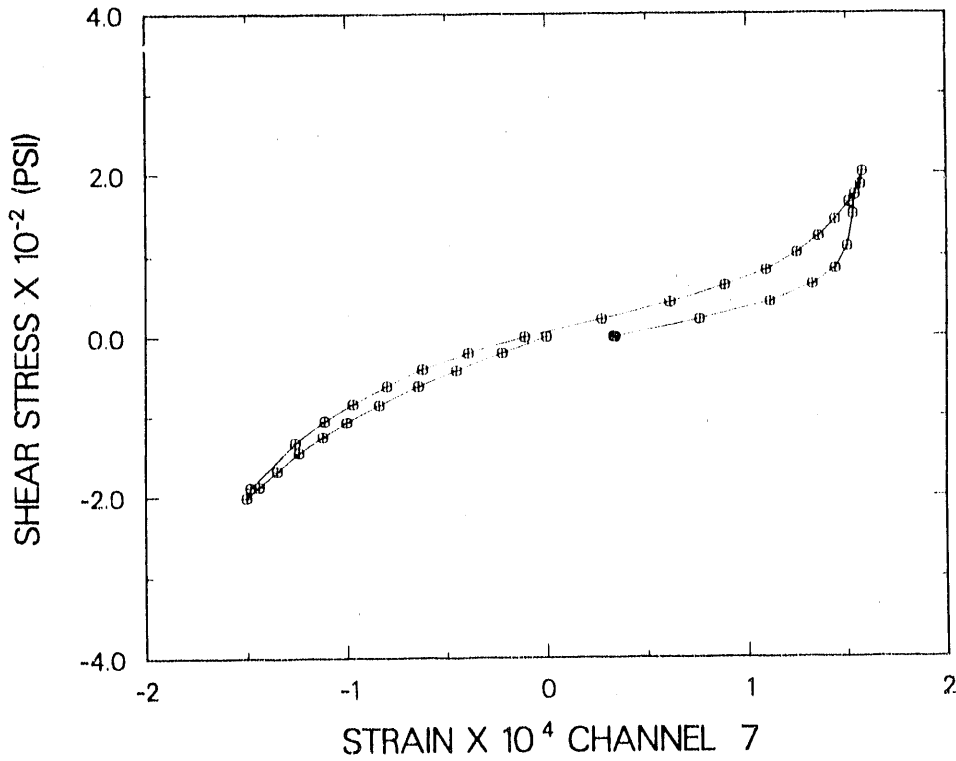


Fig. 128. Strain gage data, horizontal rebar in shear wall (channel 7), 200-psi Cycle 2.

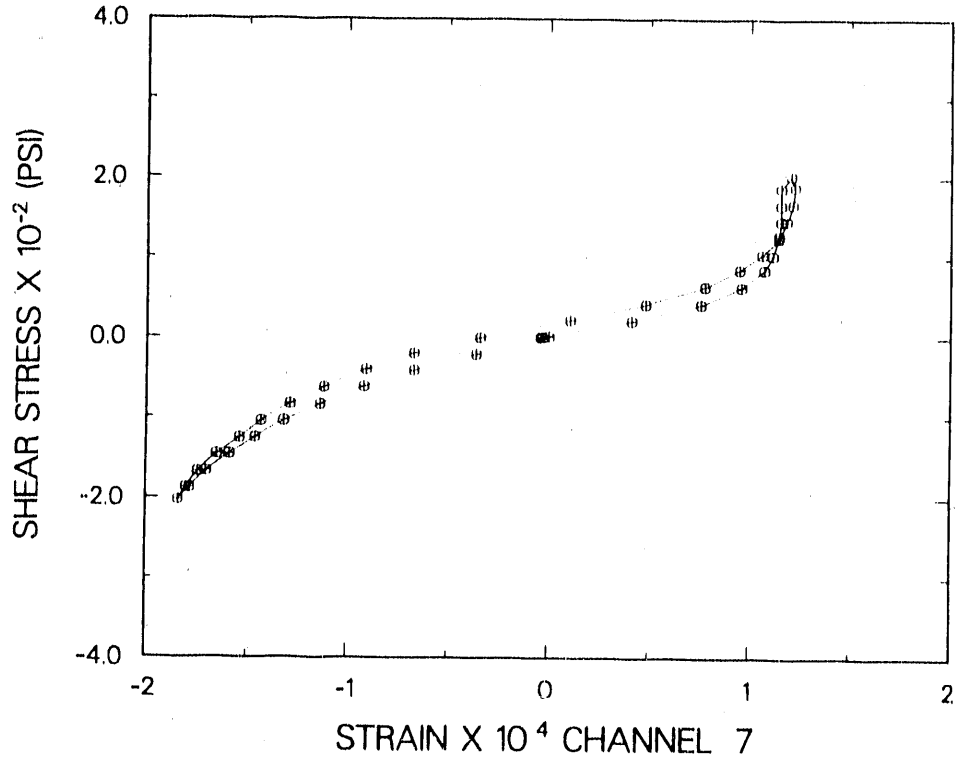


Fig. 129. Strain gage data, horizontal rebar in shear wall (channel 7), 200-psi Cycle 3.

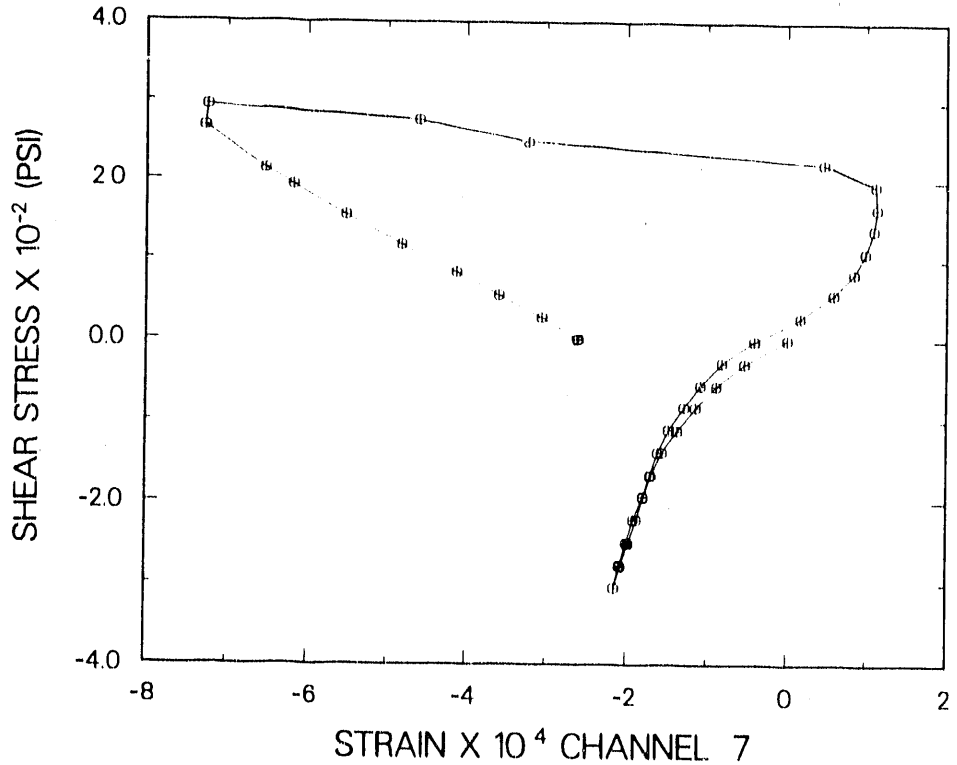


Fig. 130. Strain gage data, horizontal rebar in shear wall (channel 7), 300-psi Cycle 1.

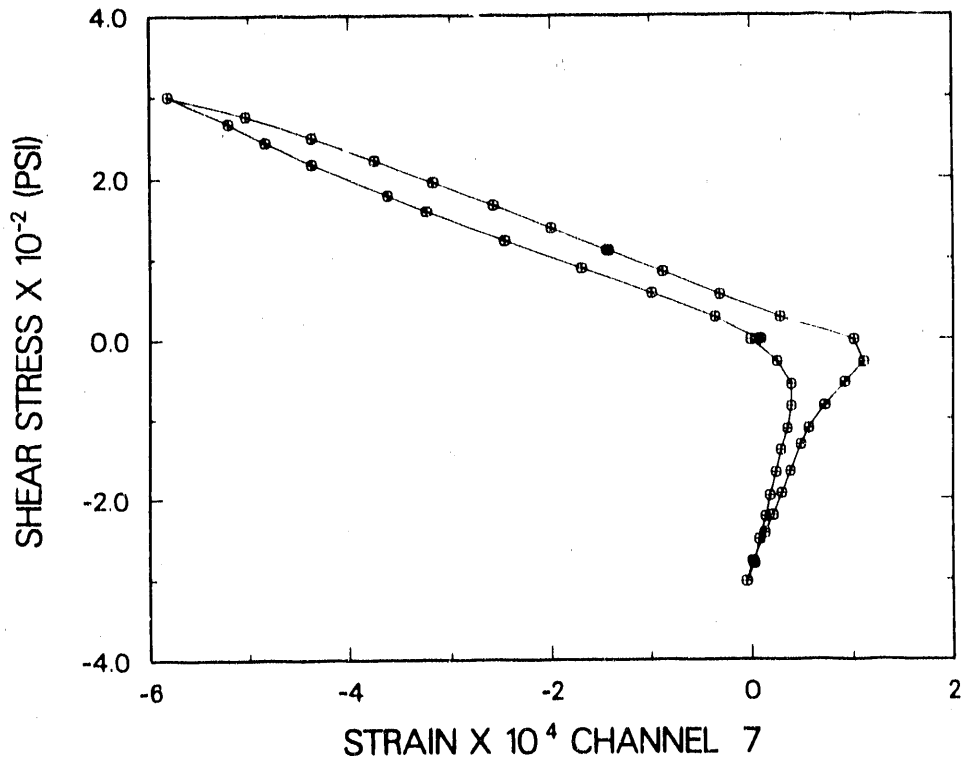


Fig. 131. Strain gage data, horizontal rebar in shear wall (channel 7), 300-psi Cycle 2.

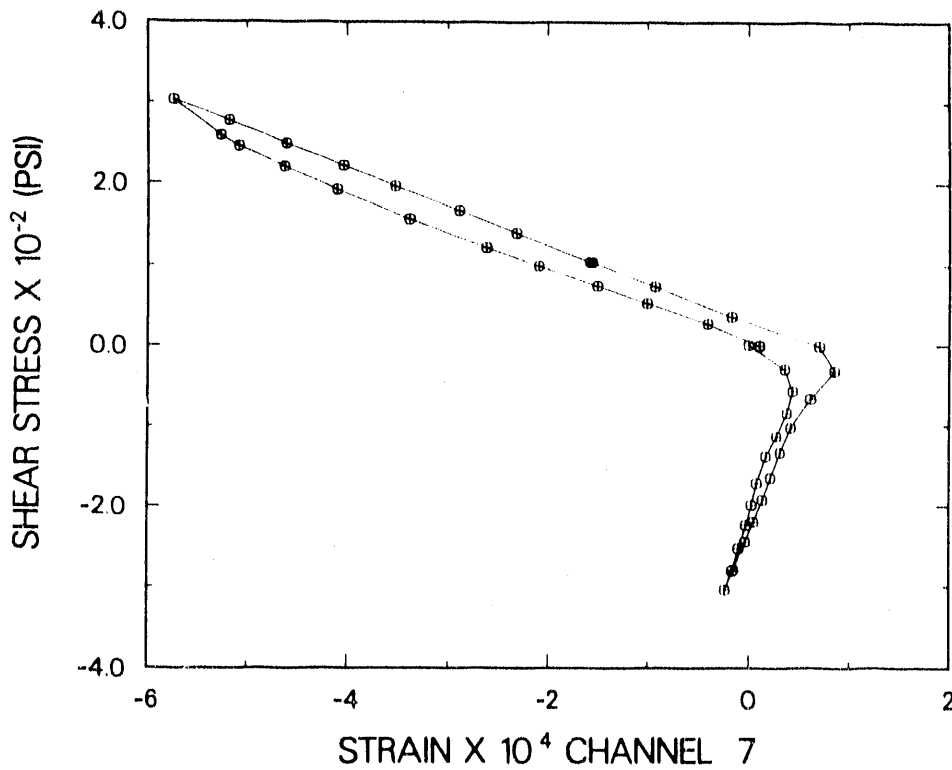


Fig. 132. Strain gage data, horizontal rebar in shear wall (channel 7), 300-psi Cycle 3.

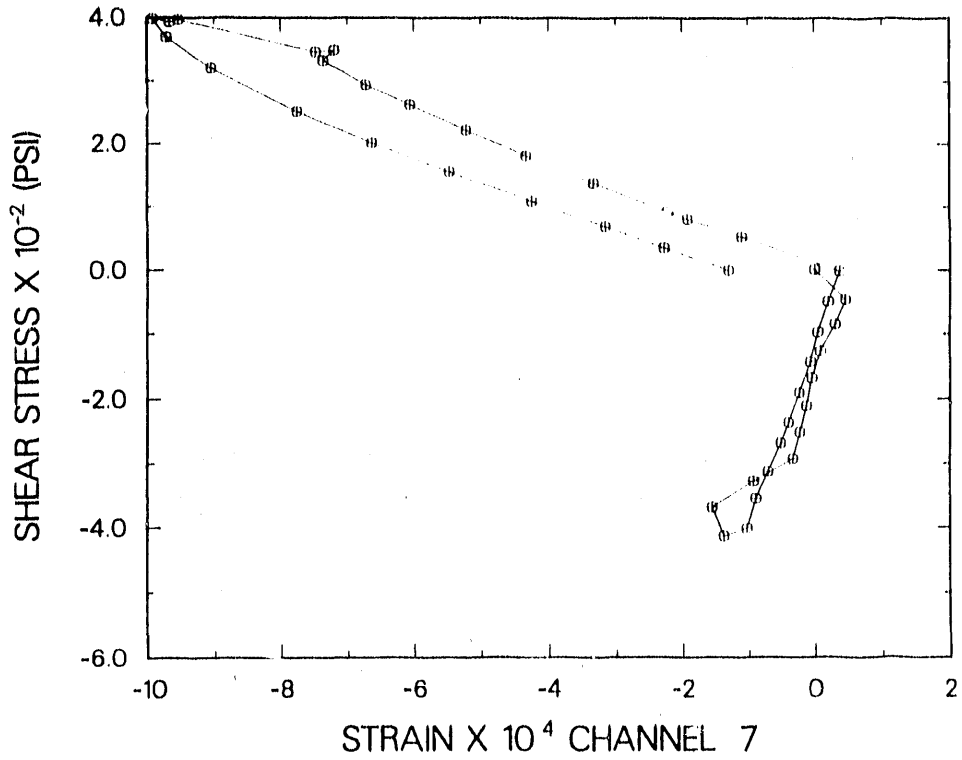


Fig. 133. Strain gage data, horizontal rebar in shear wall (channel 7), failure cycle.

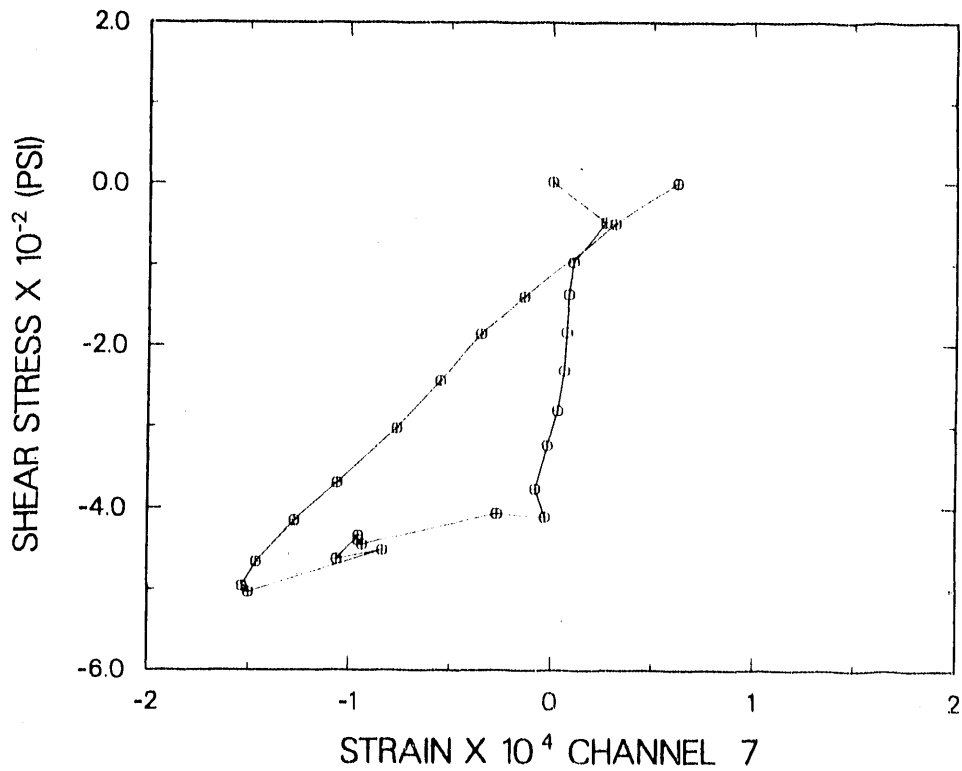


Fig. 134. Strain gage data, horizontal rebar in shear wall (channel 7), 400-psi cycle.

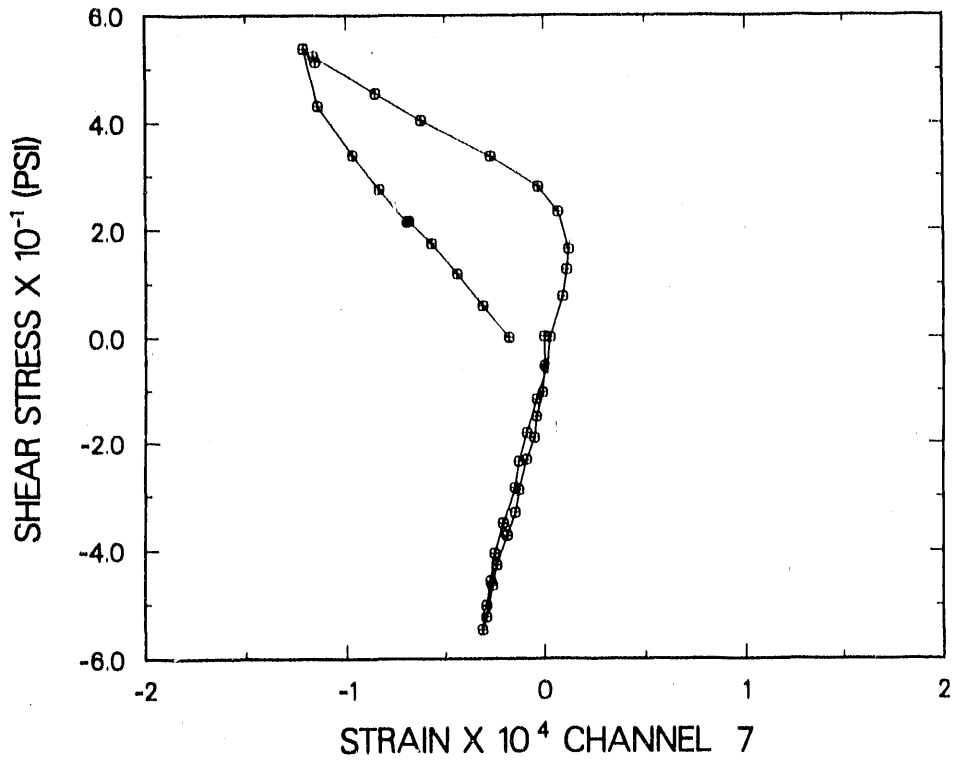


Fig. 135. Strain gage data, horizontal rebar in shear wall (channel 7), 50-psi Cycle 1.

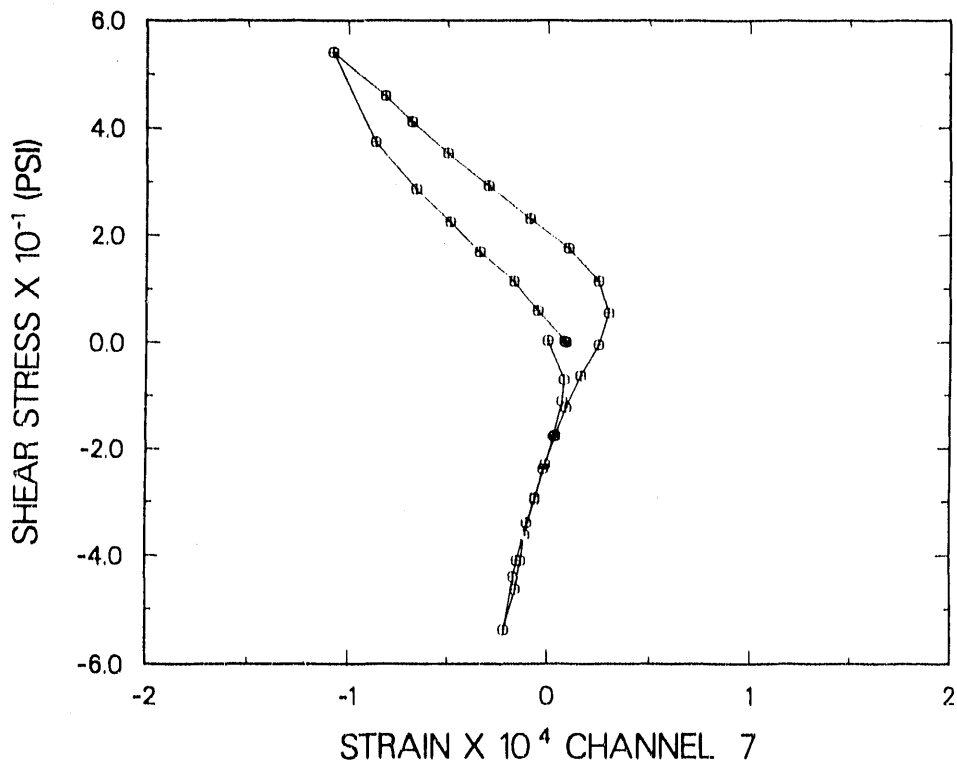


Fig. 136. Strain gage data, horizontal rebar in shear wall (channel 7), 50-psi Cycle 2.

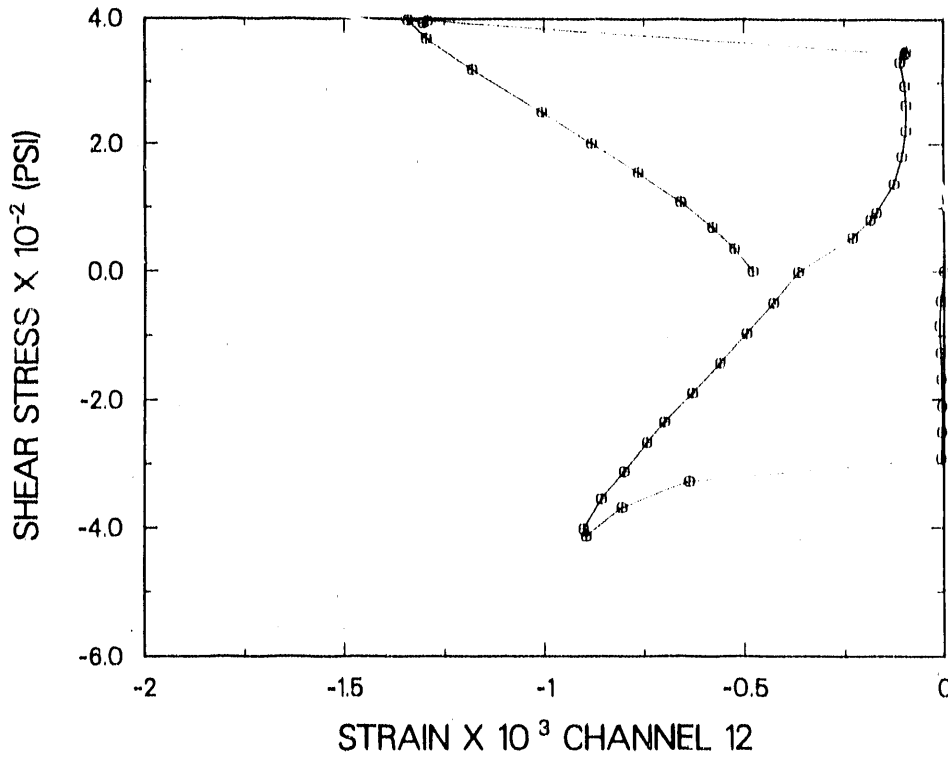


Fig. 137. Strain gage data, horizontal rebar in shear wall (channel 12), 400-psi cycle.

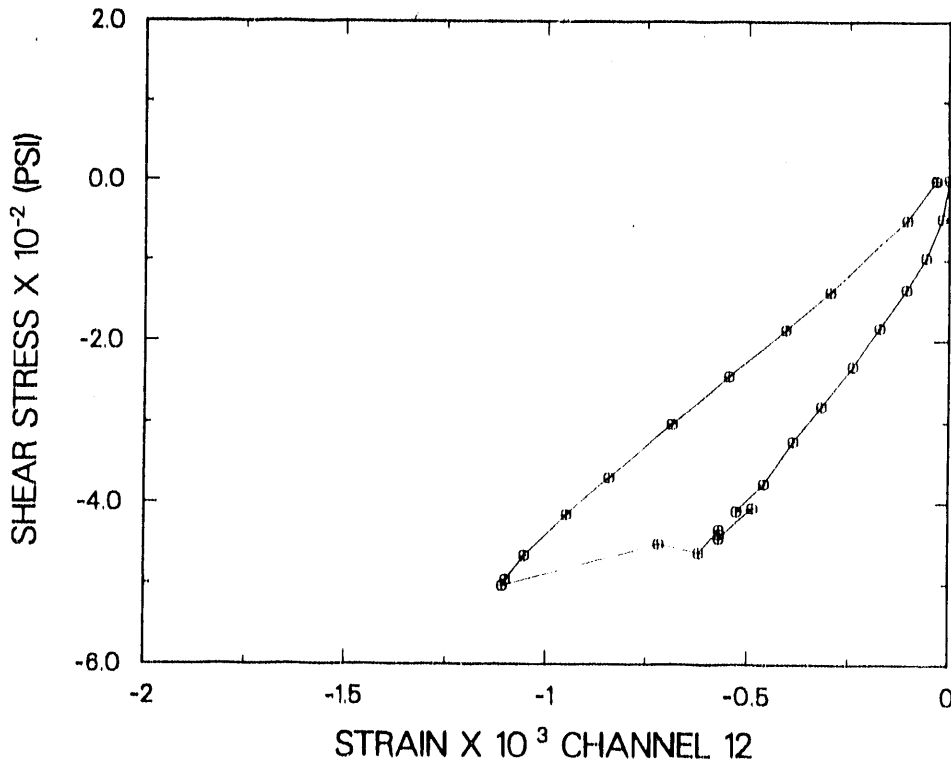


Fig. 138. Strain gage data, horizontal rebar in shear wall (channel 12), failure cycle.

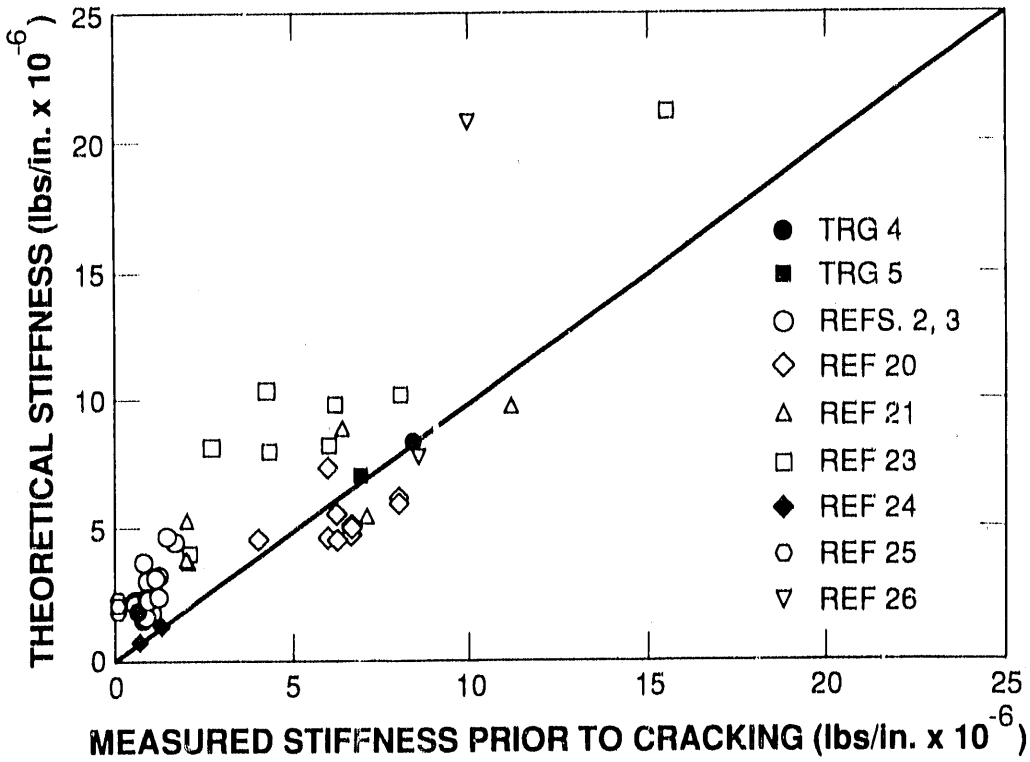


Fig. 139. Other investigators' results plus this investigation: a correlation of theoretical and measured stiffness.

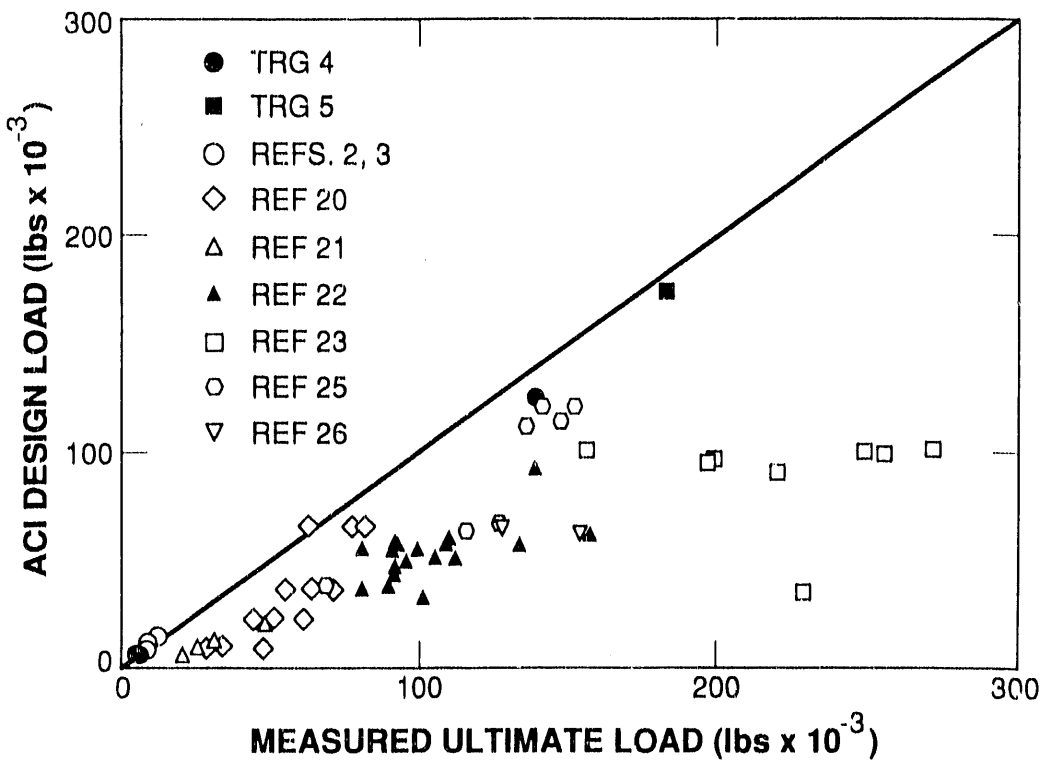


Fig. 140. Same title except: A correlation of ACI design load and the measured ultimate load.

APPENDIX A
ALBUQUERQUE TEST LABORATORY REPORT



Professional Service Industries, Inc.
Albuquerque Testing Laboratory Division

September 26, 1987

Los Alamos National Laboratory
Los Alamos, New Mexico 87544

Attention: Mr. Chuck Farrar

Subject: Concrete Testing
PSI Project No. 531-70177

Dear Sir:

As requested, tests were performed on compressive strength cylinders delivered to our laboratory by Los Alamos personnel. The cylinders were molded by Los Alamos personnel. The samples were labelled TRG #5, Truck No.1, TRG #5, Truck No. 2 and TRG #6. The tests performed were unit weight, split tensile and compressive strength with cylinders tested on September 12, 1987. In addition to these tests, strain data was gathered and stress-strain curves were plotted for each cylinder. Results of the tests are presented in this report.

If you have any questions regarding this report, please feel free to call.

Respectfully submitted,

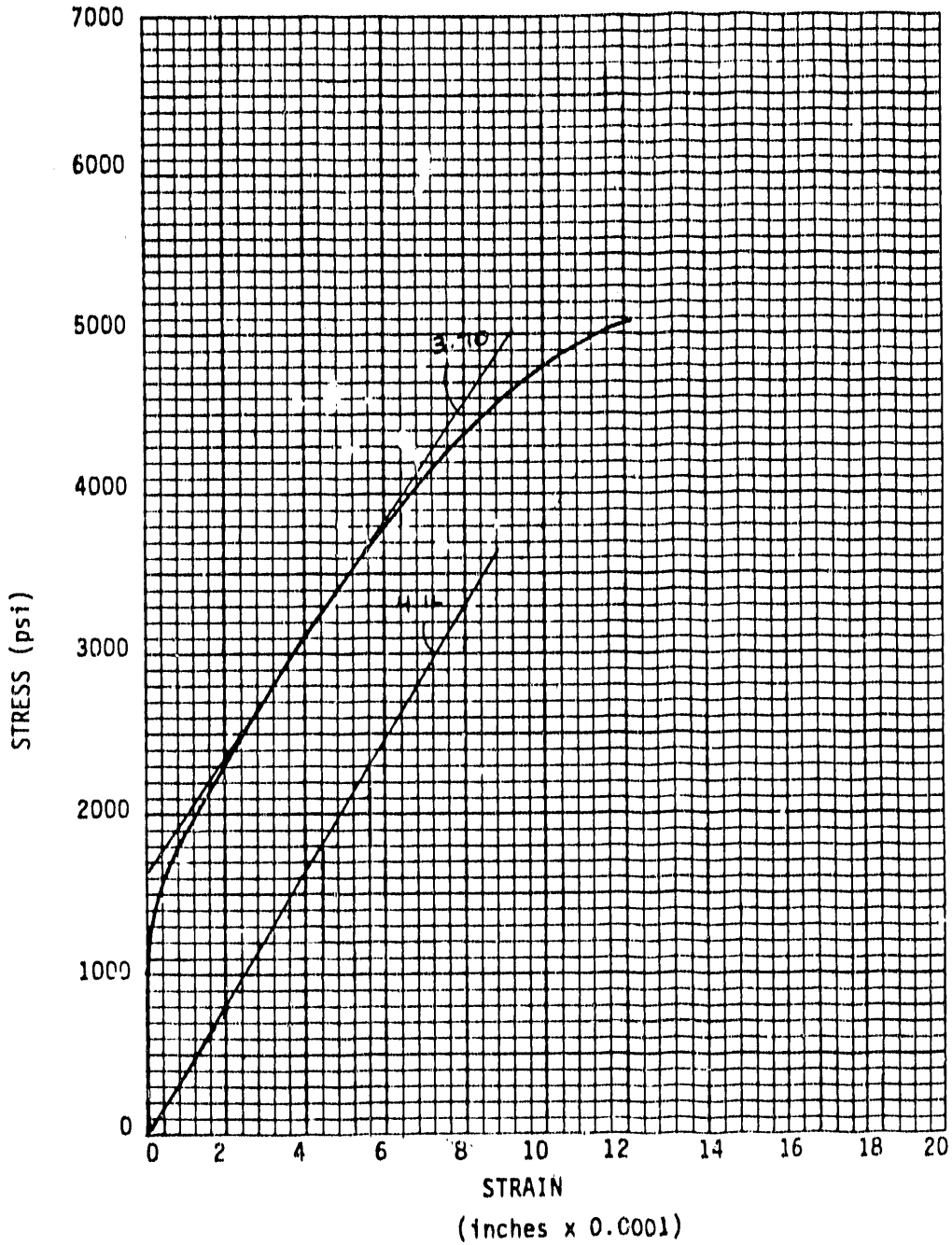
Professional Service Industries, Inc.

A handwritten signature in black ink, appearing to read "Patrick J. Conley". The signature is written in a cursive style with some loops and flourishes.

Patrick J. Conley, P.E.
Division Manager, Construction Services

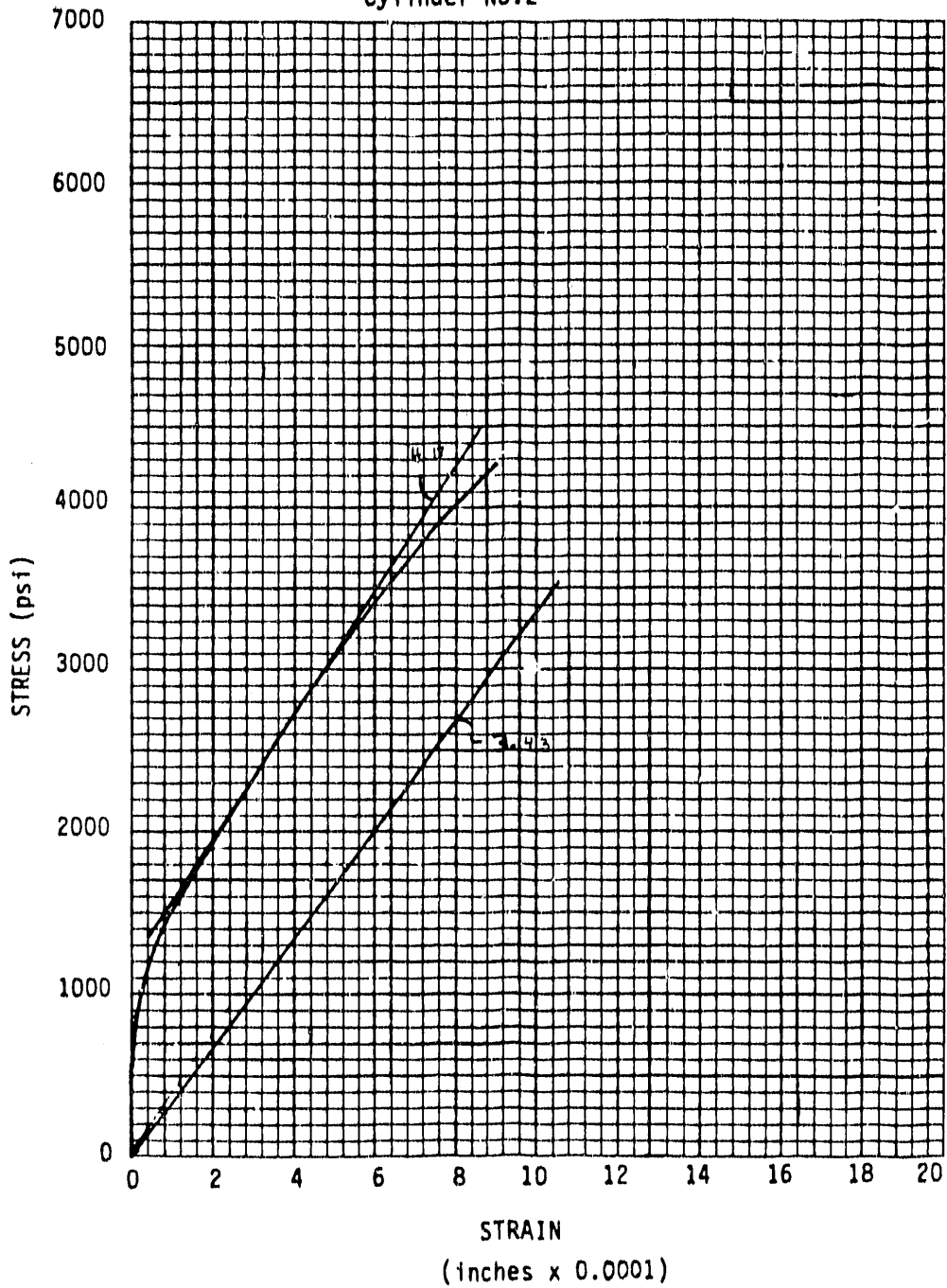
PJC/peq
Enclosure

TRG #5
 Truck No. 1
 Cylinder No. 1



PROJECT NAME Concrete Testing Los Alamos Labs Los Alamos, NM	$E = 4.160 \times 10^6$ Ult. Compressive Strength = 5040 psi	
	PROJECT NO 531-70177-1	DATE 9/26/87

TRG #5
 Truck No. 1
 Cylinder No.2



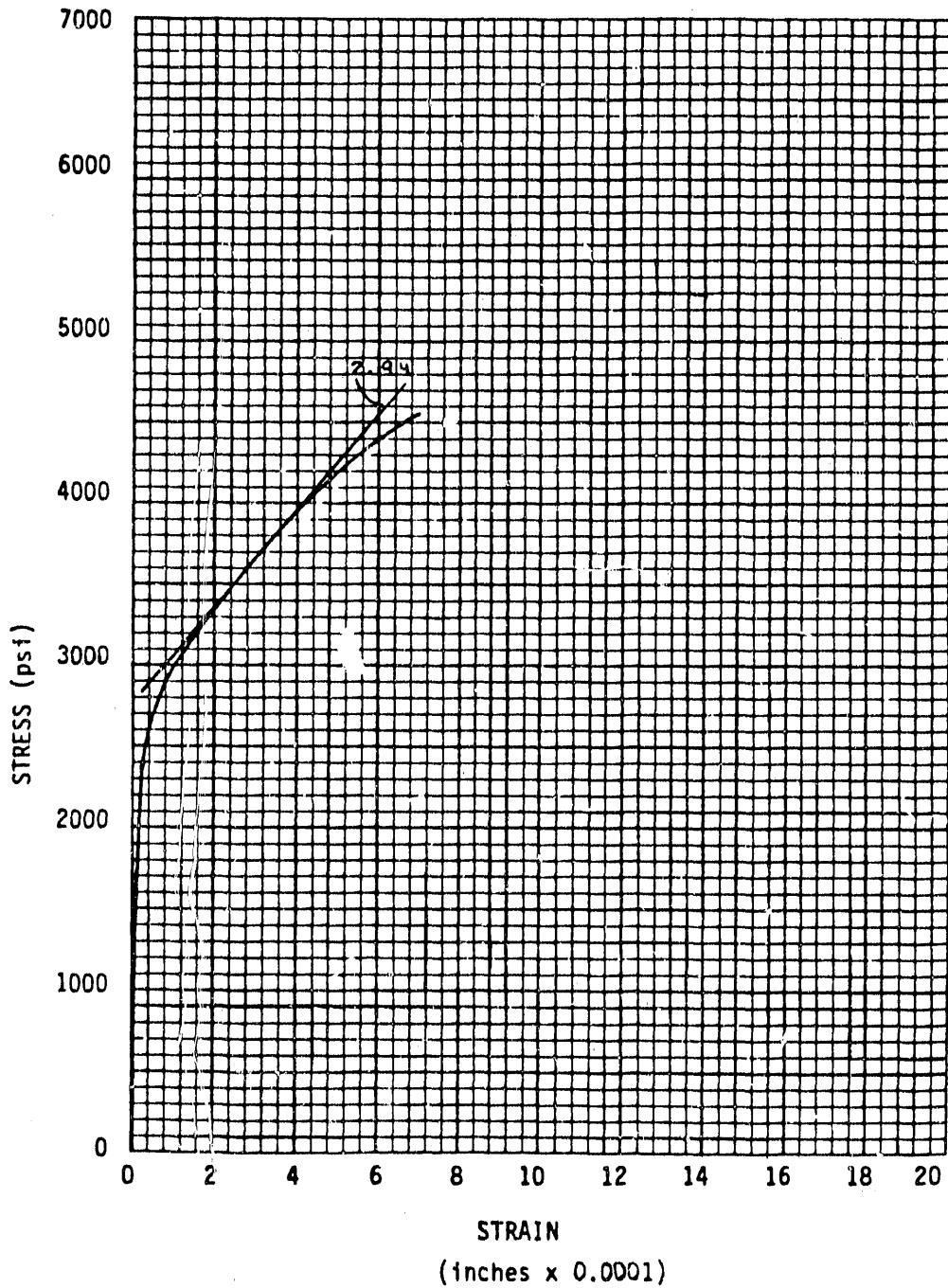
PROJECT NAME
 Concrete Testing
 Los Alamos Lab
 Los Alamos, NM

$E = 3.433 \times 10^6$
 Ult. Compressive Strength = 4460 psi

PROJECT NO
 531-70177-1

DATE
 9/26/87

TRG #5
Truck No.1
Cylinder No. 3



PROJECT NAME

Concrete Testing
Los Alamos Labs
Los Alamos, NM

E = Unknow: Faulty Test Data
Ult. Compressive Strength = 4420 psi

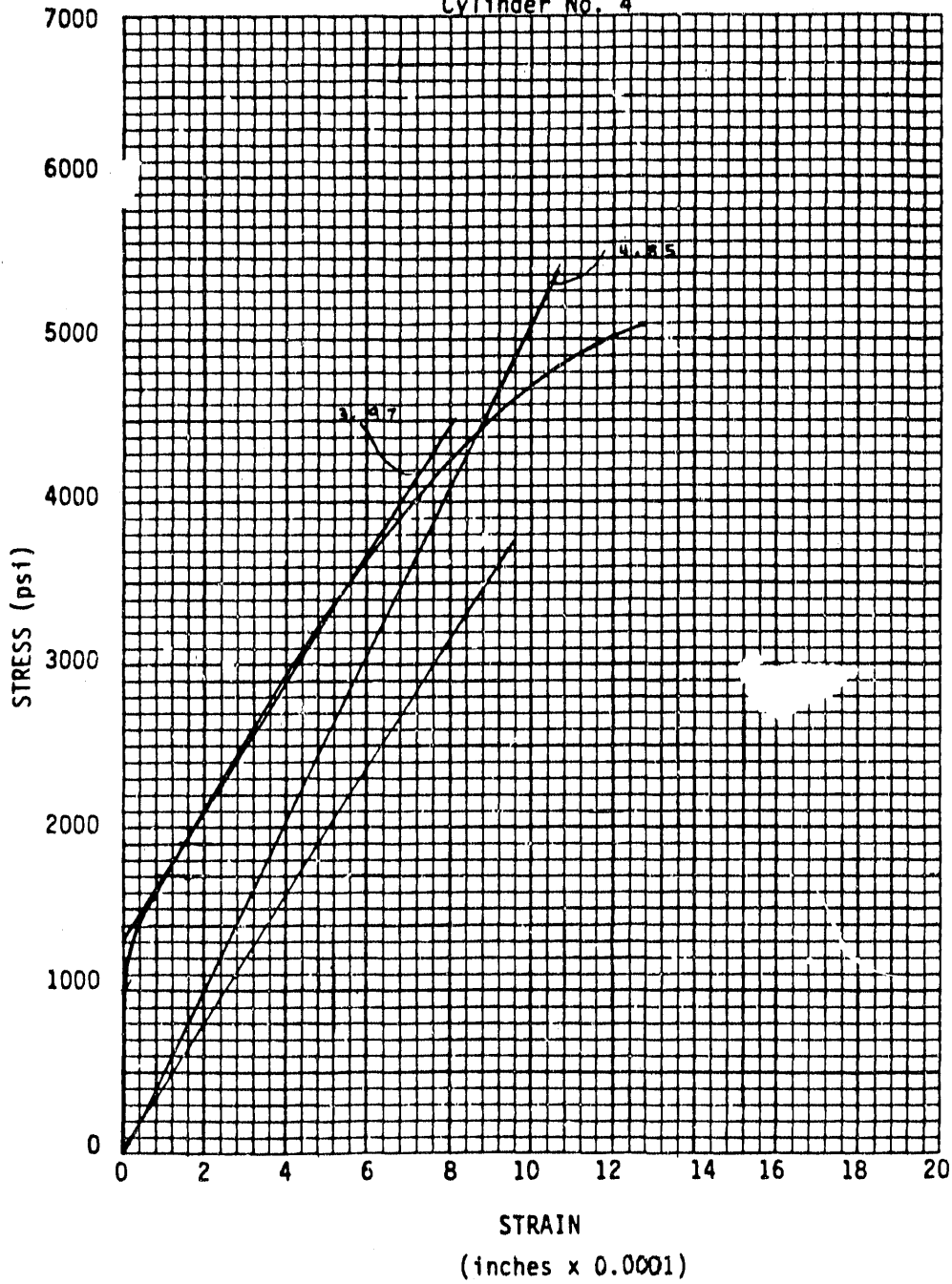
PROJECT NO

531-70177-1

DATE

9/26/87

TRG #5
 Truck No. 1
 Cylinder No. 4



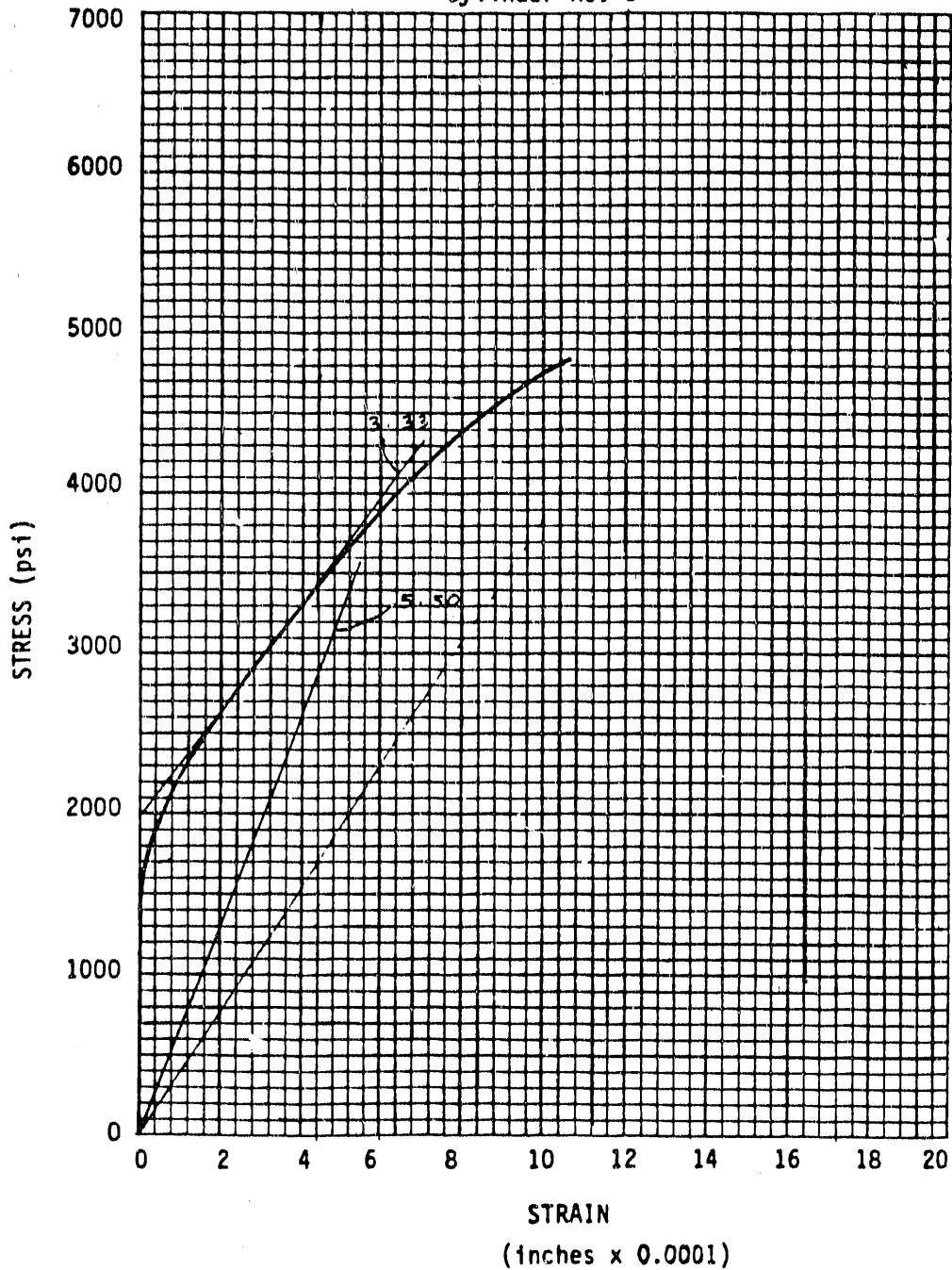
PROJECT NAME
 Concrete Testing
 Los Alamos Labs
 Los Alamos, NM

$E = 4.846 \times 10^6$
 Ult Compressive Strength = 5130 psi

PROJECT NO
 531-70177-1

DATE
 9/26/87

TRG #5
 Truck No. 1
 Cylinder No. 5



PROJECT NAME

Concrete Testing
 Los Alamos Labs
 Los Alamos, NM

$E = 5.500 \times 10^6$

Ult Compressive Strength = 5020 psi

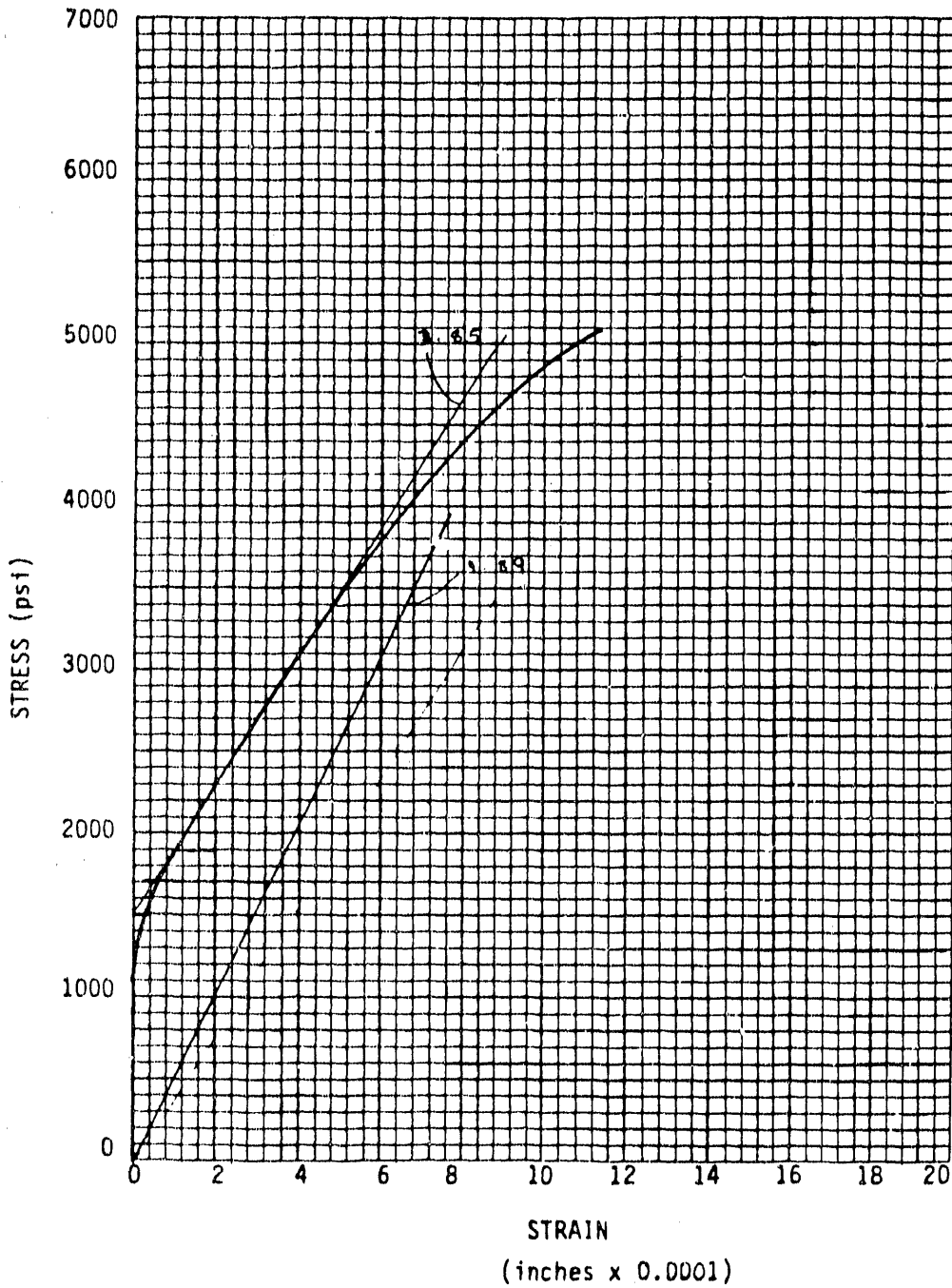
PROJECT NO

531-70177-1

DATE

9/26/87

TRG #5
 Truck No. 1
 Cylinder No. 6



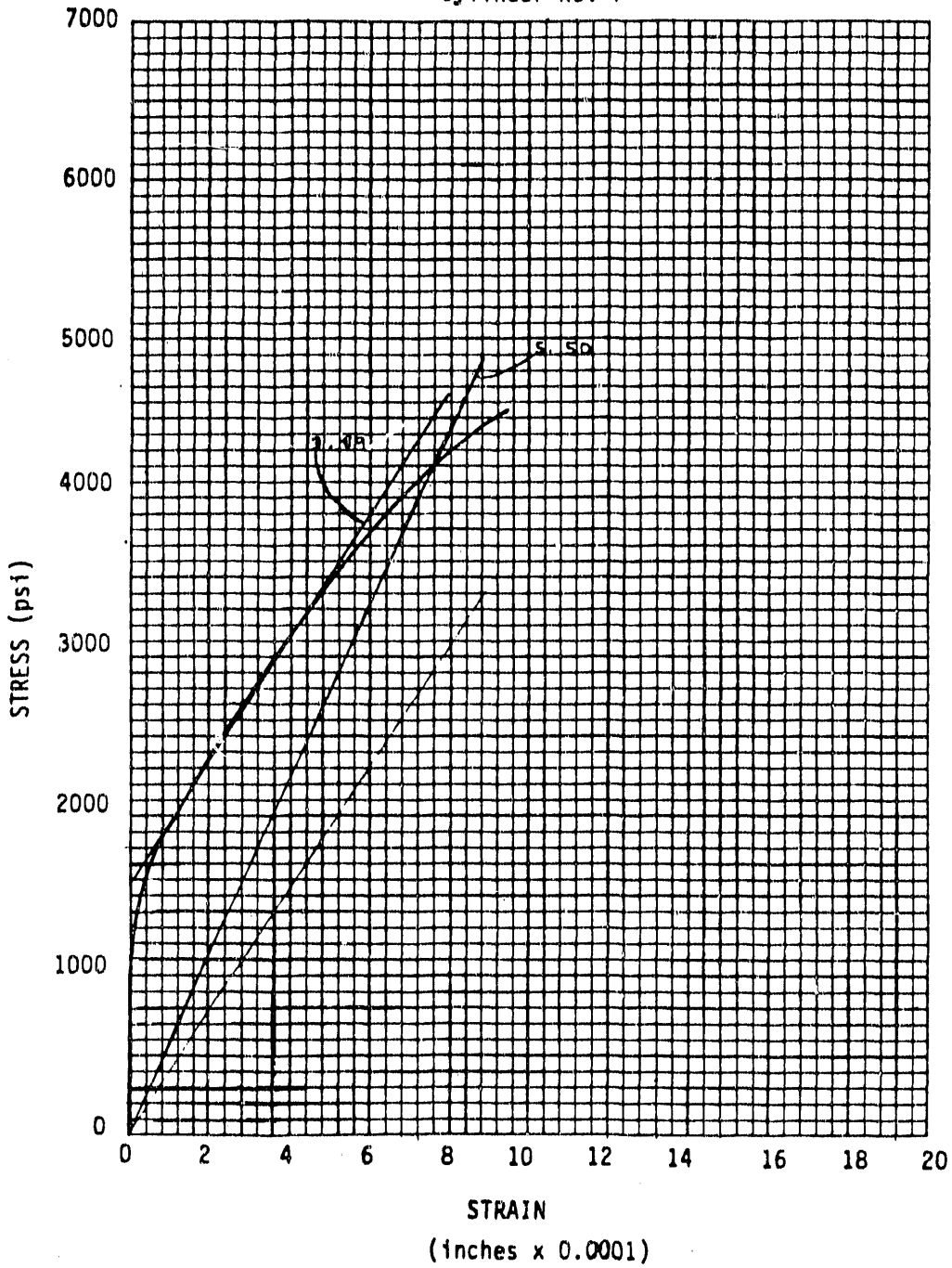
PROJECT NAME
 Concrete Testing
 Los Alamos Labs
 Los Alamos, NM

$E = 4.889 \times 10^6$
 Ult. Compressive Strength = 5095 psi

PROJECT NO
 531-70177-1

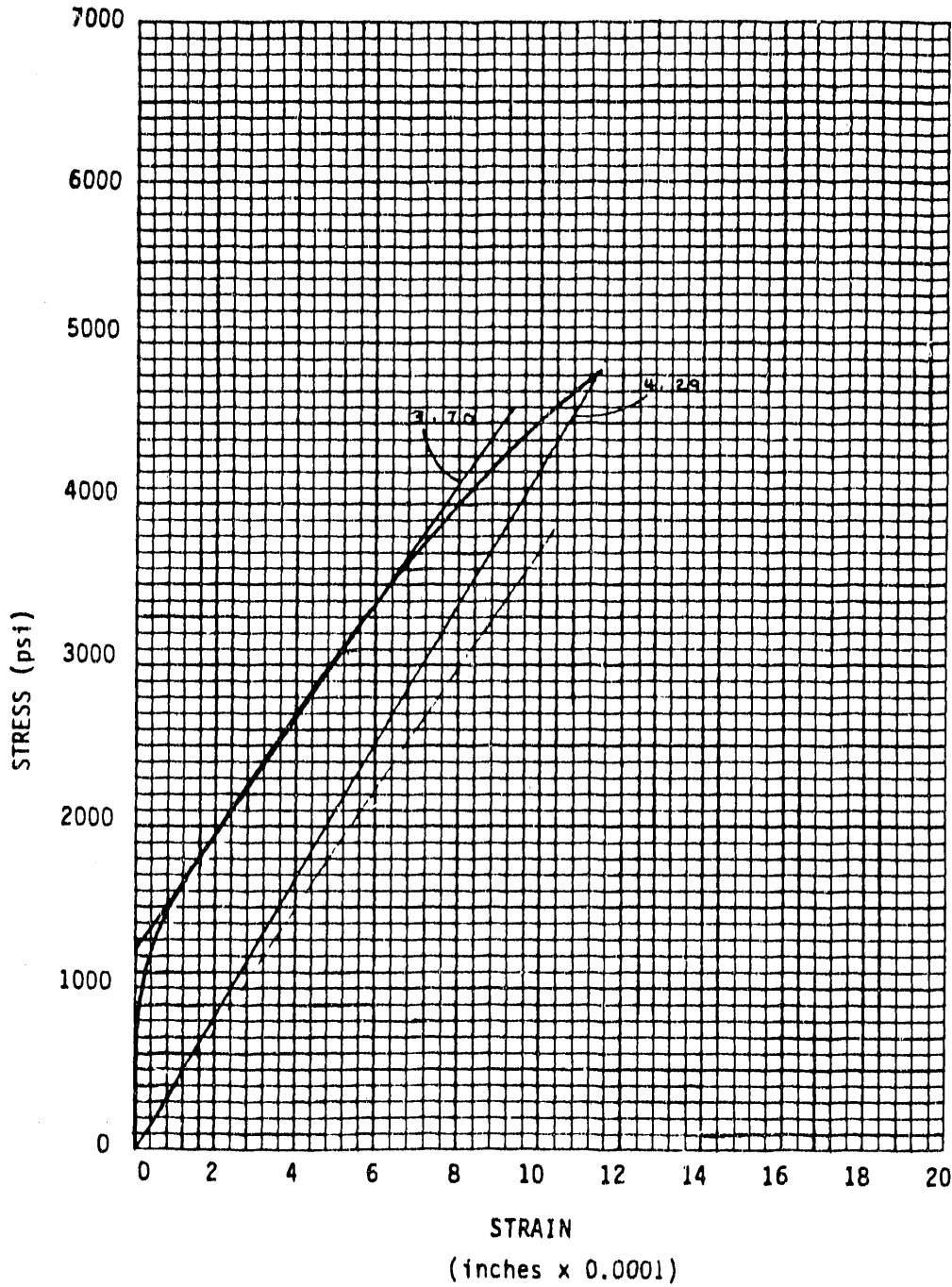
DATE
 9/26/87

TRG #5
 Truck No. 1
 Cylinder No. 7



PROJECT NAME Concrete Testing Los Alamos Labs Los Alamos, NM	E = 5.500 x 10 ⁶	
	Ult Compressive Strength = 4720 psi	
	PROJECT NO 531-70177-1	DATE 9/26/87

TRG #5
 Truck No.1
 Cylinder No.8



PROJECT NAME
 Concrete Testing
 Los Alamos Lab
 Los Alamos, NM

$E = 4.294 \times 10^6$
 Ult Compressive Strength = 5075 psi

PROJECT NO
 531-70177-1

DATE
 9/26/87

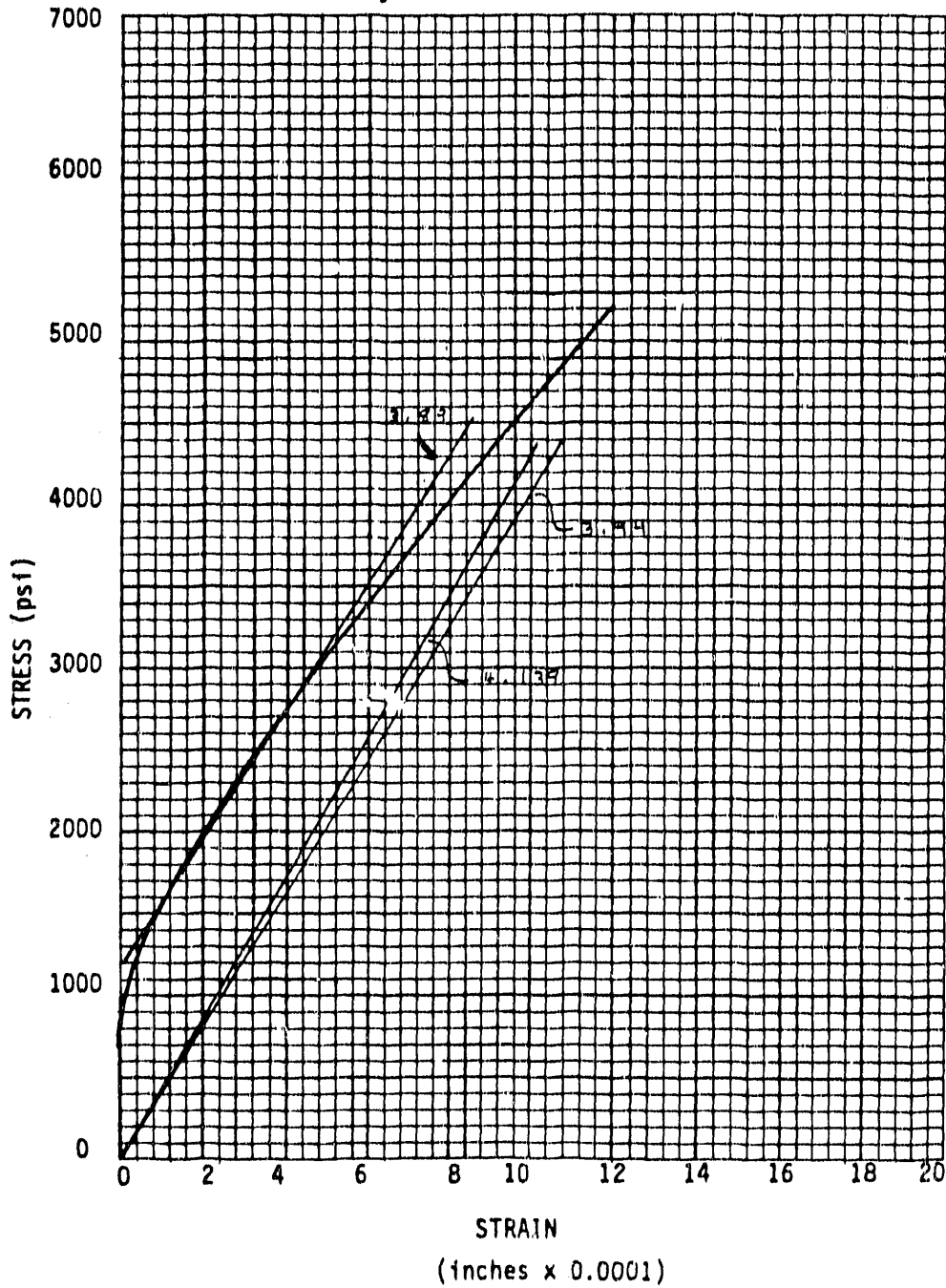
Client: Los Alamos Labs
Project: Concrete Testing
Project No. 531-70177
Date: September 26, 1987

REPORT OF SPLIT TENSILE TESTS

TRG #5 Truck No. 1

<u>Cylinder Number</u>	<u>Unit Weight (pcf)</u>	<u>Split Tensile Strength (psi)</u>
1	142.6	395
2	143.6	350
3	142.3	365
4	<u>144.1</u>	<u>305</u>
Average:	143.1	355

TRG #5
 Truck No.2
 Cylinder No. 1



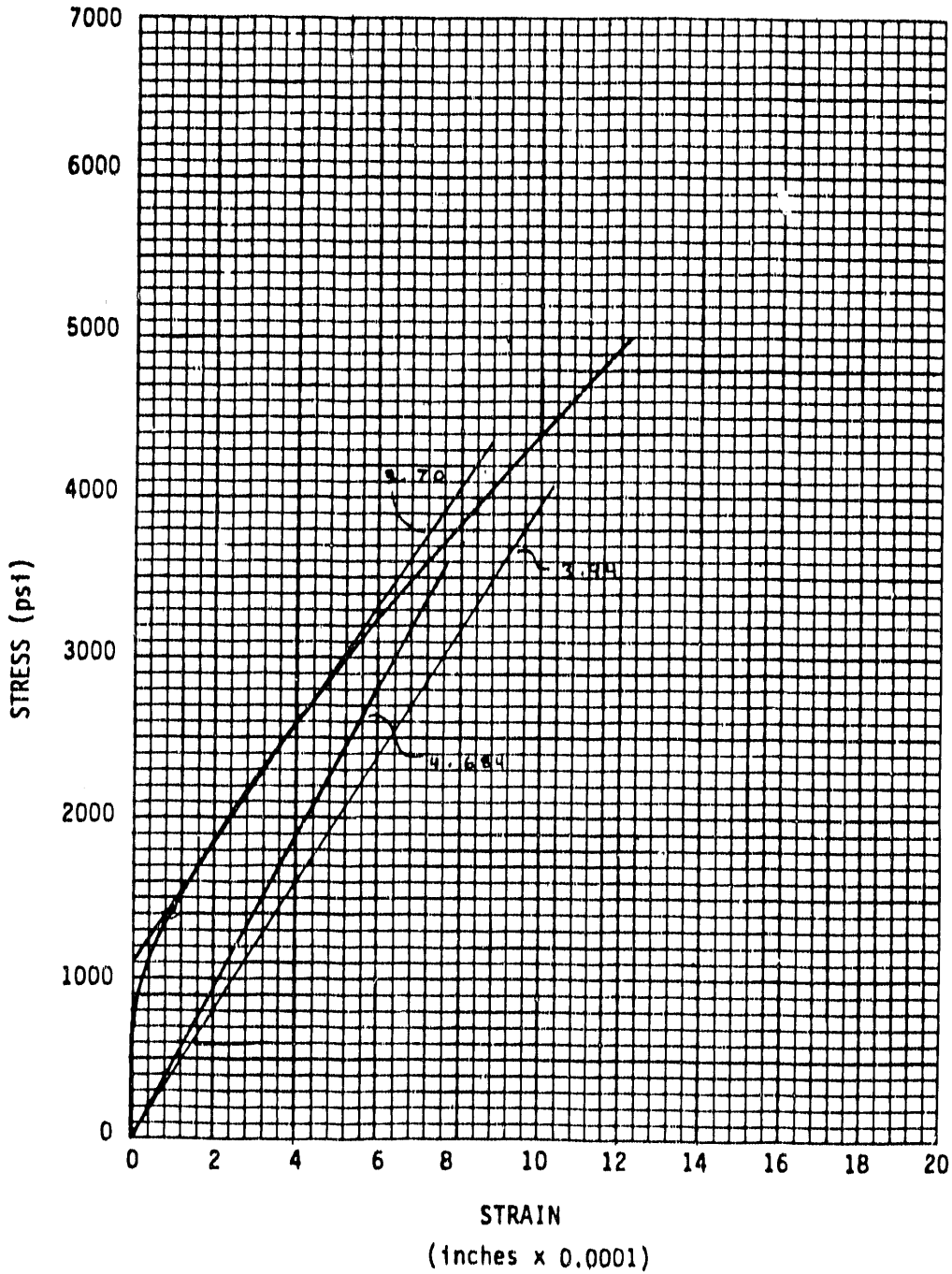
PROJECT NAME
 Concrete Testing
 Los Alamos Labs
 Los Alamos, NM

$E = 4.139 \times 10^6$
 Ult. Compressive Strength = 5240 psi

PROJECT NO
 531-70177-1

DATE
 9/26/87

TRG #5
Truck No. 1
Cylinder No. 2



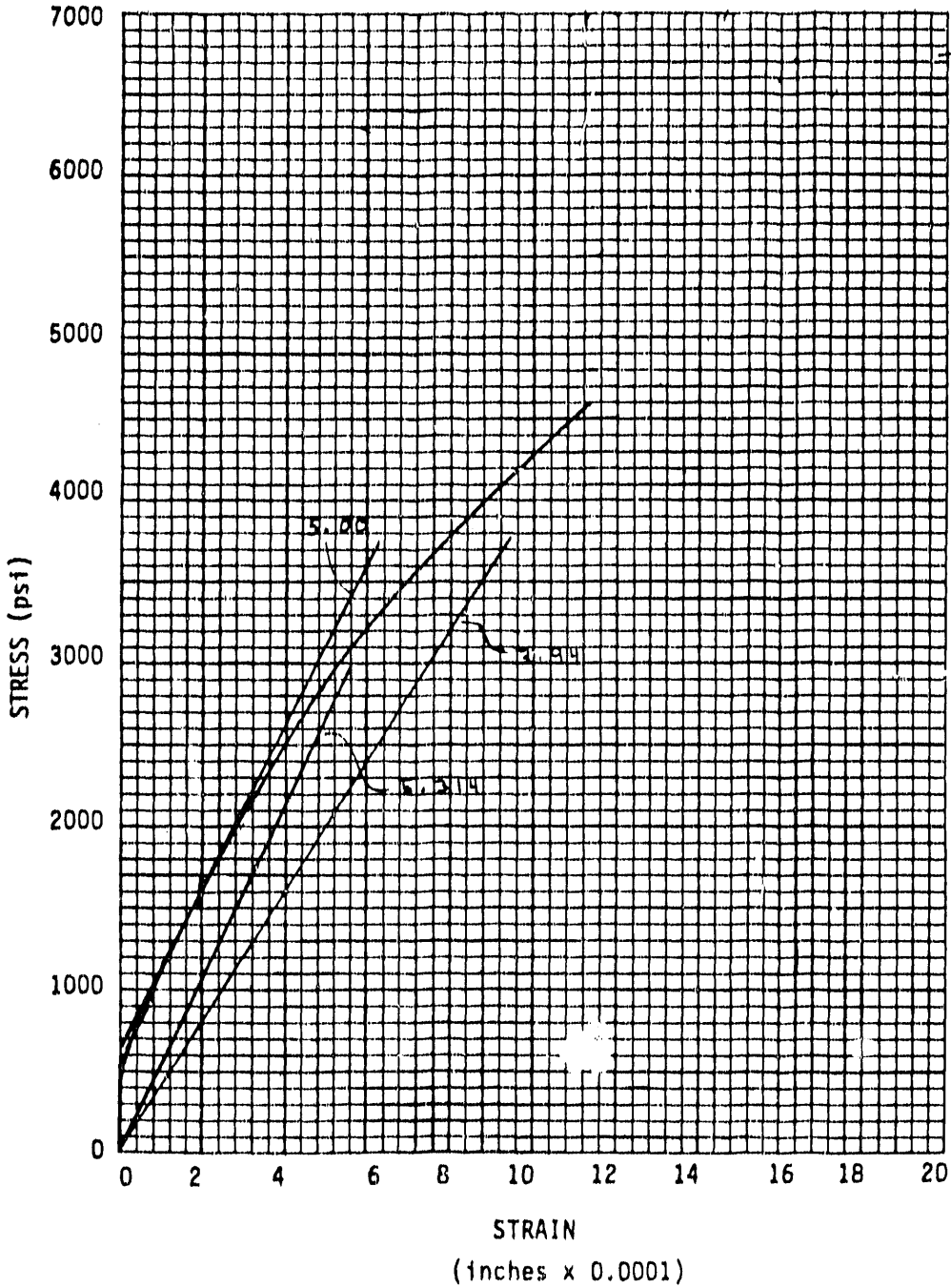
PROJECT NAME
Concrete Testing
Los Alamos Labs
Los Alamos, NM

$E = 4.684 \times 10^6$
Ult. Compressive Strength = 5020 psi

PROJECT NO
531-70177-1

DATE
9/26/87

TRG #5
 Truck No. 2
 Cylinder No.3



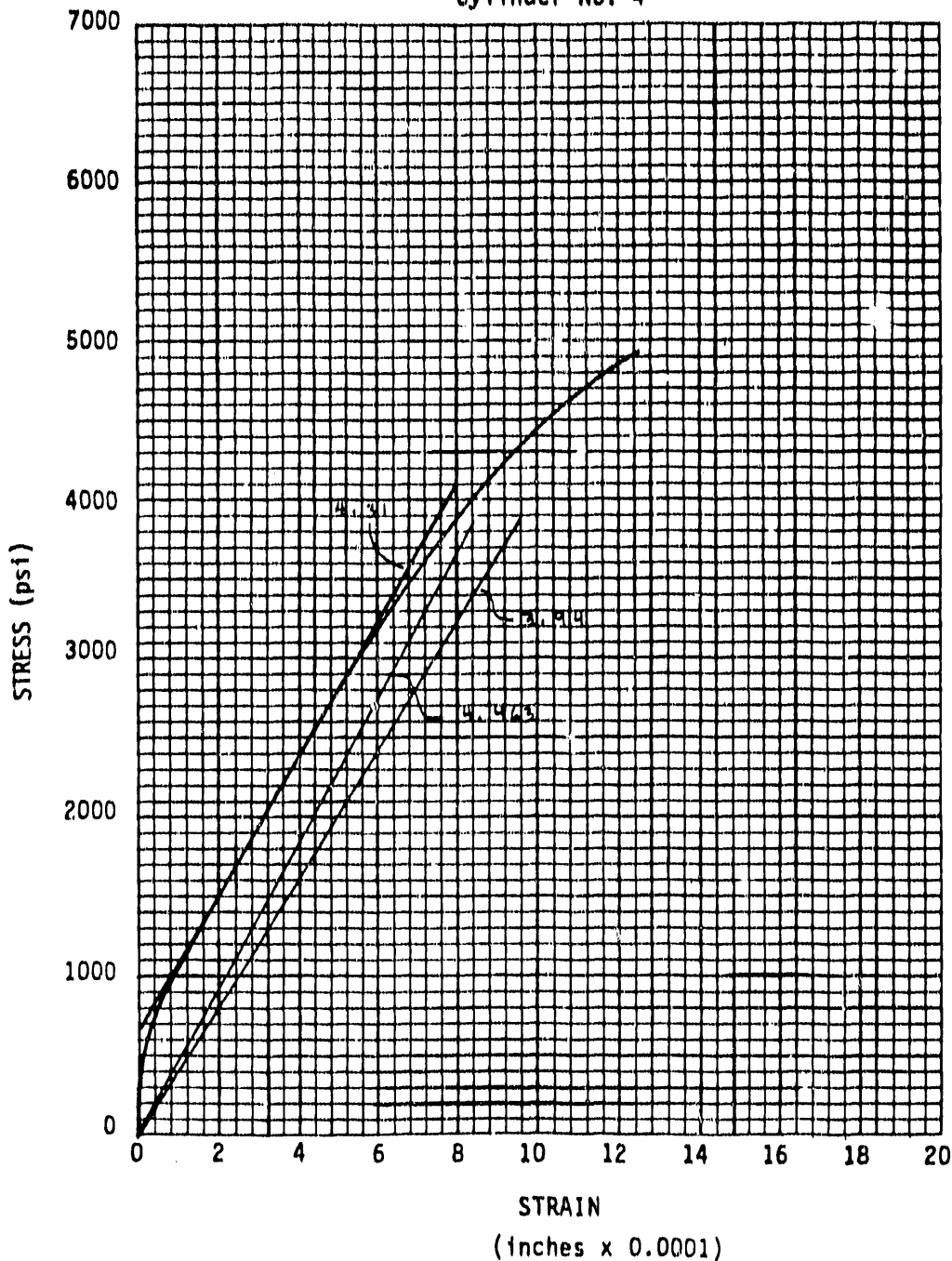
PROJECT NAME
 Concrete Testing
 Los Alamos Labs
 Los Alamos, NM

$E = 5.314 \times 10^6$
 Ult. Compressive Strength = 4790 psi

PROJECT NO
 531-70177-1

DATE
 9/26/87

TRG #5
Truck No.2
Cylinder No. 4



PROJECT NAME

Concrete Testing
Los Alamos Labs
Los Alamos, NM

$$E = 4.463 \times 10^6$$

Ult. Compressive Strength = 5220 psi

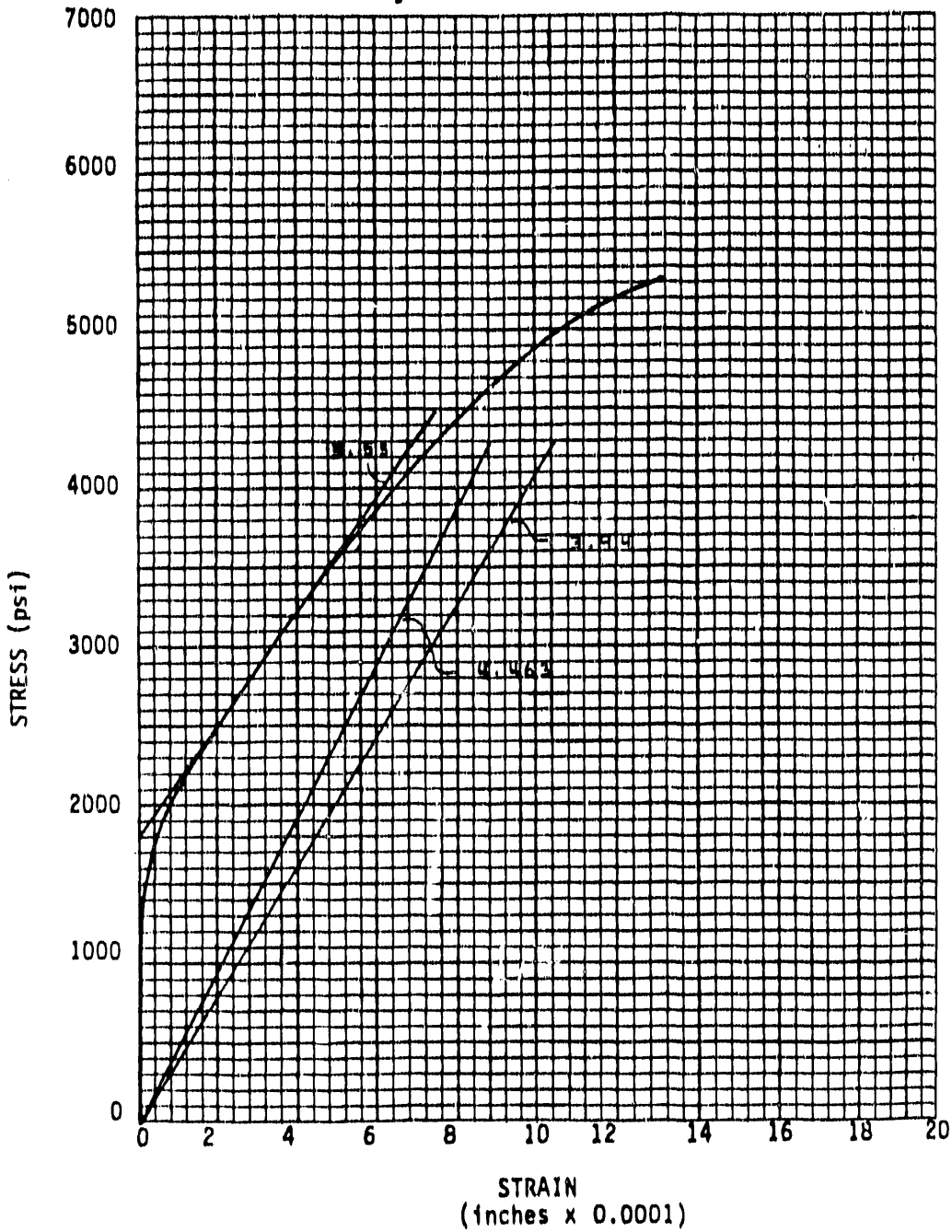
PROJECT NO

531-70177-1

DATE

9/26/87

TRG #5
 Truck No. 2
 Cylinder No. 5



PROJECT NAME

Concrete Testing
 Los Alamos Labs
 Los Alamos, NM

$E = 4.463 \times 10^6$
 Ult. Compressive Strenght = 5390 psi

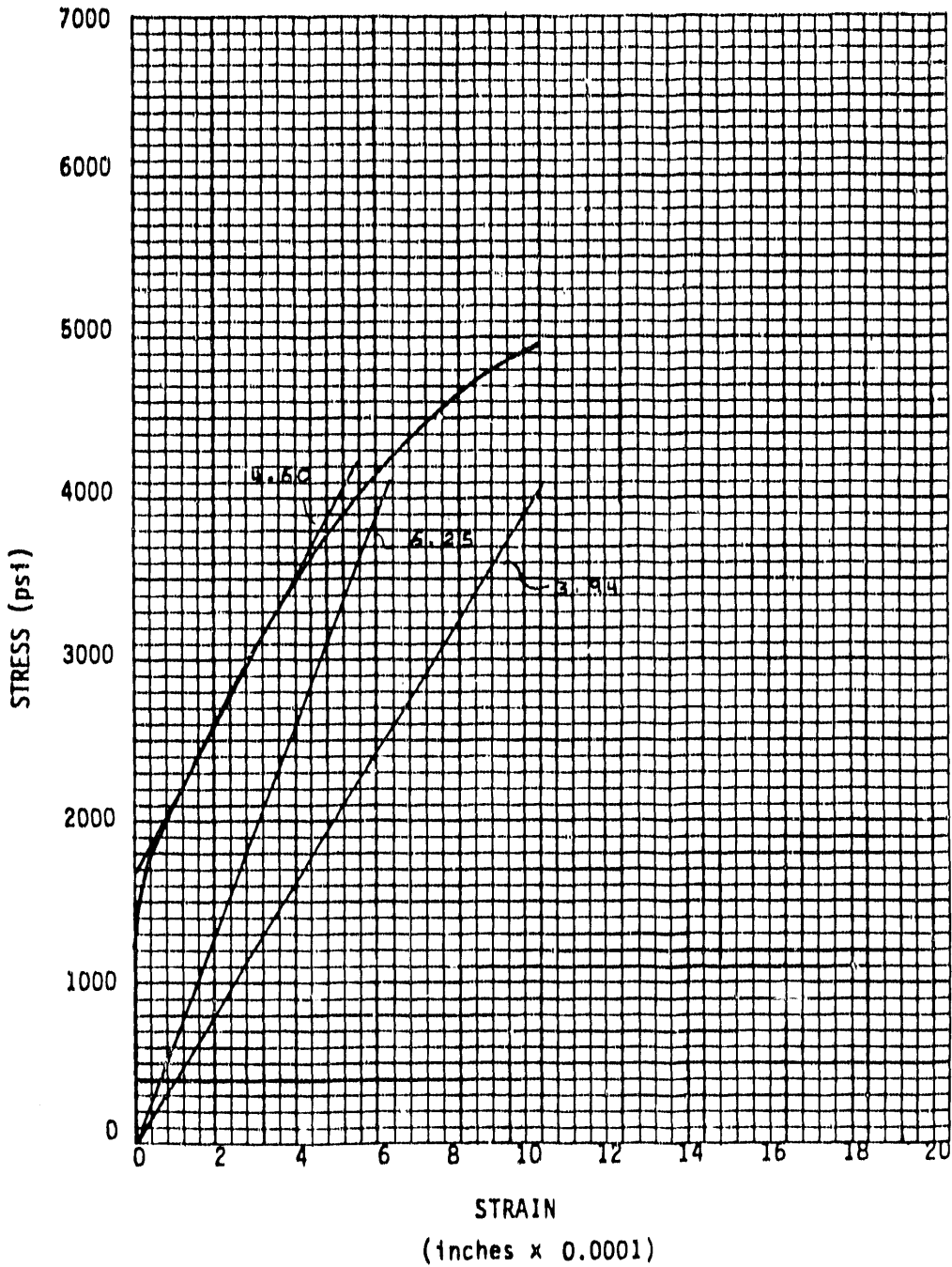
PROJECT NO

531-70177-1

DATE

9/26/87

TRG #5
Truck No. 2
Cylinder No.6



PROJECT NAME

Concrete Testing
Los Alamos Labs
Los Alamos, NM

$E = 6.250 \times 10^6$

Ult. Compressive Strength = 5130 psi

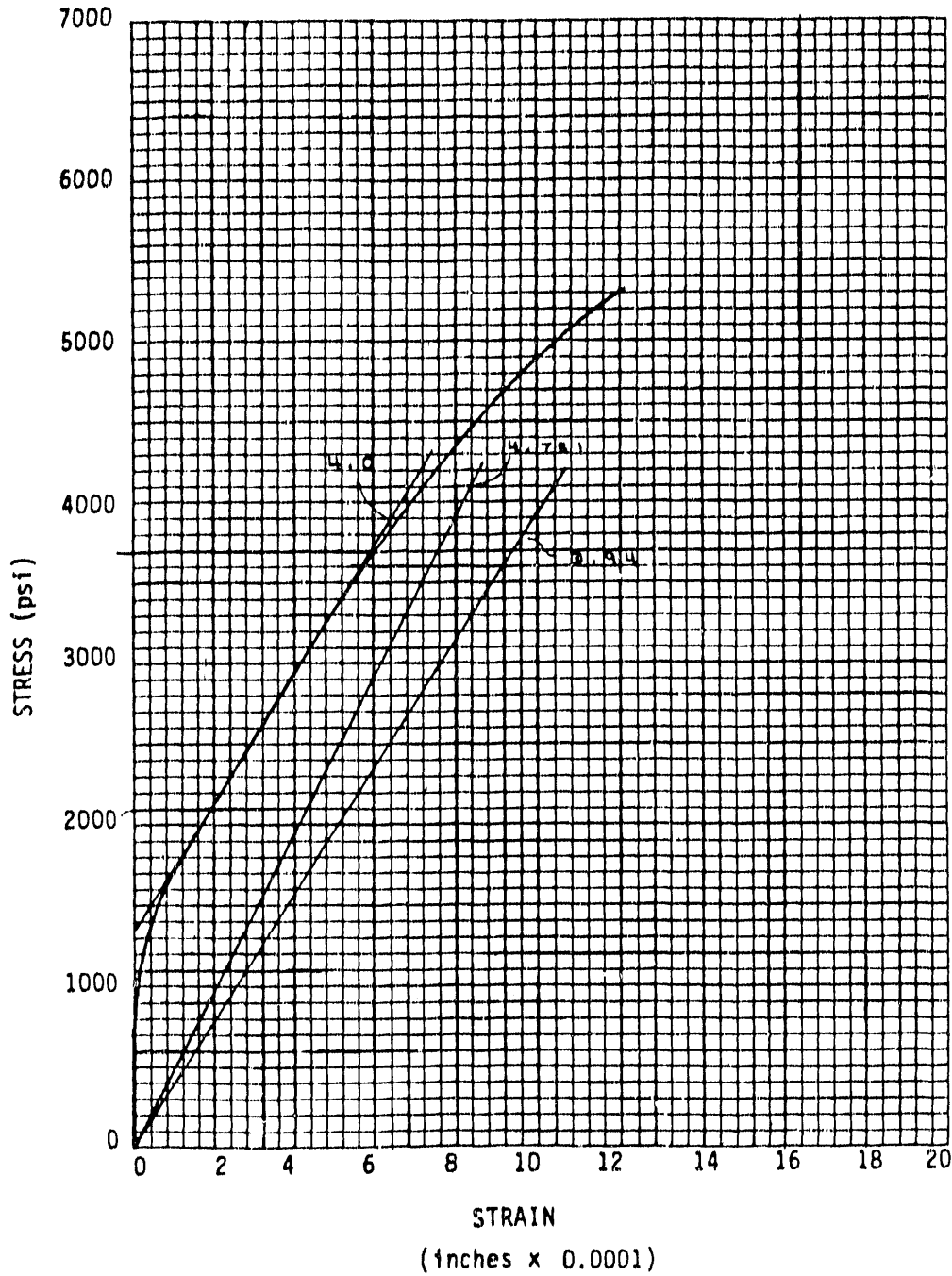
PROJECT NO

531-70177-1

DATE

9/26/87

TRG #5
 Truck No. 2
 Cylinder No. 7



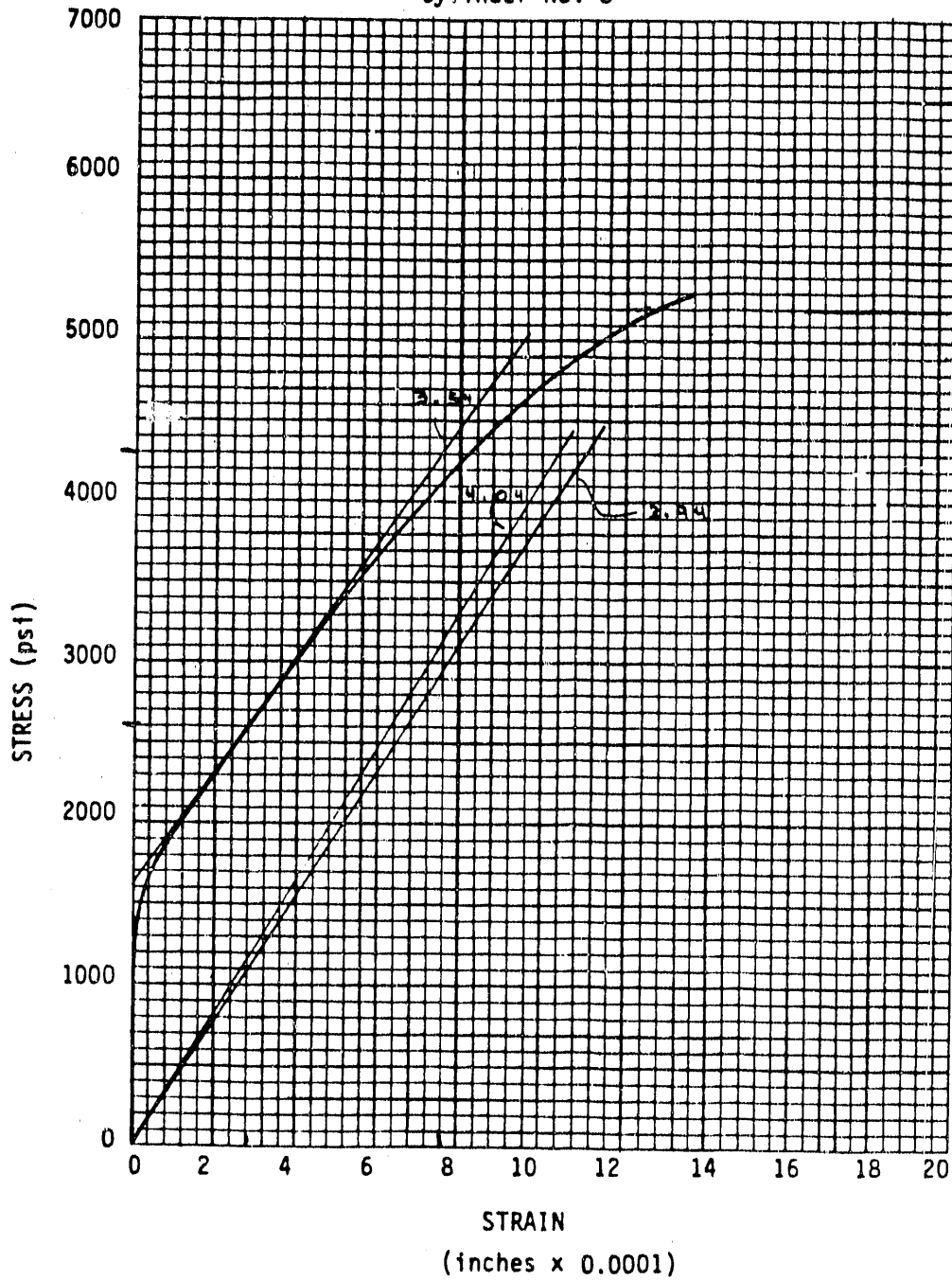
PROJECT NAME
 Concrete Testing
 Los Alamos Labs
 Los Alamos, NM

$E = 4.781 \times 10^6$
 Ult. Compressive Strength = 5410 psi

PROJECT NO
 531-70177-1

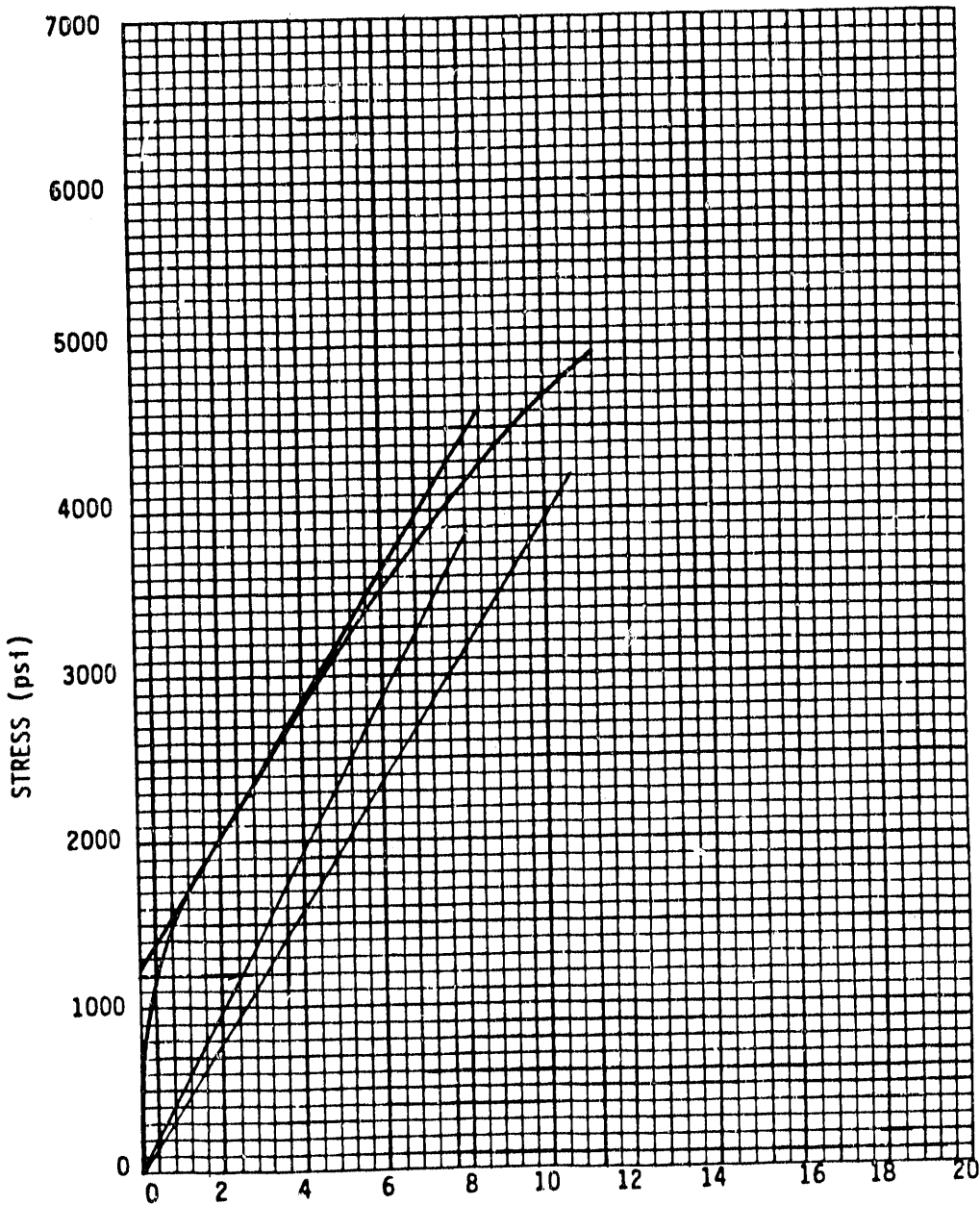
DATE
 9/26/87

TRG #5
 Truck No. 2
 Cylinder No. 8



PROJECT NAME Concrete Testing Los Alamos Labs Los Alamos, NM	E = 4.045 x 10 ⁶	
	Ult. Compressive Strenght = 5360 psi	
	PROJECT NO 531-70177-1	DATE 9/26/87

TRG #5
 Truck No. 2
 Average *



* Note: Average of
 Stress & Strain
 Readings
 Unit Wt.: 142.8 pcf

STRAIN
 (Inches x 0.0001)

PROJECT NAME

Concrete Testing
 Los Alamos Labs
 Los Alamos, NM

$E = 4.633 \times 10^6$

Ult. Compressive Strength = 5195 psi

PROJECT NO

531-70177-1

DATE

9/26/87

APPENDIX B
LUKE SNELL TEST REPORT

LUKE M. SNELL, P.E.

18 Fourth Avenue
Stardsville IL 62025

CONSTRUCTION & MATERIALS CONSULTANT

Office: (618) 692-2500
Home: (618) 692-0691

September 3, 1987

Joel Bennett
Los Alamos National Laboratory
MS J576
Los Alamos, NM 87545

Subject: Inspection of TRG-5 and TRG-6 Models
Los Alamos National Laboratory
Los Alamos, New Mexico
Our Job No. LS87-354

Gentlemen:

The writer has completed the inspection of the above referenced models. The purpose of this inspection was to determine the uniformity of the concrete and to determine if the concrete contained flaws. This report documents our findings.

On August 24 and 25, 1987, the writer examined the TRG-5 and TRG-6 models. The examination consisted of two separate inspections. The first was a visual inspection using hand-held magnifying glasses. The second inspection was to determine the velocities of ultrasonic waves through the concrete.

The velocity of the ultrasonic wave was determined by measuring the wall thickness and measuring the time for the ultrasonic wave or a pulse to travel from a sending transducer, through the concrete to a receiving transducer; the velocity of the ultrasonic wave or the pulse velocity was then calculated by: pulse velocity = distance divided by time.

Past experience and research has shown that the pulse velocity value can be related to concrete strength and the static modulus of elasticity. Also, if the pulse velocities are relatively uniform, then the concrete is assumed to be of uniform quality and without flaws.

The equipment is generically called pulse velocity equipment. Our equipment is manufactured by James Electronic Company and is called the V-meter. The testing of each model will be discussed separately.

Model TRG-5

During our testing the following was determined:

1. The visual inspection indicated that the model had several internal and external voids that had been repaired. Several of these repairs appeared to be satisfactory. Other repairs were poorly bonded to the concrete and were easily removed. Several surface voids were also noted. The model does not appear to have internal voids that had not been repaired.
2. Test cylinders: Four concrete test cylinders were examined to determine their pulse velocity. The cylinders were made from the two trucks that provided concrete to make the model. The pulse velocities ranged from 14,300 to 14,700 ft./sec. with an average velocity of 14,500 ft./sec.
3. Shear wall: 36 pulse velocities were determined for the shear wall. These pulse velocity ranged from 11,400 to 14,400 feet per second with an average of 13,100 feet per second.
4. Base: 4 pulse velocities were determined on the base. The pulse velocities ranged from 12,800 to 13,600 feet per second with an average velocity of 13,300 feet per second.
5. Roof: 8 pulse velocities were determined on the roof. The pulse velocities ranged from 12,300 to 13,300 feet per second with an average velocity of 13,000 feet per second.
6. Northwest Wing Wall: 20 pulse velocities were determined on this wing wall. These pulse velocities ranged from 12,800 to 14,300 feet per second with an average velocity of 13,400 feet per second.
7. Northeast Wing Wall: 20 pulse velocities were determined on this wing wall. These pulse velocities ranged from 12,000 to 14,300 feet per second with an average velocity of 13,200 feet per second.
8. Southwest Wing Wall: 20 pulse velocities were determined on this wing wall. These pulse velocities ranged from 12,400 to 14,900 feet per second with an average velocity of 13,600 feet per second.
9. Southeast Wing Wall: 20 pulse velocities were determined on this wing wall. These pulse velocities ranged from 13,200 to 14,100 feet per second with an average velocity of 13,700 feet per second.

The pulse velocities of the four concrete cylinders were nearly identical. This indicates that the concrete strength and static modulus of elasticity for each load of concrete would be similar.

The pulse velocities in the model were not uniform and were below the pulse velocities of the tested concrete cylinders. This indicates that the concrete in the model is not uniform and the test cylinders may not accurately describe the concrete strength and the modulus of elasticity of the model.

The use of pulse velocities to estimate compressive strength and static modulus of elasticity is inexact and should be used only to indicate approximate values. Using the generalized data developed from past research, the compressive strength of the model would be variable but should exceed 3,000 psi. The static modulus of elasticity would also be variable but should exceed 3,000,000 psi.

Model TRG-6

During our testing the following was determined:

1. Visual Inspection: The visual inspection indicated that this model did not appear to have external voids.
2. Test Cylinders: Two 6 x 12 inch cylinders were examined to determine pulse velocities. These pulse velocities had an velocity of 14,100 feet per second. There was no variation in the pulse velocity between cylinders.
3. Shearwall: 8 pulse velocities were determined for the shear wall. These pulse velocities ranged from 13,500 to 14,300 feet per second with an average of 13,900 feet per second.
4. Base: No readings were determined for the base.
5. Roof: 19 pulse velocities were determined on the roof. The pulse velocities ranged from 12,900 to 13,700 feet per second with an average velocity of 13,100 feet per second.
6. Wing Walls: 8 pulse velocities were determined on the wing walls. These pulse velocities ranged from 13,000 to 14,000 feet per second with an average velocity of 13,600 feet per second.

The pulse velocities in the model were fairly uniform and similar to the pulse velocities of the tested cylinders. This indicates that the concrete in the structure is of uniform

quality and that the concrete strength and static modulus of elasticity of the model can be accurately determined from the concrete cylinders.

Since the pulse velocities were fairly uniform and the visual inspection did not indicate any external flaws, it is our opinion that the concrete model does not contain internal flaws.

The use of pulse velocities to estimate compressive strength and static modulus of elasticity is inexact and should be used only to indicate approximate values. Using the generalized data developed from past research, the compressive strength would be in excess of 3,000 psi and static modulus of elasticity would be in excess of 3,000,000 psi.

Conclusions

I was instructed that Model TRG-5 will have additional repairs to the surface flaws. In my opinion, these repairs (if well bonded and of comparable concrete strength) will eliminate some of the non-uniformity of the concrete in the model.

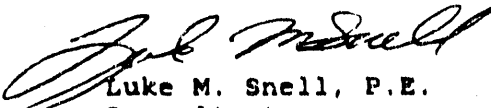
The variations of the pulse velocity in this model and the lower pulse velocities of the model to the test cylinders indicates that the concrete in the model is non-uniform and may be of lower strength than the test cylinders. The percent of repaired concrete is quite small (estimated to be less than 2%). If the repairs are successfully completed, its impact on the structural behavior would likely be insignificant.

The lower strength of the concrete in this model (as compared to the test cylinders) and the variation of the concrete may have an influence on the structural behavior.

Model TRG-6 appears to be well made and no apparent problems were noted. The concrete cylinders appear to be consistent with the concrete in the model and will be a good indication of the strength of the concrete in the model.

It has been a privilege working with you on this project. If you have any questions or if we can be of future service, please do not hesitate to call.

Very truly yours,


Luke M. Snell, P.E.
Consultant

APPENDIX

FIELD MEASUREMENTS FOR TRG-5

Cylinders (6 x 12 inch)

Truck #1	Time in 10^{-6} Seconds
Cylinder 1	68
Cylinder 2	70
Truck #2	
Cylinder 1	68
Cylinder 2	69

Shear Wall - Thickness = 4 inches

Readings on approximately 1' centers
Measured from base

Distance From Westwall (inches)	Time in 10^{-6} Seconds
10	23.2, 23.3, 24.1, 25.3, 27.9, 26.9
24	23.4, 23.5, 24.5, 25.9, 25.0, 24.9
36	24.1, 24.1, 24.3, 26.0, 25.7, 26.4
48	25.9, 27.1, 26.7, 26.9, 26.3, 26.4
60	25.5, 29.2*, 26.7, 26.9, 25.4, 25.3
72	25.1, 25.6, 25.1, 26.1, 25.3, 25.0

Test on Repair - 26.1

*Took several readings in this area. The shear wall in this area appears to have surface flaws.

Walls - Thickness = 4 inches

Readings on approximately one foot centers
Measured from Shear Wall

Distance from Base (in feet)	Time in 10^{-6} Seconds			
	Southwest Wall			
1	24.4	26.5	25.1	25.4
2	24.3	25.7	25.4	23.5
3	23.3	22.4	24.1	25.2
4	24.1	23.0	25.4	24.8
6	24.4	22.9	23.1	25.9
	Northwest Wall			
1	24.4	24.9	29.3	24.4
2	25.1	26.0	24.9	23.9
3	24.5	25.8	24.3	25.3
4	25.4	25.9	24.4	24.9
6	25.5	23.3	23.8	24.9
	Southeast Wall			
1	23.7	23.6	23.7	23.6
2	23.8	24.4	23.7	23.6
3	23.7	25.1	23.3	24.6
4	24.9	25.0	25.0	24.3
6	23.8	23.8	23.3	24.4
	Northeast Wall			
1	24.4	24.5	25.2	24.9
2	24.9	25.0	25.1	25.9
3	25.3	24.8	25.0	24.9
4	26.8	27.7	25.5	25.5
6	23.3	23.8	24.0	24.7

Roof - Thickness = 8 inches

Location	Time x 10 ⁻⁶ Seconds
	North
At quarter points	54, 51, 50, 51
	South
At quarter points	51, 50, 50, 53

Base - Thickness = 8 inches

Location	Time x 10 ⁻⁶ Seconds
	South
At front quarter points	49, 52
	North
At front quarter points	51, 49

APPENDIX

FIELD MEASUREMENTS FOR TRG-6

TRG-6

Roofs - Thickness = 8 inches

Readings on approximately 1.5 feet intervals
Measured from East Wall

North

Distance	Time x 10 ⁻⁶ Seconds
1 foot from opened end	49.5, 49.9, 49.6, 51.9
1 foot from shear wall	51.7, 50.4, 51.7, 51.6
2.5 feet from opening	50.1, -, -, 52.9

South

1 foot from open end	49.1, 48.5, 49.9, 51.9
1/2 foot from shear wall	52.5, 53.7, 51.5, 53.5

TRG-6 Shear Wall - Thickness = 8 inches

Readings on approximately 1.5 feet center
Measured from East Wall

Distance	Time x 10 ⁻⁶ Seconds
1 foot from roof	35.9, 35.7, 36.1, 37.1
1 foot from bottom	35.0, 36.1, 36.1, 35.9

TRG-6 Walls - Thickness = 6"

Readings on approximately 2 feet intervals
Measures from open end

Distance	Northwest	Time x 10 ⁻⁶ Seconds
1.5 feet from top		37.9, 38.4
	Northeast	
1.5 feet from top		36.7, 36.5
	Southwest	
1.5 feet from top		35.8, 36.8
	Southeast	
1.5 feet from top		36.5, 36.6

NRC FORM 335 <small>7-59 NRCN-1102 7001, 3202</small>		U.S. NUCLEAR REGULATORY COMMISSION		1 REPORT NUMBER <small>(Assigned by NRC. Add Vol. Supp. Rev. and Addendum Numbers, if any.)</small> NUREG/CR-5487 LA-11739-MS					
BIBLIOGRAPHIC DATA SHEET <small>(See instructions on the reverse)</small>									
2 TITLE AND SUBTITLE Static Load Cycle Testing of a Low-Aspect-Ratio Four-Inch Wall, TRG-Type Structure TRG-5-4 (1.0, 0.56)				3 DATE REPORT PUBLISHED <table border="1"> <tr> <td style="text-align: center;">MONTH</td> <td style="text-align: center;">YEAR</td> </tr> <tr> <td style="text-align: center;">November</td> <td style="text-align: center;">1990</td> </tr> </table>		MONTH	YEAR	November	1990
MONTH	YEAR								
November	1990								
5 AUTHOR(S) Charles R. Farrar, Joel G. Bennett, Wade E. Dunwoody, and William E. Baker*				4 FIN OR GRANT NUMBER A7221					
6 TYPE OF REPORT Technical				7 PERIOD COVERED (Inclusive Dates)					
8 PERFORMING ORGANIZATION - NAME AND ADDRESS (If NRC, provide Division, Office or Region, U.S. Nuclear Regulatory Commission, and mailing address; if contractor, provide name and mailing address.) Los Alamos National Laboratory Los Alamos, New Mexico 87545									
9 SPONSORING ORGANIZATION - NAME AND ADDRESS (If NRC, type "Same as above"; if contractor, provide NRC Division, Office or Region, U.S. Nuclear Regulatory Commission and mailing address.) Division of Engineering Office of Nuclear Regulatory Research U.S. Nuclear Regulatory Commission Washington, DC 20555									
10 SUPPLEMENTARY NOTES *Consultant at Los Alamos. Mechanical Engineering Department, University of New Mexico, Albuquerque, NM 87131									
11 ABSTRACT (200 words or less) <p>This report is the second in a series of test reports that details the quasi-static cyclic testing of low height-to-length aspect ratio reinforced concrete structures. The test structures were designed according to the recommendations of a technical review group for the U.S. Nuclear Regulatory Commission sponsored Seismic Category I Structures Program. The structure tested and reported here had 4-in.-thick shear and end walls, and the elastic deformation was dominated by shear. The background of the program and previous results are given for completeness. Details of the geometry, material property tests, construction history, ultrasonic testing, and modal testing to find the undamaged dynamic characteristics of the structures are given. Next, the static test procedure and results in terms of stiffness and load deformation behavior are given. Finally, results are shown relative to other known results, and conclusions are presented.</p>									
12 KEY WORDS/DESCRIP'TORS (List words or phrases that will assist researchers in locating the report.) earthquake building response reinforced concrete structures stiffness				13 AVAILABILITY STATEMENT Unlimited					
				14 SECURITY CLASSIFICATION <small>(This Page)</small> Unclassified <small>(This Report)</small> Unclassified					
				15 NUMBER OF PAGES					
				16 PRICE					

END

DATE FILMED

12 / 10 / 90

